CATALYTIC CONVERSION OF NITROGEN TO

AMMONIA BY AN IRON MODEL COMPLEX

Thesis by

John S. Anderson

In Partial Fulfillment of the Requirements for the

Degree of Doctor of Philosophy

California Institute of Technology

Pasadena, CA

2014

(Defended September 3, 2013)

Acknowledgements

Throughout the course of my doctoral studies, I have been blessed to be surrounded by some of the most intelligent, helpful, and enjoyable people in the world. Any success that I may have had during my Ph.D. reflects more on the capabilities of the people around me than on any trait of my own. A large number of people have contributed to this work either directly in the form of co-workers and collaborators, or indirectly in the form of people who did not work on the science herein, but without whom this work would not have been possible. I will do my best to thank all of them.

Firstly, I have to thank Professor Jonas Peters. As many will tell you, Jonas is a fantastic advisor and I could not have asked for a better mentor for the past five years. Jonas is far more intelligent than he gives himself credit for and has a unique gift in the design and implementation of research projects. His approach to scientific problems and his thought process in designing experiments is something I hope I will take with me as I leave my doctoral studies. I also have to thank him for the patience he has shown in developing me as a scientist. I am far from a finished product, but any progress that I have made is largely a result of his efforts. Aside from his scientific prowess, Jonas has been a thoroughly helpful and thoughtful person to work with and, in general, an exceptional human being. Any professor can attest that time comes as a premium, but Jonas has consistently managed this research lab in a remarkable manner and has been a pleasure to work with. Although it is difficult to be friends with your advisor during the course of one's Ph.D., I have enjoyed my time working for him immensely and look forward to our future interactions.

During the move from M.I.T. to CalTech, I spent a brief "sabbatical" in the laboratories of Professor Greg Fu. Although the joint project I was working on during that time was an unmitigated disaster, I enjoyed the members of the Fu lab that I met during that time, some of whom I still talk to today. I also have to thank Greg for letting me work in his lab, and for our interactions during that time and since. The Fu lab has since moved to CalTech as well and having them across the hall has been great.

Four graduate students started in the same year as I did, and then there was one. I find it unlikely that I was the only person during my year that graduated with a Ph.D. from the Peters lab, considering the exceptionally talented group of students that I came in with. I would like to thank Laura Gerber, Kenny Lotito, and Alicia Chang for the social and scientific interactions that we had during our time together. I hope our paths will cross again in the future.

Outside of my classmates, the Peters lab has been filled with a an outstanding group of people. I shared a glovebox with Caroline Saouma during my early time in the lab and I have to thank her for getting me started in the laboratory. Although the time that we spent together was relatively short, Professor Neal Mankad is an impressive scientist and continues to host our yearly fantasy football league. Professor Yunho Lee brought an incredibly cheerful demeanor to the lab every day and I thank him for it. I would also like to thank Professor Nate Szymczak for getting me started on electrochemistry and for, despite being a vegan, being an overall good labmate. I did not interact with Professor Louise Berben very much during my time in the Peters Lab, but I still have the koala she brought back from Australia for everyone in the lab. Samantha Macmillan was also a part-time glovebox mate as well as perhaps the best person in the

lab to talk to. Charlene Tsay was also a glovebox partner for some time and I have to thank her for putting up with my mess frequently.

Daniel Suess has been a brilliant, eccentric, and hysterical co-worker throughout my Ph.D. I have learned a great deal about chemistry through my discussions with Dan and I have to thank him for all of the help he has given me over the past five years. Similarly, Professor Hill Harman has brought a unique, and sometimes belligerent, outlook on chemical problems. In many ways his insights have made me re-evaluate the way I think about molecules. Dr. Ayumi Takaoka was a good friend before he fled this country for Japan. Early on in my Ph.D. Ayumi frequently referred to me as being "too much of a cowboy." Although I didn't realize it at the time, I had a lot to learn from Ayumi about scientific rigor. Fortunately, he had a lot to learn from me about fantasy football, and the lessons are ongoing. I frequently enjoyed talking to Professor Chris Uyeda, and his knowledge of synthesis has been a great resource during my doctoral studies.

Dr. Marc-Etienne Moret was a co-author with me, and is in general more enthusiastic about chemistry than any other person I know. He thinks deeply about chemical problems and one can not help but be enlightened by discussions with him. Dr. Charles McCrory has put up with many hours of my questions about electrochemistry and other physical methods which are frequently beyond the scope of my knowledge. Although he is often grumpy, I personally enjoy Charles' dour moods, and must sincerely thank him for all of his help. More recently, I have had the pleasure of working with Dr.'s Yichen Tan and Tzu-Pin Lin, who I have to thank for discussions about chemistry

and life in general. Dr. David Lacy has been a great person to talk to and I specifically have to thank him for our discussions on oxo species.

Henry Fong is likely the nicest person in the lab, and we have spent time together both in outreach (which was often laborious) as well as on the basketball court. I always look forward to seeing Henry, and I suspect that I may see more of him in the future in Chicago. Sid Creutz has had to sit in the same cubicle with me for a number of years. While Sid has never complained, he rarely speaks at all, so I can only assume that he doesn't mind. Sid has, however, been a great and very intelligent co-worker who continues to do excellent work in the lab.

During the last portion of my Ph.D., I had the privilege of monopolizing a glovebox with Jon Rittle, hereafter referred to as JR. JR is an incredibly gifted chemist and has a nearly unmatched intensity with which he attacks scientific problems. While this intensity can often lead to bad moods and arguments, JR is usually right and possesses a keen mind for chemistry. Additionally, JR has been my, potentially unwilling, partner in crime on a great deal of my Ph.D. work, and I certainly would not have been able to complete these projects without his help. Despite his love of country music, JR has been a pleasure to work with and I will miss the time we have spent together both in the lab and outside of it. Bridget Connor is a recent undergraduate addition to the lab who JR and I have both mentored. Although just beginning her research career, Bridget has already shown a knack for synthesis and it would be a shame if the lab lost her. Tanvi Ratani, Mark Nesbit, Trevor Del Castillo, Ben Matson, and Kareem Hannoun are the newest crop of Peters Lab students and I have enjoyed the time I have spent with them. I look forward to reading their papers in the future.

A number of collaborators have helped me on projects and publications during my Ph.D. I would like to specifically thank Limei Zhang, Jens Kaiser, George Cutsail, and Ruchira Chatterjee for their help in answering my sometimes incessant questions and fortheir assistance in collecting and interpreting data. MIT and CalTech have excellent staff members and I would like to thank David VanderVelde, Larry Henling, Mike Takase, Peter Muller, Bruce Brunschwig, Jay Winkler, Jeff Simpson, and Angelo DiBilio for their help in discussing and fixing scientific or chemical problems.

Outside of the Peters lab members, I have been fortunate to be surrounded by an exceptional group of people at both MIT and CalTech. Although too numerous to name individually, I have had the pleasure of interacting with a number of students from the Schrock, Fu, Cummins, Nocera, Grubbs, Agapie, Drennan, Lippard, Rees, Gray and Bercaw labs and I anticipate crossing paths with many of them in the future. I also participated in various recreational sports including volleyball, softball, and basketball during the past few years. My participation in IM basketball leagues at CalTech in particular may mark the most pitiful streak of futility in an athletic endeavor, as the collective wins for teams that I have been a part of likely number less than seven over the course of three years. Nevertheless, the people that I have been able to play with have enriched my time both on the court and off it.

My thesis committee consisted of Professors John Bercaw, Theo Agapie, and Brian Stoltz. This group has collectively referred to themselves as "The Ream Team." While I feel that I did not fully live up to their expectations during my candidacy and Ph.D. studies, I am thoroughly grateful for the time and effort they put into reading my

viii

work and offering criticism. I believe that I am a better scientist because of my interactions with them.

I would also like to thank my undergraduate advisor Professor Greg Hillhouse for taking me under his wing as a naïve undergraduate and starting me along this path. I would certainly never have made it this far without his efforts and the time that he devoted towards my education. I learned a great deal from my time working in his lab that I continue to use to this day.

I have been funded by a NSF graduate research fellowship, a Presidential Scholarship from MIT, and through the NIH. These funding agencies have made this research possible and I would like to thank them for funding the fundamental science that has gone into this dissertation.

Outside of the world of chemistry I have had an exceptional group of friends and family that have supported me for the past five years. I must certainly thank my parents Rick and Karin Anderson for raising me and giving me the opportunity to pursue this career path. My parents, along with my brother Keith, have also been a fountain of unconditional love and support throughout my life and there is no possible way to thank them enough. My Ph.D. studies have kept me from seeing the rest of my family and friends as much as I would like and I hope that living in Chicago for the next few years will allow me to spend more time with them. I also would like to thank Don and Laura Holm for visiting frequently and supporting both Emily and myself; I could not ask for better in-laws.

Finally, and most importantly, I have to thank my wife Emily Anderson. Going through a Ph.D. is a challenging process and tests virtually every area of a person's life.

Living with a person who is going through their Ph.D. is just as difficult, as we are frequently miserable humans to be around. Emily has supported my career for the past five years, moving across a continent and away from her family and friends to be with me. Although I hope that she has enjoyed some of the things we have been able to see and do in Boston and Los Angeles, I know that she has given a vast amount of herself for me to get this degree. There are no words sufficient to express my gratitude for having her support and love, but I look forward to using the rest of our lives together paying her back for it.

Abstract

Threefold symmetric Fe phosphine complexes have been used to model the structural and functional aspects of biological N_2 fixation by nitrogenases. Low-valent bridging Fe-S-Fe complexes in the formal oxidation states Fe(II)Fe(II), Fe(II)/Fe(I), and Fe(I)/Fe(I) have been synthesized which display rich spectroscopic and magnetic behavior. A series of cationic tris-phosphine borane (TPB) ligated Fe complexes have been synthesized and been shown to bind a variety of nitrogenous ligands including N_2H_4, NH_3, and NH_2^-. These complexes are all high spin $S = 3/2$ and display EPR and magnetic characteristics typical of this spin state. Furthermore, a sequential protonation and reduction sequence of a terminal amide results in loss of NH_3 and uptake of N_2. These stoichiometric transformations represent the final steps in potential N_2 fixation schemes.

Treatment of an anionic FeN_2 complex with excess acid also results in the formation of some NH_3, suggesting the possibility of a catalytic cycle for the conversion of N_2 to NH_3 mediated by Fe. Indeed, use of excess acid and reductant results in the formation of seven equivalents of NH_3 per Fe center, demonstrating Fe mediated catalytic N_2 fixation with acids and protons for the first time. Numerous control experiments indicate that this catalysis is likely being mediated by a molecular species.

A number of other phosphine ligated Fe complexes have also been tested for catalysis and suggest that a hemi-labile Fe-B interaction may be critical for catalysis. Additionally, various conditions for the catalysis have been investigated. These studies further support the assignment of a molecular species and delineate some of the conditions required for catalysis.

Finally, combined spectroscopic studies have been performed on a putative intermediate for catalysis. These studies converge on an assignment of this new species as a hydrazido(2-) complex. Such species have been known on group 6 metals for some time, but this represents the first characterization of this ligand on Fe. Further spectroscopic studies suggest that this species is present in catalytic mixtures, which suggests that the first steps of a distal mechanism for N_2 fixation are feasible in this system.

Table of Contents

List of Figures

List of Tables

List of Abbreviations

A^X	Hyperfine coupling constant due to nucleus X
Ad	1-Adamantyl
Anal	Analysis
atm	Atmosphere
Avg	Average
$BAr^F_4{}^-$	$B(3,5\text{-}C_6H_3(CF_3)_2)_4{}^-$
br	broad
Bu	n-Butyl
ca	Circa
calcd	Calculated
CCD	Charge-coupled device
cm	Centimeter
cm^{-1}	Wave number
Cp	Cyclopentadienyl
Cp*	Pentamethylcyclopentadienyl
CSD	Cambridge Structural Database
CV	Cyclic voltammogram
Cy	Cyclohexyl
d	Doublet or deuterium
dd	Doublet of doublets
d_x	Compound with x deuterium atoms
depe	1,2-Bis(diethylphosphino)ethane

DFT	Density Functional Theory
DME	1,2-dimethoxyethane
dmpe	1,2-Bis(dimethylphosphino)ethane
DMSO	Dimethylsulfoxide
e	Electron
ENDOR	Electron nuclear double resonance
EPR	Electron paramagnetic resonance
Et	Ethyl
eq	Equivalents
equiv	Equivalents
EXAFS	Extended X-ray absorption fine structure
eV	Electron volt
F	Structure factor
Fc	Ferrocene
FeMoco	Iron-Molybdenum cofactor
G	Gauss
g	Gram
g	Electron g-factor
GC	Gas chromatography
GHz	Gigahertz
H_{ab}	Electronic coupling parameter for mixed valent complexes
Hz	Hertz
Inc	Incorporated

iPr	Isopropyl
IR	Infrared
IVCT	Inter valence charge transfer
$^{x}J_{AB}$	NMR coupling constant between atoms A and B along X number of bonds
J	NMR coupling constant or magnetic coupling constant
K	Kelvin
L	Generic neutral dative ligand
kcal	Kilocalorie
keV	Kiloelectron volt
m	Multiplet
M	Concentration in molarity
max	Maximum
Me	Methyl
MeTHF	Methyltetrahydrofuran
mg	Milligram
MHz	Megahertz
mL	Milliliter
mM	Millimolar
mm	Millimeter
mV	Millivolt
mmol	Millimole
MO	Molecular orbital
mol	Mole

n	Generic number
NIR	Near infrared
nm	nanometer
NMR	Nuclear magnetic resonance
N_xH_y	Generic nitrogenous ligand with x N atoms and y H atoms
o	*Ortho*
Ph	Phenyl
$PhBP_3$	$PhB(CH_2PPh_2)_3^-$ or generically $PhB(CH_2PR_2)_3^-$
$PhBP^{iPr}_3$	$PhB(CH_2PiPr_2)_3^-$
pK_a	Acid dissociation constant
PNP	Pincer ligand with two phosphine and one nitrogen donors
q	Quartet
R	Generic organic group or R-factor
RT	Room temperature
S	Spin quantum number
s	Singlet or second
SiP_3	$(o\text{-}PR_2C_6H_4)_3Si^-$
SQUID	Superconducting quantum interference device
t	Triplet or time
TBA	Tetra-*n*-butyl ammonium
tBu	*Tert*-Butyl
Tf	SO_2CF_3
THF	Tetrahydrofuran

TMS	Trimethylsilyl
TPB	o-iPr$_2$P(C$_6$H$_4$))$_3$B or generically o-R$_2$P(C$_6$H$_4$))$_3$B
TPP	Tetraphenylporphyrin
UV	Ultraviolot
V	Volt
vbr	Very broad
Vis	Visible
wR	Weighted R-factor
X	Generic anionic atom or molecule
XAS	X-ray absorption spectroscopy
XRD	X-ray diffraction
δ	Chemical shift or Mössbauer isomer shift
°	Degree
°C	Degrees Celsius
ε	Extinction coefficient in units of M^{-1}cm^{-1}
η^x	Hapticity of order x
λ	Wavelength
λ_{max}	Wavelength of local maximum intensity
μA	Microamps
μ-X	Bridging X ligand
μ_B	Bohr magneton
μ_{eff}	Effective magnetic moment
μL	Microliter

ν_{xy}	Vibrational frequency between atoms x and y
Σ	Summation
σ	Sigma symmetry orbital or interaction
π	Pi symmetry orbital or interaction
τ_4	Index of geometry between tetrahedral and trigonal pyramidal
Θ	Weiss temperature
Å	Angstrom
12-C-4	12-crown-4
^{1}H	Hydrogen-1
^{11}B	Boron-11
^{13}C	Carbon-13
^{15}N	Nitrogen-15
^{31}P	Phosphorus-31
$\{^1H\}$	Proton-decoupled
6-31G, etc.	Basis sets for DFT
BP86 etc.	DFT functional

Chapter 1: Introduction

1.1 Opening Remarks

All of the work discussed in this thesis involves the study of complexes either indirectly or directly relevant to the Fe mediated reduction of N_2 to NH_3. Additionally, while this thesis work has been performed exclusively with synthetic complexes, a strong motivation for this work has been found in the enzymes that perform N_2 fixation that are known as nitrogenases. Whether this work has any relevance to the natural systems invoked is yet to be seen, but the conclusions drawn here at least motivate and validate new lines of thought and inquiry in the study of the natural systems. This introductory chapter will introduce the topic of N_2 fixation in a general sense, and then give a brief motivation and synopsis of the major results for each of the subsequent chapters as they relate to this over-arching theme.

1.2 Nitrogen Fixation

$$(A)\ N_2 + 3\ H_2 \rightarrow 2\ NH_3$$

$$(B)\ N_2 + 8\ H^+ + 8\ e^- \rightarrow 2\ NH_3 + H_2$$
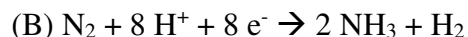
Equation 1.1. Reactions for (A) the Haber-Bosch process and (B) N_2 fixation mediated by nitrogenase.

Biogeochemical cycles play a critical role in the availability and conversion of massive amounts of elements and molecules throughout the planet. Of the myriad cycles that regulate important elements or molecules, one of the most fascinating is the nitrogen cycle, wherein elemental nitrogen is transformed between its stable gaseous N_2 form and other reduced, such as NH_3, or oxidized, such as NO_3^-, molecules.[1] The strength of the

triple bond found in N_2 (220 kcal/mol) and its non-polarity make the activation of this

molecule exceptionally challenging and have motivated interest in understanding the

conversion of N_2 into reduced species such as NH_3. Due to the importance of fixed

nitrogen molecules such as NH_3 in fertilizing crops, mankind has developed an acute

need of a catalytic process for the production of NH_3. The Haber-Bosch process, wherein

N_2 and H_2 are converted to NH_3 over an Fe-based catalyst at high temperatures and

pressures (Equation 1.1A), has been applied on a globally massive scale as a means to

effectively feed burgeoning human populations.[1]

Figure 1.1. X-Ray Diffraction (XRD) structure and chemical line drawing representation

of FeMoco. The XRD figure was made with coordinates from Reference 4b.

In nature, N_2 is fixed to NH_3 by bacteria known as diazotrophs, which are

frequently found on root nodules, via the reaction shown in Equation 1.1B.[2] The precise

enzymatic machinery with which these organisms bind N_2 and the mechanism they

employ to reduce it have been topics of great interest. Multiple studies have implicated a

series of cofactors as the site of NH_3 formation (Figure 1.1).[3] These cofactors always

consist of primarily Fe and S (FeFeco) and can additionally incorporate Mo (FeMoco) or

V (FeVco) when these elements are bio-available. Despite crystallographic information

on the structures of these sites, recently revealing a carbon as the central atom of the

cofactor,[4] consensus on the atom(s) at which N_2 reduction occurs has not been reached. Because Mo was once thought to be an essential component of all nitrogenases, the site of N_2 binding was initially thought to be the single Mo atom in the FeMoco.2 This assumption found support in studies on synthetic inorganic Mo complexes that bind and reduce N_2.[5]
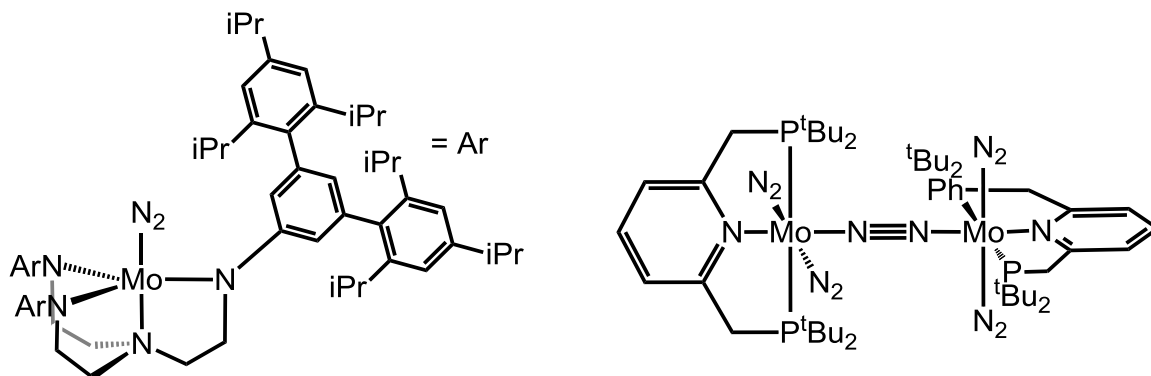
Figure 1.2. Mo complexes that mediate the catalytic reduction of N_2 to NH_3. Left: Schrock's tri-amidoamine system (Reference 9). Right: Nishibayashi's PNP system (Reference 11).

Although some ill-defined mixtures with transition metals have been shown to generate NH_3 from N_2, these systems do not allow for insight into the mechanism of reduction.[6] One avenue of research that has helped to guide discussion about possible N_2 reduction mechanisms has been the synthesis of molecular transition metal complexes that bind and reduce N_2. Since the discovery of the first N_2 complex by Allen and Senoff in 1965, there has been great interest in developing molecular species that will mimic or provide insight into biological N_2 fixation.[7] In the context of Mo, discoveries by Chatt, Hidai, and others have demonstrated that reduced metal centers can bind N_2 and functionalize it towards both silylation and protonation.5 Additionally, the feasibility of

electrochemical reduction of N_2 to NH_3 was reported by Pickett and co-workers.[8] These

studies, as well as the synthesis of a variety of other nitrogenous species, led to the

proposal of a mechanism now known as the "Chatt" or "distal" mechanism (Scheme 1.1,

bottom) for N_2 reduction.5 Despite this understanding, realization of a well-defined

molecular system for the catalytic reduction of N_2 to NH_3 at atmospheric pressure

remained elusive until Schrock and Yandulov's landmark discovery in 2003 that a Mo

tri-amidoamine (Figure 1.2) system can produce up to 8 equivalents of NH_3 per Mo from

N_2.[9] This report, and the accompanying characterization of multiple proposed

intermediates that implicated a "distal" mechanism for N_2 reduction in this system,[10]

represented the first well-defined molecular system for catalyzing N_2 reduction to NH_3.
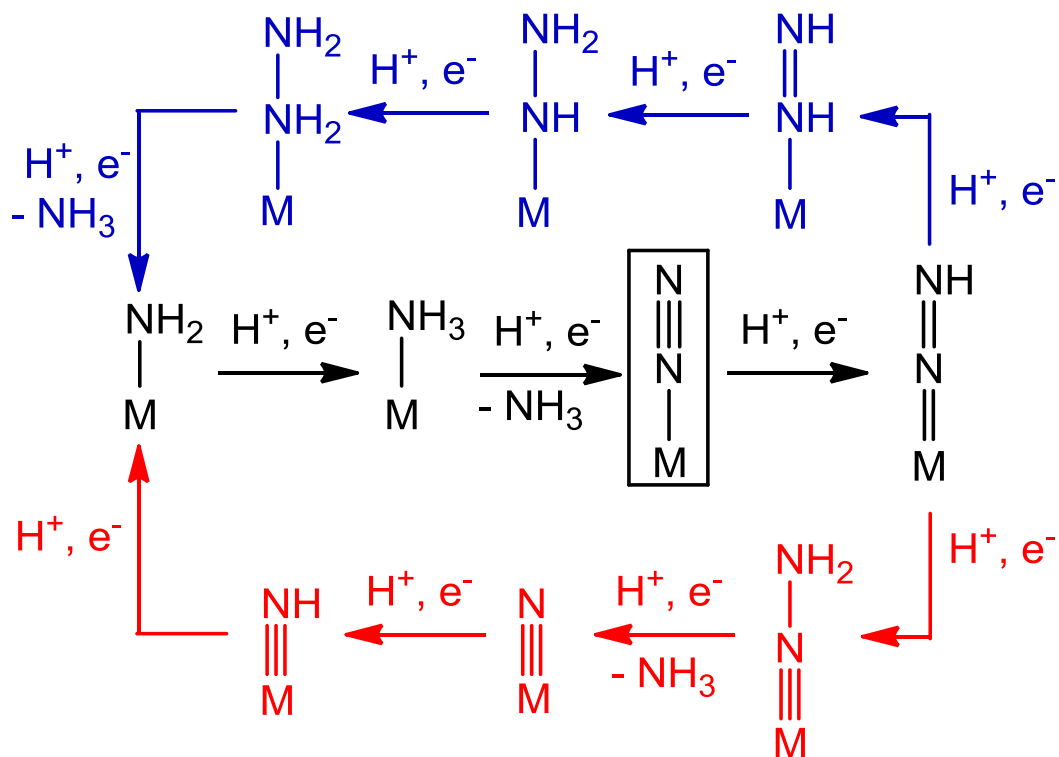
Scheme 1.1. Proposed limiting mechanisms for transition metal mediated N_2 reduction.

An "alternating" mechanism is shown on top in blue while a "distal" mechanism is

shown on bottom in red. Black intermediates are common to both mechanisms. Not

shown are possible crossover pathways between mechanisms. Note that while M could feasibly be any transition metal, Mo and Fe are the most salient elements for this discussion.

More recently, Nishibayashi and co-workers have reported a phosphine ligated Mo center that improves slightly on Schrock's system (Figure 1.2).[11] This PNP ligated Mo complex is competent for up to 12 equivalents of NH_3 per Mo center. The combined synthetic studies of Schrock and Nishibayashi were consistent with the hypothesis that Mo serves as the active metal for nitrogenase under turnover conditions.2 Despite these results, however, the functionality of nitrogenases without Mo incorporated into the cofactor and other data began to suggest that Mo was not the active N_2 binding site within nitrogenases.

A number of spectroscopic studies on nitrogenase have recently indicated that Fe may in fact be the site where N_2 is bound and reduced, and have further supported an "alternating" mechanism wherein protons are alternately added to N_2 to form intermediates such as HN=NH and H_2N-NH_2 (Scheme 1.1 top).[3,12] Such a mechanism directly contrasts with the "distal" mechanism previously mentioned, wherein protons are added consecutively to single nitrogen atoms to generate intermediates such as nitrides (Scheme 1.1 bottom). Due to this proposed binding site and differing mechanism, there has been demand for Fe complexes that can (a) serve as structural, spectroscopic, or functional models of the Fe sites in FeMoco, (b) stabilize putative intermediates along a N_2 fixation pathway (Scheme 1.1), or (c) serve as models for the highly reduced states of the FeMoco that precede N_2 binding. As such, significant effort has been directed

towards developing synthetic Fe complexes that can structurally or functionally model nitrogenase or proposed catalytic intermediates.[13] Indeed, several groups have demonstrated various Fe complexes that bind N_xH_y ligands or display corresponding reactivity directly relevant to N_2 reduction schemes.[14]

The Peters lab has had an ongoing interest in developing Fe systems that can functionally model the chemistry of nitrogenase enzymes. A guiding hypothesis for this research has been the postulation that N_2 reduction occurs at a single Fe site at the FeMoco and that this site samples multiple geometries in order to mediate catalytic turnover (Scheme 1.2). In order to model such a site, soft electron donating tris-phosphine ligands have been utilized to stabilize low-valent Fe complexes in a number of geometries. Initially, pseudo-tetrahedral complexes of Fe with the tris-phosphine borate zwitterion $PhB(CH_2PR_2)_3^-$ ($PhBP_3$) were targeted.[15] These ligands stabilize low-valent and multiply bonded metal species on Fe. There was, however, a dearth of research into sulfur based chemistry on these scaffolds, which motivated further study into these types of complexes.
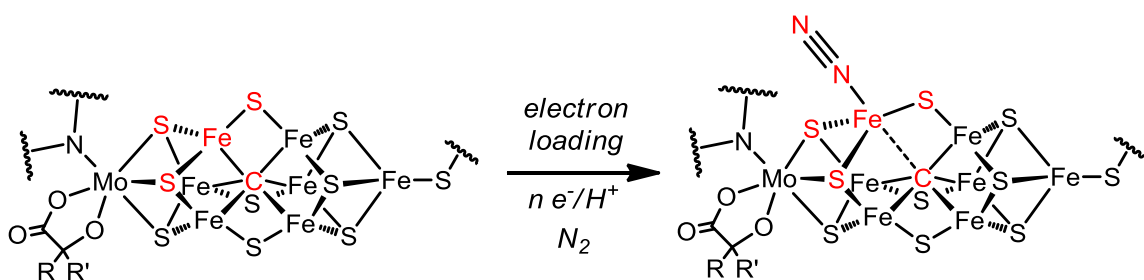
Scheme 1.2. Scheme depicting a potential mechanism for N_2 binding to FeMoco utilizing a flexible Fe-C interaction. Possible sites of protonation prior to or concurrent with N_2 binding are not shown.

1.3 Unusually Low Valent Fe-S-Fe Complexes

The active site FeMoco consists of a cluster composed primarily of Fe-S-Fe linkages.3 As such, research into the synthesis and characterization of model complexes of these linkages has been an area of significant study.[16] Unusually low formal oxidation states of iron have been implicated as important to the function of nitrogenase, and it is of increasing interest to understand whether the S^{2-} structural unit is compatible with such low-valent iron.3 In this context, Holland and co-workers have recently reported {[HC(CMeN[2,6-diisopropylphenyl])$_2$]Fe}$_2${μ-S} and its interactions with nitrogenous substrates, as well as recently reporting the reduction of this complex to form the first example of a stable Fe(I) sulfide.[17] It was of further interest to determine whether other geometries at low-valent Fe could be stable in the presence of sulfide and furthermore, whether a mixed-valent Fe(II)/Fe(I) species could be isolated and what its electronic structure might be.

Chapter 2 outlines the synthesis and characterization of a series of unusually low-valent [(PhBP$_3$)Fe]$_2$(μ-S) complexes in the formal oxidation states Fe(II)/Fe(II), Fe(II)/Fe(I), and Fe(I)/Fe(I). As mentioned, these complexes represent rare examples of Fe(I) ligated to S^{2-}, and possess fascinating structural and electronic features distinguished by exceptionally short Fe-S bonds and a high degree of magnetic coupling between the two metal centers. Furthermore, the Fe centers in these complexes undergo a transition to low-spin states upon reduction, resulting in unusual examples of tetrahedral low-spin Fe(I). Finally, these dimers display interesting reactivity towards small molecule substrates broadly relevant to N_2 fixation such as CO, H^+, and N_2H_4.

1.4 Conversion of FeNH$_2$ to FeN$_2$ with Release of NH$_3$
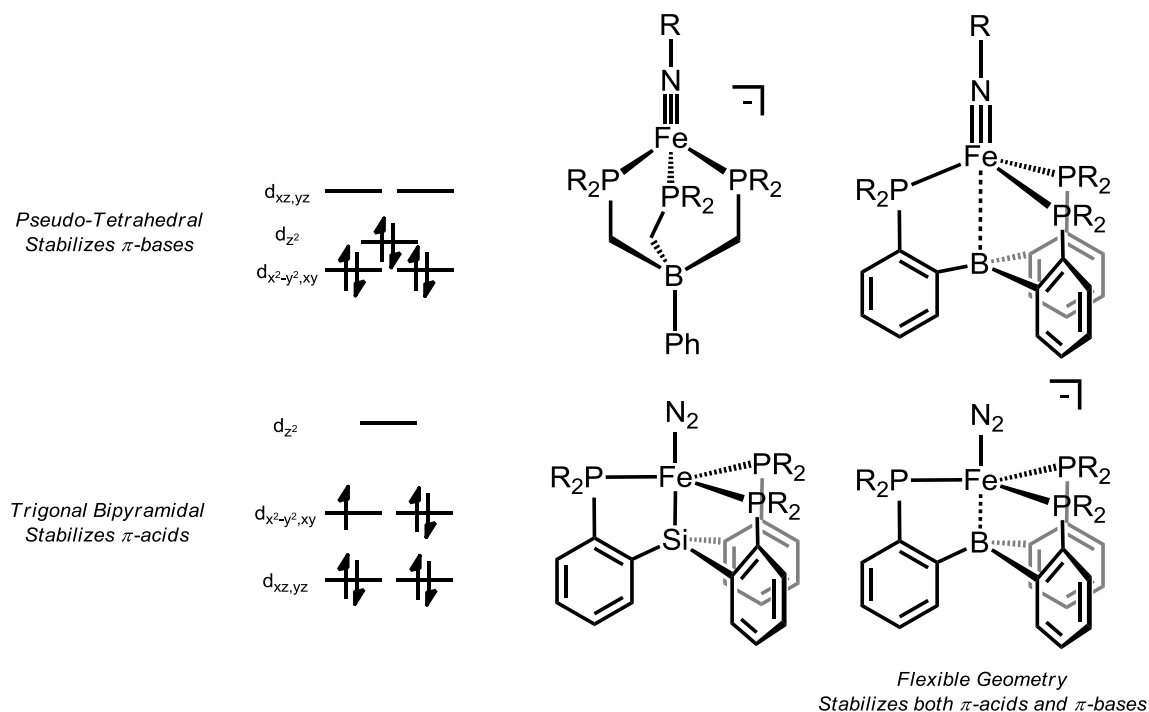
Figure 1.3. Qualitative d-orbital splitting diagrams and examples of complexes that feature pseudo-tetrahedral and trigonal bipyramidal geometries stabilizing π-bases and π-acids respectively. Note that Fe-Si or Fe-B bonding orbitals may be near or within the d-manifold, but are not shown.

As was mentioned, a key feature of (PhBP$_3$)Fe complexes was the stabilization of strong π-donors in species such as Fe nitrides or imides that would be found along a distal mechanism. Such stabilization was engendered from the pseudo-tetrahedral geometry enforced by the PhBP$_3$ ligand scaffold (Figure 1.3).[15d] A drawback to this design, however, was the limited activity of these systems towards functionalization of N$_2$, potentially due to more facile population of high spin states in a pseudo-tetrahedral geometry as well as the propensity of these systems to form bridging N$_2$ species. To

access complexes better capable of functionalizing N_2 molecules, a shift to a trigonal bipyramidal geometry was sought with a new tris-phosphino silyl ligand (o-PR$_2$C$_6$H$_4$)$_3$Si$^-$ (SiP$_3$). This shift resulted in a system poised for N_2 uptake and functionalization most clearly illustrated by the stabilization of terminal (SiP$_3$)FeN$_2$ complexes in three formal oxidation states and the subsequent silylation of N_2 on this scaffold.[18] A drawback to this system, however, is that the shift to trigonal bipyramidal geometry results in the lowering of the d_{xz} and d_{yz} orbitals such that stabilization of π-basic ligands is no longer favorable (Figure 1.3). This is most clearly evidenced by the low temperature observation of an Fe nitrene species which decays upon warming to RT, in contrast to the PhBP$_3$ systems which readily stabilize imide species.[19]

In order to combine the N_2 binding capabilities and functionalization capabilities of the trigonal bipyramidal system with the stability of the pseudo-tetrahedral systems towards π-basic ligands, a new tris-phosphine borane (TPB) ligand set was utilized.[20] A key feature to this ligand set is a flexible Fe-B interaction that allows the metal center to sample both trigonal bipyramidal and pseudo-tetrahedral geometries (Figure 1.3). Indeed, this ligand has shown the ability to both readily bind N_2 as well as stabilize π-basic nitrogenous ligands, which allows for di-functionalization of N_2 with silyl electrophiles.[21] Despite these results, little research into the installation of ligands with N-H bonds had been investigated.

Chapter 3 focuses on the installation of N_xH_y ligands onto the (TPB)Fe platform. While complexes featuring substituted NR, N_2R, and N-NR$_2$ functionalities had been synthesized with this ligand set,[21] no substrates, aside from (TPB)Fe(N$_2$), that would actually take part in a N_2 reduction scheme had yet been isolated. Utilizing the 4-

coordinate pseudo-trigonal pyramidal cationic precursor $[(TPB)Fe]^+$ as a synthon, N_2H_4,

NH_3, and NH_2^- functionalities were installed. All of these species are high-spin $S = 3/2$

and display characteristic quartet EPR signals. Finally, sequential protonation and

reduction of $(TPB)Fe(NH_2)$ results in loss of NH_3 and uptake of N_2 to yield $(TPB)Fe(N_2)$.

Significantly, this reaction sequence represents the first time that a single Fe system has

been shown to mediate the final two common reductive protonation steps of a N_2

reduction scheme (Scheme 1.1). This result motivated studies into whether NH_3 could be

produced from N_2 with this scaffold.

1.5 Catalytic Conversion of N_2 to NH_3 by an Fe Model Complex

While progress has been made towards stabilizing nitrogenous species relevant to

N_2 reduction on Fe platforms, an Fe system in which N_2 can be directly transformed into

NH_3 in a catalytic fashion was unknown. Prior to the studies described herein, even

stoichiometric conversion of FeN_2 into NH_3 was limited to yields of ~ 0.1 equivalents of

NH_3 per Fe center.[13,22] Recent advances in a related context include a system reported by

Holland and co-workers capable of splitting N_2 into two nitrides which can then release

nearly stoichiometric NH_3 upon protonolysis or hydrogenolysis and a report from

Nishibayashi and co-workers describing the catalytic silylation of N_2 with simple Fe salts

and complexes.[23,24] Despite these interesting and important examples, distinct issues are

associated with the direct conversion of N_2 into NH_3 with protons and electrons, most

notably the need to circumvent formation of H_2 which prevented the realization of a well-

defined Fe system for the catalytic reduction of N_2 to NH_3.

Na(12-C-4)$_2$

$$\left[\begin{array}{c} N_2 \\ | \\ iPr_2P—Fe^{\ldots\ldots}PiPr_2 \\ \vdots \quad PiPr_2 \\ B^{\ldots} \end{array}\right]^-$$

xs HBAr$^F_4$•2 Et$_2$O

+

xs KC$_8$ →   7 eq. NH$_3$

+   Et$_2$O
              -78 °C
1 atm N$_2$

Scheme 1.3. Catalytic reduction of N$_2$ to NH$_3$ by a molecular Fe pre-catalyst.

Chapter 4 outlines the initial studies and development of a molecular Fe based catalyst for the reduction of N$_2$ to NH$_3$. While preliminary protonation studies with (TPB)Fe(N$_2$) complexes resulted in oxidation, use of excess acid and low temperatures enabled the observation of an [(TPB)Fe(NH$_3$)]$^+$ being formed from bound N$_2$. In Chapter 3, the reduction of [(TPB)Fe(NH$_3$)]$^+$ to release NH$_3$ and uptake N$_2$ had already been shown, and canvassing several reaction conditions resulted in the discovery that anionic [(TPB)Fe(N$_2$)]$^-$ can produce an average of 7 equivalents of NH$_3$ per Fe, resulting in a yield of > 40% of protons being reliably delivered to N$_2$ (Scheme 1.3). Control studies with simple Fe salts that shown negligible NH$_3$ formation combined with the initial reactions that show the formation of a molecular NH$_3$ adduct upon acidification, offer strong support that this is indeed a molecular catalyst. The speciation of the Fe complexes under catalysis furthermore suggests that net H$_2$ addition to Fe could be

responsible for catalyst degradation. Overall, the exciting discovery of N_2 reduction by

$[(TPB)Fe(N_2)]^-$ motivated further studies of the catalytic system.

1.6 The Effect of Ligand and Reaction Conditions on Fe Mediated N_2 Fixation

With the discovery that $(TPB)Fe$ systems can catalyze N_2 reduction to NH_3, there

was an added impetus to determine the scope of the catalysis and the effect of varying the

catalytic conditions. Additionally, investigations of the competency of different pre-

catalysts were pursued as probes of what structural features of the $(TPB)Fe$ system were

essential for catalysis. Towards this end, Chapter 5 outlines comparative studies where

both the catalytic conditions and pre-catalysts have been varied.

Variations on the standard catalytic conditions by changing factors such as

solvent, temperature, acid, and reductant on catalysis have been examined, revealing that

while no improvement in NH_3 yield was observed, general trends in reactivity indicate

that the reaction must be performed in an ethereal solvent. Despite the limited solvent

scope, some flexibility in the choice of acid and reductant is available with anilinium

acids and Na/Hg amalgam as a reductant proving competent for catalysis. Canvassing a

variety of either novel or previously reported Fe phosphine complexes for efficacy as pre-

catalysts for N_2 reduction leads to the empirical conclusion that only TPB complexes are

competent for producing > 2 equivalents of NH_3 per Fe center. The cause for this

observation is unclear, but a possible explanation is the requirement of a flexible Fe-B

interaction, potentially in keeping with the hypothesis that a flexible geometry at Fe is

required for catalysis. Furthermore, the differences in activity between $(TPB)Fe$ and

other poly-phosphine complexes further supports that this catalyst system is indeed

molecular. Were a heterogeneous decomposition product were responsible for the

catalysis, a strong dependence on the ligand set would likely not be observed.

1.7 Spectroscopic Characterization of the Putative Catalytic Intermediate

[(TPB)Fe≡N-NH₂][BAr^F₄].
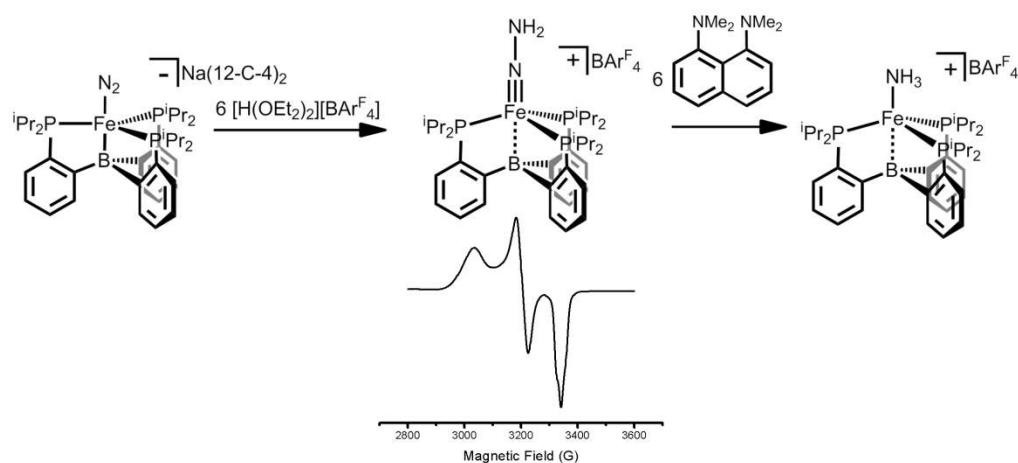
Figure 1.4. Generation of a di-protonated intermediate which partially decomposes to an NH₃ complex.

Despite the realization of catalysis in the (TPB)Fe system, there remains little to

no mechanistic information on how N_2 reduction is mediated. Specifically, questions

about whether this system is going through a "distal," "alternating," or other hybrid type

mechanism are of great interest. While direct probing of the molecular species under

turnover is challenging due to the heterogeneous nature of the favored reductant (KC_8)

and the paramagnetic Fe species involved, it was still of interest to see if a protonated N_2

ligand on Fe could be generated from the pre-catalyst. With this goal in mind, low-temperature protonation studies were undertaken.

Chapter 6 details the synthesis and spectroscopic characterization of a thermally unstable cationic $[(TPB)Fe(N_2H_2)]^+$ species. Combined EPR, ENDOR, and EXAFS analysis indicates that this complex is $S = 1/2$ and doubly protonated. Furthermore, this species possesses a short Fe-N interaction, consistent with an Fe-N triple bond. Computational studies on this complex also support the presence of an Fe-N triple bond, providing reasonable agreement with spectroscopic measurements. Such an assignment is consistent with double protonation at the βN of N_2, as would be found in a "distal" mechanism. While the assignment of this intermediate and its presence in pre-catalytic mixtures is convincing, its relevance to an active species under catalysis, or downstream processes following formation of this species, is still unclear. Further studies aimed at elucidating the mechanism of catalysis and whether this doubly protonated species is involved along the catalytic pathway will be of great interest.

References Cited

1 Smil, V. *Enriching the Earth*; MIT Press: Cambridge, MA, 2001.

2 (a) Burgess, B. K.; Lowe, D. J. *Chem. Rev.* **1996**, *96*, 2983-3011; (b) Eady, R. R. *Chem. Rev.***1996**, *96*, 3013-3030.

3 (a) Dos Santos, P. C.; Igarashi, R. Y.; Lee, H. I.; Hoffman, B. M.; Seefeldt, L. C.; Dean, D. R. *Acc. Chem. Res.* **2005**, *38*, 208-214; (b) Howard, J. B.; Rees, D. C. *Proc. Natl. Acad. Sci.* **2006**, *103*, 17088-17093; (b) Peters, J. C.; Mehn, M. P. In *Activation of Small Molecules*; Wiley: 2006, p 81-119; (c) Schwarz, G.; Mendel, R. R.; Ribbe, M. W. *Nature* **2009**, *460*, 839-847; (d) Seefeldt, L. C.; Hoffman, B. M.; Dean, D. R. *Annu. Rev. Biochem.* **2009**, *78*, 701-722.

4 (a) Lancaster, K. M.; Roemelt, M.; Ettenhuber, P.; Hu, Y. L.; Ribbe, M. W.; Neese, F.; Bergmann, U.; DeBeer, S. *Science* **2011**, *334*, 974-977; (b)Spatzal, T.; Aksoyoglu, M.; Zhang, L.; Andrade, S. L. A.; Schleicher, E.; Weber, S.; Rees, D. C.; Einsle, O. *Science* **2011**, *334*, 940.

5 (a) Chatt, J.; Dilworth, J. R.; Richards, R. L. *Chem. Rev.* **1978**, *78*, 589-625; (b) Hidai, M.; Mizobe, Y. *Chem. Rev.* **1995**, *95*, 1115-1133.

6 (a) Shilov, A.; Denisov, N.; Efimov, O.; Shuvalov, N.; Shuvalova, N.; Shilova, A. *Nature* **1971**, *231*, 460-461; (b) Bazhenova, T. A.; Shilov, A. E. *Coord. Chem. Rev.* **1995**, *144*, 69-145.

7 Allen, A. D.; Senoff, C. V. *Chem. Comm.* **1965**, 621-622.

8 Pickett, C. J.; Talarmin, J. *Nature* **1985**, *317*, 652-653.

9 Yandulov, D. V.; Schrock, R. R. *Science* **2003**, *301*, 76-78.

10 Schrock, R. R. *Acc. Chem. Res.* **2005**, *38*, 955-962.

11 Arashiba, K.; Miyake, Y.; Nishibayashi, Y. *Nature Chem.* **2011**, *3*, 120-125.

12 Hoffman, B. M.; Dean, D. R.; Seefeldt, L. C. *Acc. Chem. Res.* **2009**, *42*, 609-619.

13 (a) Crossland, J. L.; Tyler, D. R. *Coord. Chem. Rev.* **2010**, *254*, 1883-1894; (b)

  MacLeod, K. C.; Holland, P. L. *Nat. Chem.* **2013**, *5*, 559-565.

14 For a few examples see: (a) Smith, J. M.; Lachicotte, R. J.; Pittard, K. A.; Cundari, T.

  R.; Lukat-Rodgers, G.; Rodgers, K. R.; Holland, P. L. *J. Am. Chem. Soc.* **2001**, *123*,

  9222-9223; (b) Gilbertson, J. D.; Szymczak, N. K.; Tyler, D. R. *J. Am. Chem. Soc.*

  2005, *127*, 10184-10185. (c) Field, L. D.; Li, H. L.; Magill, A. M. *Inorg. Chem.* **2008**,

  48, 5-7.

15 (a) Brown, S. D.; Betley, T. A.; Peters, J. C. *J. Am. Chem. Soc.* **2002**, *125*, 322-323;

  (b) Betley, T. A.; Peters, J. C. *J. Am. Chem. Soc.* **2003**, *125*, 10782-10783; (c) Betley,

  T. A.; Peters, J. C. *J. Am. Chem. Soc.* **2004**, *126*, 6252-6254. (d) Saouma, C. T.; Peters,

  J. C. *Coord. Chem. Rev.* **2011**, *255*, 920-937.

16 Holm, R. H. *Acc. Chem. Res.* **1977**, *10*, 427-434.

17 Vela, J.; Stoian, S.; Flaschenriem, C. J.; Münck, E.; Holland, P. L. *J. Am. Chem. Soc.*

  2004, *126*, 4522-4523; (b) Rodriguez, M. M.; Stubbert, B. D.; Scarborough, C. C.;

  Brennessel, W. W.; Bill, E.; Holland, P. L. *Angew. Chem.* **2012**, *124*, 8372-8375.

18 Lee, Y.; Mankad, N. P.; Peters, J. C. *Nat. Chem.* **2010**, *2*, 558-565.

19 Mankad, N. P.; Müller, P.; Peters, J. C. *J. Am. Chem. Soc.* **2010**, *132*, 4083-4085.

20 Sircoglou, M.; Bontemps, S.; Bouhadir, G.; Saffon, N.; Miqueu, K.; Gu, W.; Mercy,

  M.; Chen, C.-H.; Foxman, B. M.; Maron, L.; Ozerov, O.V.; Bourissou, D. *J. Am. Chem.*

  Soc. **2008,** *130,* 16729-16738.

21 (a) Moret, M.-E.; Peters, J. C. *Angew. Chem. Int. Ed.* **2011**, *50*, 2063-2067; (b) Moret, M.-E.; Peters, J. C. *J. Am. Chem. Soc.* **2011**, *133*, 18118-18121.

22 Hills, A.; Hughes, D. L.; Jimenez-Tenorio, M.; Leigh, G. J.; Rowley, A. T. *J. Chem. Soc. Dalton* **1993**, 3041-3049.

23 Rodriguez, M. M.; Bill, E.; Brennessel, W. W.; Holland, P. L. *Science* **2011**, *334*, 780-783.

24 Yuki, M.; Tanaka, H.; Sasaki, K.; Miyake, Y.; Yoshizawa, K.; Nishibayashi, Y. *Nature comm..* **2012**, *3*, 1254-1254.

Chapter 2: Unusually Low Valent Fe-S-Fe Complexes

2.1 Introduction

The Fe-S-Fe unit is common to a host of metalloenzymes that mediate metabolic transformations central to life. These include proteins or cofactors that act as electron transfer conduits[1], as well as metalloenzymes that transform small molecules such as the hydrogenases[2] and nitrogenases.[3] As such, research into the synthesis and characterization of model complexes of these cofactors has been an area of significant study.[4] Holm pioneered the synthesis of lower valent iron-sulfur clusters exemplified by the synthesis of the all iron(II) cluster $[Fe_4S_4(iPr_2NHCMe_2)_4]$.[5] Unusually low formal oxidation states of iron (e.g., Fe(I) and Fe(0)) have been implicated as important to the function of hydrogenase and nitrogenase enzymes and it is of increasing interest to understand whether the S^{2-} structural unit is compatible with such low-valent iron. In this context, Holland and co-workers have recently reported {[HC(CMeN[2,6-diisopropylphenyl])$_2$]Fe}$_2${μ-S} and the first all Fe(I) sulfide {[HC(CMeN[2,6-diisopropylphenyl])$_2$]Fe}$_2${μ-S}$^{2-}$ and interactions of the former with nitrogenous substrates.[6] The Peters lab has also had an interest in the study of unusually low-valent Fe-X-Fe linkages that relate to N_2 reduction, with examples being where the bridging X unit is either imide (NH^{2-}) or nitride (N^{3-}).[7] Herein this narrative is extended by reporting a series of Fe-S-Fe complexes in the formal oxidation states Fe(II)/Fe(II), Fe(II)/Fe(I), and Fe(I)/Fe(I). This series of complexes possess rich magnetic and spectroscopic characteristics indicative of a spin-state change to unusual low-spin Fe(I) centers upon reduction. In addition to the thorough characterization of these species, the CO uptake and subsequent H^+ reduction chemistry of the Fe(II)/Fe(II) system, as well as its reactivity towards N_2H_4, have been investigated.

2.2 Results and Discussion

2.2.1 Low-Valent Fe-S-Fe Complexes

In order to install a μ-S unit to bridge two $(PhBP_3)Fe$ $(PhBP_3 = PhB(CH_2PPh_2)_3^-)$ units, a soluble source of S^{2-} was sought as a salt metathesis partner with $(PhBP_3)FeCl$. While S_8 and simple alkali metal SH^- salts did not provide clean products, use of [TBA][SH] (TBA = NBu_4^+) reacted with $(PhBP_3)FeCl$ to generate the ferrous complex $((PhBP_3)Fe)_2(\mu-S)$ (**2.1**) as a dark brown material in moderate yield (Scheme 2.1). The cyclic voltammogram (CV) of **2.1** in THF displays two reversible reduction events at -1.52 V and -2.30 V vs. Fc/Fc$^+$ which are assigned as the Fe(II)Fe(II)/Fe(II)/Fe(I) and Fe(II)Fe(I)/Fe(I)Fe(I) couples respectively (Figure 2.1). The reversibility of the CV suggested that the reduced species could be stable and thus chemical reductions were investigated.
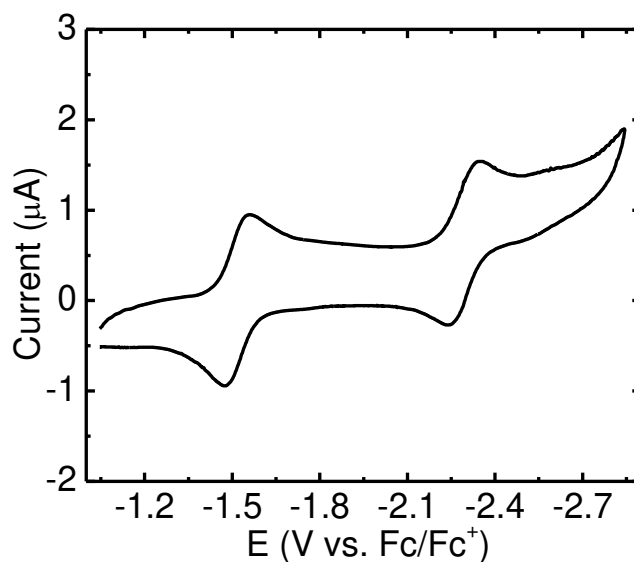
Figure 2.1. CV of **2.1**. Conditions: 100 mV/s THF, 0.01 M [NBu₄][PF₆], THF, glassy carbon working, Pt auxiliary, Ag/[Ag][NO₃] reference.

Reduction of **2.1** with an excess of Na/Hg in THF for fifteen minutes results in a color change from dark brown to deep green. Addition of 12-crown-4 and crystallization results in the isolation of [((PhBP$_3$)Fe)$_2$(μ-S)][Na(12-crown-4)$_2$] (**2.2**) as nearly black crystals (Scheme 2.1). If a stronger reductant is used and **2.1** is instead reduced with two equivalents of NaC$_{10}$H$_8$ a black solution results, which upon addition of 12-crown-4 and crystallization results in the formation of [((PhBP$_3$)Fe)$_2$(μ-S)][Na(12-crown-4)$_2$]$_2$ (**2.3**) as an extremely air sensitive black solid (Scheme 2.1).
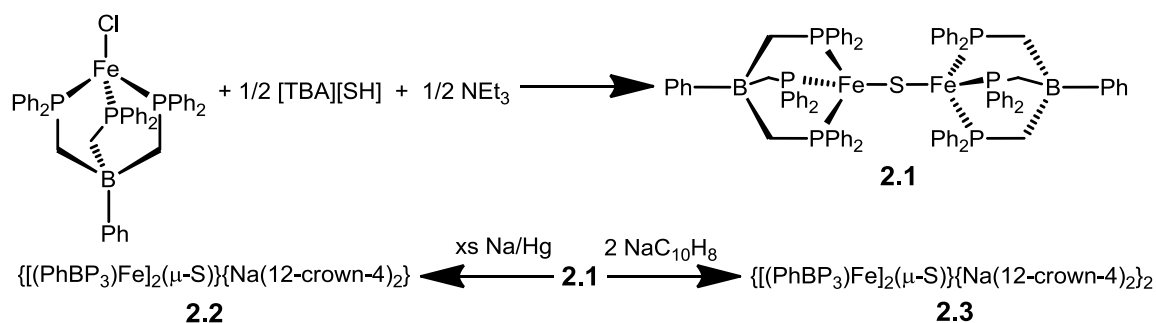
Scheme 2.1. Synthesis of complexes **2.2** and **2.3**.

Complexes **2.1**, **2.2**, and **2.3** have been structurally characterized and display several structural features of note (Figure 2.2). The most striking features present in these complexes are the uniformly short Fe-S distances that are substantially shorter than the average reported Fe-S bond length in bridging sulfides (2.2 Å).[8] The Fe-S distance of 2.071(1) (Table 2.1) Å in complex **2.3** is, within error, the shortest Fe-S distance reported in the CSD, with a close example of 2.078(8) Å reported by Coucouvanis and co-workers.[9] Such short distances are indicative of multiple bonding between Fe and S and such bonding has been invoked in other M-S-M units of the first row transition metals.[10]

Additionally, the marginal differences in Fe-S bond lengths in **2.1**-**2.3** (0.032 Å) suggest

little to no perturbation of the bonding upon reduction.

All three complexes display nearly, or perfectly in the case of **1**, linear Fe-S-Fe

angles. Sulfides of Fe are typically bent as illustrated in the example from Coucouvanis.9

The steric profile of the (PhBP₃) framework allows for substantially bent Fe-X-Fe

geometries7ᶜ and so the linearity in complexes **2.1**-**2.3** is also likely indicative of an

electronic preference for this geometry such as multiple bonding across the Fe-S-Fe unit.

Outside of the Fe-S-Fe core, two structural features deserve mention.
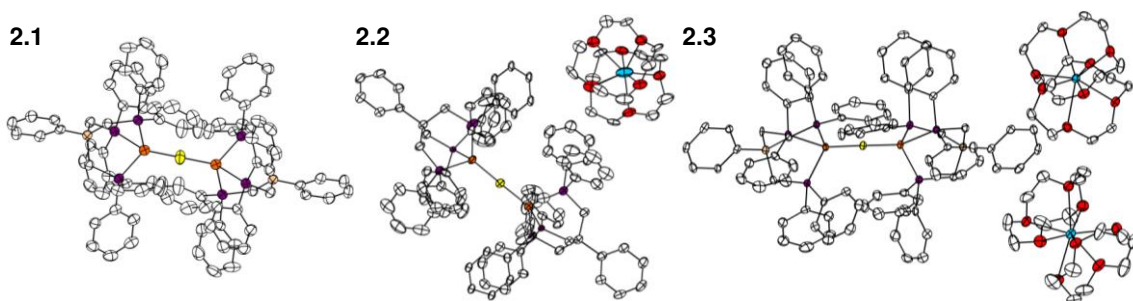
Figure 2.2. XRD structures of complexes **2.1**, **2.2**, and **2.3** with ellipsoids at 50% and hydrogens omitted for clarity. Fe atoms are shown in orange, S in yellow, P in purple, Na in blue, O in red, and C in white.

Firstly, the P-Fe-Fe-P torsion angles in **1** are 60° as demanded by the

crystallographic inversion center in this complex. Upon reduction, the complex adopts a

more "eclipsed" geometry, with P-Fe-Fe-P angles of 18° in **2.2** and 13° in **2.3**. The

origin of this structural change is not clear, as the π-bonding across the Fe-S-Fe unit

should not change upon going from D_{3d} to D_{3h} symmetry. Secondly, and more curiously,

a drastic contraction in Fe-P bond distances is apparent upon reduction of the series of

complexes. While complex **2.1** possesses Fe-P bond distances consistent with other

examples of high-spin Fe(II) from our laboratory,[7a] a contraction of 0.22 Å in the

average Fe-P bond lengths is apparent upon reduction from **2.1** to **2.3**, resulting in an

exceptionally short average Fe-P bond distance of 2.17 Å in **2.3** (The average Fe-P

distance in the CSD is 2.24 Å).[8] Some contraction in these lengths might be expected

from increased back-bonding from the reduced Fe centers, but the short distance of 2.17

Å is indicative of a low-spin state at Fe, suggesting that a spin-state change has occurred.

Complex	Fe -S (Å)	Fe-S-Fe (°)	Avg. Fe-P (Å)	Δ Fe-P (Å)
2.1	2.079(8)	180	2.393	0.04
2.2	2.1035(3)	173.18(5)	2.215	0.19
2.3	2.077	178.83(6)	2.170	0.04

Table 2.1. Selected metrics for complexes **2.1**, **2.2**, and **2.3**.

Complexes **2.1**, **2.2**, and **2.3** all display paramagnetically shifted ^{1}H NMR shifts at

RT and so variable temperature magnetic susceptibility measurements were acquired by

SQUID magnetometry (Figure 2.3). Complex **2.1** displays a magnetic moment of 2.0 μ_B

at 300 K which decreases relatively linearly upon cooling to 75 K. The room RT

magnetic moment, which is substantially smaller than the value of 6.9 μ_B that would be

expected for two non-interacting high-spin Fe(II) centers, and the decrease of moment

with temperature are both consistent with antiferromagnetic coupling between the two Fe

centers in **2.1**. A simulation of the data (Figure 2.3) indicates that the coupling constant

between the two Fe centers in **2.1** is $J = -154$ cm^{-1}, suggesting strong coupling across the

S^{2-} bridge. Such coupling across linear one-atom bridges is not uncommon and has been

observed in other Fe-S-Fe complexes.[10,11] It should also be noted that the $S_1 = S_2 = 2$ and

$S_1 = S_2 = 1$ cases should appear similar in the magnetic data and so distinguishing

between intermediate spin Fe centers by this method is challenging. The long Fe-P bond

distances and the Mössbauer data (vide infra) for **2.1** seem to support the high spin $S_1 =$

$S_2 = 2$ case as more likely.
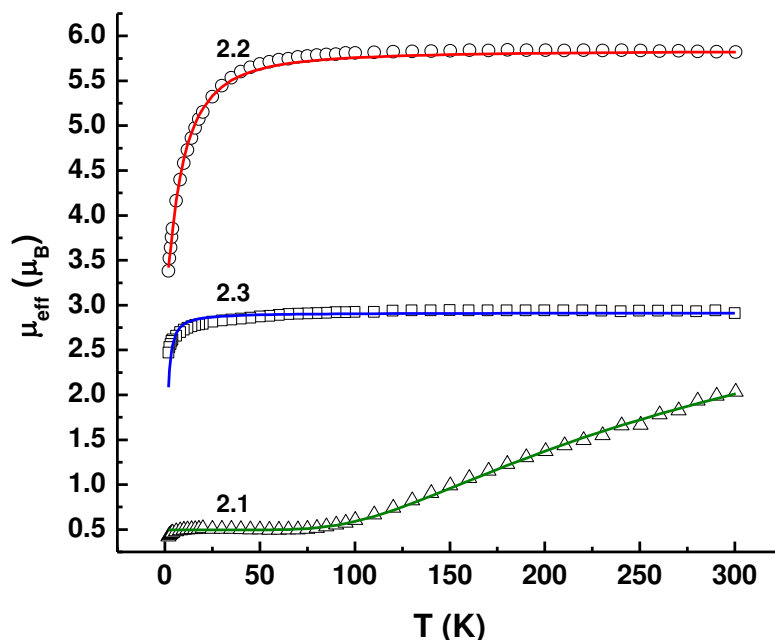
Figure 2.3. Variable temperature magnetic susceptibility measurements on complexes
2.1-**2.3**.

Unlike complex **2.1**, complex **2.2** shows a high magnetic moment of 5.8 μ_B at 300

K which does not substantially decrease until ~50 K, after which it drops, likely due to

intermolecular antiferromagnetic interactions. The lack of a downward slope suggests

little to no antiferromagnetic coupling. The possible spin states for a Fe(II)/Fe(I) dimer

are $S_1 = 2$ $S_2 = 3/2$, $S_1 = 2$ $S_2 = 1/2$, $S_1 = 1$ $S_2 = 3/2$, $S_1 = 1$ $S_2 = 1/2$, or $S_1 = 0$ $S_2 = 1/2$. If

both Fe centers were high spin, as in complex **2.1**, a spin-only moment of 6.2 μ_B for two

weakly interacting Fe centers might be expected. The fact that the moment of **2.2** is

lower than this predicted value and that the moment shows a relatively flat temperature

profile down to 50 K suggests that a high-spin state assignment is likely not reasonable

for this complex. Accordingly, simulations with $S_1 = 2$ and $S_2 = 3/2$ provide poor fits to the data.

Complex	S_1	S_2	g	J (cm^{-1})	Θ (K)
2.1	2	2	2.00	-154	0
2.2	2	1/2	2.01	110	-5.7
2.3	1/2	1/2	2.06	197	-1

Table 2.2. Simulation parameters for complexes **2.1**, **2.2**, and **2.3** for the fits shown in Figure 2.3.

The moment for **2.2** of 5.8 μ_B at 300 K is close to the spin-only value for a single $S = 5/2$ center (5.9 μ_B), suggesting that an $S_1 = 2$, $S_2 = 1/2$ or $S_1 = 1$, $S_2 = 3/2$ spin state assignment with strong ferromagnetic coupling seems appropriate. While simulation with either of these parameters provides a reasonable fit, a strongly ferromagnetically coupled $S_1 = 2$, $S_2 = 1/2$ state is the preferred assignment for reasons that will be discussed shortly. As an additional note, ferromagnetic coupling between two metal centers typically results in a magnetic moment that increases with decreasing temperature. When the coupling is very strong, however, the temperature profile can adopt a much flatter gradual slope to a plateau temperature as J becomes large.[12] The strong coupling between the Fe centers in **2.2** leads to almost exclusive population of the high-spin state even at RT, as illustrated by the magnetic data. Furthermore, although a value for J is obtained in the fit for the moment of **2.2**, it must be stressed that the lack of a significant slope for this complex precludes the accurate determination of J, with the data merely requiring a large positive value of J.

The large J value in **2.2** suggests that there should be some degree of electronic coupling between the two metal centers. Classically, in the case of mixed-valence complexes like **2.2**, one way to probe this coupling has been to examine the line shape of the inter-valence charge transfer (IVCT) band via near-IR spectroscopy.[13] Complex **2.2** does indeed show a relatively strong IVCT band at 6750 cm^{-1} (Figure 2.4A) in its near-IR spectrum. Analysis of the lineshape of this band indicates that H_{ab} for this complex is 562 cm^{-1}, suggesting a moderate degree of electronic coupling and classifying **2.2** as class II using the Robin-Day classification system.[14] In addition to the near-IR data mentioned, low temperature X-band EPR data on **2.2** have been acquired (Figure 2.4B). The 4 K spectrum of **2.2** in 2-MeTHF displays a broad signal with a large feature at $g =$ 5.64 and a smaller feature at $g = 2.12$. Although the magnetic moment at 4 K is substantially decreased, likely due to inter-molecular effect, the EPR data suggests that S > 1/2 states are populated even at very low temperatures, consistent with the ferromagnetic coupling observed.
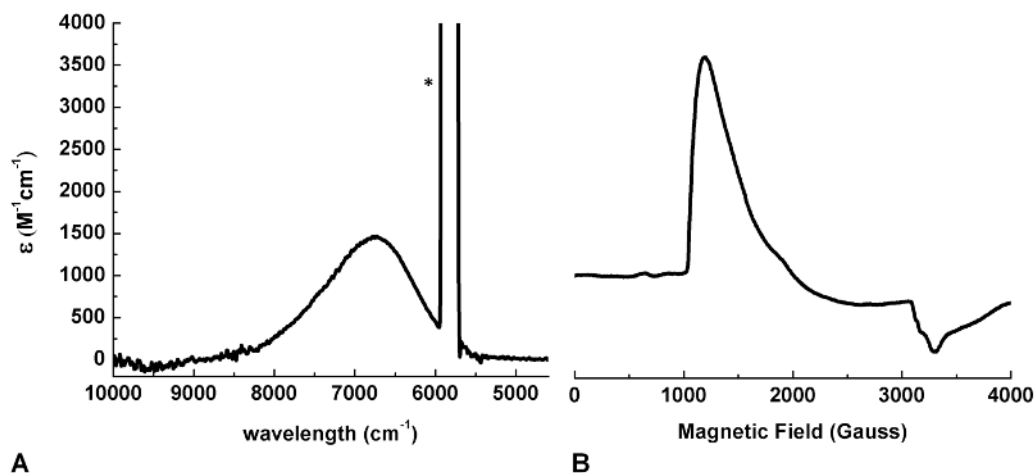
Figure 2.4. (A) Near-IR spectrum of complex **2.2**. (B) 4 K X-band EPR spectrum of **2.2**. Conditions for (A): THF, 0.013 M. Note that the asterisk denotes a large feature due to

solvent background subtraction. Conditions for (B): microwave power, 20.313 mW; microwave frequency, 9.380 GHz; modulation amplitude, 4.00 G; gain, 5020.

The dianionic complex **2.3** was analyzed similarly to monoanionic **2.2**. Complex **2.3** displays a similar temperature dependence to that observed in complex **2.2** with little to no change from the $\mu_{eff} = 2.8$ μ_B value observed at 300 K until the temperature drops below ~ 100 K. It is even more apparent for this sample that a high-spin assignment for the two Fe centers is inappropriate, as two $S = 3/2$ centers without antiferromagnetic coupling, which can again be excluded by the dependence of the moment on temperature, should have a minimum μ_{eff} of 5.5 μ_B. A similar analysis to that performed for **2.2** leads to the conclusion that an $S_1 = S_2 = 1/2$ spin state assignment with a large degree of ferromagnetic coupling between the two magnetic centers adequately describes the magnetic behavior and these parameters provide a reasonable fit to the data (Figure 2.3, table 2.2). As was found in the case of **2.2**, the absence of a well-defined slope for **2.3** precludes the accurate determination of J, but a large positive value seems required. These combined crystallographic and magnetic data suggest that the reduced Fe centers in **2.2** and **2.3** are undergoing a spin transition to $S = 1/2$ upon reduction. Low-spin Fe(I) centers are uncommon in general, and are even more rare in tetrahedral geometries. In order to obtain more confirmation of this assignment, Mössbauer data were collected on the redox series of complexes.

Complex **2.1** displays a quadrupole doublet with an isomer shift of $\delta = 0.49$ mm/s and a quadrupole splitting of $\Delta E_q = 1.91$ mm/s in its 80 K Mössbauer spectrum (Figure 2.4). Related high-spin Fe(II) complexes on the PhBP$_3$ scaffold have shown parameters

that are quite similar to these values.[15] Upon reduction, a new spectrum is obtained that can be fit as two independent sites in a 1:1 ratio. The parameters for the two signals indicate one site having $\delta = 0.47$ mm/s and $\Delta E_q = 1.14$ mm/s and the other site having drastically different parameters of $\delta = 0.16$ mm/s and a small poorly resolved quadrupole splitting of $\Delta E_q = 0.01$ mm/s. The reasonable assignment for this spectrum is that the two Fe sites are resolved on the Mössbauer timescale. While the first site is still relatively consistent with high-spin Fe(II) centers, the second site, and its negligible quadrupole splitting, suggest a different electronic structure.
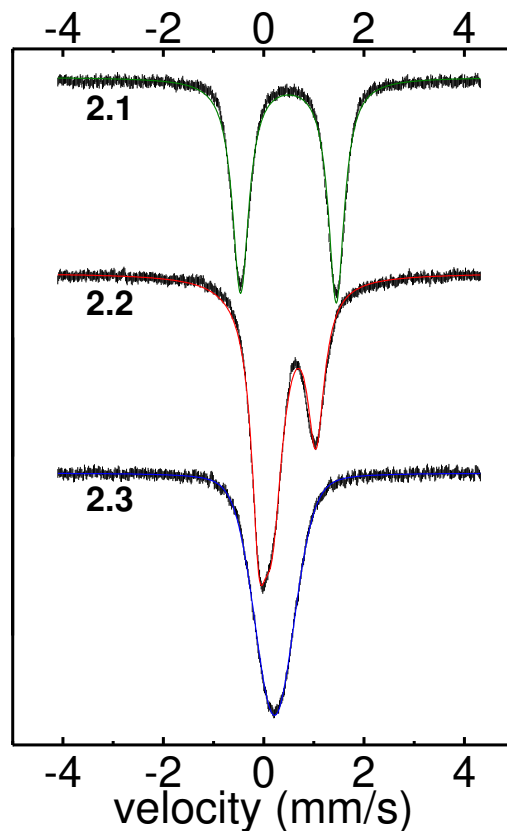
Figure 2.5. 80 K Mössbauer spectra of solid samples of complexes **2.1-2.3** and corresponding fits.

Upon further reduction to **2.3**, the quadrupole doublet signal disappears and the remaining signal has $\delta = 0.22$ mm/s with no resolvable quadrupole splitting. Previously reported Fe(I) complexes on PhBP$_3$ are high-spin, and their Mössbauer parameters do not show good agreement with the parameters found in **2.3**, suggesting that this site is not well modeled as a high-spin Fe(I) site, leaving a low-spin Fe(I) site as the most plausible alternative, especially when considering the magnetic and structural data already presented. The values for the isomer shifts of the reduced Fe centers in **2.2** and **2.3** deserve some mention, as one typically observes an increase in δ upon reduction.[16] The observed negative change in δ is likely a result of the high covalency and greater back-bonding into the phosphine ligands in this series of complexes as well as the proposed spin-state change.
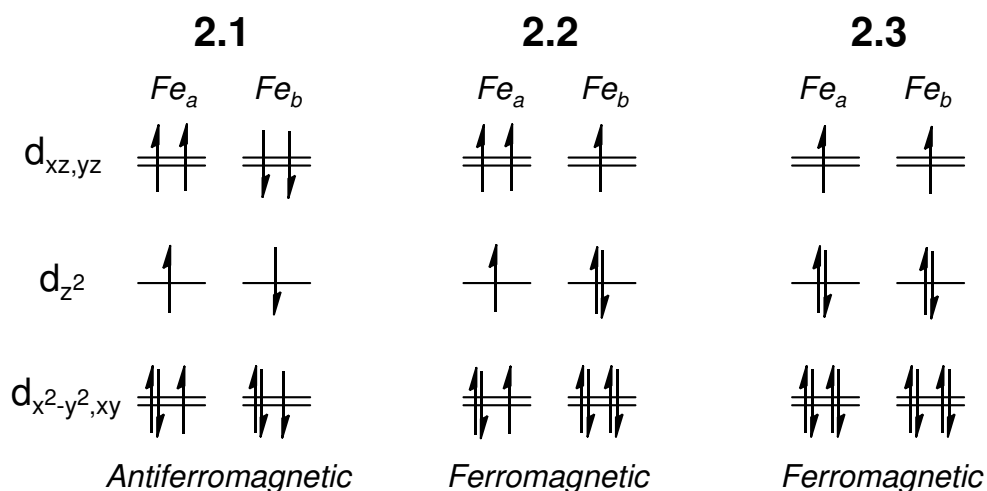
Figure 2.6. Qualitative d-orbital splitting diagrams illustrating the coupling in **2.1**-**2.3**.

A satisfying explanation for the observed structural, magnetic, and spectroscopic data for this series of redox complexes warrants consideration. The structural data,

especially the short Fe-P bond distances in the reduced complexes, certainly suggest a low-spin configuration at Fe. The magnetic data, however, show an increase in the magnetic moment, which has been attributed to change in the magnetic coupling between the Fe centers from antiferromagnetic in **2.1** to ferromagnetic in **2.2** and **2.3**. While this change may seem capricious, consideration of a qualitative orbital diagram and the interactions involved in magnetic coupling provides a clear rationale for this phenomenon (Figure 2.6).

In all three complexes there are two avenues by which magnetic coupling can occur through the diamagnetic S^{2-} linker: one σ-symmetry interaction involving metal orbitals of d_{z^2} parentage and two degenerate π-symmetry interactions involving metal orbitals of $d_{xz,yz}$ parentage. In high-spin **2.1**, both the σ and π orbitals are half-filled on both metal centers, resulting in an antiferromagnetic interaction through both manifolds. Upon reduction to **2.2** and subsequent transition of one Fe center to low-spin states, however, the σ manifold will have one filled orbital and one half-filled orbital, resulting in a ferromagnetic interaction.[17] While it is unclear whether the interaction in the π manifold will be ferromagnetic or antiferromagnetic, it is likely that the σ coupling will dominate the overall magnetism of the complex. When both Fe centers are low spin, as in **2.3**, the σ set of orbitals will be completely filled, excluding coupling through this manifold. Each metal center will have a quarter filled E set of orbitals which, due to their degeneracy, will result in a ferromagnetic interaction as required by Hund's rule.[17] When this explanation is compared with the available data, the observed change in magnetic coupling meshes well with the proposed spin-state transition and neatly ties together the observed properties of complexes **2.1**-**2.3**.

2.2.2 Reactivity with Small Molecules

With this redox series of complexes well characterized, further studies of the

reactivity of these complexes with small molecules relevant to nitrogenase and other Fe-

S-Fe containing enzymes were of interest. As an initial foray into these investigations,

the reactivity of N_2H_4 and CO with complex **2.1** was investigated (Scheme 2.2).

Reaction of **2.1** with excess N_2H_4 results in a gradual color change from dark brown to

dark red-orange. XRD data obtained on red crystals indicate that the diamagnetic product

is $((PhBP_3)Fe)(\mu-\eta^1:\eta^1-N_2H_4)(\mu-\eta^2:\eta^2-N_2H_2)((PhBP_2PS)Fe)$ ($(PhBP_2PS)$ =

$[PhB(CH_2PPh_2)_2(CH_2P(S)Ph_2)]^-$) (**2.4**) (Figure 2.7). This complex features an unusual

$SFe_2N_4H_6$ core similar to a previously reported example from our laboratory.[18] If **2.1** is

instead reacted with 1 atm of CO, a deep purple solution is obtained that is indicative of

the product $[(PhBP_3)Fe(CO)]_2(\mu-S)$ (**2.5**). Complex **2.5** is diamagnetic and displays a

strong C-O stretch at $\nu_{CO} = 1950$ cm^{-1}.
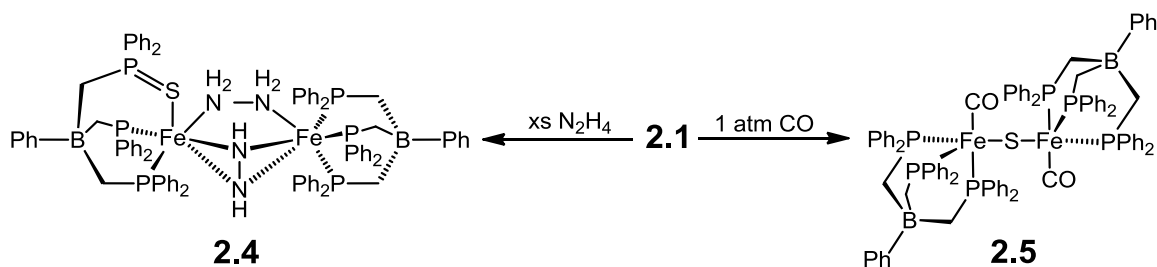
Scheme 2.2. Synthesis of complexes **2.4** and **2.5**.

Both complexes **2.4** and **2.5** have been crystallographically characterized and their

core atoms are shown in Figure 2.7. In **2.4**, the once-bridging sulfur atom has migrated to

a phosphine arm, forming a phosphine sulfide exemplified by a short P-S distance of

1.997(2). The two nitrogenous ligands are best described as a hydrazine and a

hydrazido(2-) as indicated by long N-N distances of 1.449(5) and 1.451(4) respectively.

The migration of S onto P is likely favorable due to the formation of a relatively strong P-

S bond as well as the driving force to form the octahedral and diamagnetic $Fe_2N_4H_4$ core.

XRD data for **2.5** indicate that one CO molecule is coordinated to each iron center to give

a pseudo-trigonal bipyramidal geometry about Fe. The Fe-S bond distances do not

change significantly from those in **2.1**, elongating slightly to 2.1027(7) Å while the Fe-S-

Fe linkage maintains an angle of about 162°. These bond metrics suggest some

maintenance of multiple bonding across the Fe-S-Fe unit. The observed diamagnetism of

2.5 when compared with **2.1-2.3** is likely a result of the combination of a stronger ligand

set with the addition of a CO ligand, the higher coordination number at Fe, and potential

antiferromagnetic coupling across the S^{2-} bridge.

2.4　　　　　　　　　　**2.5**
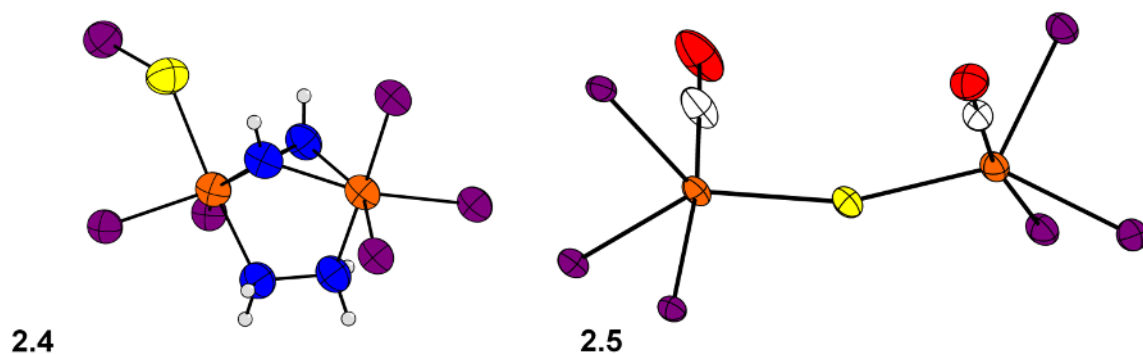
Figure 2.7. XRD structures of the cores of complexes **2.4** and **2.5** with ellipsoids at 50%.

Fe atoms are shown in orange, S in yellow, P in purple, Na in blue, O in red, H in gray,

and C in white.   Selected bond lengths (Å) and angles (°) for **2.4**: Fe(2)-S(1) =

2.3382(12), N(1)-N(2) = 1.449(5), N(3)-N(4) = 1.451(4), S(1)-P(6) = 1.9970(17).

Selected bond lengths (Å) and angles (°) for **2.5**: Fe(1)-S(1) = 2.1027(7), Fe(2)-S(1) =

2.1028(7), Fe(2)-S(1)-Fe(1) = 162.10(4).

The CV of **2.5** displays similar electrochemistry to that of **2.1** showing two reductions at -1.25 V and -2.09 V with respect to the Fc/Fc$^+$ couple (Figure 2.8A). Additionally, a new quasi-reversible oxidation appears at 0.20 V. Despite these new waves, no chemical reductions provided tractable products. The second reduction couple at -2.09 V versus Fc/Fc$^+$ displays a typical cathodic increase in current upon scanning negatively, but upon reversal of the scan polarity two re-oxidation peaks are observed. Analysis of the scan-rate dependence of these two peaks (Figure 2.8B) shows the more negative peak increasing in intensity with faster scan rates. This observation may be explained by a ligand dissociation event in which one redox event is observed with the ligand still bound at more negative potentials and one redox event is observed where a ligand is not bound at more positive potentials. This phenomenon has been observed previously in TPPFeCl (TPP = tetraphenylporphyrin).[19] In the case of **2.5** the ligand dissociation event likely involves reversible loss of a phosphine arm.
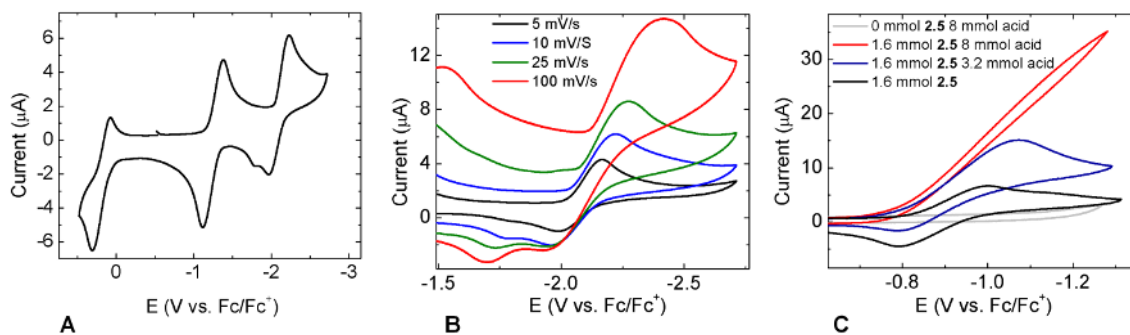
Figure 2.8. (A) CV of **2.5** at 10 mV/s. (B) CV's of **2.5** at differing scan rates. (C) CV of **2.5** at 10 mV/s with the listed concentrations of *p*-toluenesulfonic acid. All scans were taken in THF with the following conditions: [TBA][PF$_6$], THF, glassy carbon working, Pt auxiliary, Ag/[Ag][NO$_3$] reference.

Due to the resemblance of the ligand set of complex **2.5** with hydrogenase enzymes and the hydrogenase function of nitrogenase in the absence of N_2, electrocatalytic reactivity towards acid was investigated (Figure 2.8C). Complex **2.5** shows no apparent reactivity with acid sources as gauged by proton NMR. Addition of *p*-toluenesulfonic acid to a CV of **2.5**, however, results in an increase in reductive current at ~ -0.8 V vs. Fc/Fc$^+$. The electrocatalytic peak onsets near the couple assigned as Fe(II)Fe(II)/Fe(II)Fe(I), indicating that these oxidation states may be involved in the catalytic cycle. An overpotential of ~ 560 mV can be estimated[20] for the electrocatalytic reduction, which is in the typical range of 400 to 700 mV observed in most hydrogenase mimics.[4d] Bulk electrolyses of **2.5** in a standard two chamber cell show a Faradaic efficiency of 77%, indicating that the majority of protons and electrons are used in producing H_2.

2.3 Conclusion

Taken together, the Fe-S-Fe complexes presented in this chapter display rich redox, magnetic, spectroscopic, and catalytic features. The highly reduced complexes **2.2** and **2.3** illustrate that S^{2-} can still be bound to low-valent Fe as could be necessary in nitrogenase for N_2 binding. Furthermore, these reduced Fe centers adopt a low-spin state which could also prove beneficial for N_2 binding. In addition to the reduced Fe-S-Fe complexes, **2.1** shows interesting reactivity with N_2H_4 and CO, resulting in complex **2.5** which shows functionality as a hydrogen evolution catalyst. These studies begin to

highlight some of the electronic features that might be critical for the function of biological enzymatic systems with Fe-S-Fe units.

2.4 Experimental Section

2.4.1 General Considerations

Unless otherwise noted, all compounds were prepared by literature procedures or purchased from commercial sources. Specifically, the starting material $(PhBP_3)FeCl$ was made according to its literature preparation.[21] All manipulations were carried out under a dinitrogen atmosphere by utilizing standard glovebox or Schlenk techniques to exclude oxygen and water. Solvents were dried and de-oxygenated by an argon sparge followed by passage through an activated alumina column purchased from S.G. Waters Company. All solvents were tested with a standard sodium-benzophenone ketyl solution to ensure the absence of oxygen and water. NMR measurements were obtained on Varian 300 or 500 MHz or Bruker 400 MHz spectrometers. Deuterated solvents for these measurements were obtained from Cambridge Isotope Laboratories and were dried and degassed prior to use. All ^1H spectra were referenced to residual solvent peaks. IR spectra were obtained via KBr pellets on a Bio-Rad Excalibur FTS 3000 spectrometer using Varian Resolutions Pro software set at 4 cm^{-1} resolution. Near-IR spectra were obtained using a Nicolet FT-NIR spectrometer with quartz cuvettes sealed with a ground-glass stopper

2.4.2 Electrochemical Measurements

All experiments were conducted with a CH Instruments 630-C Electrochemical

Analyzer and the CHI Version 8.09 software package. Both CV and bulk electrolysis

experiments were conducted under an atmosphere of dinitrogen with 0.1 M [TBA][PF$_6$]

in THF as the electrolyte. Cyclic voltammetry experiments were conducted in a single

cell setup with a platinum wire as the auxiliary electrode, a Ag/[TBA][PF$_6$]/THF pseudo-

reference electrode separated from the solution by a Vycor frit (Bioanalytical Systems,

Inc.), and a 0.078 cm^2 glassy carbon electrode (Bioanalytical Systems, Inc.). Ferrocene

was included in scans as an internal standard of potential.

Bulk Electrolyses were performed under identical conditions in a sealed 2-

chamber cell with the working and reference electrode in the first cell and the auxiliary

electrode in the second cell. The two chambers were separated by a fine glass frit. While

an identical reference electrode was used, the working electrode was a glassy carbon slab

(Tokai Carbon USA) submerged such that roughly 64 cm^2 was in the electrolyte solution

and the auxiliary electrode was a 3.18 mm thick piece of carbon felt (Alfa Aesar) which

was similarly submerged to the working electrode. Quantification of H$_2$ was performed

by extraction of an aliquot of the headspace and analysis with an Agilent 7890A gas

chromatograph using a thermal conductivity detector.

2.4.3 EPR Measurements

EPR X-band spectrometry was obtained on a Bruker EMX spectrometer with the

aid of Bruker Win-EPR software suite version 3.0. The spectrometer was equipped with

a rectangular cavity which operated in the TE$_{102}$ mode. Temperature control was

achieved with the use of an Oxford continuous-flow helium cryostat (temperature range

3.6 – 300 K). The microwave bridge came equipped with a frequency counter which

enabled accurate measurement of the frequency values. The sample was prepared in a

9:1 THF:1-MeTHF solution in an EPR tube sealed with a Teflon stopcock.

2.4.4 Magnetic Measurements

Data was obtained using a Quantum Designs SQUID magnetometer running

MPMSR2 software (Magnetic Property Measurement System Revision 2) at a field

strength of 50000 G. Samples were inserted into the magnetometer in plastic straws

sealed under nitrogen with polycarbonate capsules. Loaded samples were centered

within the magnetometer using the DC centering scan at 35 K and 5000 gauss. Data were

acquired at 2-20 K (one data point every 2 K), and 20-310 K (one data point every 5 K).

The magnetic susceptibility was adjusted for diamagnetic contributions using the

constitutive corrections of Pascal's constants, as well as a diamagnetic subtraction due to

the holder diamagnetism. Data workup, including simulations, was performed in the

JulX software package.[22]

2.4.5 Mössbauer Spectroscopy

Spectra were recorded on a spectrometer from SEE Co (Edina, MN) operating in

the constant acceleration mode in a transmission-geometry. Spectra were recorded with

the temperature of the sample maintained at 80 K. The sample was kept in an SVT-400

dewar from Janis (Wilmington, MA) at zero field. Application of a magnetic field of 54

mT parallel to the γ-beam did not cause detectable changes in the spectra recorded at 80

K. The quoted isomer shifts are relative to the centroid of the spectrum of a metallic foil of α-Fe at RT. Samples were prepared by grinding polycrystalline material into a fine powder and then mounted in a cup fitted with a screw-cap as a boron nitride pellet. Data analysis was performed using the program WMOSS[23] and quadrupole doublets were fit to Lorentzian lineshapes.

2.4.5 X-Ray Crystallography

Data were obtained at low temperatures on a Siemens or Bruker Platform three-circle diffractometer coupled to a Bruker-AXS Smart Apex CCD detector with graphite-monochromated Mo or Cu Kα radiation (λ = 0.71073 or 1.54178 Å, respectively), performing φ-and ω-scans. All structures were solved by standard direct or Patterson methods and refined against F^2 using the SHELX program package.[24,25,26] All atoms, with the exception of hydrogens, were anisotropically refined. All hydrogen atoms were calculated using a standard riding model.

Several disordered ligand and solvent molecules were refined with the use of standard restraints. It is noteworthy that in the structure of **2.1** additional electron density was found in the central core of the molecule. This was modeled as a small percentage of a disordered bis-thiolate. While the bond lengths in **1** seem longer than what would be expected for similar molecules, these models fit the data quite well and were left in. The structure of **2.2** suffers from a large amount of disorder in solvent and counterion molecules. This leads to poor, although still acceptable, overall statistics. Additionally, there is a small component of disorder present in the phosphine ligands of **2.2**. This disorder may be a manifestation of localization of the inter-valence species.

2.4.6 Synthesis

Synthesis of ((PhBP₃)Fe)₂(µ-S), 2.1. (PhBP₃)FeCl (0.301 g, 0.39 mmol) and NEt₃ (0.1

mL, 0.72 mmol) were dissolved in benzene (10 mL) to form a bright yellow solution. To

this, a suspension of [TBA][SH] (0.081 g, 0.29 mmol) in THF (5 mL) was added

dropwise over 5 minutes. The solution rapidly turned dark brown with dark precipitate

and was allowed to stir at RT for 2 hours. After this time, solvent was removed *in vacuo*

and the remaining residue was extracted into benzene (10 mL) and filtered through a

silica plug. The benzene solution was frozen and lyophilized to yield **2.1** as a dark brown

powder (0.150 g, 0.01 mmol, 51%). X-ray quality crystals were grown from pentane

diffusion into a concentrated benzene solution of **2.1**. ^{1}H NMR (C_6D_6, δ): 28.29 (s),

14.67 (s), 10.50 (t, J = 7 Hz), 9.75 (t, J = 7 Hz), 5.56 (s), 4.20 (t, J = 7 Hz), 2.76 (br s).

UV-vis (THF) λ_{max}, nm (ε, M^{-1} cm^{-1}): 944 (sh), 905 (5550), 637 (2140), 350 (13310), 301

(16580), 263 (sh).   Anal. Calc. for $C_{90}H_{82}B_2Fe_2P_6S$: C 71.36; H 5.46. Found: C 71.04; H

5.45.

Synthesis of [((PhBP₃)Fe)₂(µ-S)][Na(12-crown-4)₂], 2.2. A solution of **2.1** (0.050 g,

0.03 mmol) in THF (5 mL) was placed over a freshly prepared amalgam of sodium (0.01

g, 0.43 mmol) and mercury (1 g) with a stir bar. The amalgam was stirred for 15

minutes, over which time the solution turned dark green. The THF solution was then

decanted from the amalgam and filtered through a celite plug before volatiles were

removed. The resulting dark green solid was triturated and washed 3x with ether and

benzene (3 ml) before being taken up in a minimum of THF. 12-crown-4 (0.1 mL, 0.6

mmol) was then added before the solution was layered with pentane and cooled to -35 °C

to crystallize overnight. After 12 hours the mother liquor was removed and the dark crystals were washed 3x with benzene (3 mL) to provide **2.2** as a black solid (0.047 g, 0.025 mmol, 76%). ^{1}H (THF-d_8, δ): 53.68 (br s), 10.54 (s), 9.64 (s), 1.93 (s), 0.053 (br s). UV-vis (THF) λ_{max}, nm (ε, M^{-1} cm^{-1}): 944 (sh), 905 (5550), 740 (sh), 638 (8463), 511 (sh), 346 (24420), 296 (28560). Elemental analysis was obtained on the bis-THF adduct obtained prior to 12-crown-4 addition, Anal. Calc. for $C_{114}H_{124}B_2Fe_2NaO_6P_6S$: C 69.70, H 6.36. Found: C 69.08, H 6.41.

Synthesis of [((PhBP$_3$)Fe)$_2$(μ-S)][Na(12-crown-4)$_2$]$_2$, 2.3. Naphthalene (0.009 g, 0.07 mmol) was mixed with sodium (0.01 g, 0.43 mmol) and a stirbar in a 20 mL scintillation vial. THF (2 mL) was added and the resulting mixture was vigorously stirred for 2 hours, over which time the liquid phase turned dark green. **2.1** (0.050 g, 0.03 mmol) in THF (5 mL) was cooled to -35 °C for 30 minutes. After this time the solution of $NaC_{10}H_8$ was filtered through a glass fiber filter paper into the solution of 1. The solution was allowed to stir at RT for 10 minutes, during which time the color of the solution darkened to black. The solution was then concentrated to half volume before 12-crown-4 (0.012 g, 0.06 mmol) was added. The solution was then layered with 3 mL of pentane before being cooled to -35 °C overnight to yield a black crystalline material which was then washed 3x with benzene (3 mL) to yield 3 (0.037 g, .015 mmol, 49%). ^{1}H NMR (THF-d_8, δ): 10.36 (br s), 8.63 (br s), 7.83 (s), 7.23 (br s), 7.04 (br s), 0.04 (br s), -1.75 (br s). Anal. Calc. for $C_{122}H_{146}B_2Fe_2Na_2O_{16}P_6S$: C 64.67, H 6.50. Found: C 63.98, H 6.85. The low solubility of the product precluded the acquisition of a UV-Vis spectrum.

Synthesis of ((PhBP$_3$)Fe)(μ-η^1:η^1-N$_2$H$_4$)(μ-η^2:η^2-N$_2$H$_2$)((PhBP$_2$PS)Fe), 2.4. Complex **2.1** (0.010 g, 0.007 mmol) was dissolved in benzene (5 mL) to form a dark brown

solution. After the solution became homogenous, a solution of hydrazine in THF (106

µL, 0.312 M, 0.033 mmol) was added at RT with stirring. The solution was allowed to

stir for 20 minutes over which time the color of the solution changed from dark brown to

deep red-orange. Volatiles were removed to provide **5** as a rust colored powder (0.010 g,

0.006 mmol, 96%). ^{1}H NMR (C$_6$D$_6$, δ): 8.67 (t, J = 6 Hz, 3H), 8.30 (br s, 3H), 8.17 (d, J =

6 Hz, 2H), 7.93 (d, J = 6 Hz, 2H), 7.67 (t, J = 6 Hz, 2H), 7.60 (m, 4H), 7.32 (m, 10H),

7.10 (m, 6H), 6.87 (m, 7H), 6.83 (t, J = 6 Hz, 3H), 6.54 (d, J = 30 Hz, 10 H), 2.91 (br s,

2H), 2.42 (t, J = 10 Hz, 3H), 2.15 (t, J = 10 Hz, 3H), 1.74 (br m, 6H), 1.61 (d, J = 10 Hz,

2H), 1.52 (br s, 2H), 0.49 (br s, 2H). ^{31}P{^{1}H} NMR (C$_6$D$_6$, δ): 68.74 (s, 2P), 63.94 (s, 1P),

63.48 (s, 1P), 59.33 (s, 2P). IR (KBr, cm^{-1}): 3310, 3225 (ν_{NH}).

Synthesis of ((PhBP$_3$)Fe(CO))$_2$(µ-S), 2.5. A schlenk tube was charged with a dark

brown solution of **1** (0.072 g, 0.047 mmol) in THF (6 mL) and a stir bar. This solution

was degassed via three freeze, pump, thaw cycles and was then exposed to 1 atm of CO.

Upon addition of CO, an immediate color change to dark reddish purple was observed.

The reaction was allowed to stir under CO for 5 minutes before solvent was removed.

The remaining purple residue was extracted back into THF and was layered with pentane.

Upon standing for 24 hours, red crystals of **4** were obtained in two crops (0.053 g, 0.034

mmol, 72%). X-ray quality crystals were grown from a pentane vapor diffusion into a

concentrated THF solution of **4**. ^{1}H NMR (C$_6$D$_6$, δ): 8.16 (d, J = 6 Hz, 3H), 7.93 (br m,

5H), 7.68 (t, J = 6 Hz, 4H), 7.42 (m, 16H), 6.88 (m, 24H), 6.71 (m, 16H), 6.45 (br s, 4H).

^{31}P{^{1}H} NMR (C$_6$D$_6$, δ): 55.97 (dd, J = 84, 60 Hz), 24.29 (t, J = 58 Hz). UV-vis (THF)

λ_{max}, nm (ε, M^{-1} cm^{-1}): 944 (sh), 905 (5550), 665 (sh), 506 (23680), 407 (sh). IR (KBr,

cm-1): 1950 (v[CO]).   Anal. Calc. for $C_{100}H_{96}B_2Fe_2O_4P_6S$: C 70.11 H 5.65. Found: C 69.36 H 5.87.

References Cited

1 (a) Beinert, H.; Holm, R. H.; Münck, E. *Science* **1997**, *277*, 653-659; (b) Johnson, D. C.; Dean, D. R.; Smith, A. D.; Johnson, M. K. *Annu. Rev. Biochem.* **2005**, *74*, 247-281.

2 (a) Evans, D. J.; Pickett, C. J. *Chem. Soc. Rev.* **2003**, *32*, 268-275; (b) Fontecilla-Camps, J. C.; Volbeda, A.; Cavazza, C.; Nicolet, Y. *Chem. Rev.* **2007**, *107*, 4273-4303

3 (a) Dos Santos, P. C.; Igarashi, R. Y.; Lee, H. I.; Hoffman, B. M.; Seefeldt, L. C.; Dean, D. R. *Acc. Chem. Res.* **2005**, *38*, 208-214; (b) Einsle, O.; Tezcan, F. A.; Andrade, S. L. A.; Schmid, B.; Yoshida, M.; Howard, J. B.; Rees, D. C. *Science* **2002**, *297*, 1696-1700; (c) Seefeldt, L. C.; Hoffman, B. M.; Dean, D. R. *Annu. Rev. Biochem.* **2009**, *78*, 701-722.

4 (a) Crossland, J. L.; Tyler, D. R. *Coord. Chem. Rev.* **2010**, *254*, 1883-1894; (b) Gloaguen, F.; Rauchfuss, T. B. *Chem. Soc. Rev.* **2009**, *38*, 100-108; (c) Rao, P. V.; Holm, R. H. *Chem. Rev.* **2004**, *104*, 527-559; (d) Tard, C. d.; Pickett, C. J. *Chem. Rev.* **2009**, *109*, 2245-2274. (e) Holm, R. H.; Kennepohl, P.; Solomon, E. I. *Chem. Rev.* **1996**, *96*, 2239-2314;

5 (a) Chakrabarti, M.; Deng, L.; Holm, R. H.; Munck, E.; Bominaar, E. L. *Inorg. Chem.* **2009**, *48*, 2735-2747; (b) Deng, L.; Holm, R. H. *J. Am. Chem. Soc.* **2008**, *130*, 9878-9886.

6 (a) Vela, J.; Stoian, S.; Flaschenriem, C. J.; Münck, E.; Holland, P. L. *J. Am. Chem. Soc.* **2004**, *126*, 4522-4523; (b) Rodriguez, M. M.; Stubbert, B. D.; Scarborough, C. C.; Brennessel, W. W.; Bill, E.; Holland, P. L. *Angew. Chem. Int. Ed.* **2012**, *51*, 8247-8250.

7 (a) Brown, S. D.; Betley, T. A.; Peters, J. C. *J. Am. Chem. Soc.* **2002**, *125*, 322-323; (b) Brown, S. D.; Mehn, M. P.; Peters, J. C. *J. Am. Chem. Soc.* **2005**, *127*, 13146-13147; (c) Brown, S. D.; Peters, J. C. *J. Am. Chem. Soc.* **2005**, *127*, 1913-1923.

8 Cambridge Structural Database, 2011 update: F. H. Allen, Acta Crystallogr. B **2002**, *B58*, 380-388.

9 Salifoglou, A.; Simopoulos, A.; Kostikas, A.; Dunham, R. W.; Kanatzidis, M. G.; Coucouvanis, D. *Inorg. Chem.* **1988**, *27*, 3394-3406.

10 (a) Greenhough, T. J.; Kolthammer, B. W. S.; Legzdins, P.; Trotter, J. *Inorg. Chem.* **1979**, *18*, 3543-3548; (b) Mautz, J.; Huttner, G. *Eur. J. Inorg. Chem.* **2008**, 1423-1434; (c) Mealli, C.; Midollini, S.; Sacconi, L. *Inorg. Chem.* **1978**, *17*, 632-637; (d) Schiemann, J.; Hubener, P.; Weiss, E. *Angew. Chem., Int. Ed. Engl.* **1983**, *22*, 980-981.

11 Mukherjee, R. N.; Stack, T. D. P.; Holm, R. H. *J. Am. Chem. Soc.* **1988**, *110*, 1850-1861.

12 (a) Birkelbach, F.; Winter, M.; Floerke, U.; Haupt, H.-J.; Butzlaff, C.; Lengen, M.; Bill, E.; Trautwein, A. X.; Wieghardt, K.; Chaudhuri, P. *Inorg. Chem.* **1994**, *33*, 3990-4001; (b) Escuer, A.; Goher, M. A. S.; Mautner, F. A.; Vicente, R. *Inorg. Chem.* **2000**, *39*, 2107-2112; (c) Kahn, O.; Sikorav, S.; Gouteron, J.; Jeannin, S.; Jeannin, Y. *Inorg. Chem.* **1983**, *22*, 2877-2883.

13 Brunschwig, B. S.; Creutz, C.; Sutin, N. *Chem. Soc. Rev.* **2002**, *31*, 168-184.

14 Schatz, P. In Inorganic Electronic Structure and Spectroscopy; Lever, A. B. P., Solomon, E. I., Eds.; John Wiley & Sons: New York, 1999; Vol. II.

15 Hendrich, M. P.; Gunderson, W.; Behan, R. K.; Green, M. T.; Mehn, M. P.; Betley, T. A.; Lu, C. C.; Peters, J. C. *Proc. Natl. Acad. Sci.* **2006**, *103*, 17107-17112.

16 Neese, F. *Inorg. Chim. Acta* **2002**, *337*, 181-192.

17 Dionne, G. F. *Magnetic Oxides*; Springer Science+Business Media, LLC, 2010; pp 107-149.

18 Saouma, C. T.; Müller, P.; Peters, J. C. *J. Am. Chem. Soc.* **2009**, *131*, 10358-10359.

19 Bottomley, L. A.; Kadish, K. M. *Inorg. Chem.* **1981**, *20*, 1348-1357.

20 (a) Ding, F.; Smith, J. M.; Wang, H. *J. Org. Chem.* **2009**, *74*, 2679-2691; (b) Felton, G. A. N.; Glass, R. S.; Lichtenberger, D. L.; Evans, D. H. *Inorg. Chem.* **2006**, *45*, 9181-9184; (c) Fourmond, V.; Jacques, P.-A.; Fontecave, M.; Artero, V. *Inorg. Chem.* **2010**, *49*, 10338-10347.

21 Brown, S. D.; Betley, T. A.; Peters, J. C. *J. Am. Chem. Soc.* **2002**, *125*, 322-323.

22 http://ewww.mpi-muelheim.mpg.de/bac/logins/bill/julX_en.php

23 www.wmoss.org

24 Sheldrick, G. M. *Acta Cryst.* **1990**, *A46*, 467.

25 Sheldrick, G. M. *Acta Cryst.* **2004**, *A64*, 112.

26 Müller, P. *Crystallography Reviews* **2009**, *15*, 57.

Chapter 3: Conversion of FeNH$_2$ to FeN$_2$ with Release of NH$_3$

3.1 Introduction

The complexity of proposed mechanisms for N_2 fixation by Fe motivates efforts to synthesize and study intermediates along these pathways, and substantial efforts have been made towards characterizing many of the different species that might be involved in a catalytic cycle.[1,2] The tris-phosphine frameworks that have been employed by the Peters lab have been particularly useful in this context, stabilizing a wide variety of nitrogenous ligands on Fe centers supported by both the (PhBP$_3$) and (SiP$_3$) ligand scaffolds.[3,4] Despite the isolation of many examples of Fe complexes featuring nitrogenous ligands of interest, such as nitrides (FeN),[5] FeNH$_2$ species remain relatively poorly precedented, with only one example reported by Bergman and co-workers.[6] This paucity of examples is even more striking when considering the fact that a terminal FeNH$_2$ is one intermediate that is common to both "distal" and "alternating" mechanisms.

Despite the success of the (TPB) ligand scaffold towards the stabilization of substituted imides and the functionalization of N_2,[7] little work had been done to install functionalities containing N-H bonds. Furthermore, in shifting from the (SiP$_3$) scaffold to the (TPB) scaffold, the cationic N_xH_y adducts which were $S = 1$ on (SiP$_3$)Fe would be non-integer spin on (TPB)Fe, making them amenable to study by EPR spectroscopy. Finally, the noted ability of (TPB)Fe to stabilize π-basic ligands suggests that it may be able to accommodate a terminal NH_2^- ligand. In this context, the synthesis of terminal (TPB)Fe complexes of N_2H_4, NH_3, and NH_2^- are described. All of these complexes are formally Fe(I) and populate $S = 3/2$ spin states. Furthermore, a reductive protonation sequence wherein FeNH$_2$ is sequentially protonated to form FeNH$_3$ and then reduced to release NH_3 and form (TPB)Fe(N_2) is shown. Such a sequence is novel for any Fe

system and links together the final steps in either a "distal" or an "alternating"

mechanism for N_2 reduction catalysis.

3.2 Results and Discussion

3.2.1 Formation of a Cationic Fe(I) Synthon.

In order to install nitrogenous ligands of interest, a suitable synthon with a labile

or vacant apical coordination site was sought. Specifically, protonation of a terminal Fe

alkyl complex was pursued as a means to generate such a species. Access to such an

alkyl complex is provided by the addition of methyllithium to (TPB)FeBr[7], which affords

the corresponding methyl complex (TPB)FeMe (**3.1**) in high yield (Scheme 3.1).

Subsequently, protonation of 1 by HBAr$^F_4$·2 Et$_2$O (BAr$^F_4^-$ = B(3,5-C$_6$H$_3$(CF$_3$)$_2$)$_4^-$) in a

cold ethereal solution releases methane to yield [(TPB)Fe][BAr$^F_4$] (**3.2**), which serves as

the desired synthon with a vacant coordination site.
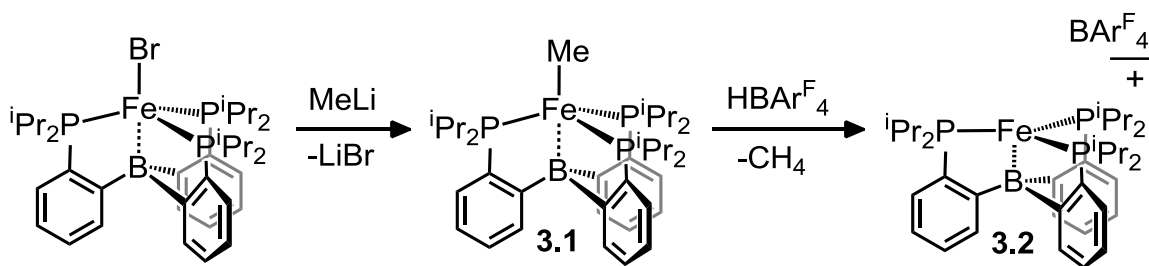
Scheme 3.1. Synthesis of complexes **3.1** and **3.2**.

XRD data were obtained for **3.1** and **3.2** (Figure 3.1). The geometry of **1** is pseudo

trigonal bipyramidal about Fe with an Fe-C bond length of 2.083(10) Å and a relatively

long Fe-B bond length of 2.522(2) Å. In the solid state **2** possesses a four-coordinate

distorted trigonal pyramidal geometry with no close contacts in the apical site trans to

boron, making this complex coordinatively unsaturated. Additionally, there is one wide P-Fe-P angle of 136° indicating that the three phosphine ligands are distorting towards a T-shaped geometry. The origin of this distortion is not clear, but a possible explanation is increased back-bonding from a relatively electron rich Fe center into the phosphine ligands that would arise from widening one P-Fe-P angle (see Appendix 2).

3.1   **3.2**
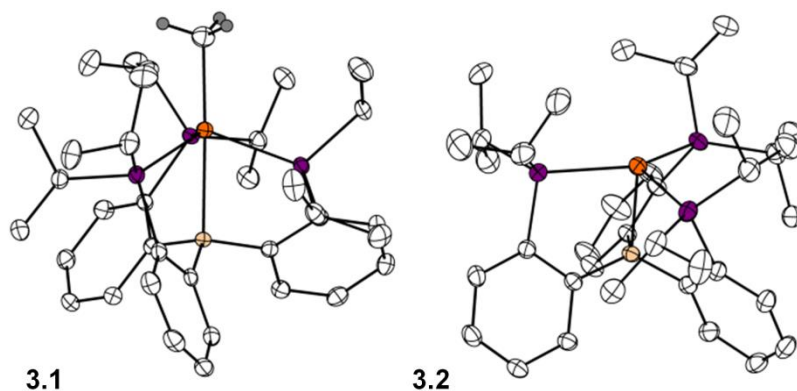
Figure 3.1. XRD structures of complexes **3.1** and **3.2** with ellipsoids at 50%. Most hydrogens and counterions have been omitted for clarity. Fe atoms are shown in orange, P in purple, B in tan, H in gray, and C in white. Selected metrics can be found in Table 3.1.

The Fe-B distance in **3.2** (2.217(2) Å) is markedly shorter than that in (TPB)FeBr (2.459(5) Å) and is the shortest Fe-B distance yet observed on any (TPB)Fe complex, shorter even than [(TPB)Fe(N$_2$)][Na(12-crown-4)$_2$] (2.292(3) Å). This short distance is noteworthy because one might expect the formal loss of an anionic σ-donor ligand in going from (TPB)FeBr to **3.2** to reduce the Lewis basicity of the metal and thus weaken the Fe-B bond. For example, the Au-B distance in (TPB)AuCl (2.318 Å) lengthens upon chloride abstraction to 2.448 Å in [(TPB)Au]$^+$.[8] Despite the comparatively short Fe-B

distance, it is noteworthy that the boron center in four-coordinate **3.2** is less pyramidalized (Σ(C−B−C) = 347.3°) than that in five-coordinate (TPB)FeBr (Σ(C−B−C) = 341.2°), pointing to a weak interaction despite the short distance. A short distance without a substantial Fe-B bonding interaction suggests that another factor may be involved in the observed geometry of **3.2**. If one assumes a weak Fe-B interaction, the observed geometry about Fe might be best understood as derived from a planar three-coordinate Fe(I) center distorted towards a T-shaped geometry which has been observed in other Fe(I) complexes,[9] with the unusually short Fe-B distance being due largely to the constraints imposed by the ligand cage structure.
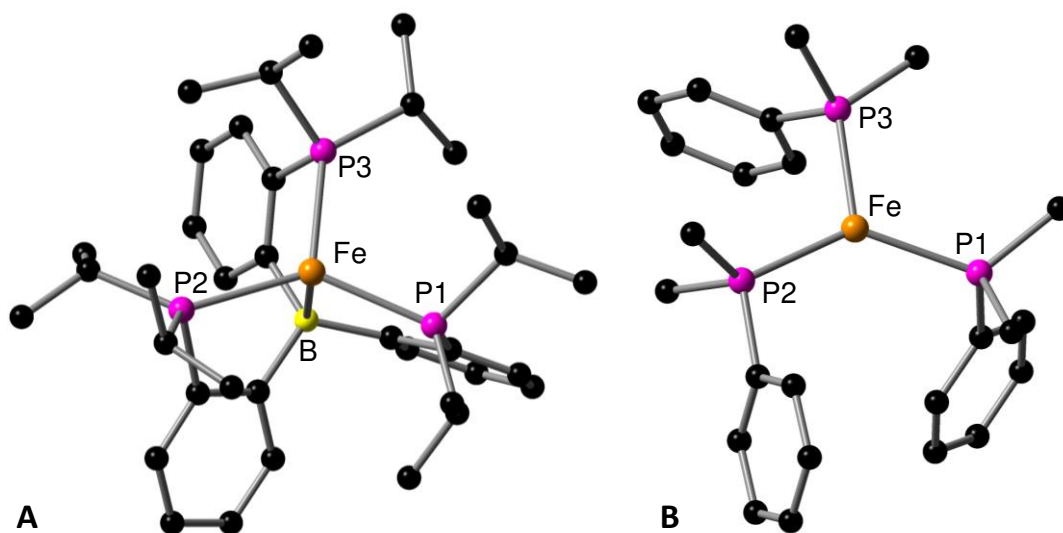
Figure 3.2. DFT optimized geometries at the B3LYP/6-31G(d) level of theory for (A) **3.2** and (B) [(Me$_2$PhP)$_3$Fe]$^+$. Selected bond distances [Å] and angles [°]: (A): Fe–P1 2.426, Fe–P2 2.481, Fe–P3 2.460, Fe–B 2.189, P1–Fe–P2 137.5, P1–Fe–P3 109.1, P2–Fe–P3 113.2; (B): Fe–P1 2.359, Fe–P2 2.328, Fe–P3 2.350, P1–Fe–P2 134.8, P1–Fe–P3 113.1, P2–Fe–P3 111.7.

This interpretation is consistent with a computational model study wherein the DFT (B3LYP/6-31G(d)) optimized geometry of the hypothetical complex $[(Me_2PhP)_3Fe]^+$ (Figure 3.2) replicates the T-shaped distortion by exhibiting a planar geometry with P-Fe-P angles of 134.8°, 113.1°, and 111.7°, very close to those measured for $[(TPB)Fe]^+$ (137.5°, 113.2°, 109.1°). These computational studies combined with the aforementioned data raise interesting questions about the nature of the Fe-B interaction.

Complex	Fe-X (Å)	Fe-B (Å)	Avg. Fe-P (Å)	ΣP-Fe-P	ΣC-B-C
3.1	2.083(10)	2.523(2)	2.40	339°	341°
3.2	-	2.217(2)	2.38	359°	347°
3.3	2.205(2)	2.392(2)	2.44	350°	339°
3.4	2.280(3)	2.433(3)	2.44	349°	341°
3.5	1.918(3)	2.449(4)	2.39	343°	339°
3.6	1.8916(7)	2.4438(9	2.39	348°	337°

Table 3.1. Selected metrics for complexes **3.1-3.6**.

When considering the bonding of the $(Fe-B)^7$ subunit of **3.2** in order to estimate the most appropriate oxidation state and valence assignment, two limiting scenarios present themselves: Fe(III)/B(I) and Fe(I)/B(III). The structural data and computations for **3.2** are suggestive of a weak Fe-B interaction and indicate that this species is better regarded as Fe(I)/B(III) rather than Fe(III)/B(I). Calculations indicate that a small amount of spin density resides on the B-atom of **3.2** (see Appendix 2) and suggest that some contribution from an Fe(II)/B(II) resonance form may also be relevant. The remainder of the complexes presented herein possess significantly longer, and therefore presumably weaker, Fe-B interactions (vide infra) and are hence also better classified as Fe(I) species. Additional spectroscopic studies (e.g., XAS and Mössbauer) may help to

better map the strength of the Fe-B bonding interaction and its relation to variable Fe-B

distances, and also as a function of the spin state of the overall complex. These studies

would help to determine the value and limitation of classically derived oxidation/valence

assignments for boratranes of these types.[10]

Regardless of the nature of the Fe-B interaction, the ability of **3.2** to bind neutral

L-type donors in its vacant apical site was investigated to probe the utility of this

complex as a synthon for installing nitrogenous ligands. One of the initial observations in

this context was that solutions of **3.2** are orange in Et_2O and pale yellow-green in THF,

potentially suggestive of solvent coordination in the apical site. Titration of THF into an

ethereal solution of **3.2** results in a distinct change in the UV-vis spectrum consistent with

weak THF binding (see Appendix 2). The evidence that THF can bind in the vacant

apical site of **3.2** suggests that binding of other L-type donors at this site should be

feasible.

3.2.2 [(TPB)Fe]$^+$ Adducts of N_2H_4 and NH_3
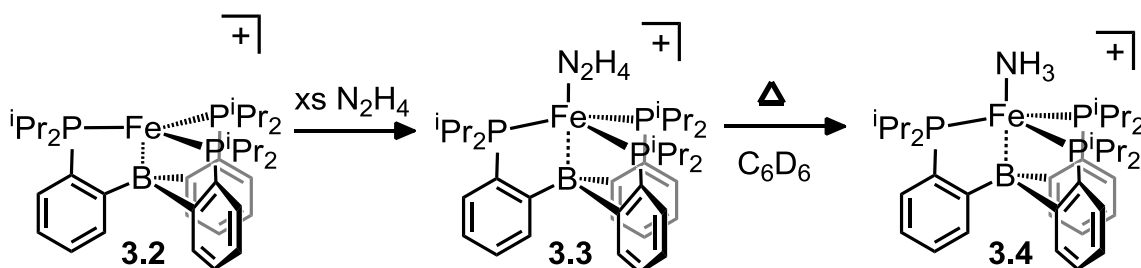
Scheme 3.2. Synthesis of complexes **3.3** and **3.4**. Counterions are not depicted, but are

$BAr^F_4{}^-$ in all cases.

Addition of an excess of N_2H_4 to an ethereal solution of **3.2** results in a slight lightening of the orange color of the solution to afford $[(TPB)Fe(N_2H_4)][BAr^F_4]$ (**3.3**) in 89% yield (Scheme 3.2). Complex **3.3** shows a paramagnetically shifted ^1H NMR spectrum indicative of an $S = 3/2$ Fe center. The proposed high-spin state of the Fe center is corroborated by a RT solution magnetic moment of $\mu_{eff} = 3.5$ μ_B. Complex **3.3** is stable to vacuum, but solutions decompose cleanly at RT over hours to form the $S = 3/2$ cationic ammonia complex $[(TPB)Fe(NH_3)][BAr^F_4]$, **3.4**, which was assigned by comparison of its ^1H NMR spectrum with an independently prepared sample formed by the addition of NH_3 to the cation **3.2**.

3.3 **3.4**
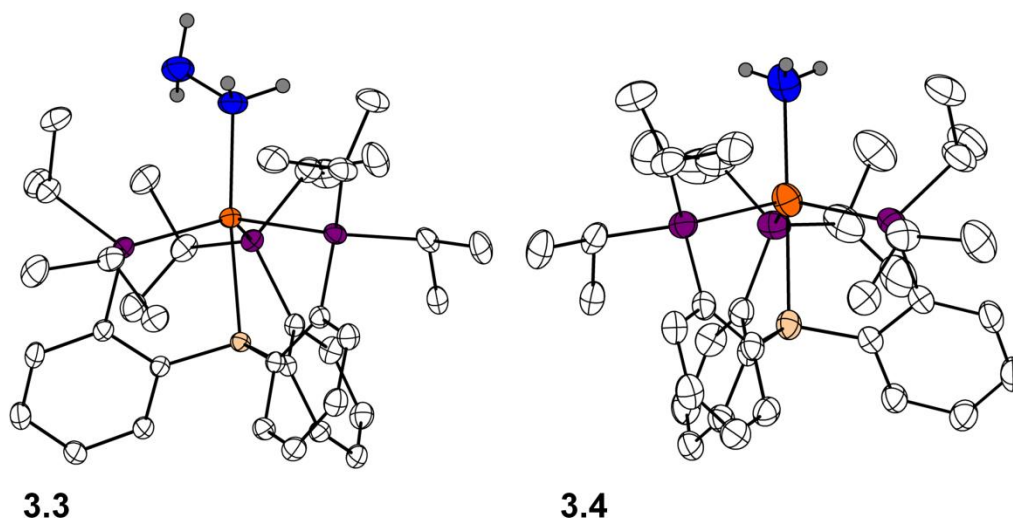
Figure 3.3. XRD structures of complexes **3.3** and **3.4** with C-H hydrogens and counterions omitted for clarity. Fe atoms are shown in orange, P in purple, N in blue, B in tan, H in gray, and C in white. Selected metrics can be found in Table 3.1.

The identities of the nitrogenous ligands in **3.3** and **3.4** were confirmed by XRD data collected on these complexes (Figure 3.3). Both complexes possess a distorted

trigonal bipyramidal geometry about Fe similar to **3.1** and the previously reported (TPB)FeBr.7[a] The Fe-N distances of 2.205(2) Å in **3.3** and 2.280(3) Å in **3.4** are unusually long (2.14 Å is the average quaternary N-Fe distance in the Cambridge Structural Database)[11] reflecting the unusual quartet spin state in these complexes. Despite these long distances, **3.4**, like **3.3**, is stable to vacuum. The unpaired spins in these complexes similarly result in long average Fe-P distances of 2.44 Å. The complexes **3.2**, **3.3**, and **3.4** are unusual by virtue of their $S = 3/2$ spin states and underscore the utility of local 3-fold symmetry with respect to stabilizing high spin states at iron, even in the presence of strong-field phosphine ligands. Finally, the Fe-B distances in **3.3** and **3.4** of 2.392(2) Å and 2.433(3) Å respectively likely indicate a minimal interaction between Fe and B and suggest that a formal oxidation state of Fe(I) is most appropriate in these complexes.

reaction: $A + B \longrightarrow 2B$ rate law: $[A]/([B]_0 + [A]_0 - [A]) = ([A]_0/[B]_0)e^{-kt([A]_0 + [B]_0)}$ Fit: $y = a/(1 + b*exp(-k*x))$

$a([A]_0) = 0.038$, $b([A_0]/[B_0]) = 10000$, $k (k[A]_0) = 0.058$, $R^2 = 0.965$
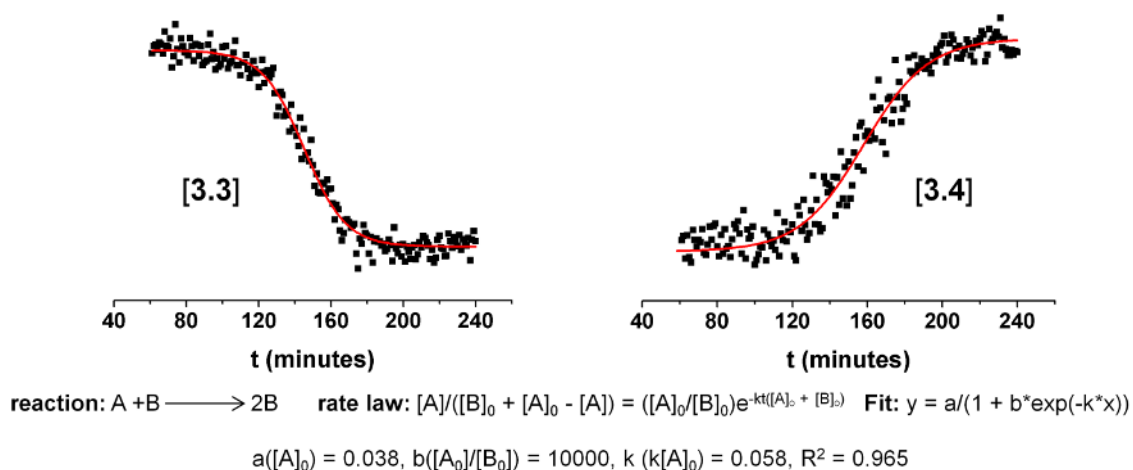
Figure 3.4. Reaction kinetics of the thermolysis of **3.3** to **3.4** at 60 °C in a 6:1 mixture of C_6D_6:THF-d_8.

The conversion of **3.3** to **3.4** deserves additional comment. As written in Scheme 3.2, the transformation is not balanced and so the reaction mixture was analyzed for the presence of additional degradation products. Two degradation pathways are likely accessible to the bound N_2H_4 molecule: degradation to 1 1/3 equivalents of NH_3 and 2/3 equivalents of N_2 or degradation to N_2 and two equivalents of H_2. The presence of NH_3 in **3.4** suggests that the former process dominates and analysis of the additional degradation products shows the formation of 0.12 equivalents NH_3 and only trace H_2.

In a further attempt to probe the mechanism of this process, the conversion of **3.3** to **3.4** was monitored by ^{1}H NMR spectroscopy at 60 °C, which showed a clean reaction with no discernible intermediates. The traces of the concentrations of **3.3** and **3.4** are shown in Figure 3.4. What is immediately obvious is the sigmoidal shape of the reactant and product curves suggestive of an auto-catalytic mechanism. The data can be fit to a crude auto-catalytic rate law with a reasonable agreement provided by the parameters shown in Figure 3.4.[12] The identity of the auto-catalyst is unclear, as doping **3.4** into solutions of **3.3** does not eliminate the observed induction period. Despite the lack of evidence of N_2H_4 or NH_3 dissociation from **3.3** or **3.4**, it is possible that the vacant species **3.2** is acting as the auto-catalyst. Further insight into the mechanism of this decomposition beyond the identity of the auto-catalyst will likely prove challenging due to the relatively complicated mechanism.

3.2.3 Conversion of FeNH₂ to FeN₂ with release of NH₃

The paucity of terminal FeNH$_2$ species prompted investigations into whether such

a species could be isolated on the (TPB) framework. The previously reported capability

of (TPB)Fe to support π-donor ligands suggested that an FeNH$_2$ complex could be

stabilized with this ligand. Addition of excess NaNH$_2$ to the cation **3.2** affords the

terminal amide, (TPB)FeNH$_2$ (**3.5**) in ca. 85% non-isolated yield by ^{1}H NMR integration

(Scheme 3.3). The XRD structure of **3.5** (Figure 3.5) shows an overall geometry similar

to that observed in **3.1**, **3.3**, and **3.4**. Of interest is the short Fe-N distance of 1.918(3) Å

by comparison to **3.4** (2.280(3) Å). The amide hydrogens were located in the difference

map and indicate a nearly planar geometry about N (with the sum of the angles around N

being 355°).
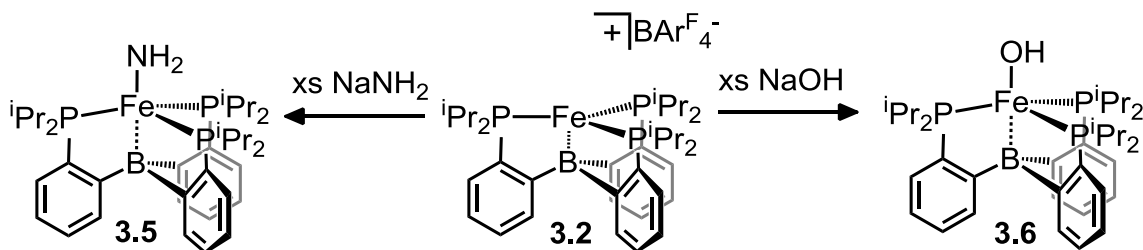
Scheme 3.3. Synthesis of complexes **3.5** and **3.6**.

While the XRD data set of **3.5** is of high quality, concern about the difficulty in

distinguishing an FeNH$_2$ group from a potentially disordered Fe-OH moiety remained.

The hydroxo complex, (TPB)Fe-OH (**3.6**) (Scheme 2), was therefore independently

synthesized and characterized similarly to **3.5** by the reaction of **3.2** with an excess of

NaOH. Complex **3.6** possesses a geometry similar to that observed in **3.5** with an Fe-B

distance of 2.4438(9) Å and an Fe-O distance of 1.8916(7) Å. Despite the structural

similarity between **3.5** and **3.6**, different spectral signatures in both their ^{1}H NMR and EPR (Figure 3.6) spectra allow for facile distinction between them.
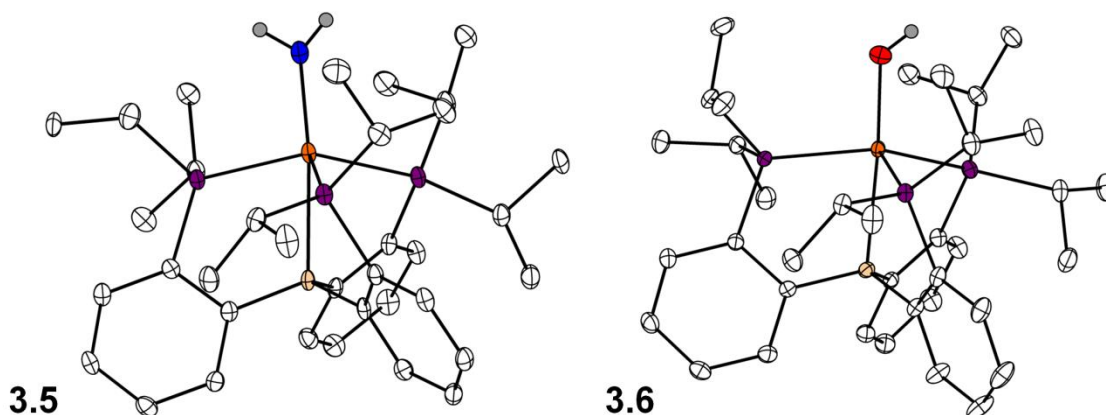
Figure 3.5. XRD structures of complexes **3.5** and **3.6** with C-H hydrogens omitted for clarity. Fe atoms are shown in orange, P in purple, N in blue, O in red, B in tan, H in gray, and C in white. Selected metrics can be found in Table 3.1.

Parent amide complexes of first row transition metals are rare.[13] Noteworthy precedent for related terminal M-NH$_2$ species includes three square planar nickel complexes[13c,e,f] and one octahedral and diamagnetic iron complex, (dmpe)$_2$Fe(H)NH$_2$.[6] In addition to their different coordination numbers, geometries, and spin-states, (dmpe)$_2$Fe(H)(NH$_2$) and **3.5** show a distinct difference at the FeNH$_2$ subunit. Six-coordinate (dmpe)$_2$Fe(H)(NH$_2$) is an 18-electron species without π-donation from the amide ligand, which is pyramidalized as a result. By contrast, five-coordinate **3.5** accommodates π-bonding and allows donation from the lone pair on the amide ligand. This donation is further borne out in its much shorter Fe-N distance (1.918(3) Å for **3.5**

versus 2.068 Å for $(dmpe)_2Fe(H)(NH_2))$, and also its comparative planarity (the sum of the angles around N is 355° for **3.5** versus 325° for $(dmpe)_2Fe(H)(NH_2))$.
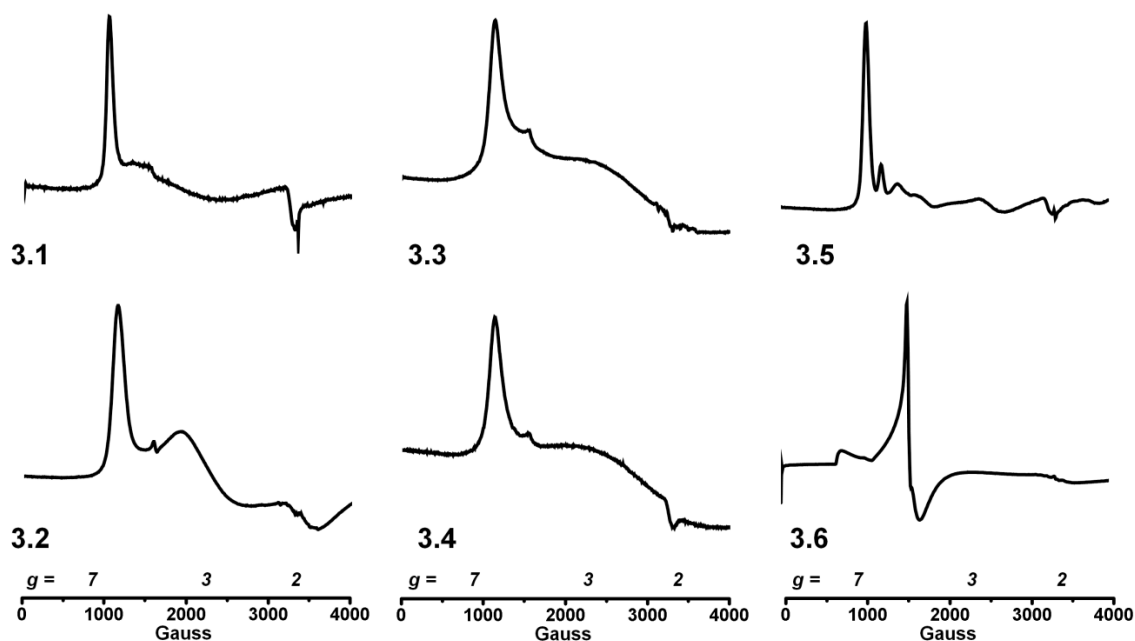
Figure 3.6. Low-temperature X-Band EPR spectra for complexes **3.1**-**3.6**. Conditions: **3.1**: Toluene, 8 K; **3.2**: 2:1 Toluene:Et_2O, 10 K **3.3**: 2-MeTHF, 10 K; **3.4**: 2-MeTHF, 10 K; **3.5**: 2-MeTHF, 10 K; **3.6**: Toluene, 10 K.

In order to further query the electronic structures of the complexes presented here, low-temperature EPR data and magnetic data have been acquired. X-Band EPR data at ~ 10 K have been obtained on complexes **3.1**-**3.6** and are shown in Figure 3.6. All complexes show intense features shifted to large g-values: ~ 5 for **3.6**, ~ 6 for **3.2**-**3.4**, and close to 7 for **3.1** and **3.5**. Such features are consistent with quartet Fe species,[14] and this assignment is verified by the solution magnetic moments obtained for these complexes. Variable temperature solid-state SQUID magnetic data for complexes **3.2**-**3.5** (see

Appendix 2) also establish quartet spin state assignments and display no evidence for spin-crossover phenomena. These data show a drop in magnetic moment in the range 50-70 K for all compounds studied. We propose that this effect is due to a large zero-field splitting in these species, which is consistent with Fe centers in related geometries.[15] Simulations with zero-field splitting of 10-20 cm^{-1} provide reasonable fits to the data (see Appendix 2).
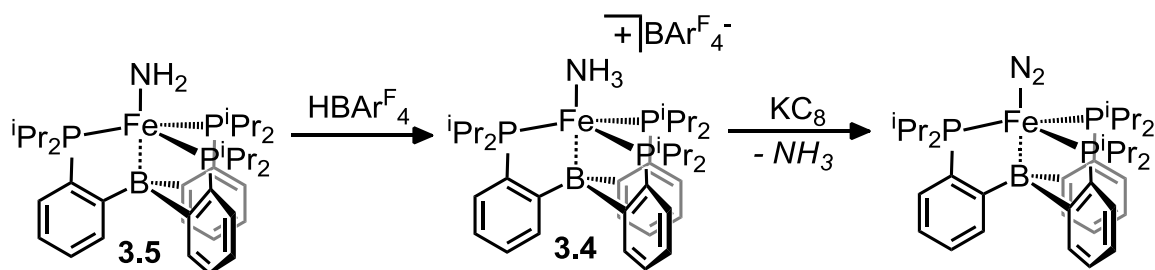
Scheme 3.4. Reductive protonation sequence to release NH_3 and take up N_2.

With the terminal amide **3.5** in hand, its suitability as a precursor to the previously reported N_2 complex (TPB)Fe(N_2) via release of NH_3 was explored. Both reduction/protonation and protonation/reduction sequences were investigated as a means of effecting overall H-atom transfer to the $FeNH_2$ unit. Attempts to carry out the one-electron reduction of **3.5** did not provide any tractable reactivity. For example, electrochemical studies of **3.5** in THF failed to show any reversible reduction waves, but the addition of harsh reductants (e.g., tBuLi) to **3.5** did show small amounts of (TPB)Fe(N_2) in the product profile, potentially via loss of NH_2^-. A more successful conversion sequence utilized protonation followed by chemical reduction. Thus, the addition of $HBAr^F_4 \cdot 2$ Et_2O to **3.5** at low temperature (-35 °C) rapidly generates the cationic ammonia adduct **3.4** (Scheme 3.4). The conversion is quantitative as determined

by ^{1}H NMR spectroscopy, and **3.4** can be isolated in ca. 90% yield from the solution. Subsequent exposure of **3.4** to one equiv of KC_8 under an atmosphere of N_2 releases NH_3 and generates the $(TPB)FeN_2$ complex in similarly high yield.

While neither of these reactions is unexpected, the ability to link these complexes together in the reactions shown illustrates for the first time that Fe can mediate these steps on a single scaffold. The conversion of an $FeNH_2$ species to an $FeNH_3$ species and then terminally to an FeN_2 species are steps common to both limiting "distal" and "alternating" mechanisms. Additionally, these processes represent the final steps of these mechanisms to regenerate an FeN_2 species and re-enter a catalytic cycle. While the uptake of N_2 via redox induced expulsion of NH_3 had been previously reported4[b] and the basicity of $FeNH_2$ species has been documented,6 the fact that the (TPB) manifold can stabilize the requisite functionalities and transformations is noteworthy. Specifically, in order to develop a catalyst for N_2 reduction, Fe based systems capable of stabilizing and interconverting multiple nitrogenous species are required.

3.3 Conclusion

Protonation of the terminal alkyl complex **3.1** gives rise to the four-coordinate cationic complex **3.2**, which possesses an unusually short Fe-B bond. Despite this bond distance, calculations suggest that the Fe-B bonding interaction is relatively weak. Complex **3.2** serves as a synthon for the installation of N_2H_4, NH_2^-, and OH^- groups to make complexes **3.3**, **3.5**, and **3.6** respectively. Furthermore, thermolysis of **3.3** results in the disproportionation of N_2H_4 to yield the cationic NH_3 adduct **3.4** via an autocatalytic degradation. All of these complexes are unusual $S = 3/2$ complexes and X-Band EPR and

magnetic measurements support this spin state assignment. Finally, protonation of **3.5** results in formation of **3.4** which can then be reduced to yield (TPB)Fe(N$_2$), demonstrating this reductive sequence for the first time on a single Fe scaffold. Collectively, these results suggest that the (TPB)Fe scaffold can support a number of potential intermediates or conversions that might be found in a N$_2$ fixation pathway.

3.4 Experimental Section

3.4.1 General Considerations

Unless otherwise noted, all compounds were prepared by literature procedures or purchased from commercial sources. The complex (TPB)FeBr[7a] and HBAr$^F_4$·2 Et$_2$O[22] were prepared according to reported literature procedures. All manipulations were carried out under a dinitrogen atmosphere by utilizing standard glovebox or schlenk techniques. Solvents were dried and de-oxygenated by an argon sparge followed by passage through an activated alumina column purchased from S.G. Waters Company. All non-halogenated solvents were tested with a standard sodium-benzophenone ketyl solution to ensure the absence of oxygen and water.

NMR measurements were obtained on Varian 300, 400, or 500 MHz spectrometers. Deuterated solvents for these measurements were obtained from Cambridge Isotope Laboratories and were dried and degassed prior to use. All ^{1}H spectra were referenced to residual solvent peaks and all ^{31}P spectra were referenced to an external H$_3$PO$_4$ standard.

3.4.2 EPR Spectroscopy

EPR X-band spectra were obtained on a Bruker EMX spectrometer with the aid of Bruker Win-EPR software suite version 3.0. The spectrometer was equipped with a rectangular cavity which operated in the TE_{102} mode. Temperature control was achieved with the use of an Oxford continuous-flow helium cryostat (temperature range 3.6 – 300 K). All spectra were recorded at 9.37 GHz with a microwave power of 20 mW, a modulation amplitude of 4 G, and a modulation frequency of 100 kHz.

3.4.3 X-Ray Crystallography

Data were obtained at low temperatures on a Siemens or Bruker Platform three-circle diffractometer coupled to a Bruker-AXS Smart Apex CCD detector with graphite-monochromated Mo Kα radiation ($\lambda = 0.71073$), performing φ-and ω-scans. Data for complex **5.4** were collected with synchrotron radiation at the Stanford Synchrotron Radiation Laboratory (SSRL) beam line 12-2 at 17 keV using a single phi axis and recorded on a Dectris Pilatus 6M. The images were processed using XDS[16], and further workup of the data was analogous to the other datasets. All structures were solved by standard direct or Patterson methods and refined against F^2 using the SHELX program package.[17,18,19] All atoms, with the exception of hydrogens, have been anisotropically refined. The hydrogen atoms bonded to atoms of interest, namely N or O, have been located in the difference map and refined semi-freely. All other hydrogen atoms were included via a standard riding model.

In the structure of complex **5.1** a minor component of TPBFeCl was found in the difference map and modeled as disorder. Additional disorder of the BAr^F_4 counterion

was found in complex 4. This disorder was modeled as a rotational disorder of the CF_3 groups on one of the phenyl rings, but some of the resulting F ellipsoids still display significantly prolate shapes. We feel that the shape of these ellipsoids accurately describes the actual electron density due to the rotational disorder.

3.4.4 Magnetic Measurements

Data were obtained using a Quantum Designs SQUID magnetometer running MPMSR2 software (Magnetic Property Measurement System Revision 2) at a field strength of 50000 G. Complexes were massed and then suspended in eicosane wax. Samples were then inserted into the magnetometer in plastic straws sealed under nitrogen with gelatin capsules. Loaded samples were centered within the magnetometer using the DC centering scan at 35 K. Data were acquired at 20-30 K (one data point every 2 K), and 30-300 K (one data point every 10 K). The magnetic susceptibility was adjusted for diamagnetic contributions using the constitutive corrections of Pascal's constants, as well as a diamagnetic correction for the eicosane and capsule. Data workup, including simulations, was performed in the JulX software package.[20] Complex **5.5** displayed a lower than expected magnetic moment. NMR analysis of the sample indicated the presence of ~15% 12-crown-4, present as a result of the protocol for generation of the complex, where it is used to aid for removal of $NaBAr^F_4$. Accounting for this impurity leads to a magnetic moment consistent with the other samples.

3.4.5 Computational Methods

Geometry optimizations were performed using the Gaussian03 package.[21] The B3LYP exchange-correlation functional was employed with a 6-31G(d) basis set. The GDIIS algorithm was used. A full frequency calculation was performed on each structure to establish true minima. A model for the initial geometry of complex **5.2** used the crystallographically determined coordinates as a starting point for subsequent minimization. Atoms were then stripped away from this structure to reveal a $Fe(PMe_2Ph)_3^+$ as the starting point to determine the theoretical structure of $Fe(PMe_2Ph)_3^+$ by another minimization. Structural models and orbital/spin density pictures were generated from Gaussview 03.

3.4.6 Synthesis

Synthesis of (TPB)FeMe , 3.1. (TPB)FeBr (0.400 g, 0.55 mmol) was dissolved in Et_2O (15 mL) and cooled to -35° C. To this stirred solution was added a 1.6 M solution of MeLi in Et_2O (0.620 mL, 0.99 mmol). After addition the solution was allowed to warm to RT and was stirred for an additional hour, over which time the solution changed in color from a dark brown to a deep orange red. After this time, volatiles were removed and the remaining solids were extracted 3x with benzene (3 mL). Lyophilization of benzene resulted in a dark orange powder which was washed with cold pentane (5 mL) to yield (TPB)FeMe (.352 g, 97%). X-ray quality crystals were grown from slow evaporation of a concentrated pentane solution of **3.1**. ^{1}H NMR (C_6D_6, δ): 74.48 (br s), 33.25 (s), 22.52 (s), 9.31 (br s), 5.73 (s), 2.65 (s), -2.33 (br s), -2.80 (s), -7.49 (br s), -16.33 (s). UV-Vis (THF) λ_{max}, nm (ε, $M^{-1}cm^{-1}$): 840 (120). Anal. Calc. for

$C_{37}H_{57}BFeP_3$: C 67.19; H 8.69. Found: C 67.26; H 8.59. Solution magnetic moment (C_6D_6): 3.9 μ_B.

Synthesis of [(TPB)Fe][BAr$^F_4$], 3.2. A dark orange solution of **1** (0.037 g, 0.06 mmol) in 5 mL of Et$_2$O was cooled to -35° C. Once cooled, the solution was stirred while a similarly cooled solution of HBAr$^F_4$·2 Et$_2$O[22] in Et$_2$O (5 mL) was added dropwise over 5 minutes. After the addition, the solution was stirred at RT for an additional hour before being concentrated down to 1 mL. This solution was layered with pentane (1 mL) and cooled to -35° C for 2 days, upon which time dark orange crystals of [(TPB)Fe][BAr$^F_4$] had formed (0.082 g, 97%). ^{1}H NMR (C_6D_6/THF-d_8, δ): 32.15 (br s), 25.78 (s), 23.99 (br s), 8.93 (br s), 8.27 (s, BAr$^F_4$), 4.55 (br s), 1.84 (br s), -1.24 (br s), -28.05 (s). UV-Vis (Et$_2$O) λ_{max}, nm (ε, M^{-1}cm^{-1}): 475 (1700), 765 (800). Anal. Calc. for $C_{68}H_{66}B_2F_{24}FeP_3$: C 54.10; H 4.41. Found: C 53.93; H 4.53.

Synthesis of [(TPB)Fe(N$_2$H$_4$)][BAr$^F_4$], 3.3. 3.2 (0.356 g, 0.24 mmol) was dissolved in Et$_2$O (10 mL) and stirred. To this was added N$_2$H$_4$ (0.076 mL, 2.36 mmol) in one portion. Upon addition, the solution lightened slightly in color to a brown-orange. The solution was allowed to stir for 15 minutes before the solution was concentrated to 5 mL and layered with pentane (5 mL). After 2 days at -35° C, dark orange crystals of [(TPB)Fe(N$_2$H$_4$)][BAr$^F_4$] had formed (0.324 g, 89%). ^{1}H NMR (C_6D_6/THF-d_8, δ): 53.72 (br s), 28.26 (s), 25.32 (s), 20.18 (br s), 8.28 (s, BAr$^F_4$) 7.67 (s, BAr$^F_4$), 8.14 (br s), 7.96 (br s), 3.00 (br s), 2.67 (br s), 0.30 (br s), -26.06 (s). UV-Vis (THF) λ_{max}, nm (ε, M^{-1} cm^{-1}): 800 (140). Anal. Calc. for $C_{68}H_{70}B_2F_{24}FeN_2P_3$: C 52.98; H 4.58; N 1.82. Found: C 53.03; H 4.63; N 1.70. Solution magnetic moment (THF-d_8): 3.46 μ_B.

Synthesis of [(TPB)Fe(NH₃)][BAr^F₄], 3.4. A solution of **3.3** (0.308 g, 0.20 mmol) in

1:6 THF:Benzene (10 mL) was rapidly stirred at RT for 12 hours. After this time, the

volatiles were removed *in vacuo* and the residue was taken up in Et_2O, filtered, and

layered with pentane before being cooled to -35°. After 2 days, dark orange-red crystals

of [(TPB)Fe(NH₃)][BAr^F₄] had formed (0.264 g, 87%). ^1H NMR (C_6D_6/THF-d^8, δ):

68.22 (br s), 28.55 (s), 24.28 (s), 17.81 (br s), 8.34 (s, BAr^F₄), 7.68 (s, BAr^F₄), 5.74 (br s),

3.53 (s), 2.15 (br s), 1.22 (br s), -25.48 (s). UV-Vis (THF) λ_{max}, nm (ε, $M^{-1}cm^{-1}$): 871

(50). IR (KBr, cm-1): 3381 (ν[NH]) Anal. Calc. for $C_{68}H_{69}B_2F_{24}FeNP_3$: C 54.24; H

4.55; N 0.92. Found: C 53.47; H 4.72; N 0.94. Solution magnetic moment (THF- d_8):

3.63 μ_B.

Synthesis of (TPB)FeNH₂, 3.5. A solution of **3.2** (0.300 g, 0.20 mmol) in Et_2O (5 mL)

was stirred over $NaNH_2$ (0.077 g, 1.99 mmol) which had been finely ground with a

mortar and pestle. The resulting mixture was allowed to stir for 1.5 hours at RT and, over

this time, the liquid phase darkened from orange to a dark brown. Volatiles were

removed and the remaining residue was extracted with pentane (40 mL) to yield a pale

orange solution. To this solution was added 12-crown-4 (0.070 g, 0.40 mmol) to aid in

the removal of NaBAr^F₄, and solids began to precipitate. The solution was allowed to

stand for 1 hour before filtration. Removal of solvent for 3 hours at 70° C resulted in

(TPB)FeNH₂ as a dark orange powder (0.060 g, 0.09 mmol, 46%). Crystals suitable for

X-ray diffraction were grown from slow evaporation of a concentrated ethereal solution.

Due to the presence of a small amount of 12-crown-4 that had similar solubility

properties to the product, satisfactory combustion analysis was not obtained for **3.5**. ^1H

NMR (C_6D_6, δ): 91.12 (br s), 38.21 (s), 25.42 (s), 4.12 (br s), 1.55 (br s), 0.21 (br s), -3.04

(br s), -5.93 (br s), -20.19(s). UV-Vis (THF) λ_{max}, nm (ε, $M^{-1}cm^{-1}$): 700 (90), 930 (80).
Solution magnetic moment (C_6D_6): 4.05 μ_B. We also wish to note that trace amounts
(<3%) of the neutral complex (TPB)Fe(N_2) are typically observed as impurities detected
by NMR spectroscopy in preparations of **3.5**. (TPB)Fe(N_2) and **3.5** also have similar
solubility properties.

Synthesis of (TPB)FeOH, 3.6. Complex **3.2** (0.80 g, 0.05 mmol) was dissolved in Et_2O
(5 mL) and stirred over NaOH (0.063 g, 1.6 mmol) at RT for 2 hours, during which the
color of the solution darkened to a deep brown. Volatiles were removed from the
solution and the resulting solids were extracted with pentane to yield the title compound
(0.027, 77%) as a brown powder. Crystals suitable for X-Ray diffraction were grown by
a slow evaporation of a concentrated Et_2O solution. ^1H NMR (C_6D_6, δ): 89.55 (br s),
39.07 (s), 24.70 (s), 6.71 (s), 4.08 (s), 1.55 (br s), -0.52 (br s), -6.00 (br s), -21.02 (s).
UV-Vis (THF) λ_{max}, nm (ε, $M^{-1}cm^{-1}$): 870 (230), 700 (218). Anal. Calc. for
$C_{36}H_{55}BFeOP_3$: C 65.18; H 8.36; N 0. Found: C 65.15; H 8.28; N none found. Solution
magnetic moment (C_6D_6): 4.12 μ_B.

Protonation of 3.5. A 20 mL scintillation vial was charged with **3.5** (0.005 g, 0.007
mmol) and HBAr$^F_4$·2 Et_2O (0.008 g, 0.007 mmol) and cooled to -35° C. Similarly cooled
Et_2O (2 mL) was added to the mixture and the color of the solution lightened rapidly.
The solution was allowed to warm to RT over 30 minutes before volatiles were removed
to yield **3.4** (0.010 g, 0.006 mmol, 91%). The identity of the product was determined via
^1H NMR chemical shifts which were identical to those observed for **3.4**.

Reduction of 3.4. A 20 mL scintillation vial was charged with **3.4** (0.025 g, 0.016
mmol) and KC_8 (0.0024 g, 0.018 mmol). Et_2O (2 mL) was added and the resulting dark

suspension was allowed to stir for 2 hours at RT. After this time, the solution was filtered and volatiles were removed to yield $(TPB)Fe(N_2)$ as a brown solid. The identity of the product was determined via ^1H NMR chemical shifts which were identical to the previously reported values for $(TPB)Fe(N_2)$.

Monitored Conversion of 3.3 to 3.4. Complex **3.3** (0.020 g, 0.013 mmol) was dissolved in a 6:1 mixture of C_6D_6:THF- d_8 (0.3 mL). The resulting solution was transferred to a NMR tube equipped with a capillary containing a solution of (TPB)FeBr in a 6:1 mixture of C_6D_6:THF- d_8 as an internal standard. This NMR tube was sealed with a J-Young valve and placed into a 500 MHz spectrometer which had been preheated to 60° C. The reaction was monitored via single scans every minute for 4 hours, during which time complete and clean conversion from **3.3** to **3.4** was observed. After the reaction was complete, an aliquot of the headspace was analyzed by GC for the presence of H_2. After this, volatiles were vacuum transferred onto a solution of HCl in THF. Volatiles were then removed and the resulting solids were diluted with water to appropriate volumes to test for the presence of NH_3 via the indophenol test,[23] or N_2H_4 with *p*-dimethylaminobenzaldehyde.[24] The relative amounts of products are compiled in Appendix 2.

References Cited

1 (a) Vela, J.; Stoian, S.; Flaschenriem, C. J.; Münck, E.; Holland, P. L. *J. Am. Chem. Soc.* **2004**, *126*, 4522-4523; (b) Field, L. D.; Li, H. L.; Dalgarno, S. J.; Turner, P. *Chem. Commun.* **2008**, 1680-1682; (c) Crossland, J. L.; Tyler, D. R. *Coord. Chem. Rev.* **2010**, *254*, 1883-1894. (d) Hazari, N. *Chem. Soc. Rev.* **2010**, *39*, 4044-4056; (e) Crossland, J. L.; Balesdent, C. G.; Tyler, D. R. *Inorg. Chem.* **2011**, *51*, 439-445; (f) MacLeod, K. C.; Holland, P. L. *Nat. Chem.* **2013**, *5*, 559-565.

2 (a) Lukoyanov, D.; Dikanov, S. A.; Yang, Z.-Y.; Barney, B. M.; Samoilova, R. I.; Narasimhulu, K. V.; Dean, D. R.; Seefeldt, L. C.; Hoffman, B. M. *J. Am. Chem. Soc.* **2011**, *133*, 11655-11664; (b) Seefeldt, L. C.; Hoffman, B. M.; Dean, D. R. *Annu. Rev. Biochem.* **2009**, *78*, 701-722.

3 (a) Betley, T. A.; Peters, J. C. *J. Am. Chem. Soc.* **2003**, *125*, 10782-10783; (b) Saouma, C. T.; Müller, P.; Peters, J. C. *J. Am. Chem. Soc.* **2009**, *131*, 10358-10359; (c) Saouma, C. T.; Kinney, R. A.; Hoffman, B. M.; Peters, J. C. *Angew. Chem. Int. Ed.* **2011**, *50*, 3446-3449; (d) Saouma, C. T.; Peters, J. C. *Coord. Chem. Rev.* **2011**, *255*, 920-937.

4 (a) Whited, M. T.; Mankad, N. P.; Lee, Y.; Oblad, P. F.; Peters, J. C. *Inorg. Chem.* **2009**, *48*, 2507-2517; (b) Lee, Y.; Mankad, N. P.; Peters, J. C. *Nat Chem* **2010**, *2*, 558-565.

5 (a) Betley, T. A.; Peters, J. C. *J. Am. Chem. Soc.* **2004**, *126*, 6252-6254; (b) Scepaniak, J. J.; Fulton, M. D.; Bontchev, R. P.; Duesler, E. N.; Kirk, M. L.; Smith, J. M. *J. Am. Chem. Soc.* **2008**, *130*, 10515-10517; (c) Scepaniak, J. J.; Young, J. A.; Bontchev, R. P.; Smith, J. M. *Angew. Chem., Int. Ed.* **2009**, *48*, 3158-3160. (d) Scepaniak, J. J.;

Vogel, C. S.; Khusniyarov, M. M.; Heinemann, F. W.; Meyer, K.; Smith, J. M. *Science* **2011**, *331*, 1049-1052;

6 Fox, D. J.; Bergman, R. G. *J. Am. Chem. Soc.* **2003**, *125*, 8984-8985.

7 (a) Moret, M.-E.; Peters, J. C. *Angew. Chem. Int. Ed.* **2011**, *50*, 2063-2067; (b) Moret, M.-E.; Peters, J. C. *J. Am. Chem. Soc.* **2011**, *133*, 18118-18121.

8 Sircoglou, M.; Bontemps, S.; Bouhadir, G.; Saffon, N.; Miqueu, K.; Gu, W.; Mercy, M.; Chen, C.-H.; Foxman, B. M.; Maron, L.; Ozerov, O.V.; Bourissou, D. *J. Am. Chem. Soc.* **2008,** *130,* 16729-16738.

9 A stable T-shaped, three-coordinate Fe(I) is known: Ingleson, M. J.; Fullmer, B. C.; Buschhorn, D. T.; Fan, H.; Pink, M.; Huffman, J. C.; Caulton, K. G. *Inorg. Chem.* **2008**, *47*, 407-409.

10 (a) Amgoune, A.; Bourissou, D. *Chem. Comm.* **2011**, *47*, 859-871; (b) Hill, A. F.; Owen, G. R.; White, A. J. P.; Williams, D. J. *Angew. Chem., Int. Ed.* **1999**, *38*, 2759-2761; (c) Pang, K.; Quan, S. M.; Parkin, G. *Chem. Comm.* **2006**, 5015-5017.

11 Cambridge Structural Database, 2011 update: F. H. Allen, Acta Crystallogr. B **2002**, *B58*, 380-388.

12 Espenson, J. *Chemical Kinetics and Reaction Mechanisms*; McGraw-Hill Education, 2002.

13(a) Redshaw, C.; Wilkinson, G.; Hussain-Bates, B.; Hursthouse, M. B. *J. Chem. Soc. Dalton*, **1992**, 1803-1811; (b) Brady, E.; Telford, J. R.; Mitchell, G.; Lukens, W. *Acta Cryst. C* **1995**, *51*, 558-560; (c) Cámpora, J.; Palma, P.; del Río, D.; Conejo, M. M.; Álvarez, E. *Organometallics* **2004**, *23*, 5653-5655; (d) Sofield, C. D.; Walter, M. D.; Andersen, R. A. *Acta Cryst. C* **2004**, *60*, 465-466; (e) Huffman, J. C.; Meyer, K.;

Mindiola, D. J. *Inorg. Chem.* **2008**, *47*, 10479-10490; (f) Gutsulyak, D. V.; Piers, W. E.; Borau-Garcia, J.; Parvez, M. *J. Am. Chem. Soc.* **2013**.

14 Stoian, S. A.; Yu, Y.; Smith, J. M.; Holland, P. L.; Bominaar, E. L.; Munck, E. *Inorg. Chem.* **2005**, *44*, 4915-4922.

15 Harman, W. H.; Harris, T. D.; Freedman, D. E.; Fong, H.; Chang, A.; Rinehart, J. D.; Ozarowski, A.; Sougrati, M. T.; Grandjean, F.; Long, G. J.; Long, J. R.; Chang, C. J. *J. Am. Chem. Soc.* **2010**, *132*, 18115-18126.

16 W. Kabsch, *J. Appl. Cryst.* **1993**, *26*, 795.

17 Sheldrick, G. M. *Acta Cryst.* **1990**, *A46*, 467.

18 Sheldrick, G. M. *Acta Cryst.* **2004**, *A64*, 112.

19 Müller, P. *Crystallography Reviews* **2009**, *15*, 57.

20 http://ewww.mpi-muelheim.mpg.de/bac/logins/bill/julX_en.php

21 Gaussian 03, Revision E.01, Frisch, M. J.; Trucks, G. W.; Schlegel, H. B.; Scuseria, G. E.; Robb, M. A.; Cheeseman, J. R.; Montgomery, Jr., J. A.; Vreven, T.; Kudin, K. N.; Burant, J. C.; Millam, J. M.; Iyengar, S. S.; Tomasi, J.; Barone, V.; Mennucci, B.; Cossi, M.; Scalmani, G.; Rega, N.; Petersson, G. A.; Nakatsuji, H.; Hada, M.; Ehara, M.; Toyota, K.; Fukuda, R.; Hasegawa, J.; Ishida, M.; Nakajima, T.; Honda, Y.; Kitao, O.; Nakai, H.; Klene, M.; Li, X.; Knox, J. E.; Hratchian, H. P.; Cross, J. B.; Bakken, V.; Adamo, C.; Jaramillo, J.; Gomperts, R.; Stratmann, R. E.; Yazyev, O.; Austin, A. J.; Cammi, R.; Pomelli, C.; Ochterski, J. W.; Ayala, P. Y.; Morokuma, K.; Voth, G. A.; Salvador, P.; Dannenberg, J. J.; Zakrzewski, V. G.; Dapprich, S.; Daniels, A. D.; Strain, M. C.; Farkas, O.; Malick, D. K.; Rabuck, A. D.; Raghavachari, K.; Foresman, J. B.; Ortiz, J. V.; Cui, Q.; Baboul, A. G.; Clifford, S.; Cioslowski, J.;

Stefanov, B. B.; Liu, G.; Liashenko, A.; Piskorz, P.; Komaromi, I.; Martin, R. L.; Fox, D. J.; Keith, T.; Al-Laham, M. A.; Peng, C. Y.; Nanayakkara, A.; Challacombe, M.; Gill, P. M. W.; Johnson, B.; Chen, W.; Wong, M. W.; Gonzalez, C.; and Pople, J. A.; Gaussian, Inc., Wallingford CT, 2004.

22 Brookhart, M.; Grant, B.; Volpe, A. F. *Organometallics* **1992**, *11*, 3920-3922.

23 Weatherburn, M.W. *Anal. Chem.* **1967**, *39*, 971-974.

24 Watt, G. W.; Chrisp, J. D. *Anal. Chem.* **1952**, *24*, 2006-2008.

Chapter 4: Catalytic Conversion of N₂ to NH₃ by an Fe Model Complex

4.1 Introduction

Although ill-defined and heterogeneous mixtures of transition metals competent for the catalytic reduction of N_2 to NH_3 have been known for some time,[1] molecular systems where potential catalytic intermediates can be studied have only recently been developed. Early work on Mo complexes supported by phosphine co-ligands could bind N_2 and facilitate its protonation to release NH_3 in near quantitative yields.[2] More recently, advancements have led to two examples of molecular N_2 reduction catalysts, both featuring Mo complexes synthesized by the groups of Schrock and Nishibayashi.[3] Although Nishibayashi's system is more recent and little about its mechanism is currently known,[4] there has been extensive work on the Schrock system and numerous potential intermediates have been isolated that strongly imply a "distal" or Chatt-type mechanism for N_2 reduction.[5]

Fe mediated NH_3 formation from N_2 has progressed much more slowly than in the Mo systems. While significant amounts of NH_3 can be generated from the protonation of Fe nitride species,[6] FeN_2 complexes typically provide only small amounts (~10 mol %) of NH_3 derived from N_2.[7] Recently, Holland and co-workers have reported an Fe complex than can split N_2 into two nitride units which can then be exposed to acid or hydrogen to yield nearly stoichiometric NH_3.[8] Additionally, Nishibayashi and co-workers have shown the catalytic formation of $N(TMS)_3$ from N_2, Na, and TMSCl in the presence of simple Fe catalysts.[9] Despite these advances, the development of a molecular system for converting N_2 into NH_3 with protons and electrons has remained a substantial challenge. In the context of nitrogen fixation by nitrogenase enzymes,[10] the lack of such a functional

system has weighed against Fe being the binding site in FeMoco, despite spectroscopic evidence to the contrary.[11]

While previous efforts with the (SiP$_3$) ligand scaffold yielded only moderate amounts of N$_2$H$_4$,[12] the species synthesized in Chapter 3 and the silylation chemistry that had been previously reported motivated a closer examination of the (TPB)Fe scaffold in the context of NH$_3$ formation.[13,14] This chapter therefore discusses initial protonation studies of [(TPB)Fe(N$_2$)][Na(12-crown-4)$_2$] which yielded the previously reported complex **3.4**. This result led to the optimization of conditions that allowed for the catalytic reduction of N$_2$ to NH$_3$ with [(TPB)Fe(N$_2$)][Na(12-crown-4)$_2$] as the pre-catalyst. Control experiments suggest that the catalysis, while occurring in a heterogeneous mixture, is mediated by a molecular catalyst. Furthermore, the speciation of the Fe containing complex after catalysis is studied, suggesting possible degradation pathways.

4.2 Results and Discussion

4.2.1 Initial Protonation Studies
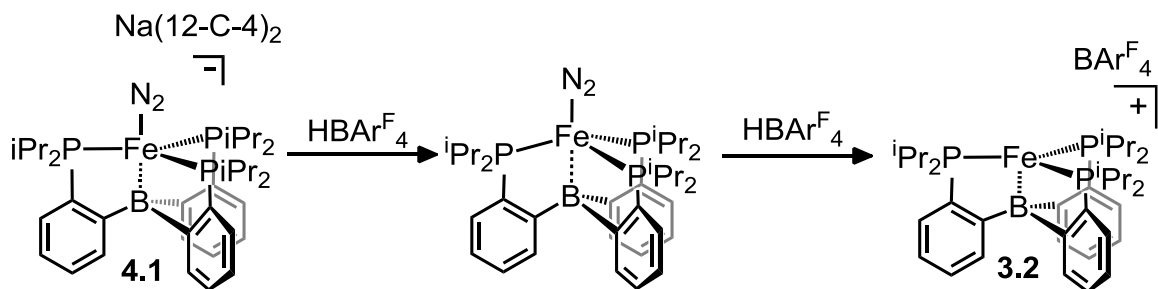
Scheme 4.1. Oxidation induced by acid addition on N$_2$ adducts of (TPB)Fe.

In order to investigate catalytic NH_3 formation with protons and electrons, several significant challenges had to be addressed. Most notable of these was the propensity of reduced Fe phosphine systems to generate H_2 more favorably than N-H bonds when exposed to acids. This phenomenon had been observed with the (TPB) ligand scaffold and can be summarized in Scheme 1, where the addition of one equivalent of acid to the previously reported anionic $[(TPB)Fe(N_2)][Na(12\text{-crown-}4)_2]$ (**4.1**) results in oxidation to $(TPB)Fe(N_2)$. Similarly, exposure of $(TPB)Fe(N_2)$ to acid also results in net oxidation and the generation of $[(TPB)Fe][BAr^F_4]$ (**3.2**). In both reactions loss of H_2 is likely, but the exact mechanism of oxidation is unclear. Any mechanistic insight into this process would be useful as a means to circumvent the oxidative pathway and lead to productive N_2 functionalization.
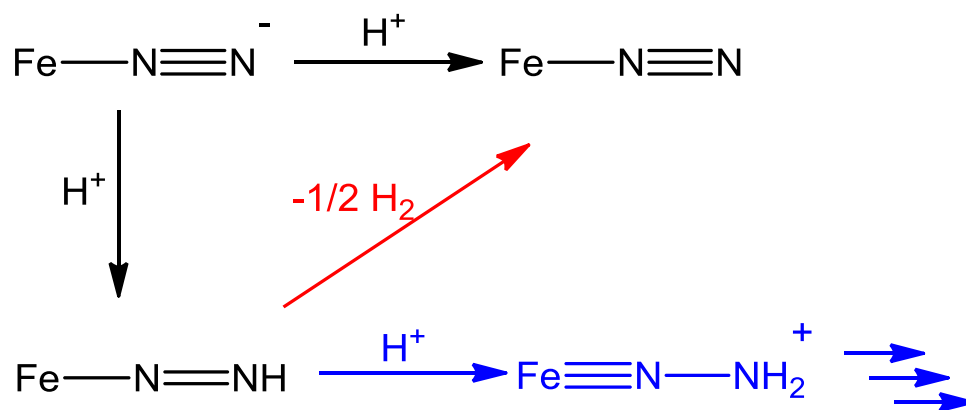
Scheme 4.2. Possible routes of protonation for an anionic FeN_2 species. The reaction shown in red indicates undesired elimination of H_2, while the reactions shown in blue indicate putative desirable protonations leading to further functionalization of N_2.

Although the products of the reactions shown in Scheme 4.1 are net oxidation, an outer-sphere oxidation of the Fe center seemed unlikely, as the reduced product of such a

reaction would be a highly reactive H· radical. This supposition, combined with the

observation that the βN of **4.1** is also nucleophilic enough to attack chlorosilanes,

suggested that protonation at the βN of N_2 might be reasonable, but that bi-metallic

elimination of H_2 from the formed diazenido (FeNNH) species might be facile and lead to

the net observed oxidation (Scheme 4.2). Diazenido species are typically unstable, with

the only crystallographically characterized example from the tri-amido amine system of

Schrock and co-workers.[15] Further protonation, however, has led to the characterization

of more stable species, such as parent hydrazido(2-) complexes, which were some of the

first ligands observed from protonating N_2 on Mo.[16]
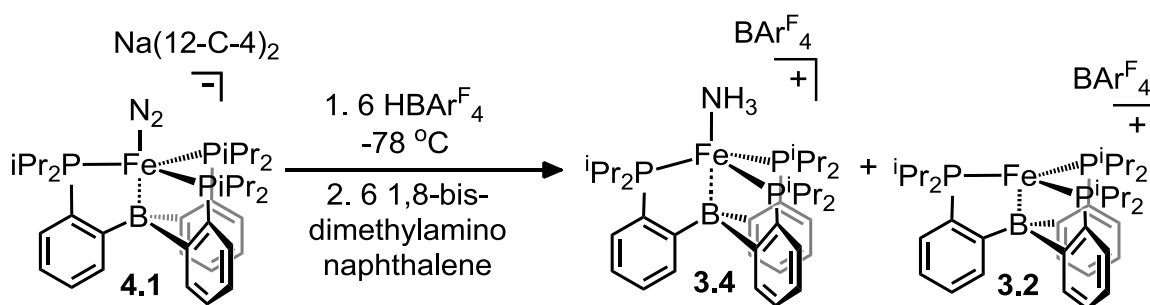
Scheme 4.3. Formation of complex **3.4** from complex **4.1** and acid.

Although stopping the loss of H_2 from a putative diazenido species might prove

challenging, a possible strategy to further functionalize the N_2 species would be trapping

the diazenido with excess protons before it can decompose (Scheme 4.2). With this

strategy in mind, reaction of **4.1** with excess acid was investigated as a means to test

whether N_xH_y species could be detected in solution or bound to Fe. Reaction of **4.1** with

6 equivalents of HBAr$^F_4$ · 2 Et$_2$O at -78 °C results in a color change from the dark red of

4.1 to yellow. Although the excess acid present in the reaction mixture complicates [1]H

proton analysis, addition of a base in the form of 1,8-bis-dimethylaminonaphthalene to

bind the excess acid allowed for the identification of $[(TPB)Fe(NH_3)][BAr^F_4]$ (**3.4**) as a major component of the reaction mixture (Scheme 4.3). Integration of the ^1H NMR signals of **3.4** versus an internal integral standard provides a crude method to estimate the yield of the paramagnetic products and shows that the yield of the NH_3 adduct **3.4** is ~ 35% with the observation of complex **3.2** in ~ 40% yield and other unidentified minor paramagnetic products. The observed yield of **3.4**, although only an estimate, suggests that NH_3 is being formed in unusually high yields in this reaction as compared with other phosphine complexes of Fe.[7]

The formation of NH_3 in this reaction led to several important observations. Firstly, the lack of additional reductant in the solution indicates that the NH_3 is being formed by some disproportionation pathway. Whether this pathway is through a disproportionation of N_xH_y species, as was seen in chapter 3 with the disproportionation of $[(TPB)Fe(N_2H_4)][BAr^F_4]$ (**3.3**) to **3.4**, or whether some portion of the initial complex **4.1** is protonated and then reduced by unreacted **4.1,** is still unclear. Secondly, the observation of **3.4** and **3.2**, as well as other putatively molecular species at the end of the reaction, suggests that a molecular process is responsible for the formation of NH_3 in this transformation. Thirdly, the reductions of **3.4** to release NH_3 and pick up N_2 to form $(TPB)Fe(N_2)$ and the subsequent reduction of $(TPB)Fe(N_2)$ to **4.1** are known. Complex **3.2** can similarly be reduced to **4.1**. Indeed, the low-temperature reduction of a mixture similarly generated to that shown in Scheme 4.3 results in regeneration of **4.1** as determined by IR spectroscopy (Appendix 3). These combined transformations suggest that a synthetic cycle for the generation of NH_3 from **4.1** should be plausible (Scheme 4.4).
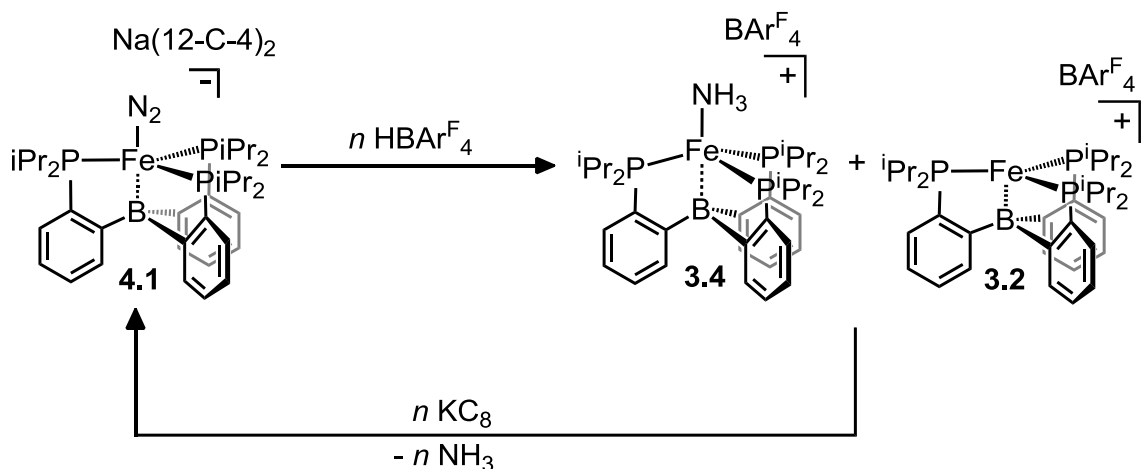
Scheme 4.4. A synthetic cycle for the formation of NH_3 mediated by (TPB)Fe.

4.2.2 Catalytic N_2 Reduction to NH_3

In order to accurately quantify the amount of NH_3 produced in any study, a reliable assay for NH_3 formation was sought. Traditionally, UV-Visible spectroscopy of highly colored chromophores formed from NH_4^+ salts have been employed for the detection of generated NH_3. Specifically, generation of indophenol dyes from NH_3, phenol, and hypochlorite is a technique that has been used by Schrock and Nishibayashi for the accurate quantification of NH_3.[17] A typical assay involves the vacuum transfer of the volatiles from a reaction mixture onto ethereal HCl. The remaining reaction residues are then digested with NaOtBu to liberate any NH_4^+ salts and then vacuum transferred again onto the same collection flask containing ethereal HCl. The collection flask is then warmed and any NH_3 is trapped as $[NH_4][Cl]$ which precipitates from solution. Upon removal of volatiles, the remaining $[NH_4][Cl]$ salts are re-dissolved in H_2O and analyzed with solutions of phenol and hypochlorite to develop the blue color indicative of the indophenol chromophore (Figure 4.1).

Studies with HBAr$^F_4 \cdot$ 2 Et$_2$O and KC$_8$ at -78 °C showed unusually high yields of NH$_3$, and the use of Et$_2$O as solvent resulted in the formation of an average of 7.0 ± 1 equivalents of NH$_3$ per Fe center, effectively demonstrating the efficacy of **4.1** as a pre-catalyst for N$_2$ reduction to NH$_3$ (Figure 4.1, Entry 1 Table 4.1) . This reaction has been performed sixteen times, with some single runs producing as much as 8.5 equivalents of NH$_3$ per Fe. In a typical reaction, complex **4.1** is suspended in Et$_2$O at -78 °C and 48 equivalents of HBAr$^F_4 \cdot$ 2 Et$_2$O similarly dissolved in Et$_2$O and cooled were added, resulting in a homogenous yellow solution. Addition of 48 equivalents of KC$_8$ to the reaction vessel as a suspension in cold Et$_2$O is then immediately followed by sealing of the reaction vessel. Quantification of NH$_3$ was then performed as described above after allowing the reaction to stir for 40 minutes at -78 °C.
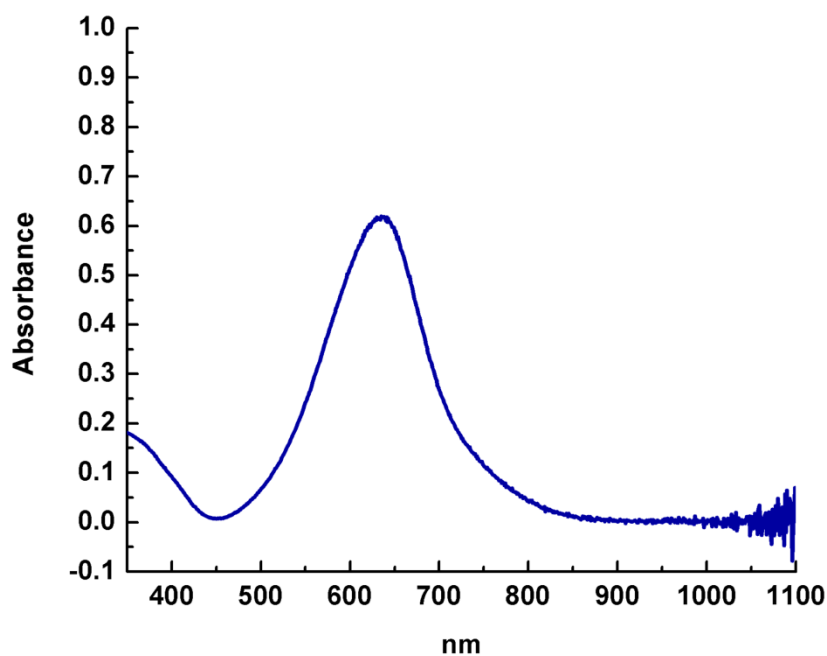
Figure 4.1. UV-Visible spectrum of the indophenol dye generated from NH$_3$. This particular absorbance spectrum corresponds to 7.5 equivalents of NH$_3$ generated per Fe center.

Entry	Fe precursor	NH$_3$ equiv/Fe
1	[(TPB)Fe(N$_2$)][Na(12-crown-4)$_2$]	7.0 ± 1
2	[(TPB)Fe][BAr$^F_4$]	6.2
3	[(TPB)Fe(NH$_3$)][BAr$^F_4$]	5.7
4	[(TPB)Fe(N$_2$H$_4$)][BAr$^F_4$]	5.9
5	(TPB)Fe(N$_2$)	2.0
6	FeCl$_2$·1.5 THF	<0.1
7	FeCl$_3$	<0.1
8	Cp$_2$Fe	<0.2
9	Fe(CO)$_5$	<0.1
10	none	<0.1

Table 4.1. Catalytic runs using the standard conditions described in the text with any changes noted in the experimental section. All numbers shown are an average of a minimum of four runs. All individual runs can be found in Appendix 3.

In addition to complex **4.1**, several other (TPB)Fe complexes have been tested (entries 2-5). In all cases, catalysis was observed with similar yields of NH$_3$ as those observed when **4.1** was used as the pre-catalyst. Most notably, species that could be potential intermediates during the catalytic cycle, such as **3.2** (entry 2), **3.3** (entry 3), and **3.4** (entry 4), all function as capable pre-catalysts. The exception to these observations is (TPB)Fe(N$_2$) (entry 5), which shows substantially decreased activity towards catalysis when compared with the other (TPB)Fe species studied. Reversal of the order of reagent addition, with reductant being added first followed by acid, resulted in an improved yield of 4.8 equivalents of NH$_3$ per Fe center. Possible explanations for the lowered activity of (TPB)Fe(N$_2$) under the standard conditions will be discussed below. As control

experiments, several simple Fe(II) and Fe(III) salts were also tested as pre-catalysts, but did not show any catalytic activity. The absence of any Fe species in the catalytic mixture also did not produce significant quantities of NH_3. Taken together, these results implicate the intermediacy of a molecular (TPB)Fe catalyst for N_2 reduction, especially when considered alongside the NMR studies discussed in 4.2.1.

Although there are no exogenous N atoms in the (TPB)Fe scaffold, the acid, or the reductant employed, it was still valuable to verify that the NH_3 being produced was coming from N_2. In this context, the catalytic reaction was run under $^{14}N_2$ or isotopically labeled $^{15}N_2$ and the resulting solids were analyzed by ^1H NMR (Figure 4.2). Under $^{14}N_2$ the triplet for $[NH_4][Cl]$ with $^1J_{N-H} = 51$ Hz was clearly observed and this signal became a doublet with $^1J_{N-H} = 71$ Hz typical of $[^{15}NH_4][Cl]$ when $^{15}N_2$ was used instead, with only trace $[^{14}NH_4][Cl]$ being observed, likely arising from the residual $^{14}N_2$ bound in **4.1**. These results verify that gaseous N_2 is the source of the resulting NH_3.
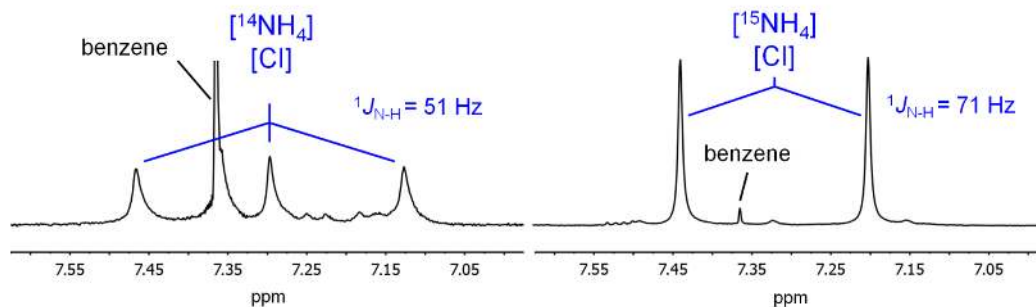
Figure 4.2. ^1H NMR spectra of $[^{14}NH_4][Cl]$ and $[^{15}NH_4][Cl]$ in DMSO-d_6 obtained from correspondingly labeled N_2 gas via catalytic reduction with complex **4.1** using the standard catalytic protocol described in the text.

It is somewhat noteworthy that the catalysis appears to be occurring at -78 °C. The disappearance of the bronze color of KC_8 at -78 °C seems to suggest that consumption of reductant occurs at low temperature as opposed to only reacting upon warming to RT. Furthermore, the fact that N-H bond formation is occurs faster than H_2 formation under these conditions is somewhat surprising, as KC_8 and $HBAr^F_4$ do react in the absence of any Fe complex under the reaction conditions to generate > 75% of the expected H_2 within 40 minutes. Formation of H_2 is nevertheless an issue, as ~ 30% of the hydrogen atom equivalents on average, as determined by GC analysis of the reaction head space, end up as H_2 during the course of catalytic runs (See Appendix 3). The formation of the N-H bonds during catalysis is likely aided by the heterogeneity of the reaction conditions, slowing H_2 formation enough to allow for effective delivery of hydrogen atom equivalents to N_2.

It is not straightforward to compare this Fe-based system to the Mo-based systems of Shrock and Nishibayashi. The turnovers for Fe (7) are quite similar to those observed for Schrock (7.5) and Nishibayashi (12.2), but the Fe system benefits from a substantially stronger reductant. It is not yet clear whether the redox potential required to form **4.1** (-2.19 V vs. Fc/Fc$^+$) mandates a stronger reductant, or whether weaker reductants only capable of accessing species such as $(TPB)Fe(N_2)$ could participate in catalysis. While a stronger reductant is required at this point, the Fe system does appear to operate at substantially lower temperatures than the Mo systems, potentially highlighting higher reactivity at the Fe based system.

4.2.3 Catalyst Speciation

With evidence of a molecular Fe-based catalyst for the fixation of N_2 in hand, initial studies on the speciation of the (TPB)Fe complexes in solution and potential causes of termination of catalysis were undertaken. A previous study on the (TPB)Fe scaffold showed that exposure of (TPB)Fe(N_2) to H_2 resulted in formation of (TPB)(μ-H)Fe(H)(N_2).[18] Because H_2 was formed as a by-product of the reaction, it was suspected that (TPB)(μ-H)Fe(H)(N_2) could be formed under the catalytic conditions. In this context, **4.1** was reacted with 10 equivalents of HBAr$^F_4 \cdot$ 2 Et$_2$O and 12 equivalents of KC$_8$. The presence of (TPB)(μ-H)Fe(H)(N_2) in a $\sim$ 30% yield was confirmed by both ^{31}P NMR and IR spectroscopy, where the strong N-N stretching vibration can be observed at ν_{NN} = 2073 cm^{-1}. These results indicate that formation of (TPB)(μ-H)Fe(H)(N_2) under the catalytic conditions is likely. To test whether (TPB)(μ-H)Fe(H)(N_2) would terminate a catalytic cycle, this complex was submitted to the standard catalytic conditions, and it was found that only 0.5 equivalents of NH_3 were formed per Fe center. This result suggests that if (TPB)(μ-H)Fe(H)(N_2) is formed under catalysis, it likely is unable to re-enter the catalytic cycle. Further evidence supporting this conclusion comes from the observation that (TPB)(μ-H)Fe(H)(N_2) does not show appreciable reactivity with either HBAr$^F_4 \cdot$ 2 Et$_2$O or KC$_8$ at RT in Et$_2$O.

When considering the comparably low yields of NH_3 provided when (TPB)Fe(N_2) (Table 1, entry 5) is used as a pre-catalyst the observation that (TPB)(μ-H)Fe(H)(N_2) can be formed from reaction of (TPB)Fe(N_2) with H_2 suggests that starting with (TPB)Fe(N_2) may allow for a greater percentage of the (TPB)Fe centers to be trapped as the catalytically inactive (TPB)(μ-H)Fe(H)(N_2), thus decreasing catalysis. Alternately, a

low-spin state such as that observed in (TPB)Fe(CO)[13] could dominate in (TPB)Fe(N$_2$) at low temperature, significantly decreasing its catalytic activity. Avoidance of this oxidation state by adding KC$_8$ initially to reduce all of the (TPB)Fe(N$_2$) to [(TPB)Fe(N$_2$)]$^-$ matches with both of these hypotheses.
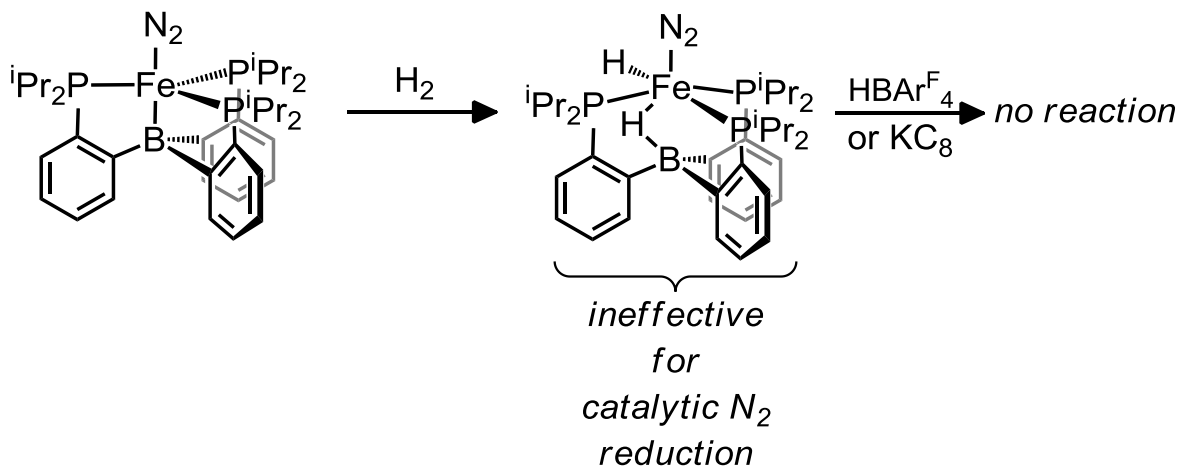
Scheme 4.5. Formation of (TPB)(μ-H)Fe(H)(N$_2$) and its reactivity with acid and reductant indicating that it is not a competent pre-catalyst.

Another possible termination pathway arises from the presence of Cl$^-$ in the reaction mixture. Since HBAr$^F_4 \cdot$ 2 Et$_2$O is made via loss of NaCl, Cl$^-$ contamination is a reasonable possibility. The most conclusive test for the effect of Cl$^-$ is use of the $S = 3/2$ complex (TPB)FeCl, which was synthesized and crystallized in an analogous manner to the previously reported (TPB)FeBr.[13a] Catalytic runs using this pre-catalyst give, on average, 3.2 equivalents of NH$_3$ per Fe center, suggesting that while Cl$^-$ does not terminate catalysis, it does hinder the reactivity of the (TPB)Fe species relative to using **4.1** as a pre-catalyst. Similarly, addition of exogenous Cl$^-$ in the form of excess KCl to the standard catalytic conditions with **4.1** also results in 3.0 equivalents of NH$_3$ being

formed. These result suggests that any residual Cl^- may lower the yield of NH_3, but should not terminate the catalytic cycle by formation of (TPB)FeCl.

In addition to termination processes, it was of great interest to determine whether N_2H_4 was involved in the catalytic cycle, as any presence of N_2H_4 would imply the involvement of an "alternating" type mechanism. A UV-Visible spectroscopic assay similar to the indophenol method for NH_3 quantification was employed to detect the presence of N_2H_4 in reaction mixtures.[19] No N_2H_4 was detected from any catalytic mixture. As an additional test, two equivalents of N_2H_4 were added to **4.1** before performing the standard catalytic protocol. In these runs, only trace N_2H_4 was observed, suggesting that if N_2H_4 is formed during catalysis, it would likely be consumed and should not be observed.

4.3 Conclusion

The anionic N_2 complex **4.1** generates NH_3 in the form of complex **4.4** upon exposure to excess acid, likely via some disproportionation pathway. Use of $HBAr^F_4 \cdot 2$ Et_2O and KC_8 in Et_2O enables the catalytic reduction of N_2 to NH_3 with 7 equivalents of NH_3 being generated per Fe center. Multiple other (TPB)Fe species also serve as pre-catalysts, but simple Fe salts and complexes do not, suggesting the agency of a molecular (TPB)Fe catalyst. Analysis of reaction mixtures indicates the formation of (TPB)(μ-H)Fe(H)(N_2) as a likely byproduct of catalysis. This complex is also not competent as a pre-catalyst and hence its formation indicates a possible pathway for the termination of catalysis. The presence of chloride appears to inhibit, but not terminate, catalysis and (TPB)FeCl still serves as a competent pre-catalyst. Finally, no N_2H_4 is detected in

catalytic reaction mixtures, but N_2H_4 is also consumed under catalysis, as determined by the addition of two equivalents of N_2H_4 to catalytic mixtures. This result suggests that if N_2H_4 were formed during catalysis it would likely not be detectable.

Due to the dearth of synthetic Fe species that can form appreciable quantities of NH_3 from N_2, Mo complexes have received a great deal of attention as the likely binding site of N_2 in the FeMoco active site of nitrogenase.[20] The results disclosed herein show for the first time that a molecular Fe species can also catalyze nitrogen fixation with protons and electrons in comparable yields to the Mo systems. This work validates the hypothesis that N_2 binding and reduction may occur at a single Fe site in the FeMoco.[21] Furthermore, the flexible nature of the Fe-B interaction in the (TPB)Fe scaffold further motivates the consideration of a similar hemi-labile role for the central C atom of the FeMoco.[22]

4.4 Experimental Section

4.4.1 General Considerations

Unless otherwise noted, all compounds were purchased from commercial sources and used without further purification.[(TPB)Fe(N_2)][Na(12-crown-4)$_2$],[13] [(TPB)Fe][BAr$^F_4$],[14] (TPB)(μ-H)Fe(H)(N_2),18 HBAr$^F_4 \cdot$ 2 Et$_2$O,[23] FeCl$_2 \cdot$ 1.5 THF,[24] KC$_8$,[25] [(TPB)Fe(NH$_3$)][BAr$^F_4$]$^{.14}$ and [(TPB)Fe(N_2H_4)][BAr$^F_4$][14] were prepared according to literature procedures ([BAr$^F_4$] = [B(3,5-(CF$_3$)$_2$-C$_6$H$_3$)$_4$B]$^-$) . All manipulations were carried out under a N_2 atmosphere utilizing standard glovebox or Schlenk techniques. Solvents were dried and de-oxygenated by an argon sparge followed by passage through an activated alumina column purchased from S.G. Waters Company.

Labeled $^{15}N_2$ (98% purity) was obtained from Cambridge Isotope Laboratories. Solvents for catalytic runs were additionally stirred for more than 2 hours over Na/K alloy and then filtered prior to use.

IR spectra were obtained *via* KBr pellets on a Bio-Rad Excalibur FTS 3000 spectrometer using Varian Resolutions Pro software set at 4 cm^{-1} resolution. NMR measurements were obtained on Varian 300 MHz or 500 MHz spectrometers. Deuterated solvents for these measurements were obtained from Cambridge Isotope Laboratories and were dried and degassed prior to use. All ^{1}H NMR spectra were referenced to residual solvent peaks. UV-Visible spectra were taken on a Cary 50 spectrometer from 1100 nm to 200 nm in the fast scan mode. Samples were prepared in a 1 cm path length quartz cuvette. All samples had a blank sample background subtraction applied.

4.4.3 Standard Catalytic Protocol

[(TPB)Fe(N$_2$)][Na(12-crown-4)$_2$] (2 mg, 0.002 mmol) was suspended in Et$_2$O (0.5 mL) in a 20 mL scintillation vial equipped with a stir bar. This suspension was vigorously stirred and cooled to -78 °C in a cold well inside of the glove box. A similarly cooled solution of HBAr$^F_4 \cdot$ 2 Et$_2$O (93 mg, 0.092 mmol) in Et$_2$O (1.5 mL) was added to the suspension in one portion with rapid stirring. Any remaining acid was dissolved in cold Et$_2$O (0.25 mL) and added subsequently. The reaction mixture turned light yellow-orange and homogeneous upon addition of acid and the resulting solution was allowed to stir for 5 minutes before being transferred into a pre-cooled Schlenk tube equipped with a stir bar. The original reaction vial was washed with cold Et$_2$O (0.25 mL) which was subsequently transferred to the Schlenk tube. Solid KC$_8$ (15 mg, 0.100 mmol) was

suspended in cold Et$_2$O (0.75 mL) and added dropwise to the rapidly stirred solution in the Schlenk tube, which was then tightly sealed. The reaction was allowed to stir for 40 minutes at -78 °C before being warmed to RT and stirred for 15 minutes.

4.4.4 Ammonia Quantification

A Schlenk tube was charged with HCl (3 mL of a 2.0 M solution in Et$_2$O, 6 mmol). Reaction mixtures were vacuum transferred into this collection flask. Residual solid in the reaction vessel was treated with a solution of [Na][OtBu] (40 mg, 0.4 mmol) in 1,2-dimethoxyethane (1 mL) and sealed. The resulting suspension was allowed to stir for 10 minutes before all volatiles were again vacuum transferred into the collection flask. After completion of the vacuum transfer, the flask was sealed and warmed to RT. Solvent was removed *in vacuo* and the remaining residue was dissolved in H$_2$O (1 mL). An aliquot of this solution (20 or 40 μL) was then analyzed for the presence of NH$_3$ (trapped as [NH$_4$][Cl]) via the indophenol method.[17] Quantification was performed with UV-Visible spectroscopy by analyzing the absorbance at 635 nm. The tables shown in Appendix 4 below list the raw data for the runs. Runs with small absorbance levels (< 0.02 absorbance units) suffer from a large degree of error due to a small signal-to-noise ratio.

4.4.5 Synthesis of (TPB)FeCl

A mixture of FeCl$_2$ (0.087 g, 0.69 mmol), TPB^{iPr} (0.400 g, 0.69 mmol), Fe powder (0.415 g, 7.40 mmol), and THF (20mL) was heated to 90 °C in a sealed schlenk tube under vigorous stirring for 3 days, during which time the color of the liquid phase

turned from pale yellow to brown. The solids were removed from the mixture by filtration, and the solvent was removed *in vacuo*. The brown residue was then triturated then extracted with pentane (200 mL) and filtered through celite to give a brown solution. Solvent evaporation *in vacuo* afforded the product as a greenish brown powder (0.422 g, 90%). An analytically pure sample was obtained by slow concentration of a saturated pentane solution. Crystals suitable for XRD analysis were obtained upon cooling a saturated solution of **5** in pentane to −35 °C . ^{1}H NMR (C_6D_6, δ): 96.9 (br s), 35.0 (s), 23.6 (s), 9.8 (br s), 5.8 (s), 1.9 (br s), 1.7 (sh), −0.3 (s), -2.3 (br s), −22.4 (s) . UV-vis (THF, nm {$cm^{-1}M^{-1}$}): 280 {$2.0 \cdot 10^4$}, 320 {sh}, 560 {sh}, 790 {150}, 960 {190}. μ_{eff} (C_6D_6, Evans method, 20 °C): 4.0 μ_B. Anal. calcd. for $C_{36}H_{54}BClFeP_3$: C 63.41 , H 7.98; found: C 63.16, H 7.72.

4.4.6 Catalytic Protocols

Catalytic protocol under $^{15}N_2$. [(TPB)Fe(N_2)][Na(12-crown-4)$_2$] (4 mg, 0.004 mmol) was suspended in Et_2O (3 mL) in a 25 mL three neck flask (ground-glass, 14/20) equipped with a stir bar. The flask was then equipped with a stopcock adaptor in the central opening, a solid addition arm containing HBAr$^F_4 \cdot$ 2 Et_2O (188 mg, 0.186 mmol) in one of the side openings, and an additional solid addition arm containing KC_8 (37 mg, 0.274 mmol) in the final opening. The apparatus was sealed, brought out of the glovebox, and connected to a high-vacuum manifold. The solution was degassed via four freeze-pump-thaw cycles and then allowed to thaw to -78 °C with stirring. The flask was backfilled with 1 atm $^{15}N_2$. At this point the acid was added to the solution in one portion via the solid addition arm. The resulting solution was allowed to stir for 5 minutes before

KC_8 was added via the other solid addition arm resulting in a dark suspension. This suspension was allowed to stir for 40 minutes at -78 °C and then an additional 10 minutes at RT prior to the standard work-up. The presence of $[^{15}NH_4][Cl]$ was verified by ^1H NMR spectroscopy (Figure 4 in the SI). The yield of NH_3 was 3.64 equiv NH_3/Fe as measured using the indophenol method. The NH_3 yield, while still showing catalysis, was lower than the average obtained by the standard protocol, presumably due to differences associated with adding the $HBAr^F_4 \cdot 2 Et_2O$ and KC_8 solids via the solid addition arms.

Runs with $[(TPB)Fe][BAr^F_4]$ as precursor. The procedure was identical to that of the standard catalytic protocol with the changes noted. The precursor used was $[(TPB)Fe][BAr^F_4]$ (2.3 mg, 0.002 mmol), which is a dark orange solid. Note that $[(TPB)Fe][BAr^F_4]$ was soluble in Et_2O and formed a yellow solution. No substantial color change was observed upon addition of acid.

Runs with $(TPB)(\mu-H)Fe(H)(N_2)$ as precursor. The procedure was identical to that of the standard catalytic protocol with the changes noted. The precursor used was $(TPB)(\mu-H)Fe(H)(N_2)$ (1.3 mg, 0.002 mmol), which is a yellow solid. Note that $(TPB)(\mu-H)Fe(H)(N_2)$ was insoluble in Et_2O and did not dissolve upon addition of acid. As such, the resulting mixture was a suspension through the remaining manipulations.

Runs with $FeCl_2 \cdot 1.5$ THF as precursor. The procedure was identical to that of the standard catalytic protocol with the changes noted. The precursor used was $FeCl_2 \cdot 1.5$ THF (0.5 mg, 0.002 mmol), which is an off white powder. Note that $FeCl_2 \cdot 1.5$ THF did not dissolve upon addition of acid. As such, the resulting mixture was a suspension through the remaining manipulations.

Runs with FeCl₃ as precursor. The procedure was identical to that of the standard catalytic protocol with the changes noted. The precursor used was $FeCl_3$ (0.3 mg, 0.002 mmol), which is a dark solid. Note that $FeCl_3$ was soluble in Et_2O and formed a yellow solution. No substantial color change was observed upon addition of acid.

Runs with Fe(CO)₅ as precursor. The procedure was identical to that of the standard catalytic protocol with the changes noted. The precursor used was $Fe(CO)_5$ (0.35 mg, 0.002 mmol), which is a pale yellow liquid. Note that $Fe(CO)_5$ was soluble in Et_2O and formed a colorless solution. No substantial color change was observed upon addition of acid.

Runs with FeCp₂ as precursor. The procedure was identical to that of the standard catalytic protocol with the changes noted. The precursor used was $FeCp_2$ (0.35 mg, 0.002 mmol), which is an orange solid. Note that $FeCp_2$ was soluble in Et_2O and formed a yellow solution. No substantial color change was observed upon addition of acid.

Runs without an Fe precursor. The procedure was identical to that of the standard catalytic protocol with the changes noted. A 2 mL Et_2O solution of $HBAr^F_4 \cdot 2\ Et_2O$ (93 mg, 0.092 mmol), was added directly into a Schlenk tube equipped with a stir bar and cooled to -78 °C. Addition of KC_8 and subsequent work-up was identical to the standard catalytic protocol.

Runs with [(TPB)Fe(NH₃)][BArᶠ₄] as precursor. The procedure was identical to that of the standard catalytic protocol with the changes noted. The precursor used was $[(TPB)Fe(NH_3)][BAr^F_4]$ (2.9 mg, 0.002 mmol), which is an orange solid . Note that the solution became homogeneous with no significant color change upon addition of acid.

Runs with [(TPB)Fe(N$_2$H$_4$)][BAr$^F_4$] as precursor. The procedure was identical to that

of the standard catalytic protocol with the changes noted. The precursor used was

[(TPB)Fe(N$_2$H$_4$)][BAr$^F_4$] (2.9 mg, 0.002 mmol), which is an orange solid. Note that the

solution became homogeneous with no significant color change upon addition of acid.

Runs with (TPB)FeCl as precursor. The procedure was identical to that of the standard

catalytic protocol with the changes noted. The precursor used was (TPB)FeCl (1.3 mg,

0.002 mmol), which is a brown solid. Note that the solution became homogeneous with

no significant color change upon addition of acid.

Inclusion of hydrazine in a catalytic run with [(TPB)Fe(N$_2$)][Na(12-crown-4)$_2$]. The

procedure was identical to that of the standard catalytic protocol with the following

changes noted. Hydrazine (0.12 µL, 0.004 mmol) was added directly to the suspension of

[(TPB)Fe(N$_2$)][Na(12-crown-4)$_2$] prior to subjecting the mixture to the standard catalytic

protocol. No color change was observed upon addition of N$_2$H$_4$. After workup the

aqueous solution was analyzed for NH$_3$ as described above, and also for N$_2$H$_4$ *via* a

literature protocol.[19] The results obtained show most all of the N$_2$H$_4$ had been consumed,

indicating that if it is produced in some amount under the standard catalytic protocol it is

unlikely to be detectable. As a control experiment it was shown that N$_2$H$_4$ was not

degraded to NH$_3$ under the standard catalytic conditions in the absence of

[(TPB)Fe(N$_2$)][Na(12-crown-4)$_2$].

4.4.7 Other Reaction Protocols

IR spectral analysis of addition of 2 equiv HBAr$^F_4$ · 2 Et$_2$O to [(TPB)Fe(N$_2$)][Na(12-

crown-4)$_2$], followed by 3 equiv KC$_8$. A 20 mL scintillation vial was charged with a stir

bar and [(TPB)Fe(N$_2$)][Na(12-crown-4)$_2$] (8 mg, 0.0074 mmol). In a separate vial,

HBAr$^F_4 \cdot$ 2 Et$_2$O (15 mg, 0.015 mmol) was dissolved in Et$_2$O (1 mL). Finally, a third vial

was prepared containing a suspension of potassium graphite (3 mg, 0.023 mmol) in Et$_2$O

(1 mL). All three vials were chilled in the cold well to -70 +/- 5 ^{o}C for 30 minutes. The

solution of HBAr$^F_4 \cdot$ 2 Et$_2$O was quickly added to the stirring suspension of

[(TPB)Fe(N$_2$)][Na(12-crown-4)$_2$] with a glass pipette pre-cooled to -70 ^{o}C. Any residue

of the acid was washed with pre-chilled Et$_2$O (0.5 mL) and transferred to the stirring

solution. The resulting solution turned homogeneous. After stirring for 5 minutes, the

suspension of KC$_8$ was added rapidly to the stirring solution. Any additional KC$_8$ was

washed with pre-chilled Et$_2$O (0.5 mL) and the resulting suspension was transferred to

the stirring mixture. After addition of KC$_8$ the solution adopted a red color. This mixture

was capped and stirred at -70 ^{o}C for 40 minutes and then brought to RT and stirred for 10

minutes. The red color persisted upon thawing to RT. Graphite was removed by filtration

through glass filter paper. To the red solution was added 12-crown-4 (13.1 mg, 74.3

μmol) in Et$_2$O (1 mL) and the resulting solution was stirred for 10 minutes. The solution

was then cooled to -70 ^{o}C for 30 minutes and stirred vigorously, leading to a red

precipitate. The precipitate was collected on a filter pad and the light orange filtrate was

concentrated to dryness *in vacuo*. IR analysis of the precipitate (KBr pellet) showed an

intense band at ν_{NN} = 1904 cm^{-1}, identical to that of authentic [(TPB)Fe(N$_2$)][Na(12-

crown-4)$_2$] (ν_{NN} = 1905 cm^{-1}, KBr pellet). No assignable ν_{NN} IR bands were observed for

the filtrate in the window of 1700 – 2300 cm^{-1}. See Figure S6 of the SI.

IR and ^{31}P NMR spectral analysis of addition of 10 equiv HBAr$^F_4 \cdot$ 2 Et$_2$O to

[(TPB)Fe(N$_2$)][Na(12-crown-4)$_2$], followed by 12 equiv KC$_8$. A 20 mL scintillation

vial was charged with a stir bar and [(TPB)Fe(N$_2$)][Na(12-crown-4)$_2$] (10.4 mg, 10.2 µmol). In a separate vial, HBAr$^F_4$ · 2 Et$_2$O (103 mg, 102 µmol) was dissolved in Et$_2$O (1 mL). Finally, a third vial was prepared containing a suspension of potassium graphite (16.5 mg, 122 µmol) in Et$_2$O (1 mL). All three vials were chilled in the cold well to -70 +/- 5 °C for 30 minutes. The solution of HBAr$^F_4$ · 2 Et$_2$O was quickly added to the stirring suspension of [(TPB)Fe(N$_2$)][Na(12-crown-4)$_2$] with a glass pipette pre-cooled to -70 °C. Any residue of the acid was washed with pre-chilled Et$_2$O (0.5 mL) and transferred to the stirring solution. The resulting solution turned homogeneous. After stirring for 5 minutes, the suspension of KC$_8$ was added rapidly to the stirring solution. Any additional KC$_8$ was washed with pre-chilled Et$_2$O (0.5 mL) and the resulting suspension was transferred to the stirring mixture. The large amount of graphite present in the vial prevented the color of the resulting solution from being accurately discerned. This mixture was capped and stirred at -70 °C for 40 minutes and then brought to RT and stirred for 10 minutes. Graphite was removed by filtration through glass filter paper. To the resulting orange solution was added 12-crown-4 (60 mg, 340 µmol) in Et$_2$O (1 mL) and a ^{31}P NMR integration standard of triphenylphosphine (11.9 mg, 45.4 µmol) in toluene (1 mL) followed by stirring for 10 minutes. The solution was then cooled to -70°C for 30 minutes and stirred vigorously. No precipitate formed and volatiles were removed *in vacuo*. The orange powder was dissolved in THF and integration of ^{31}P NMR resonances suggest the formation of (TPB)(µ-H)Fe(N$_2$)(H) (3.4 µmol) in 30% yield. Solid-state IR analysis of the orange solid (KBr pellet) showed a strong, sharp band at $\nu_{NN} = 2073$ cm^{-1} (s), identical to that of authentic (TPB)(µ-H)Fe(N$_2$)(H). Additional broad, weak bands were observed at 1942, 1875, 1802, 1734 cm^{-1} that could not be

assigned. $^{31}P\{^{1}H\}$ NMR (400 MHz, THF): 72.6, 63.1 ppm. See Figures S6 and S7 of the SI.

Reactivity of (TPB)(μ-H)Fe(H)(N₂) with KC₈. A 20 mL scintillation vial was charged with a stir bar and (TPB)(μ-H)Fe(H)(N₂) (11 mg, 0.016 mmol) suspended in Et₂O (2 mL). A separate vial was charged with KC₈ (2.6 mg, 0.019 mmol) suspended in Et₂O (2 mL). Both vials were cooled to -70 +/- 5 °C and the Fe-containing vial was stirred vigorously. The suspension of KC₈ was quickly transferred to the vial containing (TPB)(μ-H)Fe(H)(N₂) and stirred for 10 minutes at low temperature. The vial was then brought to RT and the brown color of KC₈ slowly turned to black over 1 hour. Graphite was filtered through a glass filter pad and the orange filtrate was transferred to a vial containing 12-crown-4 (21.0 mg, 119.17 μmol, 7.25 equivalents) and stirred vigorously at -70 °C for 10 minutes. No precipitate formed and the resulting orange solution was brought to RT and concentrated to dryness *in vacuo*. IR analysis of the residue (KBr pellet) showed a strong stretch at $\nu_{NN} = 2073$ cm^{-1}, consistent with authentic (TPB)(μ-H)Fe(H)(N₂) (2073 cm^{-1}, KBr pellet). ^{1}H NMR analysis was consistent with the presence of predominately (TPB)(μ-H)Fe(H)(N₂) and minor amounts of unidentified paramagnetic species.

Reactivity of (TPB)(μ-H)Fe(H)(N₂) with HBArᶠ₄ · 2 Et₂O. A 20 mL scintillation vial was charged with a stir bar and (TPB)(μ-H)Fe(H)(N₂) (9 mg, 0.014 mmol) suspended in Et₂O (2 mL). A separate vial was charged with HBArᶠ₄ · 2 Et₂O (15 mg, 0.015 mmol, 1.08) suspended in Et₂O (2 mL). Both vials were cooled to -70 +/- 5°C and the Fe-containing vial was stirred vigorously. The solution of HBArᶠ₄ · 2 Et₂O was quickly transferred to the vial containing (TPB)(μ-H)Fe(H)(N₂) and stirred for 10 minutes at low

temperature. The vial was then brought to RT and no noticeable color change was observed over 1 hour. The solution was concentrated to dryness *in vacuo* and the remaining residue was analyzed with IR spectroscopy (KBr pellet), which showed a strong stretch at $\nu_{NN} = 2073$ cm^{-1}, consistent with authentic (TPB)(μ-H)Fe(H)(N$_2$) (2073 cm^{-1}, KBr pellet). The residue was then re-dissolved in C$_6$D$_6$ and analyzed by ^{1}H NMR spectroscopy, which showed (TPB)(μ-H)Fe(H)(N$_2$) with minor amounts of unidentified paramagnetic species and resonances from the BAr$^F_4$ anion. Complete consumption of (TPB)(μ-H)Fe(H)(N$_2$) to unidentified paramagnetic species was observed after 12 hours at RT.

Identification of [(TPB)Fe(NH$_3$)][BAr$^F_4$] from protonation of [(TPB)Fe(N$_2$)][Na(12-crown-4)$_2$]. [(TPB)Fe(N$_2$)][Na(12-crown-4)$_2$] (5 mg, 0.005 mmol) was dissolved in 2 mL of THF and cooled to -78 °C. This dark red solution was added dropwise to a similarly cooled 2 mL THF solution of HBAr$^F_4 \cdot$ 2 Et$_2$O (29 mg, 0.029 mmol) with stirring. The resulting yellow-orange solution was allowed to stir for 10 minutes at low temperature before being warmed to RT and stirred for an additional 40 minutes. 1,8-Bis(dimethylamino)naphthalene (6 mg, 0.029 mmol) was added and the solution was allowed to stir for 15 minutes with no noticeable color change. Volatiles were removed from the solution and the resulting yellow residue was taken up in THF-d_8. The presence of [(TPB)Fe(NH$_3$)][BAr$^F_4$] was determined by comparison of the ^{1}H NMR spectrum with that of an authentic sample prepared as recently reported.[14] Addtionally, a capillary insert of the previously reported (TPB)FeMe[14] in THF-d_8 was added to the NMR sample, which allowed for crude measurements of the yield of [(TPB)Fe(NH$_3$)][BAr$^F_4$], a species tentatively assigned as [(TPB)Fe][BAr$^F_4$], and the total amount of $S = 3/2$ TPB species as

roughly 30%, 50%, and 100% respectively. Note that there is likely a significant degree of error on these measurements due to the broad paramagnetic peaks used for integration. See Figure S1of the SI.

Identification of H₂ in standard catalytic runs. The catalytic runs were performed according to the standard procedure. Prior to the vacuum transfer of volatiles, the solutions inside of the Schlenk tubes were frozen. The ground glass joint of the Schlenk tube was then sealed with a rubber septum and the head space between the Teflon stopcock of the Schlenk tube and the septum was evacuated. This head space was left under static vacuum and the Teflon stopcock of the reaction vessel was opened after which a 10 mL aliquot of the headspace was sampled through the septa *via* a gas-tight syringe. This sample was then analyzed for hydrogen with an Agilent 7890A gas chromatograph using a thermal conductivity detector. After H_2 analysis, the reaction vessel was sealed and subjected to the standard analysis for NH_3. As some H_2 leakage is unavoidable by the procedure used, these values represent lower limits of the H_2 yield. The values for NH_3 and H_2 yield are included in Appendix 4

Identification of H₂ in runs without an Fe precursor. A Schlenk tube was charged with a stir bar and a suspension of KC_8 (14 mg, 0.100 mmol) in Et_2O (0.5 mL). The Schlenk tube was then fitted with a Teflon stopcock, but not sealed. The ground glass joint on the Schlenk tube was sealed with a rubber septum. This reaction vessel was then cooled to -78 °C. A pre-cooled solution of $HBAr^F_4 \cdot$ 2 Et_2O (92 mg, 0.092 mmol) in Et_2O (2 mL) was then syringed directly into the reaction vessel with stirring, after which the vessel was rapidly sealed with its Teflon stopcock. The reaction was allowed to stir for 40 minutes at low temperature before the headspace between the Teflon valve and the septa

was evacuated. After evacuation, the Teflon stopcock was opened and a 10 mL aliquot of the headspace was sampled *via* a gas tight syringe. This sample was then analyzed for hydrogen with an Agilent 7890A gas chromatograph using a thermal conductivity detector. The yield of hydrogen observed, based on proton-equivalents was 66% and 88% for each of two runs, respectively. As some H_2 leakage is unavoidable by the procedure used, these values represent lower limits of the H_2 yield.

References Cited

1 (a) Shilov, A.; Denisov, N.; Efimov, O.; Shuvalov, N.; Shuvalova, N.; Shilova, A. *Nature* **1971**, *231*, 460-461; (b) Bazhenova, T. A.; Shilov, A. E. *Coord. Chem. Rev.* **1995**, *144*, 69-145.

2 Chatt, J.; Dilworth, J. R.; Richards, R. L. *Chem. Rev.* **1978**, *78*, 589-625.

3 (a) Yandulov, D. V.; Schrock, R. R. *Science* **2003**, *301*, 76-78; (b) Arashiba, K.; Miyake, Y.; Nishibayashi, Y. *Nature Chem.* **2011**, *3*, 120-125.

4 Kinoshita, E.; Arashiba, K.; Kuriyama, S.; Miyake, Y.; Shimazaki, R.; Nakanishi, H.; Nishibayashi, Y. *Organometallics* **2012**, *31*, 8437-8443.

5 Schrock, R. R. *Acc. Chem. Res.* **2005**, *38*, 955-962.

6 (a) Betley, T. A.; Peters, J. C. *J. Am. Chem. Soc.* **2004**, *126*, 6252-6254; (b) Brown, S. D.; Peters, J. C. *J. Am. Chem. Soc.* **2005**, *127*, 1913-1923; (c) Scepaniak, J. J.; Young, J. A.; Bontchev, R. P.; Smith, J. M. *Angew. Chem. Int. Ed.* **2009**, *48*, 3158-3160.

7 (a) Leigh, G. J.; Jimenez-Tenorio, M. *J. Am. Chem. Soc.* **1991**, *113*, 5862-5863; (b) Leigh, G. J. *Acc. Chem. Res.* **1992**, *25*, 177-181; (c) Hills, A.; Hughes, D. L.; Jimenez-Tenorio, M.; Leigh, G. J.; Rowley, A. T. *J. Chem. Soc., Dalton* **1993**, 3041-3049; (d) Crossland, J. L.; Tyler, D. R. *Coord. Chem. Rev.* **2010**, *254*, 1883-1894.

8 Rodriguez, M. M.; Bill, E.; Brennessel, W. W.; Holland, P. L. *Science* **2011**, *334*, 780-783.

9 Yuki, M.; Tanaka, H.; Sasaki, K.; Miyake, Y.; Yoshizawa, K.; Nishibayashi, Y. *Nature comm.* **2012**, *3*, 1254-1254.

10 (a) Burgess, B. K.; Lowe, D. J. *Chem. Rev.* **1996**, *96*, 2983-3011; (b) Eady, R. R. *Chem. Rev.* **1996**, *96*, 3013-3030.

11 (a) Dos Santos, P. C.; Igarashi, R. Y.; Lee, H. I.; Hoffman, B. M.; Seefeldt, L. C.; Dean, D. R. *Acc. Chem. Res.* **2005**, *38*, 208-214; (b) Hoffman, B. M.; Dean, D. R.; Seefeldt, L. C. *Acc. Chem. Res.* **2009**, *42*, 609-619; (c) Seefeldt, L. C.; Hoffman, B. M.; Dean, D. R. *Annu. Rev. Biochem.* **2009**, *78*, 701-722; (d) Doan, P. E.; Telser, J.; Barney, B. M.; Igarashi, R. Y.; Dean, D. R.; Seefeldt, L. C.; Hoffman, B. M. *J. Am. Chem. Soc.* **2011**, *133*, 17329-17340.

12 Mankad, N. P.; Whited, M. T.; Peters, J. C. *Angew. Chem. Int. Ed.* **2007**, *46*, 5768-5771.

13 (a) Moret, M.-E.; Peters, J. C. *Angew. Chem. Int. Ed.* **2011**, *50*, 2063-2067; (b) Moret, M.-E.; Peters, J. C. *J. Am. Chem. Soc.* **2011**, *133*, 18118-18121.

14 Anderson, J. S.; Moret, M.-E.; Peters, J. C. *J. Am. Chem. Soc.* **2012**, *135*, 534-537.

15 Yandulov, D. V.; Schrock, R. R. *Inorg. Chem.* **2005**, *44*, 1103-1117.

16 (a) Chatt, J.; Heath, G. A.; Richards, R. L. *J. Chem. Soc., Dalton* **1974**, 2074-2082; (b) Hidai, M.; Kodama, T.; Sato, M.; Harakawa, M.; Uchida, Y. *Inorg. Chem.* **1976**, *15*, 2694-2697; (c) Takahashi, T.; Mizobe, Y.; Sato, M.; Uchida, Y.; Hidai, M. *J. Am. Chem. Soc.* **1980**, *102*, 7461-7467.

17 Weatherburn, M. W. *Anal. Chem.* **1967**, *39*, 971-974.

18 Fong, H.; Moret, M.-E.; Lee, Y.; Peters, J. C. *Organometallics* **2013**, *32*, 3053-3062.

19 Watt, G. W.; Chrisp, J. D. *Anal. Chem.* **1952**, *24*, 2006-2008.

20 (a) Leigh, G. J. *Science* **2003**, *301*, 55-56; (b) Schrock, R. R. *Nature Chem.* **2011**, *3*, 95-96.

21 Hendrich, M. P.; Gunderson, W.; Behan, R. K.; Green, M. T.; Mehn, M. P.; Betley, T. A.; Lu, C. C.; Peters, J. C. *Proc. Natl. Acad. Sci. U. S. A.* **2006**, *103*, 17107-17112.

22 (a) Lancaster, K. M.; Roemelt, M.; Ettenhuber, P.; Hu, Y. L.; Ribbe, M. W.; Neese, F.; Bergmann, U.; DeBeer, S. *Science* **2011**, *334*, 974-977; (b) Spatzal, T.; Aksoyoglu, M.; Zhang, L. M.; Andrade, S. L. A.; Schleicher, E.; Weber, S.; Rees, D. C.; Einsle, O. *Science* **2011**, *334*, 940-940.

23 Brookhart, M.; Grant, B.; Volpe, A. F. *Organometallics* **1992**, *11*, 3920-3922.

24 Kern, R. J. *J. Inorg. Nucl. Chem.* **1962**, *24*, 1105-1109.

25 Weitz, I. S.; Rabinovitz, M. *J. Chem. Soc., Perkin* **1993**, 117-120.

Chapter 5: The Effect of Ligand and Reaction Conditions on Fe Mediated N_2 Fixation

5.1 Introduction

Chapter 4 described the development of a catalytic system for the Fe mediated conversion of N_2 to NH_3 with protons and electrons.[1] The fact that Mo centers have been known to catalyze this reaction for some time had been viewed as supporting evidence for Mo being the N_2 binding site in FeMoco.[2] The discovery of an Fe based system serves to illustrate that Fe mediated N_2 reduction to NH_3 is feasible and bolsters arguments that Fe is the site of N_2 binding and reduction in nitrogenase enzymes.[3] Despite this initial result, relatively little is known about what factors enable catalysis or about the mechanism of N_2 reduction. Understanding of these factors could help to guide thought on the mechanism of N_2 reduction by the FeMoco.

Motivated by these questions, this chapter describes the preparation of three new phosphine supported Fe complexes analogous to $[(TPB^{iPr})Fe(N_2)][Na(12\text{-crown-4})_2]$ (**4.1**): $[(TPB^{Cy})Fe(N_2)][Na(12\text{-crown-4})_2]$ (**5.1**) ($TPB^{Cy} = (o\text{-}Cy_2P(C_6H_4))_3B$), $[(TPB^{Ph})Fe(N_2)][Na(12\text{-crown-4})_2]$ (**5.2**) ($TPB^{Ph} = (o\text{-}Ph_2P(C_6H_4))_3B$), and $[(DPB)Fe(N_2)][K(Bz15\text{-crown-5})_2]$[4] (**5.3**) ($DPB = (o\text{-iPr}_2P(C_6H_4))_2BPh$) (Figure 5.1). The efficacy of these complexes as well as the previously reported complexes $[(SiP^{iPr}_3)Fe(N_2)][Na(12\text{-crown-4})_2]$ (**5.4**),[5] $[(PhBP^{iPr}_3)Fe(N_2)][MgCl(THF)_2]$ (**5.5**),[6] $(Cy_2P(C_2H_4))_3PFe(N_2)$ (**5.6**),[7] and $(depe)_2Fe(N_2)$ (**5.7**)[8] ($depe = 1,2\text{-}(Et_2P)_2C_2H_4$) has been tested for N_2 reduction under the standard catalytic conditions used for **4.1** (Figure 5.1). Empirically, of the complexes studied, only species with flexible Fe-B interactions produce substantial quantities of NH_3 with both $[(TPB^{Cy})Fe(N_2)][Na(12\text{-crown-4})_2]$ and $[(TPB^{Ph})Fe(N_2)][Na(12\text{-crown-4})_2]$ serving as pre-catalysts. While these systems are not as efficient as the parent complex **4.1**, they nevertheless demonstrate that the ligand field supplied by the TPB ligands is beneficial for catalytic conversion of N_2 to NH_3. In

addition to these studies, further variations of the catalytic conditions for **4.1** including

solvent, reductant, acid, and temperature have been studied and suggest additional factors

that may be crucial for turnover.
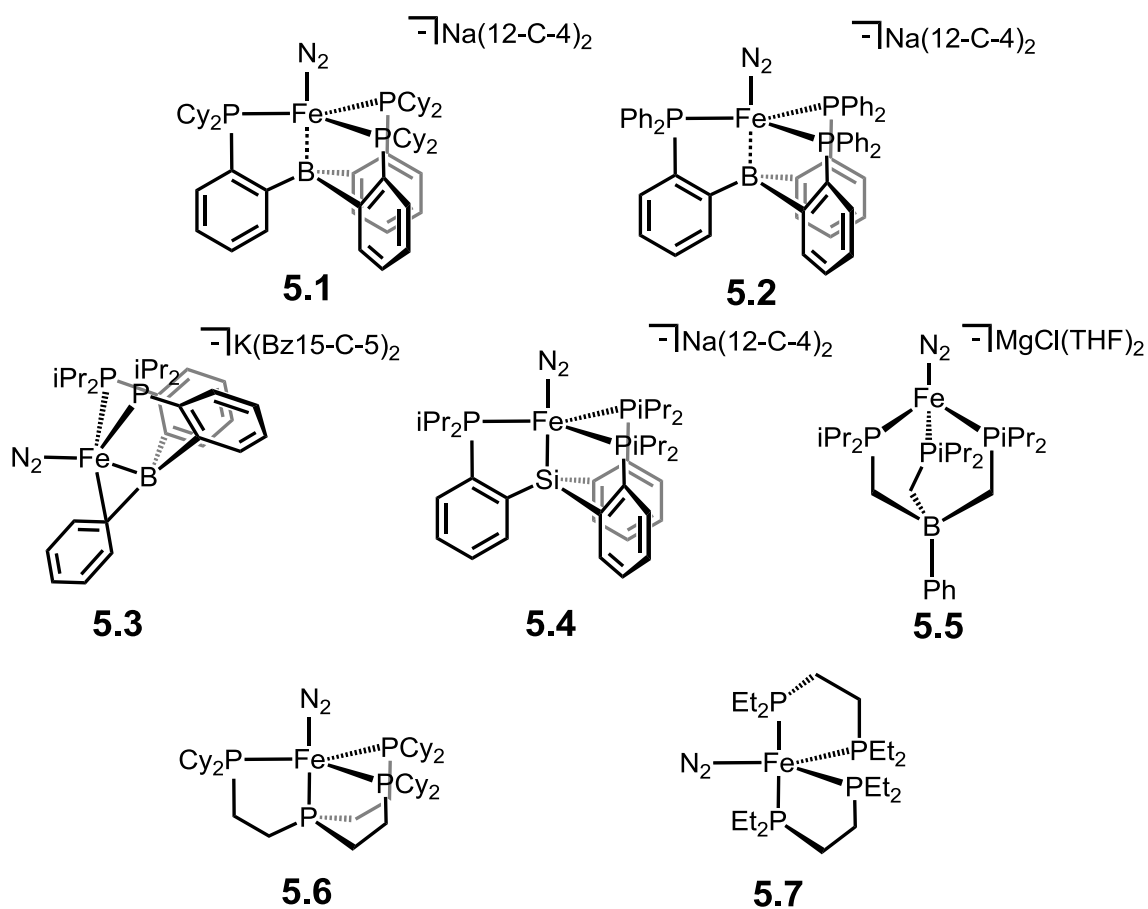
Figure 5.1. Complexes synthesized and studied towards N_2 reduction. Note that complexes **5.4**, **5.5**, **5.6**, and **5.7** have been previously reported in the literature (see references 5 (**5.4**), 3 (**5.5**), 4 (**5.6**), and 8 (**5.5**)).

5.2 Results and Discussion

5.2.1 Ligand and Complex Synthesis
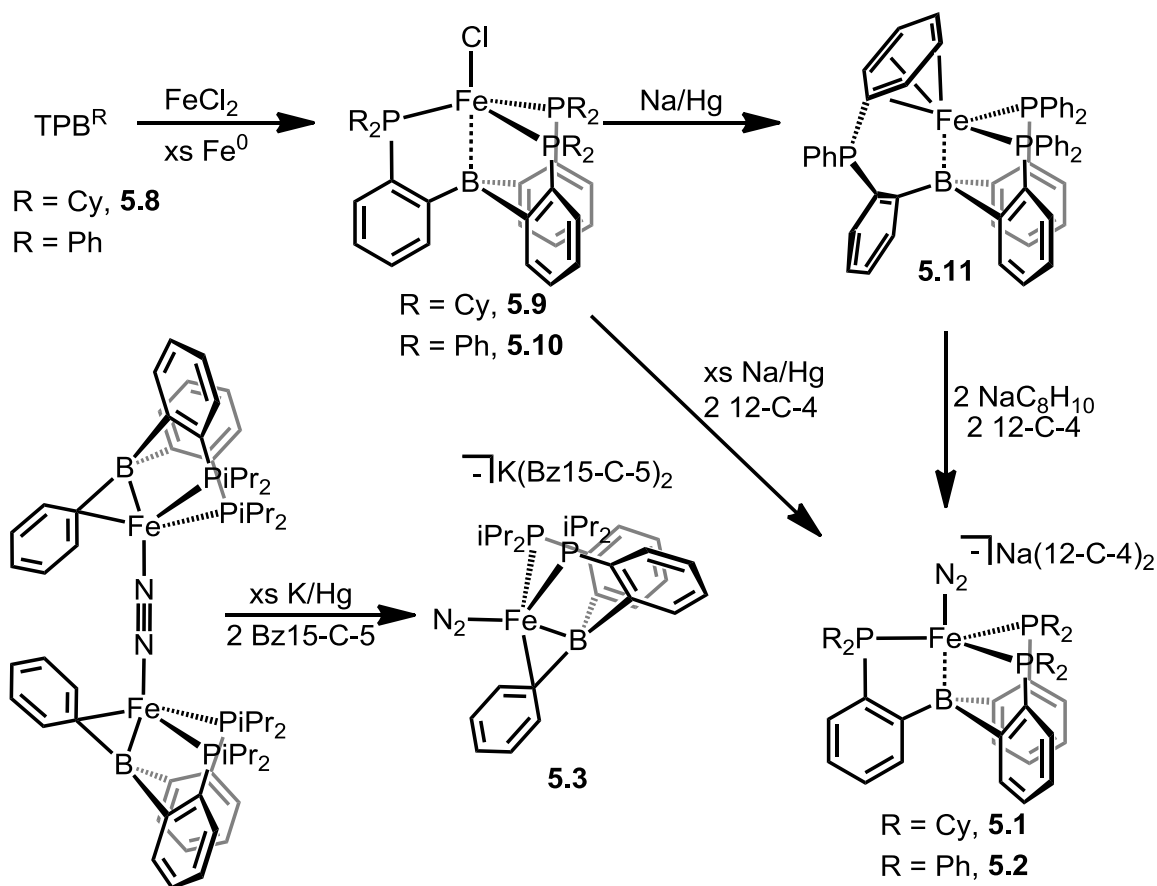
Scheme 5.1. Synthesis of complexes **5.1**, **5.2**, **5.3**, **5.8**, **5.9**, **5.10**, and **5.11**.

With the desire of investigating the structural features that enable catalytic turnover, several variations on the TPB ligand scaffold were targeted. To probe the effect of a larger steric profile of the ligand scaffold, a cyclohexyl based TPB^{Cy} scaffold was synthesized that would closely mimic the electronics of the TPB system while providing additional steric bulk. The previously reported[9] TPB^{Ph} ligand also serves as an obvious variation on TPB to test the effect of weaker phosphine donors.[10] Finally, the Peters lab recently reported the synthesis of Fe complexes of the previously reported PhB(o-iPr$_2$P(C$_6$H$_4$)$_2$ (DPB) ligand.[11,12] This DPB ligand ligates the Fe center through two

phosphine donors and replaces one phosphine donor of TPB with an interaction through a BPh unit. The DPB scaffold hence provides a larger variation on the TPB scaffold than the simple change in phosphine substituent.

The preparation of TPB^{Ph} has already been reported9 and the synthesis of TPB^{Cy} (**5.8**) involves the lithiation of o-Br(C$_6$H$_4$)PCy$_2$ and subsequent reaction with 1/3 of an equivalent of BCl$_3$ analogously to the preparation of TPB.[13] Metallation of these tris-phosphine ligands also proceeds in an analogous manner to that reported for (TPB)FeBr[17a] (Scheme 2) to yield the halides (TPB^{Cy})FeCl[14] (**5.9**) and (TPB^{Ph})FeCl (**5.10**), which are brown solids and possess $S = 3/2$ spin states as judged from their solution magnetic moments of $\mu_{eff} = 3.8$ and **4.0** μ_B respectively. Reduction of **5.9** with an excess of Na/Hg amalgam followed by addition of 12-crown-4 results in formation of **5.1** as a dark red $S = 1/2$ complex with a N-N stretch at 1901 cm^{-1}, very close to the reported value for **4.1** (1905 cm^{-1}), suggesting that the N$_2$ molecule is similarly activated in both of these complexes.

Reduction of **5.10** with one equivalent of Na/Hg does not result in the uptake of N$_2$ as is observed in the alkyl systems. Alternately, a diamagnetic species is obtained with ^{1}H NMR resonances shifted into the olefinic region. These shifted peaks suggest the possibility of an η^6 coordinated aryl ring, and XRD data (vide infra) confirm that one phosphine arm has dissociated and one of the phenyl groups attached to the phosphine is coordinated to the Fe center to give the bis-phosphino borane aryl complex (TPB$^{Ph'}$)Fe **5.11**.[14] Further reduction of **5.11** with NaC$_{10}$H$_8$ and addition of 12-crown-4 enables isolation of **5.2** as a red solid. Complex **5.2** similarly displays a strong N-N stretching vibration in the IR at 1988 cm^{-1} which occurs at substantially higher energy than that

found in **5.1** or **4.1**, reflecting the weaker donor ability of the tri-aryl phosphine donors

consistent with similar shifts that have been observed in (SiP$_3$) examples from the Peters

laboratory as well as in tetraphosphine FeN$_2$ adducts.[16a,15,]8 Finally, reduction of the

previously reported [(DPB)Fe]$_2$(μ-1,2-N$_2$) with an excess of K/Hg amalgam followed by

addition of benzo-15-crown-5 results in dark red **5.3**. The N-N stretch for complex **5.3** is

observed at 1935 cm^{-1}. This vibration suggests that the DPB scaffold still results in a

strongly activated N$_2$ despite the loss of one phosphine donor.

5.2.2 Structural Characterization

Complexes **5.1**, **5.3**, **5.9**, **5.10**, and **5.11** have been crystallographically

characterized and their structures are depicted in Figure 2. The halide complexes **5.9** and

5.10 display relatively similar geometries about Fe, with relatively long Fe-P bonds

consistent with other examples of formally Fe^I $S = 3/2$ Fe centers from related complexes

(Table 5.1).[17a] A trend in increasing Fe-P distances is observed upon moving from

complex **5.10** to (TPB)FeCl to **5.9**, potentially arising from the increasing steric demands

from the substituents on phosphorus (Table 5.1). The Fe-B distance in these halide

complexes is also quite long, likely indicating a minimal interaction between Fe and B.

The geometry about Fe, consistent with the long Fe-B distance, can best be described as

pseudo-trigonal bipyramidal, with a strong distortion towards tetrahedral with τ_4 values of

< 0.5 for all of the halide complexes.
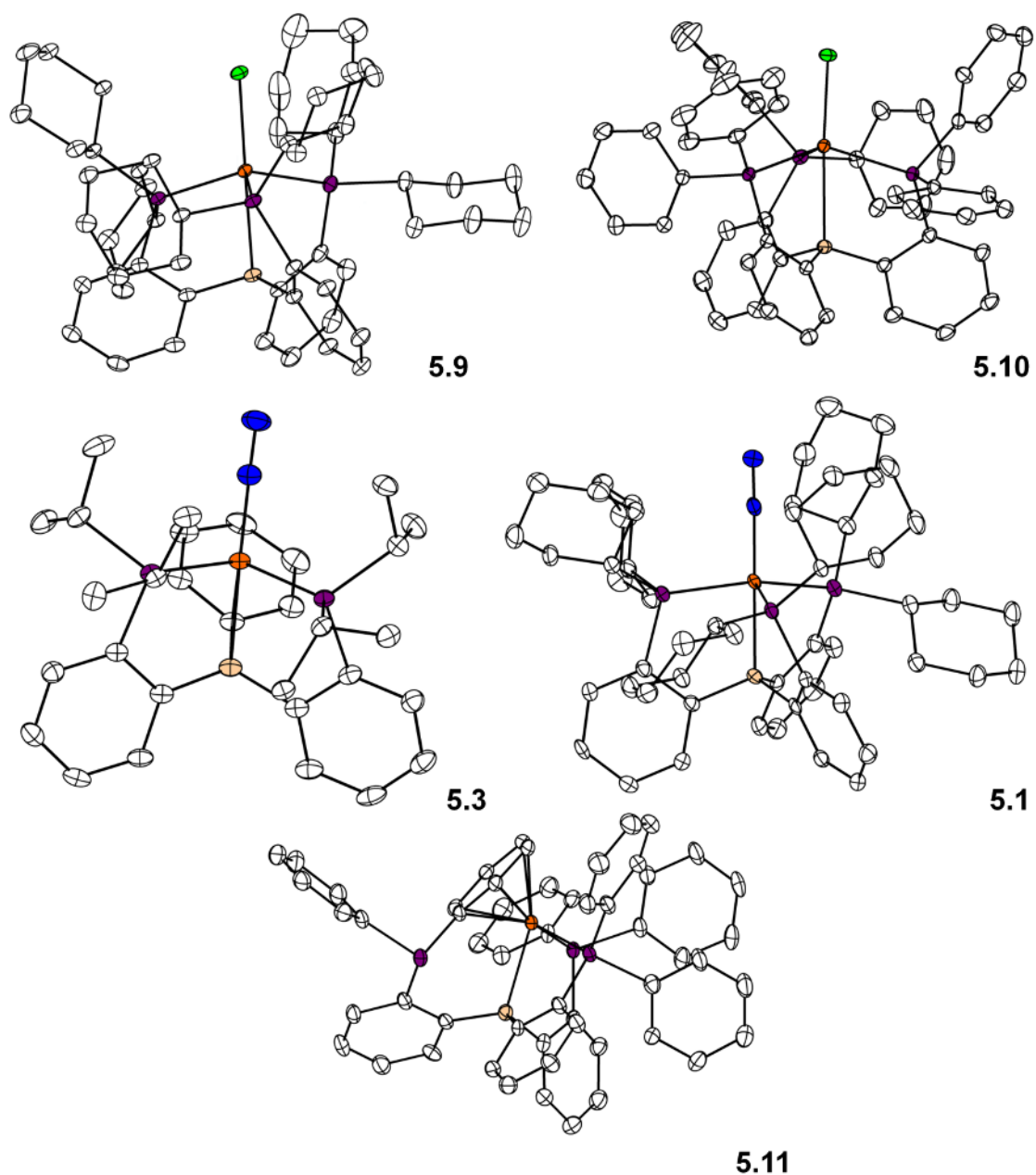
Figure 5.2. XRD structures of complexes **5.1**, **5.3**, **5.9**, **5.10**, and **5.11** with ellipsoids at 50% and hydrogens and counterions omitted for clarity. Fe atoms are shown in orange, P in purple, B in tan, Cl in green, and N in blue. See Table 5.1 for bonding metrics.

The assignment of **5.11** as an η^6 aryl adduct was confirmed by its XRD structure, which shows the Fe interacting with a phenyl ring and one phosphine arm dissociated from Fe (Fe-P > 3.5 Å). The Fe-C distances range from 2.095(3) Å to 2.172(3) Å, with the *ipso* carbon having the shortest distance and an Fe-centroid distance of 1.595 Å. The other two Fe-P distances are substantially shorter than those observed in the halide complexes, reflecting the diamagnetism of **5.11** (Table 5.1). Despite the other short Fe ligand bonds, the Fe-B distance of 2.457(4) Å remains long. The ΣC-B-C in **5.11**, however, shows a value of 334° compared with an average of 341° in complexes (TPB)FeCl, **5.9**, and **5.10**, indicating that the B is more pyramidalized in **10** and further suggesting that there is more donation to B in this complex than in the halide complexes.

Complex	Fe-X	Fe-B	Fe-P1	Fe-P2	Fe-P3	τ_4
5.1	1.792(3)	2.292(3)	2.3157(9)	2.2228(9)	2.2219(9)	0.60
5.3	1.792(2)	2.246(2)	2.2265(7)	2.2179(7)	-	-
5.9	2.296	2.429	2.456	2.419	2.390	0.39
5.10	2.2712(4)	2.5418(16)	2.3622(4)	2.3451(4)	2.3325(4)	0.33
5.11	-	2.457(4)	2.2466(10)	2.1846(9)	-	-

Table 5.1. Selected bond lengths (Å) and τ_4 values for complexes **5.1**, **5.3**, **5.9**, **5.10**, and **5.11**. Note that the values reported for **5.9** are the average of four molecules in the unit cell.

Although crystals of **5.2** suitable for XRD analysis could not be obtained, both complexes **5.1** and **5.3** were structurally characterized. Complex **5.3** shows a pseudo tetrahedral geometry about Fe, consistent with other DPB complexes,[12] and displays a strong Fe-C$_{ipso}$ interaction of 2.055(2) Å. In addition to the short Fe- C$_{ipso}$ there is a moderately shortened Fe-C$_{ortho}$ distance of 2.326(2) Å. The Fe-B distance of 2.246(2) Å **5.3** is also short when compared with other DPB complexes of Fe. All of these bond

metrics point to a strong interaction between the Fe center and the BCC unit in **5.3**, and this conclusion is supported by bond alteration in the bound Ph ring with two short C-C distances of 1.378(3) Å and 1.385(3) Å with the remainder of the C-C distances > 1.408 Å. Finally, the Fe-N distance of 1.792(2) Å and the N-N distance of 1.135(3) Å are comparable to the analogous distances from **4.1** of 1.781(2) and 1.144(3) Å, suggesting a slightly weaker degree of N_2 activation consistent with the IR data for these complexes.

Complex **5.1** is similar to [(TPB)Fe(N_2)][Na(12-crown-4)$_2$] in overall structure, as both complexes have pseudo-trigonal bipyramidal geometries with τ_4 values of 0.60 and 0.61 respectively. Both complexes possess one large P-Fe-P angle which is 136.21(3)° in **5.1** and 134.99(3)° in [(TPB)Fe(N_2)][Na(12-crown-4)$_2$]. Unlike the corresponding halide complexes **5.9** and (TPB)FeCl, which show longer Fe-P distances on average with cyclohexyl substituents, **5.1** displays very similar average Fe-P distances to [(TPB)Fe(N_2)][Na(12-crown-4)$_2$], with values of 2.254 and 2.251 Å respectively. The Fe-B distance is also essentially identical in both **5.1** and [(TPB)Fe(N_2)][Na(12-crown-4)$_2$] with a value of 2.292(3) Å in both complexes. Finally, **5.1** has an Fe-N distance of 1.792(3) Å and a N-N distance of 1.143(4) Å, very close to the values observed in [(TPB)Fe(N_2)][Na(12-crown-4)$_2$] and consistent with their similar vibrational features.

5.2.3 Comparison of Pre-Catalysts

With the above-mentioned complexes isolated and characterized, comparative studies of their efficacy as pre-catalysts were conducted. Specifically targeted were complexes **5.1**, **5.2**, and **5.3** as well as the previously reported phosphine N_2 complexes **5.4**, **5.5**, **5.6** and **5.7**. The results from these studies are summarized in Table 5.2. While

none of the investigated catalysts outperform the original system featuring **4.1** as a pre-catalyst (7 eq. NH_3/Fe), several trends relevant to catalysis become apparent. Most notably, the only complexes that are competent for catalytic turnover within this study, that is, complexes that can on average produce > 2 eq. NH_3/Fe, bear a great deal of structural similarity to **4.1**. Specifically, of the new complexes, **5.1** differs from **4.1** only in a slightly larger steric profile on the phosphine substituents and is otherwise very similar, which is manifested in the similar ν_{NN} frequencies and bond metrics for these two species. While **5.1** is a competent pre-catalyst for N_2 reduction, producing 3.2 equivalents of NH_3 per Fe (Table 5.2, entry 1), it is less active than **4.1**, suggesting a negative effect of the larger steric profile of the TPB^{Cy} ligand.

Complex **5.2** also serves as a pre-catalyst for N_2 reduction under these standard conditions, albeit only nominally. While the Ph substituted ligand scaffold has substantially different electronic properties that the iPr or Cy systems, the fact that it can still mediate catalysis suggests that the tris-phosphine borane ligand set common to all three catalysts is critical to enable catalytic turnover. Another potentially mechanistic observation arises from the Ph system. Because this scaffold preferentially binds an arene ring over N_2 in its Fe(0) state, there is no evidence for an Fe(0) N_2 adduct with this system. The fact that catalysis is still observed might suggest that an Fe(0) N_2 adduct is not required for catalysis. This conclusion is further supported by the lower observed turnover number when (TPB)Fe(N_2) is utilized as a precatalyst (Chapter 4).

In contrast to the TPB based complexes, the DPB based **5.3** does not produce > 2 eq. of NH_3/Fe on average, although it does produce substantial quantities of NH_3. Even though **5.3** activates N_2 more strongly than **5.2**, as evidenced by the IR spectra of these

two complexes, the fact that **5.3** produces less NH_3 again suggests the importance of the

tris-phosphine borane scaffold. Additionally, the DPB scaffold might be expected to be

more labile than the TPB scaffold due to the weaker coordinating ability of the BPh unit.

If the catalysis is indeed mediated by a molecular species, this lability may compromise

the stability of the species towards decomposition and explain the diminished capability

of **5.3** for catalysis. Furthermore, the fact that **5.3** performs more poorly than **5.1** or **5.2**

suggests that such a pathway is not beneficial for catalysis, circumstantially supporting

the agency of a molecular species versus some heterogeneous species derived from

decomposition.

Entry	Complex	NH_3 eq./Fe
5.1	$[(TPB^{Cy})Fe(N_2)][Na(12\text{-crown-}4)_2]$	3.2
5.2	$[(TPB^{Ph})Fe(N_2)][Na(12\text{-crown-}4)_2]$	2.2
5.3	$[(DPB)Fe(N_2)][K(Bz15\text{-crown-}5)_2]$	1.7
5.4	$[(SiP^{iPr}_3)Fe(N_2)][Na(12\text{-crown-}4)_2]$	0.7
5.5	$[(PhBP^{iPr}_3)Fe(N_2)][MgCl(THF)_2]$	1.2
5.6	$(C_2H_4PCy_2)_3PFe(N_2)$	0.7
5.7	$(depe)_2Fe(N_2)$	0.4

Table 5.2. N_2 reduction with phosphine Fe complexes. All data shown as an average of

at least 3 runs (see Appendix 4) using the conditions described in the experimental

section.

Complex **5.4** provides an interesting comparison to the original catalytic system

with **4.1** in that the two complexes are isostructural, with the only difference being a

substitution of a Si atom for the B atom of the TPB ligand. While there are certainly

electronic differences to consider, one of the most striking differences between these two

systems involves the flexibility of the Fe-Si or Fe-B bond. The Fe-Si bond in $(SiP_3)Fe$

complexes is quite rigid, with little variation in distance over a number of complexes.[5,16]

This inflexibility strongly contrasts with the TPB system, where large variations in the Fe-B distance take place to accommodate geometric and electronic changes at the Fe center.[17] The fact that complex **5.4** is not a competent catalyst for N_2 reduction while **4.1** is further implies that the flexible linkage in the TPB system may be important for catalysis.

Similarly, the tris-phosphino borate ligated complex **5.5** produces a sub-stoichiometric amount of NH_3, which is again consistent with the empirical observation of a need for a hemi-labile interaction between the Fe and the apical B. Interestingly, in the tetraphosphine complex **5.6** there exists, in principle, the possibility of a hemi-labile interaction with the apical P atom of the ligand scaffold. The low yields of NH_3 for this system when compared with the other entries in Table 5.2 suggest that if any flexibility of the Fe-P bond exists, it does not enable catalysis in this system. Finally, complex **5.7** was subjected to the standard catalytic conditions to test a different tetra-phosphine complex but also did not exhibit catalytic NH_3 formation. Similar Fe phosphine complexes had been tested for NH_3 formation previously and had shown only ~ 10% of an equivalent of NH_3 per Fe.[18] While it is difficult to draw definite comparisons, the higher yields observed here may be reflective of the conditions used for catalysis in this study.

5.2.4 Comparison of Catalytic Conditions

In an effort to further explore the effect of variations on the standard catalytic conditions previously reported, several additional reaction variables were tested for catalysis. The first condition investigated was changing the solvent from Et_2O. As entries 1-5 in Table 5.3 illustrate, the solvent scope for catalysis is limited to relatively non-polar

ethereal solvents. Unsurprisingly, iPr$_2$O serves equally well as Et$_2$O in the reaction, but

moving to a more polar solvent in DME results in a drop in NH$_3$ yield. Furthermore, the

presence of some ethereal solvent is critical, likely due to solubility of the HBAr$^F_4 \cdot$ 2

Et$_2$O acid, as is evidenced by the low yields of NH$_3$ in toluene (entry 4) compared with

much higher yields when even a small amount of Et$_2$O is included in the reaction mixture

(entry 5). The lower yield of NH$_3$ in Bu$_2$O is likely similarly explained by lowered

solubility of HBAr$^F_4 \cdot$ 2 Et$_2$O. The requirement for an ethereal solvent likely stems from

the need for good solubility of the acid and any BAr$^F_4{}^-$ ions. Additionally, it is not clear

whether KC$_8$ will be thermodynamically or kinetically suitable to form **4.1** in less polar

solvents such as toluene. Conversely, the lowered activities in more polar ethers likely

result from accelerated H$_2$ formation.

Entry	Solvent	NH$_3$ eq./Fe
1	iPr$_2$O	6.53
2	DME	3.37
3	Bu$_2$O	3.16
4	Toluene	0.78
5	1:6 Et$_2$O:Toluene	3.12

Table 5.3. Effect of different solvents on the catalytic reduction of N$_2$ to NH$_3$ by complex

4.1. Note that all reported values are an average of at least 2 runs (See Appendix 4).

Aside from solvent, the reaction is quite sensitive to the choice of reductant

(Table 5.4). The use of weaker reducing agents such as Cp$^*_2$Co or Cp$^*_2$Cr results in very

low yields of NH$_3$. It is unclear whether this is a reflection of the need for a reducing

agent strong enough to generate [(TPB)Fe(N$_2$)]$^-$ or whether the potentially higher

solubility of these reagents increases side reactions with the acid. The higher yields

obtained with NaC$_{10}$H$_8$ (entry 3), which should be a strong and soluble reductant, suggest

that the potentials of the reductants in entries 1 and 2 do hinder the reactivity. The use of

K metal or $MgC_{14}H_{10}$ also leads to low yields of NH_3. Finally, although other evidence

supports the presence of a molecular catalyst, some sort of graphite bound complex as the

catalytically active species cannot be ruled out. Entry 6 illustrates that Na/Hg is also

competent for catalysis, albeit only nominally, suggesting that graphite is not an essential

component of the reaction mixture and further supporting the homogeneity of the

catalyst.

Entry	Reductant	NH_3 eq./Fe
1	Cp^*_2Co	0.6
2	Cp^*_2Cr	<0.2
3	$NaC_{10}H_8$	1.0
4	K metal	0.4
5	$MgC_{14}H_{10} \cdot 3$ THF	0.3
6	Na/Hg	2.1

Table 5.4. Effect of different reductants on the catalytic reduction of N_2 to NH_3 by

complex 4.1. Note that all reported values are an average of at least 2 runs (See

Appendix 4). Note that the Na/Hg was 10% Na by weight.

A number of different acids were tested in the catalysis with the results shown in

Table 5.5. The use of $HBAr^F_4 \cdot 2$ Et_2O in the standard catalytic runs was chosen due to

its high acidity and the poor coordinating ability of the $BAr^F_4{}^-$ counterion. Other strong

acids, with potentially better coordinating counterions in HOTf and HCl, showed very

low yields of NH_3 (entries 1 and 2). The use of a weaker acid in [Lutidinium][BAr^F_4]

also showed very low yields of NH_3. Interestingly, the use of a slightly stronger acid in

[2,6-dimethylanilinium][OTf] or [2,6-dimethylanilinium][BAr^F_4] resulted in catalytic

turnover. This result is somewhat surprising, as the pK_a of [Lutidinium] is 6.77 versus

3.95 for [2,6-dimethylanilinium].[19,20] The cause for the disparity in activity between

these two acids is unclear, but could potentially arise from different redox properties

between anilinium and pyridinium acids. Alternately, the relatively narrow pK_a range

between these acids could bracket the acidity required for one of the catalytic steps. The

last observation of note is that the two anilinium acids in entries 4 and 5 show similar

activity despite having different counterions, which seems to suggest that the difference

between $[OTf]^-$ and $[BAr^F_4]^-$ is not significant for catalysis.

Entry	Acid	NH₃ eq./Fe
1	HOTf	0.4
2	HCl	<0.1
3	[Lutidinium][BAr$^F_4$]	<0.1
4	[2,6-dimethylanilinium][OTf]	2.1
5	[2,6-dimethylanilinium][BAr$^F_4$]	2.9

Table 5.5. Effect of different acids on the catalytic reduction of N_2 to NH_3 by complex

4.1. Note that all reported values are an average of at least 2 runs (See Appendix 4).

Note that [2,6-dimethylanilinium][BAr$^F_4$] was obtained as a 1.5 Et$_2$O adduct.

Finally, while the initial reaction screening was carried out at -78 °C, it was

desirable to determine whether low temperature was a prerequisite for NH_3 formation, or

whether higher temperatures could still be viable for N_2 reduction. In this context, the

catalysis was tested at -110 and 25 °C. The reduced yield of 1.33 equivalents of NH_3 per

Fe at RT illustrates that NH_3 yields are drastically reduced at higher temperatures and that

cooling of the reaction is necessary. Interestingly, the catalysis is still viable at

temperatures as low as -110 °C with a yield of 5.40 equivalents of NH_3 per Fe. Although

it will be difficult to exclude the possibility that reaction only occurs upon warming the

solution, the conversion of the bronze color of KC_8 to black graphite in the cold reaction

mixture suggests reaction at these temperatures may be occurring. Furthermore, attempts

to quench the catalysis at low temperature with either [TBA][CN] or with *t*-BuNC have resulted in diminished, but still substantial yields of NH_3, suggesting that catalysis is occurring at low temperature.

5.3 Conclusions

These combined studies varying both the pre-catalyst and the reaction conditions for the Fe-mediated reduction of N_2 to NH_3 provide several key insights on the catalysis. Firstly, all evidence still supports the agency of a molecular species. While a heterogeneous process will be difficult to completely exclude, the narrow range of viable pre-catalysts and the observation that other reduced Fe phosphine complexes are not competent for catalysis suggest that decomposition to a heterogeneous catalyst is unlikely. Furthermore, the catalysis is sensitive to even small variations in the substituents on the phosphine arms, suggesting the possibility of finding substituents that would improve catalysis. Such an observation is not completely surprising, as a similar dependence has been observed in both the of the previously reported Mo systems.[21,22] Finally, the flexible Fe-B linkage in the TPB scaffold is empirically required for catalysis, at least among the complexes studied herein. Although recent results suggest that other ligand scaffolds with a carbon atom in the axial position are viable for catalysis, it is unclear in this system whether a flexible interaction is operative in this system and further studies will need to be performed to determine the role of the carbon atom.[23] The apparent requirement for a flexible Fe-B interaction in the systems studied here parallels the hypothesis that a flexible Fe-C interaction in nitrogenase is involved in catalysis.

Furthermore, the catalysis is also strongly dependent on the catalytic conditions employed. While all of the conditions surveyed showed a decrease in catalytic activity relative to the original results with **4.1**, several variations on the reaction conditions did preserve catalytic activity, suggesting some features required for catalysis. For example, only relatively non-polar ethereal solvents appear to be compatible with catalysis, likely due to the respective solubility of the acid and insolubility of the reductant in these solvents. It was also shown that catalysis is still viable with Na/Hg as the reductant, suggesting that a graphite adsorbed complex is not crucial for the catalytic turnover. Anilinium acids are also compatible with catalysis while lutidinium acids are not. This observation raises interesting questions on what difference between these two acids leads to activity. Finally, the catalysis must be performed at low temperature and also seems to be active at temperatures as low as -110 °C, suggesting unusually high activity for this system. Taken together, the studies presented here begin to delineate the conditions and structures that are required for catalysis.

5.4 Experimental Section

5.4.1 General Considerations

Unless otherwise noted, all compounds were purchased from commercial sources and used without further purification. Complexes **5.4**,[5] **5.5**,[6] **5.6**,[7] and **5.7**[8] as well as $[(TPB)Fe(N_2)][Na(12\text{-crown-}4)_2]$,[17] $[(DPB)Fe]_2(\mu\text{-}1,2\text{-}N_2)$,[12] $MgC_{14}H_{10}$,[24] TPB^{Ph},[13] 2-$Cy_2PC_6H_4Br$,[25] and $HBAr^F_4 \cdot 2\ Et_2O$[26] were prepared according to literature procedures. All manipulations were carried out under a N_2 atmosphere utilizing standard glovebox or Schlenk techniques. Solvents were dried and de-oxygenated by an argon sparge, followed

by passage through an activated alumina column purchased from S.G. Waters Company. Solvents for catalytic runs were additionally stirred for more than 2 hours over Na/K alloy and then filtered prior to use.

IR spectra were obtained via KBr pellets on a Bio-Rad Excalibur FTS 3000 spectrometer using Varian Resolutions Pro software set at 4 cm^{-1} resolution. Alternately, IR spectra were obtained on a Bruker Alpha Diamond ATR spectrometer on solid samples. NMR measurements were obtained on Varian 300 MHz or 500 MHz spectrometers. Deuterated solvents for these measurements were obtained from Cambridge Isotope Laboratories and were dried and degassed prior to use. All ^{1}H NMR spectra were referenced to residual solvent peaks, while ^{31}P NMR measurements were referenced to an external standard of H_3PO_4 and ^{11}B NMR spectra were referenced to an external standard of $Et_2O \cdot BF_3$. UV-Visible spectra were taken on a Cary 50 spectrometer from 1100 nm to 200 nm in the fast scan mode. Samples were prepared in a 1 cm path length quartz cuvette in the solvent indicated below. All samples had a blank sample background subtraction applied.

XRD data were obtained at low temperatures on a Siemens or Bruker Platform three-circle diffractometer coupled to a Bruker-AXS Smart Apex CCD detector with graphite-monochromated Mo Kα radiation ($\lambda = 0.71073$), performing φ-and ω-scans. All structures were solved by standard direct or Patterson methods and refined against F^2 using the SHELX program package.[27,28,29] All atoms, with the exception of hydrogens, were anisotropically refined. All hydrogen atoms were included via a standard riding model.

5.4.3 Synthesis

Synthesis of TPB^{Cy}, 5.8. A schlenk tube with a stir bar was filled with a solution of 2-
dicyclohexylphosphinebromobenzene (1.000 g, 2.830 mmol) in toluene (10 mL) and
sealed. The schlenk tube was then hooked up to a schlenk line under a stream of N_2 and
the Teflon stopper of the schlenk tube was replaced with a rubber septum. The reaction
vessel was then cooled to -78 °C. A 1.6 M solution of n-BuLi in hexane (1.77 mL, 2.830
mmol) was then slowly added via syringe. The resulting solution turned slightly orange
while stirring for 15 min at -78 °C. The solution was then warmed to ambient
temperature and stirred for an additional hour before being cooled back to -78 °C. At this
time a 1 M solution of BCl_3 in heptane (0.92 mL, 0.920 mmol) was added to the stirring
reaction vessel. The pale orange color of the solution lightened slightly upon addition of
the BCl_3. The septa was exchanged with a Teflon stopcock and the solution was allowed
to stir at -78 °C for 1 hour before being warmed to RT and stirred for an additional 2
hours, during which time a brown color developed in the solution. The mixture was then
heated to 90 °C for 16 hours, during which time the brown color lightened to orange and
solids precipitated. Solvent was removed *in vacuo* and the remaining waxy solid was
extracted 3x with Et_2O (10 mL) and filtered. The remaining pale orange solution was
concentrated to half volume and cooled to -35 °C for 16 hours, which resulted in the
formation of white crystals of the title compound (0.426 g, 0.513 mmol, 55%). ^{1}H NMR
(C_6D_6, δ): 8.30 (br s, 4H), 7.46 (br s, 4H), 7.24 (br s, 2H), 7.18 (m, 2H), 1.93 (br m, 12H),
1.71 (br m, 12H), 1.63 (br s, 12H), 1.36 (br s, 8H), 1.17 (br m, 22H). ^{31}P{^{1}H} NMR
(C_6D_6, δ): -2.54 (br s). ^{11}B{^{1}H} NMR (C_6D_6, δ): 25.1 (vbr s). ^{13}C{^{1}H} NMR (C_6D_6, δ):

159.69 (br s), 136.12 (br s), 131.97 (s), 127.30 (s), 35.83 (s), 31.29 (br s), 30.27 (s), 27.86 (d, J = 20 Hz), 27.01 (s).

Synthesis of (TPB^{Cy})FeCl, 5.9. A mixture of $FeCl_2$ (0.076 g, 0.60 mmol), **7** (0.500 g, 0.60 mmol), Fe powder (0.333 g, 6.02 mmol), and THF (10 mL) was heated to 90 °C in a sealed schlenk tube under vigorous stirring for 3 days, during which time the color of the liquid phase turned from pale yellow to brown. The solids were removed from the mixture by filtration, and the solvent was removed *in vacuo*. The brown residue was then triturated, extracted with pentane (200 mL), and filtered through celite to give a brown solution. Solvent evaporation *in vacuo* afforded the product as a greenish brown powder (0.460 g, 83%). An analytically pure sample and crystals suitable for XRD analysis were obtained by slow concentration of a saturated pentane solution. ^{1}H NMR (C_6D_6, δ): 81.73 (br s), 36.11 (s), 25.66 (s), 17.64 (br s), 5.01 (s), 3.77 (br s), 1.84 (s), 1.57 (br s), 0.13 (s), -0.13 (s), -0.58 (s), −0.75 (sh), -1.54 (s), -1.98 (br s), -3.87 (br s), -5.91 (br s), -7.12 (br s), -23.01 (s). UV-vis (THF, nm {cm^{-1} M^{-1}}): 560 {130}, 750 {100}, 950 {150}. μ_{eff} (C_6D_6, Evans method, 20 °C): 3.8 μ_B. Anal. calcd. for $C_{54}H_{78}BClFeP_3$: C 70.33 , H 8.52; found: C 70.45, H 8.49.

Synthesis of (TPB^{Ph})FeCl, 5.10. A Schlenk tube was charged with TPB^{Ph} (0.923 g, 1.240 mmol), $FeCl_2$ (0.198 g, 1.560 mmol), Fe powder (0.176 g, 3.160 mmol), and THF (50 mL). The reaction was stirred vigorously for 3 days at 70 °C, during which time the slurry turned dark brown. The mixture was filtered through celite to remove the excess iron powder and the volatiles removed *in vacuo*. The residual solids were triturated with toluene, slurried in CH_2Cl_2, and filtered to collect a dark brown powder (0.841 g, 76%). Crystals suitable for X-ray analysis were grown by slow concentration of a C_6H_6 solution.

^{1}H NMR (d_8-THF, δ): 34.23, 23.91, 9.89, 7.30, 4.73, 2.31, -23.84. $μ_{eff}$ (d_8-THF, Evans method, 25 °C): 4.0 $μ_B$. We were unable to obtain satisfactory elemental analysis.

Synthesis of (TPB$^{Ph'}$)Fe, 5.11. Sodium (0.003 g, 0.148 mmol) and mercury (0.500 g) were stirred vigorously with C_6H_6 (1 mL). A slurry of (TPB^{Ph})FeCl (0.095 g, 0.107 mmol) in C_6H_6 (10 mL) was added and the reaction mixture stirred for 6 hours at RT. The resulting dark red mixture was filtered and lyophilized (0.080 g, 88%). Crystals suitable for X-ray analysis were grown by vapor diffusion of diethyl ether into a concentrated THF solution at -35 °C. ^{1}H NMR (C_6D_6, δ): 8.38 (t, J = 8.4 Hz, 2H), 7.94 (d, J = 7.4 Hz, 1H), 7.85 (t, J = 7.3 Hz, 2H), 7.59 (ddt, J = 9.6, 7.3, 3.1 Hz, 4H), 7.41 (d, J = 7.5 Hz, 1H), 7.31-7.17 (m, 6H), 7.09-6.79 (m, 12H), 6.73 (dd, J = 4.4, 2.6 Hz, 3H), 6.60 (t, J = 8.6 Hz, 2H), 6.54-6.42 (m, 2H), 6.33-6.15 (m, 2H), 6.04 (t, J = 5.9 Hz, 1H), 4.42 (q, J = 6.7 Hz, 1H), 4.16 (q, J = 5.6 Hz, 1H), 3.89 (d, J = 6.1 Hz, 1H), 3.62 (q, J = 6.6 Hz, 1H). ^{13}C{^{1}H} NMR (C_6D_6, δ): 160.5 (s), 145.7 (d, J = 7.0 Hz), 144.1 (s), 143.8 (s), 142.9 (s), 142.5 (s), 141.9 (s), 141.5 (s), 140.9 (s), 140.6 (s), 139.8 (s), 139.7 (s), 137.7 (s), 137.4 (s), 136.0 (d, J = 10.8 Hz), 135.6 (s), 135.2 (m), 134.8 (s), 134.6 (s), 132.9 (m), 132.3 (d, J = 8.7 Hz), 132.0 (d, J = 7.3 Hz), 130.9 (m), 129.2 (s), 129.0 (s), 128.7 (s), 126.9 (m), 126.3 (d, J = 8.7 Hz), 125.9 (s), 124.3 (s), 123.8 (d, J = 6.6 Hz), 123.6 (d, J = 6.5 Hz), 109.2 (d, J = 15.7 Hz), 94.0 (d, J = 14.3 Hz), 88.6 (s), 87.0 (s), 85.8 (s), 85.5 (m). ^{31}P{^{1}H} NMR (C_6D_6, δ): 86.1 (d, J = 81.8 Hz), 69.8 (d, J = 82.2 Hz), -12.1 (s). ^{11}B{^{1}H} (C_6D_6, δ): 15.9. Anal. calcd. for $C_{54}H_{42}BFeP_3$: C, 76.26; H, 4.98. Found: C, 76.69; H, 5.59.

Synthesis of [(TPB^{Cy})Fe(N$_2$)][Na(12-crown-4)$_2$], 5.1. Sodium (0.030 g, 1.304 mmol) and mercury (1.0 g) were mixed in a vial with a stir bar. Complex **8** (0.137 g, 0.150

mmol) was dissolved in THF (10 mL) and added to the freshly prepared Na/Hg amalgam.
The resulting mixture was vigorously stirred for 1 hour during which time the color of the
solution changed from dark brown to a deep red. The solution was then filtered through
celite and volatiles were removed *in vacuo* to yield a red residue. This residue was taken
up in Et_2O (10 mL) and again filtered through celite to provide a dark red solution. 12-
crown-4 (0.052 g, 0.297 mmol) was added and the resulting solution was allowed to sit,
over which time the product precipitated as red crystals. ^{1}H NMR (THF-d_8, δ): 18.83
(vbr s), 12.50 (br s), 10.02 (s), 8.01 (vbr s), 7.88 (br s), 5.92 (br s), 5.51 (br s), 4.25 (br s),
3.80 (s, [Na(12-crown-4)$_2$]), 2.15 (br s), 1.66 (br s), 1.51 (br s), 0.97 (vbr s), 0.58 (br s),
0.31 (br s), 0.07 (br s), -1.11 (sh), -3.66 (vbr s). IR (ATR, solid): v_{NN}= 1905 cm^{-1}. UV-vis
(THF, nm {cm^{-1} M^{-1}}): 500 {sh}, 850 {40}. μ_{eff} (THF-d_8, Evans method, 20 °C): 1.6 μ_B.
Anal. calcd. for $C_{70}H_{110}BFeN_2NaO_8P_3$: C 65.16 , H 8.59, N 2.17; found: C 64.89, H 8.57,
N 2.21.

Synthesis of [(TPB^{Ph})Fe(N$_2$)][Na(12-crown-4)$_2$], 5.2. Naphthalene (0.005 g, 0.039
mmol) was weighed into a vial with Na (0.01 g, 0.435 mmol), THF (2 mL) and a stir bar.
The resulting mixture was then vigorously stirred for 2 hours over which time the liquid
phase became dark green. The resulting solution of $NaC_{10}H_8$ was then filtered through a
glass fiber filter paper into a -35 °C solution of **10** (0.030 g, 0.035 mmol) in THF (2 mL),
which rapidly changed color from orange to dark red. The resulting solution was stirred
for an additional 10 minutes before volatiles were removed. The dark red residue was
washed 3x with pentane (2 mL) and then extracted into Et_2O (10 mL) and filtered
through celite. The resulting red solution was then treated with 12-crown-4 (0.013 g,
0.074 mmol) and a fine red powder immediately precipitated. The mixture was allowed

to stand for 1 hour before the supernatant was decanted and the resulting red solids were washed 3x with Et_2O (2 mL) to yield the title compound as a red powder (0.029 g, 66%). ^{1}H NMR (THF-d_8, δ): 11.63 (br s), 9.77 (br s), 8.67 (s), 6.97 (vbr s), 6.04 (sh), 3.67 (s, [Na(12-crown-4)$_2$]), 0.35 (vbr s), -0.06 (s), -0.81 (vbr s). IR (ATR, solid): ν_{NN} = 1988 cm^{-1}. UV-vis (THF, nm {cm^{-1} M^{-1}}): 500 {sh}. μ_{eff} (THF-d_8, Evans method, 20 °C): 1.7 μ_B. Complex **2** is unstable to prolonged vacuum which precluded satisfactory combustion analysis.

Synthesis of [(DPB)Fe(N$_2$)][K(benzo-15-crown-5)$_2$], 5.3. A solution of [(DPB)Fe]$_2$(μ-1,2-N$_2$) (0.025 g, 0.023 mmol) and K/Hg amalgam (1 g, 1% K by weight) in THF (1 mL) was stirred at RT for 4 hr. The dark red solution was decanted and filtered through glass fiber filter paper onto solid benzo-15-crown-5 (0.026 g, 0.098 mmol). Solvent was removed *in vacuo* and the resulting solids were washed 3x with Et_2O (1 mL) and C_6H_6 (3 x 1 mL) to give dark solids of **3** (0.048 g, 0.042 mmol, 90%). Single crystals were grown by layering a THF solution with Et_2O and pentane. ^{1}H NMR (THF-d_8, δ) 14.50, 12.05, 6.86 (crown), 6.73 (crown), 3.85 (crown), 3.72 (crown), 2.80, 1.01, -2.72, -4.78. IR (ATR, thin film): ν_{NN} = 1935 cm^{-1}. Anal. calcd. for $C_{58}H_{81}BFeKN_2O_{10}P_2$: C 61.43, H 7.20, N 2.47; found: C 60.09, H 7.33, N 1.71.

Synthesis of [2,6-dimethylanilinium][OTf]. 2,6-dimethylaniline (0.500 g, 4.1 mmol) was dissolved in pentane (10 mL). This solution was then cooled to -35 °C before HOTf (0.619 g, 4.1 mmol) was added to the solution with stirring. Upon addition of HOTf, white precipitate formed, and the resulting suspension was allowed to warm to RT and was stirred for 1 hour. After this time, the solids were allowed to settle before the supernatant was decanted off. The solids were then dried under vacuum and

subsequently washed 3x with pentane (5 mL) and 3x with Et$_2$O (5 mL) to yield the title

compound as a white powder (0.894 g, 3.30 mmol, 80%). ^{1}H NMR (10:1 CDCl$_3$:DMSO-

d_6, δ) 7.06 (vbr s), 6.84 (m, 3H), 2.14 (s, 6H).

Synthesis of [2,6-dimethylanilinium][BAr$^F_4$] · 1.5 Et$_2$O. 2,6-dimethylaniline (0.036 g,

0.296 mmol) was dissolved in Et$_2$O (3 mL). To this was added a solution of HBAr$^F_4$ · 2

Et$_2$O (0.300 g, 0.296 mmol) in Et$_2$O (3 mL) and the resulting clear solution was allowed

to stir for 1 hour. After this time, the solution was concentrated to 3 mL and layered with

pentane (3 mL) and cooled to -35 °C for 3 days, over which time white crystals of the

product formed (0.200 g, 0.182 mmol, 62%). ^{1}H NMR (C$_6$D$_6$, δ) 8.60 (br s, 3H), 8.24 (s,

8H), 7.64 (s, 4H), 6.88 (m, 1H), 6.75 (m, 2H), 3.26 (q, J = 7 Hz, 6H), 1.91 (s, 6H), 1.09

(t, J = 7 Hz, 8H).

5.4.3 Catalytic Protocols

Variations on the standard catalytic conditions were performed with the

procedures described below. The protocol for the standard catalytic runs can be found in

chapter 4. Ammonia collection and quantification was also performed as previously

described in chapter 4.[30] All data for individual runs can be found in Appendix 4.

Runs with [(TPB^{Cy})Fe(N$_2$)][Na(12-crown-4)$_2$] (5.1) as precursor. The procedure was

identical to that of the standard catalytic protocol with the changes noted. The precursor

used was [(TPB^{Cy})Fe(N$_2$)][Na(12-crown-4)$_2$] (2.5 mg, 0.002 mmol), which is a dark red

solid.

Runs with [(TPB^{Ph})Fe(N$_2$)][Na(12-crown-4)$_2$] (5.2) as precursor. The procedure was

identical to that of the standard catalytic protocol with the changes noted. The precursor

used was [(TPB^{Ph})Fe(N$_2$)][Na(12-crown-4)$_2$] (2.5 mg, 0.002 mmol), which is a dark red solid.

Runs with [(DPB)Fe(N$_2$)][K(Bz15-crown-5)$_2$] (5.3) as precursor. The procedure was identical to that of the standard catalytic protocol with the changes noted. The precursor used was [(TPB^{Ph})Fe(N$_2$)][Na(12-crown-4)$_2$] (2.3 mg, 0.002 mmol), which is a dark red solid.

Runs with [(SiP^{iPr}$_3$)Fe(N$_2$)][Na(12-crown-4)$_2$] (5.4) as precursor. The procedure was identical to that of the standard catalytic protocol with the changes noted. The precursor used was [(SiP^{iPr}$_3$)Fe(N$_2$)][Na(12-crown-4)$_2$] (2 mg, 0.002 mmol), which is a dark purple solid.

Runs with [(PhBP^{iPr}$_3$)Fe(N$_2$)][MgCl(THF)$_2$] (5.5) as precursor. The procedure was identical to that of the standard catalytic protocol with the changes noted. The precursor used was [(PhBP^{iPr}$_3$)Fe(N$_2$)][MgCl(THF)$_2$] (1.4 mg, 0.002 mmol), which is a brown solid. Note that the solution became homogeneous with no substantial color change upon addition of acid.

Runs with (C$_2$H$_4$PCy$_2$)$_3$PFe(N$_2$) (5.6) as precursor. The procedure was identical to that of the standard catalytic protocol with the changes noted. The precursor used was (C$_2$H$_4$PCy$_2$)$_3$PFe(N$_2$) (2.4 mg, 0.003 mmol), which is an orange solid. Note that the solution became homogeneous with no substantial color change upon addition of acid.

Runs with (depe)$_2$Fe(N$_2$) as precursor. The procedure was identical to that of the standard catalytic protocol with the changes noted. The precursor used was (depe)$_2$Fe(N$_2$) (1 mg, 0.002 mmol), which is a dark red solid. Note that the solution became homogeneous with no significant color change upon addition of acid.

Runs with iPr$_2$O as solvent. The procedure was identical to that of the standard

catalytic protocol with the changes noted. The solvent used was iPr$_2$O. The solubility of

the reagents was similar to that observed in Et$_2$O.

Runs with DME as solvent. The procedure was identical to that of the standard catalytic

protocol with the changes noted. The solvent used was DME. Complex **4.1** dissolved in

the DME to form a red solution which turned yellow upon addition of the acid.

Runs with Bu$_2$O as solvent. The procedure was identical to that of the standard catalytic

protocol with the changes noted. The solvent used was Bu$_2$O. While complex **4.1** and

KC$_8$ were similarly insoluble in Bu$_2$O as in Et$_2$O, HBAr$^F_4 \cdot$ 2 Et$_2$O was only sparingly

soluble in Bu$_2$O and was added as a suspension.

Runs with toluene as solvent. The procedure was identical to that of the standard

catalytic protocol with the changes noted. The solvent used was toluene. While complex

4.1 and KC$_8$ were similarly insoluble in toluene as in Et$_2$O, HBAr$^F_4 \cdot$ 2 Et$_2$O was also

insoluble and was added as a suspension. Notably, the bronze color associated with KC$_8$

persisted for much longer during these runs.

Runs with 1:6 Et$_2$O:Toluene as solvent. The procedure was identical to that of the

standard catalytic protocol with the changes noted. The solvent used was a 1:6 mixture of

Et$_2$O:toluene. While complex **4.1** and KC$_8$ were similarly insoluble in Bu$_2$O as in Et$_2$O,

HBAr$^F_4 \cdot$ 2 Et$_2$O was only sparingly soluble in Bu$_2$O and was added as a suspension.

Runs with CoCp$^*_2$ as reductant. The procedure was identical to that of the standard

catalytic protocol with the changes noted. The reductant used was

decamethylcobaltocene, CoCp$^*_2$, (19 mg, 0.058 mmol), which was added as a solid. A

heterogeneous mixture resulted at -78 °C that homogenized at RT, producing a yellow solution.

Runs with CrCp*$_2$ as reductant. The procedure was identical to that of the standard catalytic protocol with the changes noted. The reductant used was decamethylchromocene, CrCp*$_2$, (20 mg, 0.062 mmol), which was added as a solid. The resulting suspension darkened before gradually returning to a yellow color.

Runs with NaC$_{10}$H$_8$ as reductant. The procedure was identical to that of the standard catalytic protocol with the changes noted. The reductant used was a freshly prepared solution of NaC$_{10}$H$_8$, which was made by stirring a solution of naphthalene (13 mg, 0.101 mmol) in THF (1 mL) over Na (10 mg, 0.435 mmol) for two hours. This solution was then filtered through a glass fiber filter paper directly into the catalytic mixture which turned red upon addition of the reductant before gradually fading to yellow.

Runs with K as reductant. The procedure was identical to that of the standard catalytic protocol with the changes noted. The reductant used was K metal (4 mg, 0.1 mmol), which was added as a solid. The reaction mixture was allowed to stir at -78 °C for 40 minutes and was then warmed slowly to RT overnight. After this time, a pale red-orange solution was present. Longer reaction times were employed to ameliorate the effect of the small surface area of the K metal.

Runs with MgC$_{14}$H$_{10}$ · 3 THF as reductant. The procedure was identical to that of the standard catalytic protocol with the changes noted. The reductant used was MgC$_{14}$H$_{10}$ · 3 THF (20 mg, 0.048 mmol), which is a yellow-orange solid. The reductant is insoluble in Et$_2$O and was added as a suspension. The solution gradually became more homogeneous over the 40 minute reaction time.

Runs with 10% Na by weight Na/Hg as reductant. The procedure was identical to that of the standard catalytic protocol with the changes noted. The reductant used was Na/Hg (10% Na by weight) (280 mg, 1.217 mmol), a dark grey solid which is insoluble in Et_2O and was added as a solid. The solution stayed heterogeneous and no noticeable color change was observed over the course of the reaction. The larger excess of Na/Hg was employed to help ameliorate the low surface area of the reductant.

Runs with trifluoromethanesulfonic acid as acid. The procedure was identical to that of the standard catalytic protocol with the changes noted. The acid used was trifluoromethanesulfonic acid (131 µL of a 0.7 M solution in Et_2O, 0.092 mmol), which was added without further dilution. The red suspension turned light yellow-green and homogenized upon addition of acid.

Runs with HCl as acid. The procedure was identical to that of the standard catalytic protocol with the changes noted. The acid used was anhydrous HCl (46 µL of a 2.0 M solution in Et_2O, 0.092 mmol), which was added without further dilution. The red suspension turned light yellow upon addition of acid, and subsequently precipitated a fine yellow solid. All subsequent manipulations were carried out with this suspension.

Runs with [Lutidinium][BArF4] as acid. The procedure was identical to that of the standard catalytic protocol with the changes noted. The acid used was [Lutidinium][BArF4] (90 mg, 0.092 mmol).

Runs with [2,6-dimethylanilinium][BArF4] · 1.5 Et2O as acid. The procedure was identical to that of the standard catalytic protocol with the changes noted. The acid used was [2,6-dimethylanilinium][BArF4] · 1.5 Et_2O (100 mg, 0.092 mmol).

Runs with [2,6-dimethylanilinium][OTf] as acid. The procedure was identical to that of the standard catalytic protocol with the changes noted. The acid used was [2,6-dimethylanilinium][OTf] (25 mg, 0.092 mmol). The acid was only sparingly soluble in Et_2O and was added as a suspension. Upon addition, complex **4.1** dissolved and the solution color became yellow.

Runs at RT. The procedure was identical to that of the standard catalytic protocol with the changes noted. All manipulations were performed analogously to the standard conditions at RT.

Runs at -110 °C. The procedure was identical to that of the standard catalytic protocol with the changes noted. All manipulations were performed analogously to the standard conditions at -110 °C. Temperature control was achieved with a liquid N_2/EtOH cold bath cooling the cold well of a glove box. The temperature was monitored with a thermocouple inside the cold well.

Run with [TBA][CN] added. The procedure was identical to that of the standard catalytic protocol with the changes noted. [TBA][CN] (0.01 g, 0.037 mmol) was added immediately after addition of KC_8 and the solution was then allowed to warm to room temperature before being worked up via the standard protocol. Absorbance: 0.294, Equiv NH_3/Fe: 3.50, % Yield: 21.9.

Run with *t*-BuNC added. The procedure was identical to that of the standard catalytic protocol with the changes noted. *t*-BuNC (0.01 g, 0.12 mmol) was added immediately after addition of KC_8 and the solution was then allowed to warm to room temperature before being worked up via the standard protocol. Absorbance: 0.140, Equiv NH_3/Fe: 1.67, % Yield: 10.4.

References Cited

1 Anderson, J. S.; Rittle, J.; Peters, J. C. *Nature* **2013**, in press, DOI: 10.1038/nature12435.

2 (a) Yandulov, D. V.; Schrock, R. R. *Science* **2003**, *301*, 76-78; (b) Arashiba, K.; Miyake, Y.; Nishibayashi, Y. *Nature Chem.* **2011**, *3*, 120-125; (c) Schrock, R. R. *Nature Chem.* **2011**, *3*, 95-96.

3 (a) Dos Santos, P. C.; Igarashi, R. Y.; Lee, H. I.; Hoffman, B. M.; Seefeldt, L. C.; Dean, D. R. *Acc. Chem. Res.* **2005**, *38*, 208-214; (b) Hoffman, B. M.; Dean, D. R.; Seefeldt, L. C. *Acc. Chem. Res.* **2009**, *42*, 609-619; (c) Seefeldt, L. C.; Hoffman, B. M.; Dean, D. R. *Annu. Rev. Biochem.* **2009**, *78*, 701-722; (d) Doan, P. E.; Telser, J.; Barney, B. M.; Igarashi, R. Y.; Dean, D. R.; Seefeldt, L. C.; Hoffman, B. M. *J. Am. Chem. Soc.* **2011**, *133*, 17329-17340.

4 Suess, D.L.M. Dissertation, California Institute of Technology, Pasadena **2013**.

5 Lee, Y.; Mankad, N. P.; Peters, J. C. *Nat Chem* **2010**, *2*, 558-565.

6 Betley, T. A.; Peters, J. C. *J. Am. Chem. Soc.* **2003**, *125*, 10782-10783.

7 Gilbert-Wilson, R.; Field, L. D.; Colbran, S. B.; Bhadbhade, M. M. *Inorg. Chem.* **2013**, *52*, 3043-3053.

8 Komiya, S.; Akita, M.; Yoza, A.; Kasuga, N.; Fukuoka, A.; Kai, Y. *Chem. Comm.* **1993**, 787-788.

9 Kameo, H; Hashimoto, Y.; Nakazawa, H. *Organometallics* **2012**, *31*, 3155-3162

10 Tolman, C. A. *Chem. Rev.* **1977**, *77*, 313-348.

11 Bontemps, S.; Gornitzka, H.; Bouhadir, G.; Miqueu, K.; Bourissou, D. *Angew. Chem. Int. Ed.* **2006**, *45*, 1611-1614.

12 Suess, D. L. M.; Peters, J. C. *J. Am. Chem. Soc.* **2013**, *135*, 4938-4941.

13 Bontemps, S.; Bouhadir, G.; Dyer, P. W.; Miqueu, K.; Bourissou, D. *Inorg. Chem.* **2007,** *46,* 5149-5151.

14 MacMillan, S.N. Dissertation, California Institute of Technology, Pasadena **2013**.

15 Cable, R. A.; Green, M.; Mackenzie, R. E.; Timms, P. L.; Turney, T. W. *J. Chem. Soc., Chem. Commun.* **1976**, 270b-271.

16 (a) Mankad, N. P.; Whited, M. T.; Peters, J. C. *Angew. Chem. Int. Ed.* **2007**, *46*, 5768-5771; (b) Whited, M. T.; Mankad, N. P.; Lee, Y.; Oblad, P. F.; Peters, J. C. *Inorg. Chem.* **2009**, *48*, 2507-2517; (c) Mankad, N. P.; Müller, P.; Peters, J. C. *J. Am. Chem. Soc.* **2010**, *132*, 4083-4085.

17 (a) Moret, M.-E.; Peters, J. C. *Angew. Chem. Int. Ed.* **2011**, *50*, 2063-2067; (b) Moret, M.-E.; Peters, J. C. *J. Am. Chem. Soc.* **2011**, *133*, 18118-18121.

18 Leigh, G. J.; Jimenez-Tenorio, M. *J. Am. Chem. Soc.* **1991**, *113*, 5862-5863; (b) Leigh, G. J. *Acc. Chem. Res.* **1992**, *25*, 177-181; (c) Hills, A.; Hughes, D. L.; Jimenez-Tenorio, M.; Leigh, G. J.; Rowley, A. T. *J. Chem. Soc., Dalton* **1993**, 3041-3049; (d) Crossland, J. L.; Tyler, D. R. *Coord. Chem. Rev.* **2010**, *254*, 1883-1894.

19 Chrystiuk, E.; Williams, A. *J. Am. Chem. Soc.* **1987**, *109*, 3040-3046.

20 Beale, R. N. *J. Chem. Soc.* **1954**, 4494-4499.

21 Ritleng, V.; Yandulov, D. V.; Weare, W. W.; Schrock, R. R.; Hock, A. S.; Davis, W. M. *J. Am. Chem. Soc.* **2004**, *126*, 6150-6163.

22 Kinoshita, E.; Arashiba, K.; Kuriyama, S.; Miyake, Y.; Shimazaki, R.; Nakanishi, H.; Nishibayashi, Y. *Organometallics* **2012**, *31*, 8437-8443.

23 Creutz S.E.; Peters, J.C. *J. Am. Chem. Soc.* **2013**.

24 Freeman, P. K.; Hutchinson, L. L. *The Journal of Organic Chemistry* **1983**, *48*, 879-881.

25 Murata, M.; Buchwald, S. L. *Tetrahedron* **2004**, *60*, 7397-7403.

26 Brookhart, M.; Grant, B.; Volpe, A. F. *Organometallics* **1992**, *11*, 3920-3922.

27 Sheldrick, G. M. *Acta Cryst.* **1990**, *A46*, 467.

28 Sheldrick, G. M. *Acta Cryst.* **2004**, *A64*, 112.

29 Müller, P. *Crystallography Reviews* **2009**, *15*, 57.

30 Weatherburn, M. W. *Anal. Chem.* **1967**, *39*, 971-974.

Chapter 6: Spectroscopic Characterization of the Putative Catalytic Intermediate [(TPB)Fe≡N-NH$_2$][BAr$^F_4$]

6.1 Introduction

A primary goal of using synthetic model complexes as a tool to study biological

N_2 fixation is to gain insight into feasible mechanisms or intermediates en route to NH_3

formation. While information gained in a molecular system can be difficult to

extrapolate to an enzyme, general trends in reactivity can be established. In order to draw

any comparisons, however, studies on the mechanism of model systems must be

performed. Very little is known about the mechanism of the catalytic system described in

chapters 4 and 5,[1] and there is a great deal of interest in elucidating potential

intermediates and pathways in this process. Previous synthetic work on Mo has outlined

a "distal" mechanism, wherein protons are sequentially added to one nitrogen atom along

with electrons to release NH_3 and form a metal nitride which is then protonated and

reduced to release NH_3.[2] Alternately, some of the spectroscopic and enzymatic studies

on nitrogenase that have implicated Fe as the binding site of N_2 have also supported a

different "alternating" mechanism wherein protons are alternately added to the β and the

α nitrogens.[3]
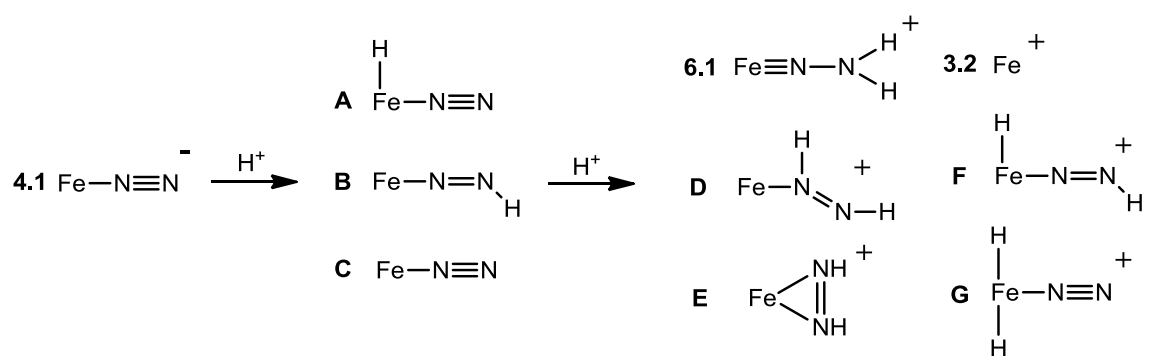
Scheme 6.1. Considered (TPB)Fe protonation products on from the reaction of **4.1** with acid.

Although synthetic examples of Fe complexes and their reactivity supporting both

"distal" and "alternating" mechanisms have been reported,[4,5] none of these examples

have come from a system that actually catalyzes N_2 reduction. Presented here are initial

studies directed towards the identification of a thermally unstable potential intermediate

that is generated by the addition of excess acid to the pre-catalyst $[(TPB)Fe(N_2)][Na(12-$

crown-4$)_2]$ (**4.1**) at low temperatures. There are a number of reasonable products of

protonation (Scheme 6.1), but combined EPR, ENDOR, XAS, and computational studies

suggest that this species is likely the doubly protonated hydrazido(2-) complex

$[(TPB)Fe\equiv N-NH_2)][BAr^F_4]$ (**6.1**). While this intermediate has not been observed under

turnover, the conditions for its generation map closely with the catalytic conditions and it

can be observed in mixtures prior to the addition of reductant for catalysis. Taken

together, these combined observations suggest that this doubly protonated species is

likely an intermediate en route to NH_3 formation.

6.2 Results and Discussion

6.2.1 EPR Studies

As mentioned in chapter 3, (TPB)Fe complexes are shifted by one electron from

their (SiP$_3$) congeners, which in many cases makes them EPR active. For example,

complex $[(TPB)Fe(N_2)][Na(12$-crown-4$)_2]$ (**4.1**) is $S = 1/2$ and displays an apparent axial

spectrum in its 77K EPR spectrum (Figure 6.1A). Furthermore, silylation of the βN of

4.1 results in the formation of (TPB)FeN$_2$SiMe$_3$, which also displays an apparent axial

signal in its 20K EPR spectrum (Figure 6.1B) which is substantially different that that

observed for **4.1**. These complexes contrast with the species characterized in Chapter 3

which were high spin and displayed very different EPR signatures. These combined results indicate EPR spectroscopy should be an attractive method for monitoring whether successful protonation is occurring at **4.1** as opposed to effective oxidation of the metal, which would result in an EPR silent species.
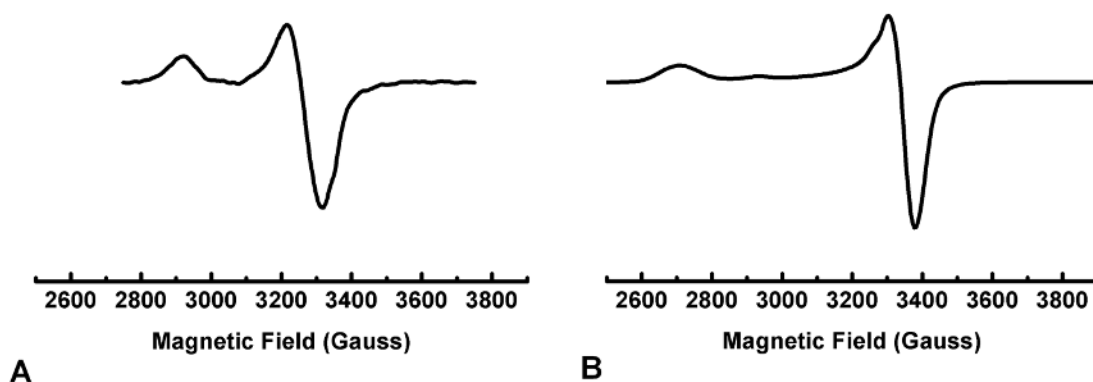
Figure 6.1. X-Band EPR spectra of: (A) Complex **4.1** and (B) (TPB)FeN$_2$SiMe$_3$. Conditions for (A) 77 K, 2-MeTHF, 9.39 GHz. Conditions for (B) 20 K, toluene, 9.38 GHz.

Mixing of **4.1** and 10 equivalents of HBAr$^F_4 \cdot$ 2 Et$_2$O in thawing 2-MeTHF solutions at -140 °C resulted in the disappearance of the dark red color characteristic of **4.1** and the formation of a brown-yellow solution. Analysis by X-band EPR indicates complete consumption of **4.1** and formation of a new distinctly rhombic $S = 1/2$ signal (Figure 6.2A) at 77 K that was assigned as a new species (**6.1**). This signal can be generated with as little as 2 equivalents of acid, however, the use of 1 equivalent of acid results in no formation of **6.1** as judged by EPR spectroscopy (Appendix 5). A wider scan at 10 K reveals no significant amount of higher spin products being formed (6.2B). A simulation of the spectrum (6.2A) reveals g values of $g_1 = 2.221$, $g_2 = 2.090$, $g_3 = 2.006$

and poorly resolved hyperfine coupling that has been simulated as coupling to two independent H atoms with coupling constants of 56 and 38 MHz. Interestingly, the spectrum of **6.1** is shows distinctly enhanced rhombicity when compared with **4.1** and (TPB)FeN$_2$SiMe$_3$. The fact that (TPB)FeN$_2$SiMe$_3$ displays a much more axial spectrum than **6.1** suggests that these two species are electronically different and that the rhombic spectrum may not belong to a diazenido (Scheme 6.1B) species.
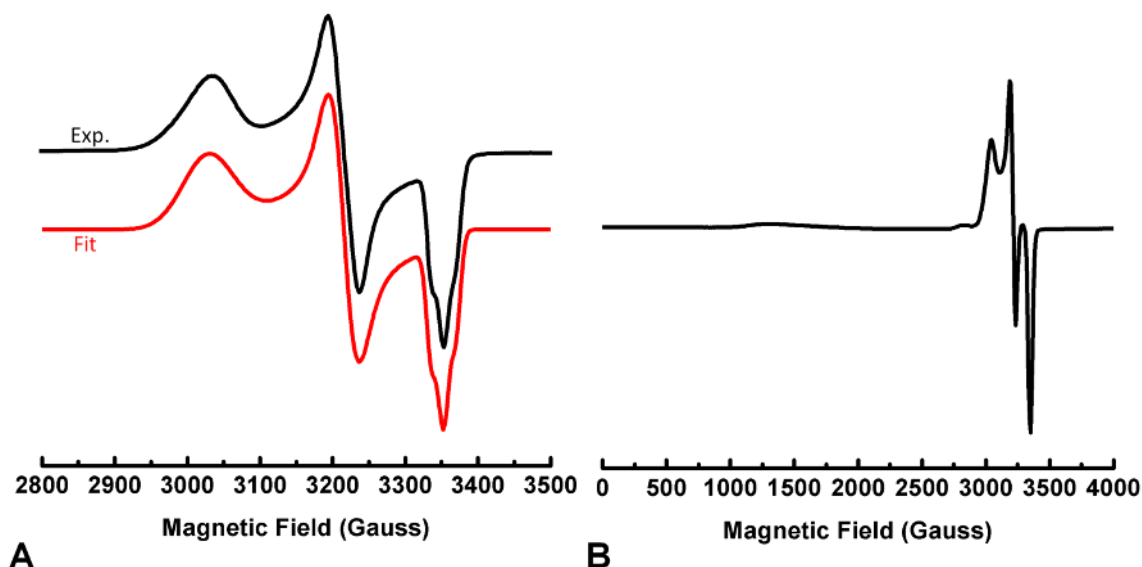
Figure 6.2. X-Band EPR spectra of the species generated from adding excess HBAr$^F_4 \cdot$ 2 Et$_2$O to **4.1**. (A) Scan from 2800 to 2500 gauss (B) Scan from 0 to 4000 G. Conditions: (A) 77 K (B) 10 K, 2-MeTHF, 9.38 GHz. Fit parameters: $g_1 = 2.221$, $g_2 = 2.090$, $g_3 = 2.006$, $A^{H1} = 56$ MHz, $A^{H2} = 38$ MHz.

If **6.1** is not a diazenido complex, then a few alternate scenarios are feasible. Single oxidation of **4.1** and concomitant formation of H$_2$ would lead to the known integer spin species (TPB)Fe(N$_2$) (Scheme 6.1C) while net 2 e$^-$ oxidation would lead to the known cation [(TPB)Fe][BAr$^F_4$] (Scheme 6.1, **3.2**) which is $S = 3/2$ and displays a distinctly different EPR spectrum from that observed for **6.1**. These observations

eliminate these simple oxidation products and suggest that protonated products should be considered. In one scenario, protonation at the metal could be occurring to generate an Fe-H, potentially with N_2 bound (Scheme 6.1A). Some examples of (TPB)Fe hydrides have already been explored, and no evidence for any EPR active hydride species was observed in this work.[6] Regardless, protonation at the metal center is possible and cannot be excluded on the basis of the EPR data alone. Another possibility is that two protons have been transferred to the N_2 ligand, either with both protons at the βN or with one proton on each of the N atoms. Precedence for double protonation at the βN was demonstrated early in Mo N_2 complexes,[7] and so this initial hypothesis was targeted as a starting point for further investigations.
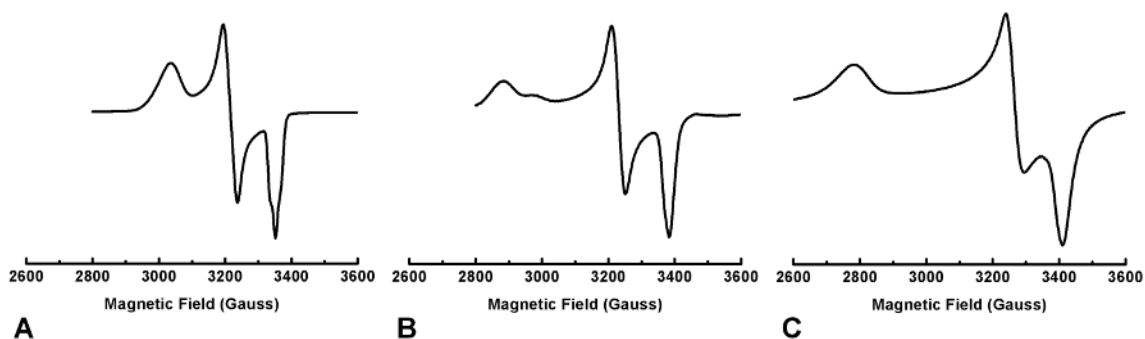
Figure 6.3. X-Band EPR spectra of (A) **6.1**, (B) [(TPB)Fe≡N(C_6H_4OMe)]$^+$, and (C) [(TPB)Fe≡NAd][BAr$^F_4$]. Conditions for all: 77 K, 2-MeTHF, (A) 9.38 GHz, (B) 9.40 GHz, (C) 9.42 GHz.

Such a putative hydrazido(2-) structure for **6.1** should possess a multiply bonded Fe-N interaction, similar to that observed in related silylated N_2 complexes on (TPB)Fe.[4d] As such, it seemed that **6.1** should electronically resemble formally Fe(III)

imide species. In order to test this hypothesis, EPR spectra of complexes with related

electronic structures were obtained (Figure 6.3). Initially, the known imide complex

(TPB)Fe≡N(C_6H_4OMe) was oxidized with [Fc][BAr$^F_4$] in situ to generate a rhombic

signal very similar to that observed in **6.1**. More recently, the stable cationic imide

[(TPB)Fe≡NAd][BAr$^F_4$] has been isolated and also displays an EPR signal that is very

similar to that observed in **6.1**. Furthermore, spin quantitation of the signal from **6.1**

against samples of both [(TPB)Fe≡NAd][BAr$^F_4$] and **4.1** indicates that the new rhombic

signal is formed in a ~80% yield, suggesting a relatively high conversion to this new

species. Qualitatively, these EPR spectra support the structural assignment of **6.1** as

[(TPB)Fe≡N-NH_2][BAr$^F_4$], but additional experiments were needed to validate the

presence of a hydrazido(2-) structural unit.

6.2.2 ENDOR Studies

ENDOR spectroscopy has been a technique that has been used effectively to

discern information about some paramagnetic species observed in the FeMoco as well as

in model complexes.[8] This technique involves a 2-D correlation between EPR and NMR

spectroscopies, where an EPR transition is saturated and the coupling of this transition to

nearby NMR active nuclei, such as ^{1}H or ^{15}N, is observed. As such, this technique allows

for greater structural information than would be provided by EPR alone. Specifically,

this technique will allow for the observation of the nuclei corresponding to a nitrogenous

ligand on Fe. Through a collaboration with the Hoffman lab at Northwestern University,

multi-nuclear ENDOR data have been collected on **4.1** and **6.1** and some of their

isotopically labeled congeners.
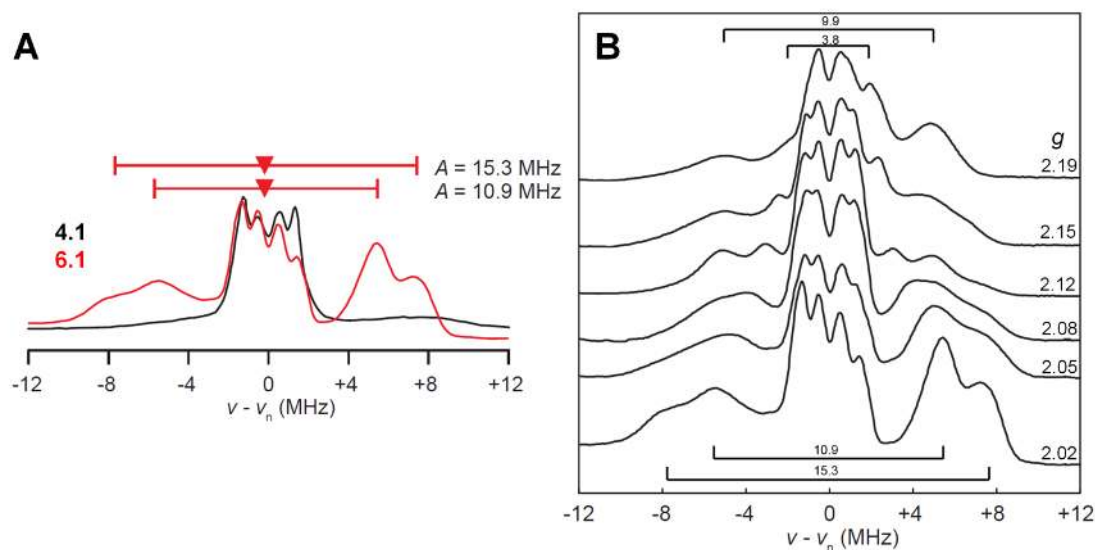
Figure 6.4. (A) Proton CW-ENDOR at 12.4 kG and 35.24 GHz of **4.1** (black) and **6.1** (red). (B) 35.01 GHz CW-ENDOR of **6.1** at the variable fields shown.

^{1}H ENDOR spectroscopy should be especially useful in identifying any protonation intermediates, as this technique allows for the direct observation of ^{1}H nuclei coupling with the unpaired spin. As such, this data was obtained on both **4.1** and **6.1** (Figure 6.4A). The spectrum of **4.1** shows only very weak couplings of < 3 MHz, which likely arise from ^{1}H associated with the TPB ligand scaffold. Upon reaction with acid to form **6.1**, however, two strong features appear with moderate couplings of 15.3 and 10.9 MHz. When adjusted for the differing magnetic fields, these coupling values agree well with the values obtained from the simulation of the X-band EPR spectrum of **6.1**. Furthermore, these couplings vary with g-value as shown in Figure 6.4B, achieving their highest values near g_3 and decreasing to lower values of 9.9 and 3.8 MHz near g_1. The observation of two new and independent signals in the ^{1}H ENDOR spectrum requires that there be at least two different types of protons and is consistent with the hypothesis of **6.1**

being a doubly protonated species. Furthermore, the fact that the couplings do not show

a large dependence on g-value suggests that they are likely located far from the nucleus,

making protonation at an αN less likely than at a βN. Furthermore, this result suggests

that protonation at the metal is highly unlikely. Distinguishing between protonation on Fe

or N_2 is difficult to determine from the coupling constants alone as the magnitude of the

coupling constant associated with hydrogenated Fe species as well as a bridging $Fe_2(\mu$-

NH) complex have been known to vary from 17 MHz to 56 MHz.[9] It should be noted,

however, that the observed coupling constant is at the very low end of this range species

and further suggests that protonation at Fe is unlikely.
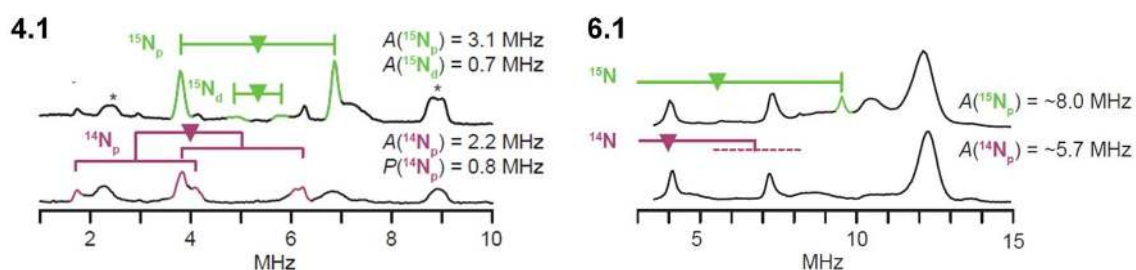
Figure 6.5. 35.0 GHz Davies ^{14}N and ^{15}N ENDOR spectra from **4.1** and **6.1** acquired at

$g = 2.005$. Note that the additional signals are either overtones from [11]B or ^{31}P or

artifacts.

Further information can be gleaned from the ^{14}N and ^{15}N ENDOR signals (Figure

6.5). Probing near $g = 2.005$, Complex **4.1** shows two resolvable couplings of

approximately 3.1 and 0.7 MHz in the ^{15}N ENDOR spectrum which are assigned as the

αN and βN of the bound N_2, respectively. Upon protonation to **6.1** only one coupling

constant of approximately 8 MHz in the ^{15}N ENDOR spectrum is observed. These

signals validate the presence of a nitrogenous ligand on Fe and hence eliminate any

structures for **6.1** that include loss of N_2 such as **3.2**. The observation of only one signal in the ^{15}N ENDOR spectrum of **6.1** furthermore preclude an η^2-diazene adduct of Fe (Scheme 6.1E) as the presence of two inequivalent ^1H signals in such a molecule would similarly require two inequivalent ^{15}N signals.

The ^{15}N ENDOR spectrum is consistent with the assignment of a hydrazido(2-) species with an Fe-N triple bond. Such a species would be expected to have a stronger coupling to the αN as is observed. While the two protons on such a complex could be in fast rotation at RT, rotation is likely hindered at low temperature, giving rise to the two independent proton signals. Alternately, a canting of the NNH_2 unit could also yield two inequivalent proton signals. In addition to the ^1H data, the ^{11}B ENDOR spectrum of **6.1** also shows a decrease in coupling constant from 19.5 MHz in **4.1** to 9.0 MHz in **6.1**, which is also consistent with an elongation of the Fe-B distance that would likely accompany the formation of an Fe-N triple bond as has been observed with other (TPB)Fe≡NR complexes.[10] Although all of this data is consistent with a hydrazido(2-) structure for **6.1**, direct and unique evidence of this functionality is not completely demonstrated by the ENDOR studies.

6.2.3 Fe K-Edge X-ray Absorption Spectroscopy Measurements

Although crystallization of **6.1** at low temperature was unsuccessful, structural data can be obtained via Fe K-edge X-ray absorption spectroscopy (XAS), and specifically Extended X-ray absorption fine structure (EXAFS) data has been collected on a frozen solution of **6.1** (Figure 6.6). The data show the presence of three primary peaks which can be fit with a first order approximation using the parameters shown in

Table 6.1. The fit suggests a short light atom scatter at 1.639(7) Å and two sets of heavier scatterers observed at 2.279(5) and 2.422(3) Å, respectively, which are best fit in a 1:2 ratio. These parameters provide a reasonable fit to the data and are consistent with the assignment of a short Fe-N bond and two inequivalent sets of Fe-P distances. The regions where the fit is poorest, specifically between 3 and 4 Å, arise from longer range interactions with light scatterers that have not been included in the fit. Finally, the observation that the Debye-Waller factor for the Fe-N bond is larger than for the Fe-P may potentially be explained by either some percentage of a species with a different Fe-N distance or some vibrational contribution.
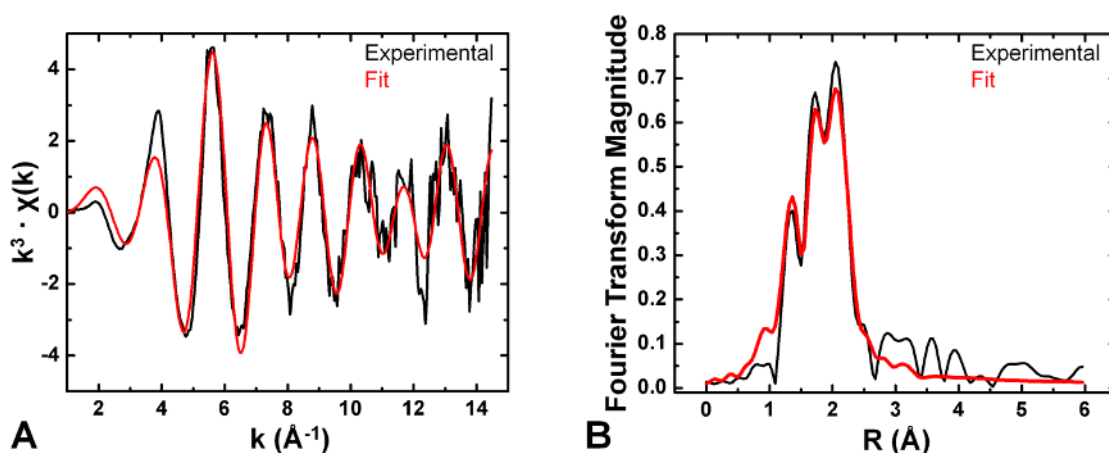
Figure 6.6. (A) EXAFS data. (B) Fourier transform of the EXAFS data. Fit parameters from those listed in Table 6.1.

When comparing these observed distances with those found in the known compound $[(TPB)Fe\equiv NAd][BAr^F_4]$ several similarities become apparent. The similar Fe-N distances of 1.64 and 1.66 Å in **6.1** and $[(TPB)Fe\equiv NAd][BAr^F_4]$ respectively are quite similar and both complexes display the pattern of two long and one short Fe-P bonds.

These observations further support a hydrazido(2-) structural assignment for **6.1**.

Notably, while shortened bonds of ~1.8 Å might be expected with other complexes under

consideration, no complex in Scheme 6.1 should display a Fe-N distance under ~1.70 Å

aside from the hydrazido(2-) structure for **6.1**. Iron nitrogen bonds of this length are

typically only observed with Fe-N multiple bonds, such as those seen in

[(TPB)Fe≡NAd][BAr$^F_4$] and other neutral Fe imides or hydrazido(2-) complexes

supported by TPB.4[d,10]

	N	*R (Å)*	*σ^2 (Å^2)*	*F-factor*
Fe-P	1	2.279(5)	0.0021(2)	0.377
Fe-P	2	2.422(3)	0.0021(2)	
Fe-N	1	1.639(7)	0.0085(2)	
Fe-B	1	2.674(12)	0.0085(17)	

Table 6.1. Extended X-ray absorption fine structure (EXAFS) curve-fitting results. N,

Coordination numbers, R, interatomic distances, σ^2 , Debye-Waller factors (the mean-

square deviations in interatomic distance). The values in parentheses are the estimated

standard deviations. The fit-error function $F = \sqrt{\sum k^6(\chi(k)_{calcd} - \chi(k)_{exp})^2 / \sum \chi(k)_{exp}^2}$

where k is the photo-electron wave number.

6.2.4 Computational Studies

In addition to the spectroscopic studies already mentioned, computational studies

offer an additional means to evaluate the proposed structure for **6.1**, especially in

comparison to other structural isomers that could be formed in the reaction mixture. DFT

calculations have therefore been carried out with two levels of theory. Both the postulated hydrazido(2-) complex and a terminal diazene complex (Scheme 6.1D) were considered in their $S = 1/2$ spin states. The geometries of these complexes were effectively minimized and frequency calculations showed no imaginary vibrations, indicating that the optimized structures represent global minima.
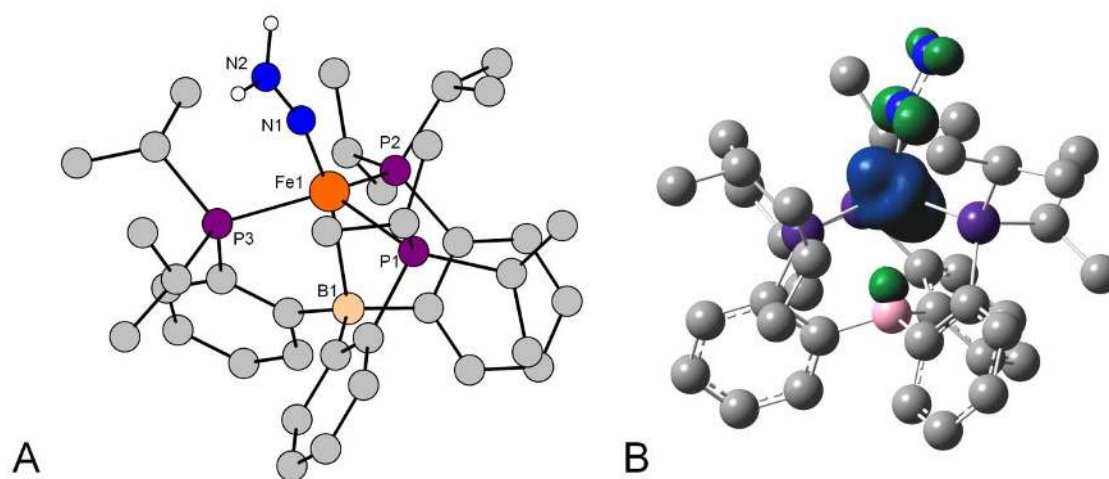
Figure 6.7. (A) Computed geometry for $[(TPB)Fe\equiv N\text{-}NH_2]^+$ and (B) spin density plot for $[(TPB)Fe\equiv N\text{-}NH_2]^+$.

Of particular interest is the optimized geometry of the proposed structure of **6.1** (Figure 6.7A) using the M06L functional. The predicted Fe-N and Fe-P bond lengths of 1.70 Å and 2.29, 2.31, and 2.36 Å respectively agree well with the observed distances from the EXAFS data for **6.1**. Additionally, a relatively long Fe-B distance of 2.56 Å is predicted, 0.3 Å longer than that observed in **4.1** and consistent with the weaker coupling observed in the ^{11}B ENDOR spectrum of **6.1** versus **4.1**. Analysis of the spin density in this computed structure (Figure 6.7B) indicates that while the majority of the spin is

centered on Fe, appreciable spin is also present on B and on the αN, which is consistent with the coupling observed in the ^{11}B and ^{15}N ENDOR spectra.

In addition to the minimized doublet hydrazido(2-) structure, the structure of the doublet diazene adduct (Scheme 6.1D) has also been computed (Appendix 5). The hydrazido(2-) structure A is lower than the diazene structure by 8 or 17 kcal/mol in energy depending on the level of theory used, suggesting that the proposed structure is preferred. Additionally, while the spin density in the doublet diazene structure is similarly primarily centered on Fe, there is virtually no spin density on boron, which is inconsistent with the observed coupling in the ^{11}B ENDOR spectrum. Again, these calculations are consistent with the observed data and suggest that the proposed hydrazido(2-) structure is more reasonable.

As a final set of calculations, high spin $S = 3/2$ calculations of both the hydrazido(2-) and diazene adducts have been considered. Interestingly, when using the M06L functional with TZVP, SVP, and 6-31G basis sets, the $S = 3/2$ spin state of the both the hydrazido(2-) and the diazene adduct (Scheme 6.1D) are lower in energy than the $S = 1/2$ hydrazido(2-) complex. While these spin states cannot correspond to the EPR or ENDOR data collected on **6.1**, the calculations do suggest that $S = 3/2$ states could be stable and perhaps accessible under the reaction conditions employed for catalysis. As will be discussed shortly, it seems plausible that thermal conversion to quartet spin states could occur in solutions of **6.1**.

6.2.5 Decomposition Studies

As was mentioned, **6.1** is thermally unstable and its decomposition was of interest in order to determine its relevance to the catalysis mediated by **4.1**. Additionally, while **6.1** is formed from conditions very similar to those used in catalysis, it was desirable to determine whether **6.1** is formed in catalytic mixtures. Towards this end, further EPR studies on warmed samples were undertaken. The first test was to determine whether the signal associated with **6.1** is formed when acid is added to **4.1** analogously to the first step in the catalytic protocol at -78 °C. When **4.1** is exposed to 10 equivalents of $HBAr^F_4$ $\cdot$ 2 Et_2O under these conditions the rhombic signal associated with **6.1** is observed, along with a substantial amount of new $S = 3/2$ signals similar to those observed for the complexes reported in chapter 3 (Figure 6.8, left).[11] It is likely that the new quartet features are a result of decomposition of **6.1** as solutions of **6.1** made at low temperature decompose at -40 °C to give the same quartet signals observed in the reaction at -78 °C (Figure 6.8, middle). Further warming of the solution to RT results in further decay of **6.1** and further evolution of the quartet features (Figure 6.8, right). Notably, however, there appears to be no difference in the behavior of the solutions as a result of their preparations at -140 °C or -78 °C, suggesting that **6.1** is likely formed in the initial catalytic mixture prior to reductant addition.

Finally, if acid is added at -78 °C and then an excess of KC_8 is added, also at -78 °C, and an EPR spectrum is then taken, the signal associated with **6.1** as well as the $S = 3/2$ signals disappear and a new roughly axial signal, similar to that observed for **4.1**, results (Appendix 5). Taken together, these EPR studies suggest that some $S = 3/2$ species are thermally accessible upon warming, which is consistent with the calculations.

Furthermore, the intermediate generated by addition of acid to **4.1** is likely present in the

catalytic mixture. Finally, this mixture, when exposed to reductant, regenerates what

appears to be a species similar to **4.1**, consistent with the stoichiometric reactions

reported in Chapter 4.
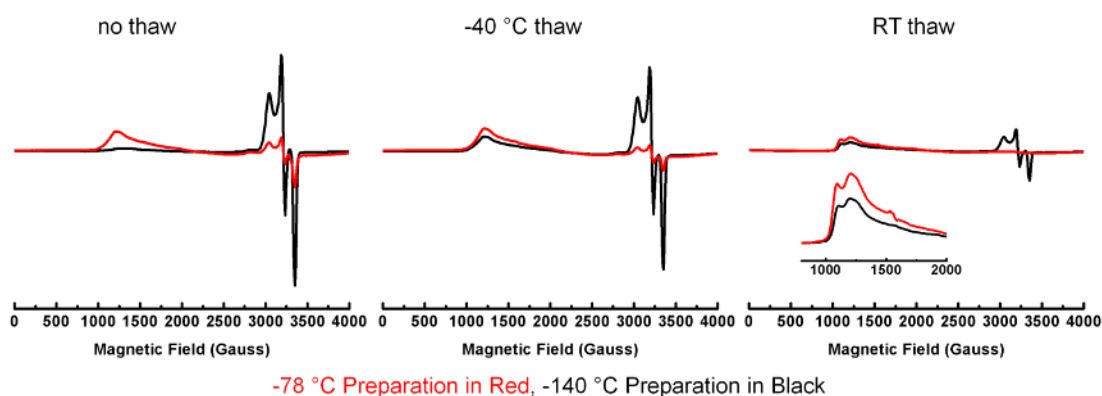
Figure 6.8. 77 K X-Band EPR spectrum comparing the addition of acid to **4.1** at different

temperatures and the effect of thawing this sample to different temperatures. Conditions:

2-MeTHF, 9.4 GHz.

6.3 Conclusions

Addition of excess acid to **4.1** at low temperatures results in the formation of a

new $S = 1/2$ species **6.1** in good yield. EPR spectroscopy on this complex suggests that it

is not a diazenido species and that its electronic structure resembles other cationic imide

species of (TPB)Fe such as [(TPB)Fe≡NAd][BAr$^F_4$]. ENDOR studies confirm the

presence of a nitrogenous ligand with two independent but similar protons. Furthermore,

the dependence of the ^{1}H proton signal on g-value suggests that these protons are

relatively far away from the Fe center. EXAFS spectroscopy confirms the presence of a

short Fe-N scatterer, which should only be observed in a species with Fe-N multiple bonds. Finally, computations suggest that a hydrazido(2-) complex is the most favorable isomer for this species.

Taken together, these studies offer convincing evidence for the assignment of **6.1**. Although parent hydrazido(2-) species were some of the first species identified from the protonation of N_2 on Mo and W,[12] **6.1** represents the first example of such a species on Fe and also is likely the first example of a species en-route to NH_3 formation. Indeed, structurally characterized examples of M-N-NR_2 linkages on first row metals later than V are quite rare.[13] This is somewhat remarkable, as other species such as nitrides and diazene adducts have been detected or isolated for some time.[14,15] The rarity of species arising from the protonation of N_2 on Fe speaks to the instability of these complexes and the difficulties associated with their characterization.

The potential role of this complex in a catalytic cycle is less clear at this point. Complex **6.1** is present in pre-catalytic mixtures prior to the addition of reductant and does appear to convert to other $S = 3/2$ species upon warming even to -78 °C. It should be noted that these same mixtures have been shown, upon warming, to produce $[(TPB)Fe(NH_3)][BAr^F_4]$. The fact that **6.1** has N-H bonds already formed strongly implies the intermediacy of this species in the formation of NH_3. While this certainly suggests that successive protonation at the βN of N_2 is feasible under the catalytic conditions, the subsequent steps resulting in NH_3 formation are still unclear. It is certainly still reasonable to think that a diazene species could be accessed subsequent to diprotonation of the βN. The observed $S = 3/2$ species being formed in the reaction mixture do not correspond to the reported complexes from chapter 3, although it is

unclear whether this is a result of the convolution of multiple species, or the presence of a new quartet signal. This still leaves the mechanism of further steps in the catalytic cycle up for debate. Although reasonable arguments can be made for both distal and alternating mechanisms, another intriguing possibility is a disproportionation pathway from **6.1** to generate diazene, hydrazine, and finally NH_3. The disproportionation chemistry shown in Chapter 3 offers further support for the feasibility of such a mechanism. Nevertheless, the identification of further species en route to NH_3 formation will be of great interest in future studies and will be required to further elucidate the mechanism of NH_3 formation.

6.4 Experimental Section

6.4.1 General Considerations

Unless otherwise noted, all compounds were purchased from commercial sources and used without further purification. [(TPB)Fe(N_2)][Na(12-crown-4)$_2$],[10] (TPB)Fe(N_2),[10] HBAr$^F_4 \cdot$ 2 Et$_2$O,[16] [Cp$_2$Fe][BAr$^F_4$],[17] and KC$_8$,[18] were prepared according to literature procedures ([BAr$^F_4$] = [B(3,5-(CF$_3$)$_2$-C$_6$H$_3$)$_4$B]$^-$) . All manipulations were carried out under a N_2 atmosphere utilizing standard glovebox or Schlenk techniques. Solvents were dried and de-oxygenated by an argon sparge followed by passage through an activated alumina column purchased from S.G. Waters Company. Labeled $^{15}N_2$ (98% purity) was obtained from Cambridge Isotope Laboratories.

6.4.2 EPR Spectroscopy

EPR X-band spectra were obtained on a Bruker EMX spectrometer with the aid of Bruker Win-EPR software suite version 3.0. The spectrometer was equipped with a rectangular cavity which operated in the TE_{102} mode. Temperature control was achieved with the use of an Oxford continuous-flow helium cryostat (temperature range 3.6 – 300 K). All spectra were recorded at 9.37 GHz with a microwave power of 20 mW, a modulation amplitude of 4 G, and a modulation frequency of 100 kHz. Simulations were performed with the Easyspin software suite.[19] EPR samples were thawed to -40 °C with a dry ice/acetonitrile slush bath for a time period of 5 minutes or alternately thawed to RT for a time period of 5 minutes.

6.4.3 ENDOR Spectroscopy

Both pulse and continuous wave (CW) EPR and ENDOR spectroscopic data were collected at 35 GHz on home-built spectrometers, which have been described previously.[20] Temperature control was achieved with liquid He immersion dewars for measurements at 2 K. A field modulation of 100 kHz and dispersion mode detection under rapid passage conditions were employed in the CW. In order to improve signal-to-noise, RF broadening of 100 kHz was employed in the ^{1}H CW ENDOR spectra.[21] The stochastic-field modulation detected ENDOR sequence was used on ^{1}H CW ENDOR spectra to improve ENDOR lineshapes.[22] Data acquisition for all pulse experiments utilized the SpecMan software package (http://specman4epr.com) in conjunction with a Spin-Core PulseBlaster ESR_PRO 400 MHz word generator and an Agilent Technologies Acquiris DP235 500MS/s digitizer.

6.4.4 XAS Measurements

XAS measurements were conducted at the Stanford Synchrotron Radiation Laboratory (SSRL) with the SPEAR 3 storage ring containing 500 mA at 3.0 GeV. Fe K-edge data were collected on the beamline 9-3 operating with a wiggler field of 2 T and employing a Si(220) double-crystal monochromator. Beamline 9-3 is equipped with a rhodium-coated vertical collimating mirror upstream of the monochromator and a bent-cylindrical focusing mirror (also rhodium-coated) downstream of the monochromator. Harmonic rejection was accomplished by setting the energy cutoff angle of the mirrors to 10 keV. The incident and transmitted X-ray intensities were monitored using Nitrogen-filled ionization chambers, and X-ray absorption was measured as the Fe Kα fluorescence excitation spectrum using an array of 100 Canberra germanium detectors. During data collection, samples were maintained at a temperature of approximately 10 K using an Oxford instruments liquid helium flow cryostat. The energy was calibrated by reference to the absorption of a standard iron metal foil measured simultaneously with each scan, assuming a lowest energy inflection point of the iron foil to be 7111.2 eV.

The extended x-ray absorption fine structure (EXAFS) oscillations $\chi(k)$ were quantitatively analyzed by curve-fitting using the EXAFSPAK suite of computer programs.[23] Ab-initio theoretical phase and amplitude functions were calculated using the program FEFF version 8.[24] No smoothing, filtering, or related operations were performed on the data.

6.4.5 Computational Methods

Geometry optimizations were performed using the Gaussian03 or the Gaussian09 packages.[25,26] The BP86 exchange-correlation functional was employed with a 6-31G(d) basis set on Fe, P, N, and B and the 6-31G basis set on C and H for the Gaussian03 calculations. Alternately, the M06L functional with the TZVP basis set on Fe, the SVP basis set on P, B, and N, and the 6-31G basis set on C and H. A full frequency calculation was performed on each structure to establish true minima. The initial geometries used for the calculations were the XRD coordinates for [(TPB)Fe≡NAd][BAr$^F_4$], which was modified to feature the correct nitrogenous ligands. Computed energies were corrected for thermal energy. Structural models were generated as .mol files and plotted in Diamond 3.2 and orbital/spin density pictures were generated from Gaussview 03.

6.4.6 Synthesis

Synthesis of [(TPB)Fe≡N-NH₂][BAr$^F_4$], 6.1. Complex **4.1** (4 mg, 0.004 mmol) was dissolved in 2-MeTHF (0.25 mL) and added into a quartz EPR tube. This solution was then frozen in a liquid N$_2$ cooled cold well. A thawing solution of HBAr$^F_4$ · 2 Et$_2$O (38 mg, 0.037 mmol) in 2-MeTHF (0.25 mL) was then added to the EPR tube and frozen before reaching the bottom of the tube. A long needle, which was also cooled to 77K, was then inserted into the tube and used to mechanically mix the solutions over 10 minutes. The tube was also raised slightly out of the cold well to slightly thaw the solutions and aid in mixing. After mixing was complete, the dark red color of **4.1** had

disappeared and a brown yellow solution was obtained. This frozen tube solution was then brought out of the glovebox and subjected to EPR analysis.

Synthesis of [(TPB)Fe≡N(C₆H₄OMe)][BAr^F₄]. An EPR sample of this complex was generated by dissolving (TPB)Fe≡N(p-C₆H₄OMe) (3 mg, 0.004 mmol) in 2-MeTHF (0.25 mL). This solution was then cooled to -78 °C and then mixed with a similarly cooled solution of [Fc][BAr^F₄] (Fc = ferrocenium) (4 mg, 0.004 mmol) in 2-MeTHF (0.25 mL) with rapid stirring. Upon mixing the dark blue color of [Fc][BAr^F₄] disappeared and the dark green color of (TPB)Fe≡N(p-C₆H₄OMe) lightened slightly to green-yellow. The solution was allowed to stir for an additional 10 minutes and then transferred to a quartz EPR tube and frozen. Note that there is a small signal resulting from an unknown $S = 1/2$ component in the product mixture.

Synthesis of (TPB)Fe≡NAd. Under an atmosphere of nitrogen, a 0.1 M solution of adamantyl azide in benzene (1.27 mL, 0.127 mmol) was added to a solution of (TPB)FeN₂ (86 mg, 0.127 mmol) in benzene (5 mL) and stirred, giving a deep red solution. The solution was transferred to a sealed Schlenk tube and stirred overnight at 80°C, resulting in a deep green solution. Lyophilization yielded a green powder which was washed twice in THF, leaving a bright green powder ((TPB)Fe≡NAd). The product was suspended in benzene and lyophilized in preparation for elemental analysis. Elemental analysis yielded the following results: Calculated: C 69.44, H 8.74, N 1.76; Experimental: C 69.29, H 8.47, N 1.67. NMR analysis was not obtained due to the poor solubility properties of the product.

Synthesis of [(TPB)Fe≡NAd][BAr^F₄]. A solution of (TPB)FeNAd (.101 g, 0.126 mmol) in THF (3 mL) was added to a solution of [FeCp₂][BAr^F₄] (.133 g, 0.126 mmol) in THF

(2 mL), giving a dark green solution which was stirred for 15 minutes. The solvent was removed, leaving a dark green sludgy solid [(TPB)Fe≡NAd][BAr$^F_4$] which was washed 3x with pentane (3 mL). Crystals for XRD were obtained by vapor diffusion of pentane into a solution of [(TPB)Fe≡NAd][BAr$^F_4$] in diethyl ether. ^{1}H NMR (THF-d_8, δ): 26.56 (vbr s), 10.66 (br s), 7.77 (s, BAr$^F_4$$^-$), 7.69 (br s), 7.56 (s, BAr$^F_4$$^-$), 6.67 (vbr s), 6.48 (br s), 5.44 (br s), 4.96 (br s), 3.16 (br s), -2,85 (vbr s), −5.96 (br s), -6.53 (br s), -8.23 (vbr s), -13.96 (br s). Anal. calcd. for C$_{78}$H$_{81}$B$_2$F$_{24}$FeNP$_3$: C 56.48 , H 4.92, N 0.84; found: C 56.24, H 4.83, N 0.80.

Preparation of ENDOR samples. Samples of **4.1** were prepared by dissolving the complex (1.2 mg, 0.001 mmol) in 2-MeTHF (0.5 mL) and transferring this solution to an ENDOR before freezing the solution prior to shipping. Samples of **6.1** were prepared analogously as described above with **4.1** (1 mg, 0.0009 mmol) and HBAr$^F_4$ · 2 Et$_2$O (10 mg, 0.0099 mmol) in 2-MeTHF (total volume of 0.5 mL). The only deviation from the above described procedure was that **6.1** was initially prepared in a 5 mL scintillation vial before being slightly thawed and transferred into the ENDOR tube while cold. The samples were then frozen and packaged for shipment. They were shipped to Northwestern University under liquid N$_2$.

Preparation of ^{15}N labeled ENDOR samples. Two stock solutions of **4.1** (5 mg, 0.0048 mmol) and HBAr$^F_4$ · 2 Et$_2$O (50 mg, 0.049 mmol) in 2-MeTHF (0.5 mL each) and 2-MeTHF (1 mL) were each placed into three short test tubes. These test tubes and the ENDOR tubes were placed into a round-bottom schlenk flask with a glass stopcock side-arm. The flask was then sealed with a rubber septum and brought out of the glovebox. The solution was freeze-pump-thawed 3x before backfilling with an atmosphere of ^{15}N$_2$.

The solutions were then sparged with $^{15}N_2$ from the headspace of the flask with the use of a long needled syringe through the rubber septum. The syringe was rinsed with the 2-MeTHF from the third test tube to avoid cross contamination. The solution of **4.1** was then distributed to the ENDOR tubes with the use of the syringe. To generate **6.1**, the apparatus was cooled to 77 K with liquid nitrogen. The solutions were then briefly thawed and the solution of $HBAr^F_4 \cdot 2$ Et_2O was layered on top of the solutions of **4.1** in the ENDOR tubes. The solutions were then mechanically mixed with the syringe as described above. After mixing was complete, the solutions were frozen, and the septum was removed, after which the samples were quickly dumped into liquid N_2 before being sealed for shipment. The samples were shipped to Northwestern University under liquid N_2.

Preparation of XAS samples. The sample of **6.1** for XAS analysis was prepared analogously to that reported earlier with **4.1** (10 mg, 0.0095 mmol) and $HBAr^F_4 \cdot 2$ Et_2O (100 mg, 0.099 mmol) in 2-MeTHF (0.5 mL total volume). The solution was prepared in a 5 mL scintillation vial before being slightly thawed and transferred into the XAS sample holder with a syringe. The sample was then re-frozen before being packaged for shipping to SSRL. The sample was shipped under liquid N_2.

Preparation and EPR analysis of 6.1 at -78 °C. Complex **4.1** (8 mg, 0.0076 mmol) was suspended in Et_2O (0.25 mL) and cooled to -78 °C in a 5 mL scintillation vial. $HBAr^F_4 \cdot 2$ Et_2O (80 mg, 0.079 mmol) was dissolved in Et_2O (0.25 mL) in a 20 mL scintillation vial equipped with a stir bar and cooled to -78 °C as well. Once cooled, the suspension of **4.1** was added to the $HBAr^F_4 \cdot 2$ Et_2O with stirring. The resulting solution was dark yellow-brown and homogeneous and was allowed to stir at -78 °C for 10

minutes. To this solution was then added 2-MeTHF (0.5 mL) which had been similarly cooled to -78 °C. The resulting solution was then transferred into an EPR tube and frozen with liquid N_2 before analysis.

EPR analysis of the reaction of complex 4.1 with one equivalent of HBAr$^F_4 \cdot$ 2 Et$_2$O. The procedure employed was identical to that used for the generation of **6.1** with the exception that a only one equivalent of HBAr$^F_4 \cdot$ 2 Et$_2$O (3.8 mg, 0.0038 mmol) was used.

Preparation and EPR analysis of 6.1 after reduction at -78 °C. Complex **4.1** (8 mg, 0.0076 mmol) was suspended in Et$_2$O (0.25 mL) and cooled to -78 °C in a 5 mL scintillation vial. HBAr$^F_4 \cdot$ 2 Et$_2$O (80 mg, 0.079 mmol) was dissolved in Et$_2$O (0.25 mL) in a 20 mL scintillation vial equipped with a stir bar and cooled to -78 °C as well. Once cooled, the suspension of **4.1** was added to the HBAr$^F_4 \cdot$ 2 Et$_2$O with stirring. The resulting solution was dark yellow-brown and homogeneous and was allowed to stir at -78 °C for 10 minutes. After this time KC$_8$ (20 mg, 0.15 mmol) was added as a solid. The resulting suspension was allowed to stir for 30 minutes at -78 °C before it was filtered through a glass fiber filter paper. Pre-cooled 2-MeTHF (0.5 mL) was then added to the resulting dark red-brown solution, which was then transferred to an EPR tube and frozen with liquid N_2 before analysis.

References Cited

1 Anderson, J. S.; Rittle, J.; Peters, J. C. *Nature* in press, DOI: 10.1038/nature12435.

2 (a) Chatt, J.; Dilworth, J. R.; Richards, R. L. *Chem. Rev.* **1978**, *78*, 589-625; (b) Hidai, M.; Mizobe, Y. *Chem. Rev.* **1995**, *95*, 1115-1133; (c) Schrock, R. R. *Acc. Chem. Res.* **2005**, *38*, 955-962.

3 (a) Dos Santos, P. C.; Igarashi, R. Y.; Lee, H. I.; Hoffman, B. M.; Seefeldt, L. C.; Dean, D. R. *Acc. Chem. Res.* **2005**, *38*, 208-214; (b) Hoffman, B. M.; Dean, D. R.; Seefeldt, L. C. *Acc. Chem. Res.* **2009**, *42*, 609-619; (c) Seefeldt, L. C.; Hoffman, B. M.; Dean, D. R. *Annu. Rev. Biochem.* **2009**, *78*, 701-722; (d) Lukoyanov, D.; Dikanov, S. A.; Yang, Z.-Y.; Barney, B. M.; Samoilova, R. I.; Narasimhulu, K. V.; Dean, D. R.; Seefeldt, L. C.; Hoffman, B. M. *J. Am. Chem. Soc.* **2011**, *133*, 11655-11664.

4 For recent examples see: (a) Betley, T. A.; Peters, J. C. *J. Am. Chem. Soc.* **2004**, *126*, 6252-6254; (b) Scepaniak, J. J.; Fulton, M. D.; Bontchev, R. P.; Duesler, E. N.; Kirk, M. L.; Smith, J. M. *J. Am. Chem. Soc.* **2008**, *130*, 10515-10517; (c) Scepaniak, J. J.; Young, J. A.; Bontchev, R. P.; Smith, J. M. *Angew. Chem., Int. Ed.* **2009**, *48*, 3158-3160; (d) Moret, M.-E.; Peters, J. C. *J. Am. Chem. Soc.* **2011**, *133*, 18118-18121. (e) Scepaniak, J. J.; Vogel, C. S.; Khusniyarov, M. M.; Heinemann, F. W.; Meyer, K.; Smith, J. M. *Science* **2011**, *331*, 1049-1052.

5 For recent examples see: (a) Field, L. D.; Li, H. L.; Dalgarno, S. J.; Turner, P. *Chem. Comm.* **2008**, 1680-1682; (b) Field, L. D.; Li, H. L.; Magill, A. M. *Inorg. Chem.* **2008**, *48*, 5-7; (c) Saouma, C. T.; Müller, P.; Peters, J. C. *J. Am. Chem. Soc.* **2009**, *131*, 10358-10359. (d) Crossland, J. L.; Balesdent, C. G.; Tyler, D. R. *Inorg. Chem.* **2011**,

51, 439-445. (e) Saouma, C. T.; Kinney, R. A.; Hoffman, B. M.; Peters, J. C. *Angew. Chem. Int. Ed.* **2011**, *50*, 3446-3449.

6 Fong, H.; Moret, M.-E.; Lee, Y.; Peters, J. C. *Organometallics* **2013**, *32*, 3053-3062.

7 (a) Chatt, J.; Heath, G. A.; Richards, R. L. *J. Chem. Soc., Dalton* **1974**, 2074-2082; (b) Hidai, M.; Kodama, T.; Sato, M.; Harakawa, M.; Uchida, Y. *Inorg. Chem.* **1976**, *15*, 2694-2697; (c) Takahashi, T.; Mizobe, Y.; Sato, M.; Uchida, Y.; Hidai, M. *J. Am. Chem. Soc.* **1980**, *102*, 7461-7467.

8 Hoffman, B. M.; Dean, D. R.; Seefeldt, L. C. *Acc. Chem. Res.* **2009**, *42*, 609-619.

9 (a) Lee, Y.; Kinney, R. A.; Hoffman, B. M.; Peters, J. C. *J. Am. Chem. Soc.* **2011**, *133*, 16366-16369; (b) Chiang, K. P.; Scarborough, C. C.; Horitani, M.; Lees, N. S.; Ding, K.; Dugan, T. R.; Brennessel, W. W.; Bill, E.; Hoffman, B. M.; Holland, P. L. *Angew. Chem. Int. Ed.* **2012**, *51*, 3658-3662; (c) Kinney, R. A.; Saouma, C. T.; Peters, J. C.; Hoffman, B. M. *J. Am. Chem. Soc.* **2012**, *134*, 12637-12647.

10 Moret, M.-E.; Peters, J. C. *Angew. Chem. Int. Ed.* **2011**, *50*, 2063-2067.

11 Anderson, J. S.; Moret, M.-E.; Peters, J. C. *J. Am. Chem. Soc.* **2012**, *135*, 534-537.

12 (a) Chatt, J.; Heath, G. A.; Richards, R. L. *J. Chem. Soc., Dalton* **1974**, 2074-2082; (b) Hidai, M.; Kodama, T.; Sato, M.; Harakawa, M.; Uchida, Y. *Inorg. Chem.* **1976**, *15*, 2694-2697; (c) Takahashi, T.; Mizobe, Y.; Sato, M.; Uchida, Y.; Hidai, M. *J. Am. Chem. Soc.* **1980**, *102*, 7461-7467.

13 (a) Mahy, J. P.; Battioni, P.; Mansuy, D.; Fisher, J.; Weiss, R.; Mispelter, J.; Morgenstern-Badarau, I.; Gans, P. *J. Am. Chem. Soc.* **1984**, *106*, 1699-1706; (b) Körner, V.; Huttner, G.; Vogel, S.; Barth, A.; Zsolnai, L. *Chem. Ber.* **1997**, *130*, 489-

492; (c) Paulat, F.; Lehnert, N.; Ishikawa, Y.; Okamoto, K.-I.; Fujisawa, K. *Inorg. Chim. Acta* **2008**, *361*, 901-915.

14 (a) Grapperhaus, C. A.; Mienert, B.; Bill, E.; Weyhermüller, T.; Wieghardt, K. *Inorg. Chem.* **2000**, *39*, 5306-5317; (b) Brown, S. D.; Peters, J. C. *J. Am. Chem. Soc.* **2005**, *127*, 1913-1923; (c) Vogel, C.; Heinemann, F. W.; Sutter, J.; Anthon, C.; Meyer, K. *Angew. Chem. Int. Ed.* **2008**, *47*, 2681-2684; (d) Scepaniak, J. J.; Young, J. A.; Bontchev, R. P.; Smith, J. M. *Angew. Chem. Int. Ed.* **2009**, *48*, 3158-3160.

15 (a) Sellmann, D.; Soglowek, W.; Knoch, F.; Moll, M. *Angew. Chem. Int. Ed.* **1989**, *28*, 1271-1272; (b) Field, L. D.; Li, H. L.; Dalgarno, S. J.; Turner, P. *Chem. Comm.* **2008**, 1680-1682; (c) Field, L. D.; Li, H. L.; Magill, A. M. *Inorg. Chem.* **2008**, *48*, 5-7; (e) Crossland, J. L.; Balesdent, C. G.; Tyler, D. R. *Inorg. Chem.* **2011**, *51*, 439-445.

16 Brookhart, M.; Grant, B.; Volpe, A. F. *Organometallics* **1992**, *11*, 3920-3922.

17 Chávez, I.; Alvarez-Carena, A.; Molis, E.; Roig, A.; Maniukiewicz, W.; Arancibia, A.; Arancibia, V.; Brand, H.; Manríquez, J. M. *J. Organomet. Chem.* **2000**, 601, 126-132.

18 Weitz, I. S.; Rabinovitz, M. *J. Chem. Soc. Perkin* **1993**, 117-120.

19 Stoll, S.; Schweiger, A. *J. Magn. Reson.* **2006**, *178*, 42-55.

20 (a) Werst, M. M.; Davoust, C. E.; Hoffman, B. M. *J. Am. Chem. Soc.* **1991**, *113*, 1533; (b) Davoust, C. E.; Doan, P. E.; Hoffman, B. M. *J. Magn. Reson.* **1996**, *119,* 38; (c) Zipse, H.; Artin, E.; Wnuk, S.; Lohman, G. J. S.; Martino, D.; Griffin, R. G.; Kacprzak, S.; Kaupp, M.; Hoffman, B.; Bennati, M.; Stubbe, J.; Lees, N. *J. Am. Chem. Soc.* **2009**, *131*, 200.

21 Hoffman, B. M.; DeRose, V. J.; Ong, J. L.; Davoust, C. E. J. Magn. Reson. 1994, 110, 52.

22 Lee, H.-I.; Igarashi, R. Y.; Laryukhin, M.; Doan, P. E.; Dos Santos, P. C.; Dean, D. R.; Seefeldt, L. C.; Hoffman, B. M. *J. Am. Chem. Soc.* **2004**, *126*, 9563.

23 George, G.N., http://ssrl.slac.stanford.edu/exafspak.html.

24 Ankudinov, A. L.; Ravel, B.; Rehr, J. J.; Conradson, S. D. *Physical Review B* **1998**, *58*, 7565-7576.

25 Gaussian 03, Revision C.02, Frisch, M. J.; Trucks, G. W.; Schlegel, H. B.; Scuseria, G. E.; Robb, M. A.; Cheeseman, J. R.; Montgomery, Jr., J. A.; Vreven, T.; Kudin, K. N.; Burant, J. C.; Millam, J. M.; Iyengar, S. S.; Tomasi, J.; Barone, V.; Mennucci, B.; Cossi, M.; Scalmani, G.; Rega, N.; Petersson, G. A.; Nakatsuji, H.; Hada, M.; Ehara, M.; Toyota, K.; Fukuda, R.; Hasegawa, J.; Ishida, M.; Nakajima, T.; Honda, Y.; Kitao, O.; Nakai, H.; Klene, M.; Li, X.; Knox, J. E.; Hratchian, H. P.; Cross, J. B.; Bakken, V.; Adamo, C.; Jaramillo, J.; Gomperts, R.; Stratmann, R. E.; Yazyev, O.; Austin, A. J.; Cammi, R.; Pomelli, C.; Ochterski, J. W.; Ayala, P. Y.; Morokuma, K.; Voth, G. A.; Salvador, P.; Dannenberg, J. J.; Zakrzewski, V. G.; Dapprich, S.; Daniels, A. D.; Strain, M. C.; Farkas, O.; Malick, D. K.; Rabuck, A. D.; Raghavachari, K.; Foresman, J. B.; Ortiz, J. V.; Cui, Q.; Baboul, A. G.; Clifford, S.; Cioslowski, J.; Stefanov, B. B.; Liu, G.; Liashenko, A.; Piskorz, P.; Komaromi, I.; Martin, R. L.; Fox, D. J.; Keith, T.; Al-Laham, M. A.; Peng, C. Y.; Nanayakkara, A.; Challacombe, M.; Gill, P. M. W.; Johnson, B.; Chen, W.; Wong, M. W.; Gonzalez, C.; and Pople, J. A.; Gaussian, Inc., Wallingford CT, 2004.

26 Gaussian 09, Revision A.1, Frisch, M. J.; Trucks, G. W.; Schlegel, H. B.; Scuseria, G. E.; Robb, M. A.; Cheeseman, J. R.; Scalmani, G.; Barone, V.; Mennucci, B.; Petersson, G. A.; Nakatsuji, H.; Caricato, M.; Li, X.; Hratchian, H. P.; Izmaylov, A. F.; Bloino, J.;

Zheng, G.; Sonnenberg, J. L.; Hada, M.; Ehara, M.; Toyota, K.; Fukuda, R.; Hasegawa, J.; Ishida, M.; Nakajima, T.; Honda, Y.; Kitao, O.; Nakai, H.; Vreven, T.; Montgomery, Jr., J. A.; Peralta, J. E.; Ogliaro, F.; Bearpark, M.; Heyd, J. J.; Brothers, E.; Kudin, K. N.; Staroverov, V. N.; Kobayashi, R.; Normand, J.; Raghavachari, K.; Rendell, A.; Burant, J. C.; Iyengar, S. S.; Tomasi, J.; Cossi, M.; Rega, N.; Millam, J. M.; Klene, M.; Knox, J. E.; Cross, J. B.; Bakken, V.; Adamo, C.; Jaramillo, J.; Gomperts, R.; Stratmann, R. E.; Yazyev, O.; Austin, A. J.; Cammi, R.; Pomelli, C.; Ochterski, J. W.; Martin, R. L.; Morokuma, K.; Zakrzewski, V. G.; Voth, G. A.; Salvador, P.; Dannenberg, J. J.; Dapprich, S.; Daniels, A. D.; Farkas, Ö.; Foresman, J. B.; Ortiz, J. V.; Cioslowski, J.; Fox, D. J. Gaussian, Inc., Wallingford CT, 2009.

Appendix 1: Supplementary Data for Chapter 2

Table A1.1. Crystal data and structure refinement for $((PhBP_3)Fe)_2(\mu\text{-}S)$ (**2.1**).

Identification code	temp
Empirical formula	C90 H82 B2 Fe2 P6 S1.11
Formula weight	1518.28
Temperature	100(2) K
Wavelength	0.71073 Å
Crystal system	Monoclinic
Space group	P2(1)/n
Unit cell dimensions	a = 12.9215(13) Å α= 90°.
	b = 13.3515(14) Å β= 92.191(2)°.
	c = 22.126(2) Å γ= 90°.
Volume	3814.4(7) Å^3
Z	2
Density (calculated)	1.322 Mg/m^3
Absorption coefficient	0.584 mm^{-1}
F(000)	1584
Crystal size	0.30 x 0.20 x 0.05 mm^3
Theta range for data collection	1.78 to 31.44°.
Index ranges	-18<=h<=18, -19<=k<=18, -31<=l<=31
Reflections collected	66507
Independent reflections	11930 [R(int) = 0.1232]
Completeness to theta = 31.44°	94.5 %
Absorption correction	Semi-empirical from equivalents
Max. and min. transmission	0.9714 and 0.8444
Refinement method	Full-matrix least-squares on F^2
Data / restraints / parameters	11930 / 15 / 467
Goodness-of-fit on F^2	1.010
Final R indices [I>2sigma(I)]	R1 = 0.0702, wR2 = 0.1559
R indices (all data)	R1 = 0.1644, wR2 = 0.1971
Largest diff. peak and hole	1.222 and -0.566 e.Å^{-3}

Table A1.2. Crystal data and structure refinement for [((PhBP$_3$)Fe)$_2$(μ-S)][Na(12-crown-4)$_2$] (**2.2**).

Identification code	jsa01_0m
Empirical formula	C6.62 H7.12 B0.12 Fe0.12 Na0.06 O0.50 P0.38 S0.06
Formula weight	118.14
Temperature	296(2) K
Wavelength	0.71073 Å
Crystal system	Monoclinic
Space group	C2/C
Unit cell dimensions	a = 25.1189(12) Å α= 90°.
	b = 13.2882(6) Å β= 94.365(2)°.
	c = 28.3900(13) Å γ= 90°.
Volume	9448.7(8) Å^3
Z	64
Density (calculated)	1.329 Mg/m^3
Absorption coefficient	0.493 mm^{-1}
F(000)	3972
Crystal size	0.57 x 0.34 x 0.26 mm^3
Theta range for data collection	1.73 to 26.43°.
Index ranges	-31<=h<=31, -16<=k<=16, -35<=l<=35
Reflections collected	74372
Independent reflections	9722 [R(int) = 0.0624]
Completeness to theta = 26.43°	99.8 %
Refinement method	Full-matrix least-squares on F^2
Data / restraints / parameters	9722 / 4000 / 1059
Goodness-of-fit on F^2	1.035
Final R indices [I>2sigma(I)]	R1 = 0.0472, wR2 = 0.1148
R indices (all data)	R1 = 0.0751, wR2 = 0.1329
Largest diff. peak and hole	1.020 and -0.341 e.Å^{-3}

Table A1.3. Crystal data and structure refinement for [((PhBP$_3$)Fe)$_2$(μ-S)][Na(12-crown-4)$_2$]$_2$ (**2.3**).

Identification code	jsa42_0m
Empirical formula	C138 H178 B2 Fe2 Na2 O20 P6 S
Formula weight	2553.98
Temperature	100(2) K
Wavelength	0.71073 Å
Crystal system	Triclinic
Space group	P-1
Unit cell dimensions	a = 12.5634(6) Å α= 82.174(3)°.
	b = 18.2367(10) Å β= 79.885(3)°.
	c = 29.0547(17) Å γ= 88.640(2)°.
Volume	6492.4(6) Å^3
Z	2
Density (calculated)	1.306 Mg/m^3
Absorption coefficient	0.387 mm^{-1}
F(000)	2712
Crystal size	0.5 x 0.2 x 0.1 mm^3
Theta range for data collection	1.42 to 24.71°.
Index ranges	-14<=h<=14, -21<=k<=21, -34<=l<=34
Reflections collected	113949
Independent reflections	21981 [R(int) = 0.1035]
Completeness to theta = 24.71°	99.3 %
Absorption correction	Semi-empirical from equivalents
Max. and min. transmission	0.7456 and 0.6813
Refinement method	Full-matrix least-squares on F^2
Data / restraints / parameters	21981 / 1697 / 1544
Goodness-of-fit on F^2	1.011
Final R indices [I>2sigma(I)]	R1 = 0.0623, wR2 = 0.1286
R indices (all data)	R1 = 0.1182, wR2 = 0.1507
Largest diff. peak and hole	0.919 and -0.767 e.Å^{-3}

Table A1.4. Crystal data and structure refinement for $((PhBP_3)Fe)(\mu-\eta^1:\eta^1-N_2H_4)(\mu-\eta^2:\eta^2-N_2H_2)((PhBP_2PS)Fe)$ (**2.4**).

Identification code	jsa218
Empirical formula	C90 H88 B2 Fe2 N4 O P6 S
Formula weight	1592.84
Temperature	293(2) K
Wavelength	0.71073 Å
Crystal system	Monoclinic
Space group	P-1
Unit cell dimensions	a = 12.575(3) Å α= 85.92(3)°.
	b = 15.871(3) Å β= 75.18(3)°.
	c = 22.750(5) Å γ= 76.30(3)°.
Volume	4264.2(15) Å^3
Z	2
Density (calculated)	1.241 Mg/m^3
Absorption coefficient	0.525 mm^{-1}
F(000)	1664
Crystal size	
Theta range for data collection	0.93 to 25.23°.
Index ranges	-15<=h<=15, -18<=k<=18, -27<=l<=27
Reflections collected	47144
Independent reflections	12523 [R(int) = 0.0466]
Completeness to theta = 25.23°	81.3 %
Refinement method	Full-matrix least-squares on F^2
Data / restraints / parameters	12523 / 4582 / 1243
Goodness-of-fit on F^2	1.056
Final R indices [I>2sigma(I)]	R1 = 0.0570, wR2 = 0.1738
R indices (all data)	R1 = 0.0612, wR2 = 0.1777
Largest diff. peak and hole	0.518 and -0.777 e.Å^{-3}

Figure A1.1. XRD Structure of $((PhBP_3)Fe)(\mu\text{-}\eta^1\text{:}\eta^1\text{-}N_2H_4)(\mu\text{-}\eta^2\text{:}\eta^2\text{-}N_2H_2)((PhBP_2PS)Fe)$ (**2.4**) with ellipsoids at 50% and C-H hydrogens and solvents removed for clarity.
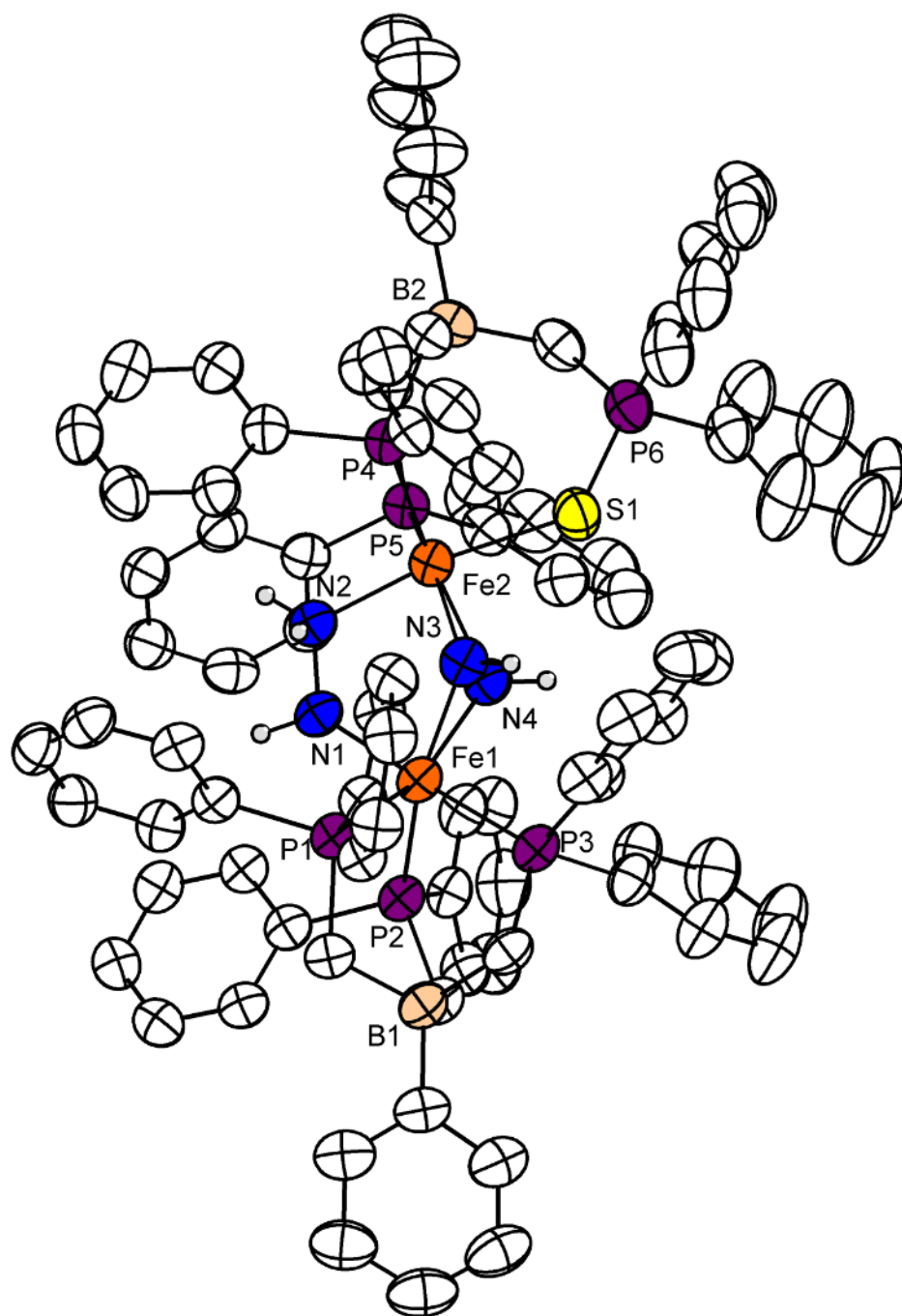
Table A1.5. Crystal data and structure refinement for $((PhBP_3)Fe(CO))_2(\mu\text{-}S)$ (**2.5**).

Identification code	jsa05_0m
Empirical formula	C100 H98 B2 Fe2 O4 P6 S
Formula weight	1714.98
Temperature	296(2) K
Wavelength	0.71073 Å
Crystal system	Monoclinic
Space group	P2(1)/m
Unit cell dimensions	a = 23.8929(7) Å $\quad$ α= 90°.
	b = 13.1133(4) Å $\quad$ β= 91.443(2)°.
	c = 26.9690(8) Å $\quad$ γ= 90°.
Volume	8447.1(4) Å^3
Z	4
Density (calculated)	1.349 Mg/m^3
Absorption coefficient	0.536 mm^{-1}
F(000)	3592
Crystal size	0.23 x 0.19 x 0.13 mm^3
Theta range for data collection	1.77 to 29.14°.
Index ranges	-32<=h<=32, -17<=k<=17, -36<=l<=36
Reflections collected	164026
Independent reflections	22722 [R(int) = 0.0829]
Completeness to theta = 29.14°	99.9 %
Refinement method	Full-matrix least-squares on F^2
Data / restraints / parameters	22722 / 2460 / 1235
Goodness-of-fit on F^2	1.077
Final R indices [I>2sigma(I)]	R1 = 0.0518, wR2 = 0.1452
R indices (all data)	R1 = 0.0873, wR2 = 0.1683
Largest diff. peak and hole	0.970 and -0.781 e.Å^{-3}

Figure A1.2. XRD Structure of ((PhBP₃)Fe(CO))₂(μ-S) (**2.5**) with ellipsoids at 50% and hydrogens and solvents removed for clarity.
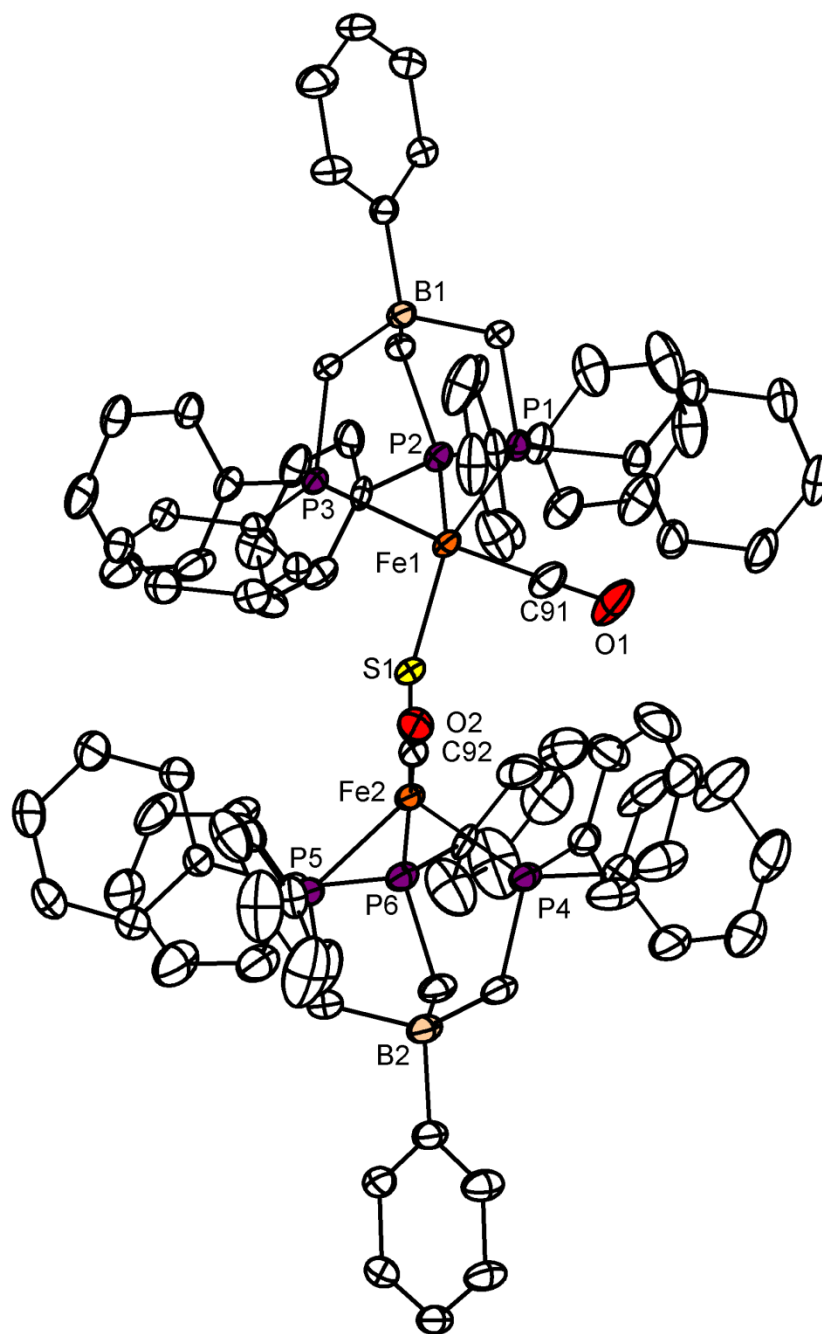
Figure A1.3. Comparison of Variable Temperature Magnetic Fits of $[((PhBP_3)Fe)_2(\mu\text{-}S)][Na(12\text{-}crown\text{-}4)_2]$ (**2.2**)
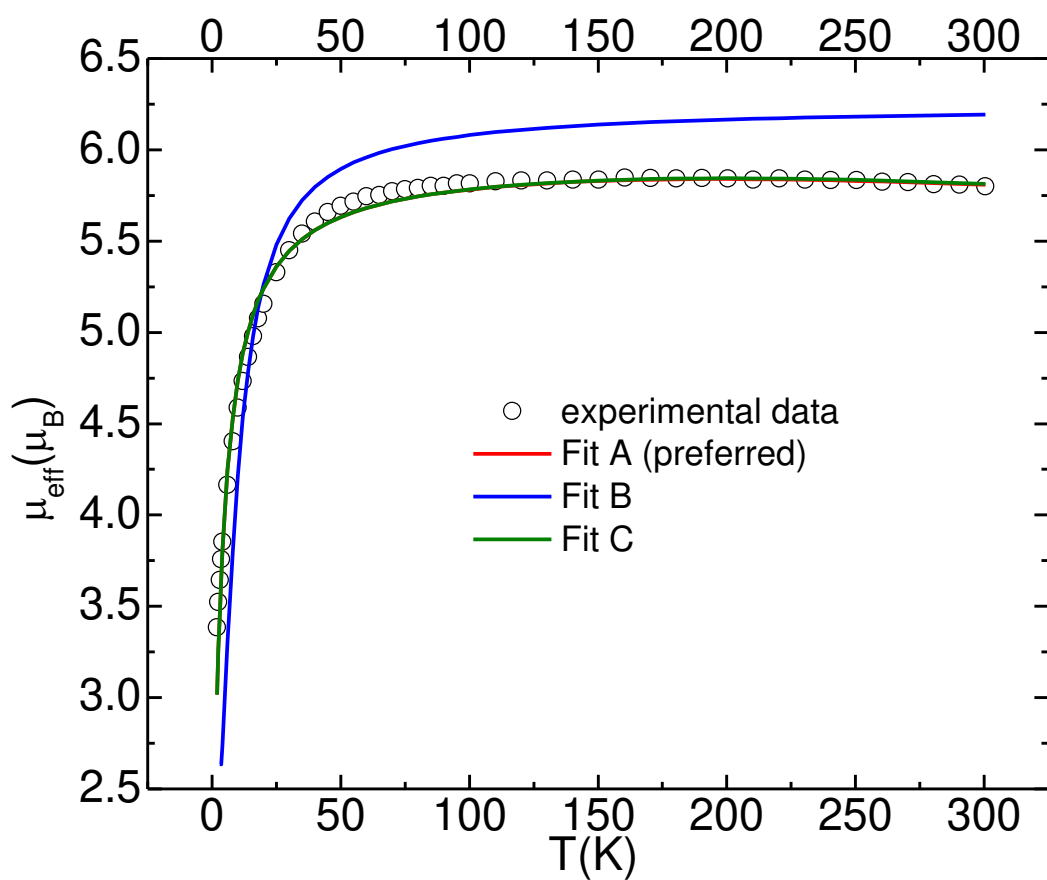
Fit Parameters	A	B	C
g	2.01	2.00	2.01
S_1	2	2	1
S_2	0.5	1.5	1.5
J_{12} (cm^{-1})	110	-1.5	118
Θ (K)	-5.7	1.6	-5.7

Appendix 2: Supplementary Data for Chapter 3

Table A2.1. Crystal data and structure refinement for (TPB)FeMe (**3.1**).

Identification code	jsa200m
Empirical formula	C37 H57 B Cl Fe P3
Formula weight	696.85
Temperature	293(2) K
Wavelength	0.71073 Å
Crystal system	Triclinic
Space group	P-1
Unit cell dimensions	a = 10.9554(3) Å α= 91.4010(10)°.
	b = 11.5075(3) Å β= 95.4060(10)°.
	c = 15.9312(4) Å γ= 117.8130(10)°.
Volume	1763.16(8) Å^3
Z	2
Density (calculated)	1.313 Mg/m^3
Absorption coefficient	0.665 mm^{-1}
F(000)	744
Crystal size	.456 x .304 x .209 mm^3
Theta range for data collection	1.29 to 27.10°.
Index ranges	-14<=h<=14, -14<=k<=14, -20<=l<=20
Reflections collected	36496
Independent reflections	7758 [R(int) = 0.0311]
Completeness to theta = 27.10°	99.8 %
Refinement method	Full-matrix least-squares on F^2
Data / restraints / parameters	7758 / 338 / 402
Goodness-of-fit on F^2	1.086
Final R indices [I>2sigma(I)]	R1 = 0.0321, wR2 = 0.0813
R indices (all data)	R1 = 0.0371, wR2 = 0.0860
Largest diff. peak and hole	0.890 and -0.305 e.Å^{-3}

Table A2.2. Crystal data and structure refinement for [(TPB)Fe][BAr$^F_4$] (**3.2**).

Identification code	mem130
Empirical formula	C68 H66 B2 F24 Fe N0 P3 Si0
Formula weight	1509.59
Temperature	100(2) K
Wavelength	0.71073 Å
Crystal system	Orthorhombic
Space group	Pbca
Unit cell dimensions	a = 26.4056(9) Å α= 90°.
	b = 19.7833(7) Å β= 90°.
	c = 26.4402(9) Å γ= 90°.
Volume	13812.1(8) Å^3
Z	8
Density (calculated)	1.452 Mg/m^3
Absorption coefficient	0.393 mm^{-1}
F(000)	6168
Crystal size	0.32 x 0.30 x 0.26 mm^3
Theta range for data collection	1.85 to 33.73°.
Index ranges	-35<=h<=41, -30<=k<=30, -41<=l<=41
Reflections collected	379408
Independent reflections	27590 [R(int) = 0.0500]
Completeness to theta = 33.73°	100.0 %
Absorption correction	Semi-empirical from equivalents
Max. and min. transmission	0.9046 and 0.8844
Refinement method	Full-matrix least-squares on F^2
Data / restraints / parameters	27590 / 18 / 951
Goodness-of-fit on F^2	1.062
Final R indices [I>2sigma(I)]	R1 = 0.0496, wR2 = 0.1239
R indices (all data)	R1 = 0.0744, wR2 = 0.1400
Largest diff. peak and hole	0.740 and -0.532 e.Å^{-3}

Table A2.3. Crystal data and structure refinement for [(TPB)Fe(N$_2$H$_4$)][BAr$^F_4$] (**3.3**).

Identification code	jsa19_0m
Empirical formula	C78 H68 B2 F24 Fe N2 P3
Formula weight	1659.72
Temperature	296(2) K
Wavelength	0.71073 Å
Crystal system	Orthorhombic
Space group	Pbca
Unit cell dimensions	a = 20.0031(7) Å $\quad$ α= 90°.
	b = 25.7862(8) Å $\quad$ β= 90°.
	c = 26.6970(8) Å $\quad$ γ = 90°.
Volume	13770.4(8) Å^3
Z	8
Density (calculated)	1.601 Mg/m^3
Absorption coefficient	0.404 mm^{-1}
F(000)	6776
Crystal size	0.46 x 0.26 x 0.15 mm^3
Theta range for data collection	2.00 to 32.59°.
Index ranges	-30<=h<=30, -39<=k<=39, -40<=l<=40
Reflections collected	347031
Independent reflections	25087 [R(int) = 0.0696]
Completeness to theta = 32.59°	99.9 %
Max. and min. transmission	0.9419 and 0.8361
Refinement method	Full-matrix least-squares on F^2
Data / restraints / parameters	25087 / 971 / 981
Goodness-of-fit on F^2	0.937
Final R indices [I>2sigma(I)]	R1 = 0.0531, wR2 = 0.1373
R indices (all data)	R1 = 0.0872, wR2 = 0.1681
Largest diff. peak and hole	1.295 and -0.755 e.Å^{-3}

Table A2.4. Crystal data and structure refinement for [(TPB)Fe(NH$_3$)][BAr$^F_4$] (**3.4**).

Identification code	xds_ascii
Empirical formula	C68 H80 B4 F24 Fe N2 O2 P3
Formula weight	1605.34
Temperature	293(2) K
Wavelength	0.71073 Å
Crystal system	Orthorhombic
Space group	Pbca
Unit cell dimensions	a = 19.846(4) Å α= 90°.
	b = 25.821(5) Å β= 90°.
	c = 26.862(5) Å γ = 90°.
Volume	13765(5) Å^3
Z	8
Density (calculated)	1.549 Mg/m^3
Absorption coefficient	0.402 mm^{-1}
F(000)	6600
Crystal size	.25 x .15 x .15 mm^3
Theta range for data collection	1.50 to 25.18°.
Index ranges	-23<=h<=23, -30<=k<=30, -32<=l<=32
Reflections collected	155016
Independent reflections	12232 [R(int) = 0.0175]
Completeness to theta = 25.18°	99.0 %
Refinement method	Full-matrix least-squares on F^2
Data / restraints / parameters	12232 / 972 / 961
Goodness-of-fit on F^2	1.041
Final R indices [I>2sigma(I)]	R1 = 0.0606, wR2 = 0.1680
R indices (all data)	R1 = 0.0620, wR2 = 0.1692
Largest diff. peak and hole	1.741 and -1.346 e.Å^{-3}

Table A2.5. Crystal data and structure refinement for (TPB)FeNH$_2$ (**3.5**).

Identification code	jsa23_0m
Empirical formula	C36 H56 B Fe N P3
Formula weight	662.39
Temperature	100(2) K
Wavelength	0.71073 Å
Crystal system	Triclinic
Space group	P-1
Unit cell dimensions	a = 10.9229(9) Å α= 77.268(7)°.
	b = 11.2493(13) Å β= 84.862(5)°.
	c = 16.5084(15) Å γ = 61.117(4)°.
Volume	1732.1(3) Å^3
Z	2
Density (calculated)	1.483 Mg/m^3
Absorption coefficient	0.615 mm^{-1}
F(000)	812
Crystal size	0.23 x 0.15 x 0.15 mm^3
Theta range for data collection	2.11 to 28.28°.
Index ranges	-14<=h<=14, -14<=k<=14, -22<=l<=22
Reflections collected	52847
Independent reflections	8561 [R(int) = 0.0706]
Completeness to theta = 28.28°	99.7 %
Max. and min. transmission	0.9134 and 0.8715
Refinement method	Full-matrix least-squares on F^2
Data / restraints / parameters	8561 / 2 / 397
Goodness-of-fit on F^2	1.120
Final R indices [I>2sigma(I)]	R1 = 0.0545, wR2 = 0.1236
R indices (all data)	R1 = 0.0810, wR2 = 0.1324
Largest diff. peak and hole	1.541 and -0.646 e.Å^{-3}

Table A2.6. Crystal data and structure refinement for (TPB)FeOH (**3.6**).

Identification code	jsa21_0m
Empirical formula	C36 H56 B Fe N O P3
Formula weight	678.39
Temperature	100(2) K
Wavelength	0.71073 Å
Crystal system	Triclinic
Space group	P-1
Unit cell dimensions	a = 10.9554(4) Å α= 77.466(2)°.
	b = 11.3311(4) Å β= 78.105(2)°.
	c = 16.6454(7) Å γ = 61.338(2)°.
Volume	1757.30(12) Å^3
Z	2
Density (calculated)	1.282 Mg/m^3
Absorption coefficient	0.595 mm^{-1}
F(000)	726
Crystal size	10.00 x 0.29 x 0.17 mm^3
Theta range for data collection	2.07 to 37.78°.
Index ranges	-18<=h<=17, -19<=k<=19, -28<=l<=28
Reflections collected	142106
Independent reflections	18846 [R(int) = 0.0433]
Completeness to theta = 37.78°	100.0 %
Max. and min. transmission	0.9056 and 0.0661
Refinement method	Full-matrix least-squares on F^2
Data / restraints / parameters	18846 / 1 / 382
Goodness-of-fit on F^2	1.024
Final R indices [I>2sigma(I)]	R1 = 0.0316, wR2 = 0.0745
R indices (all data)	R1 = 0.0477, wR2 = 0.0810
Largest diff. peak and hole	0.810 and -0.493 e.Å^{-3}

Figure A2.1. Crystal Structure for (TPB)FeOH (**3.6**) with ellipsoids at 50% and C-H

hydrogens omitted for clarity.
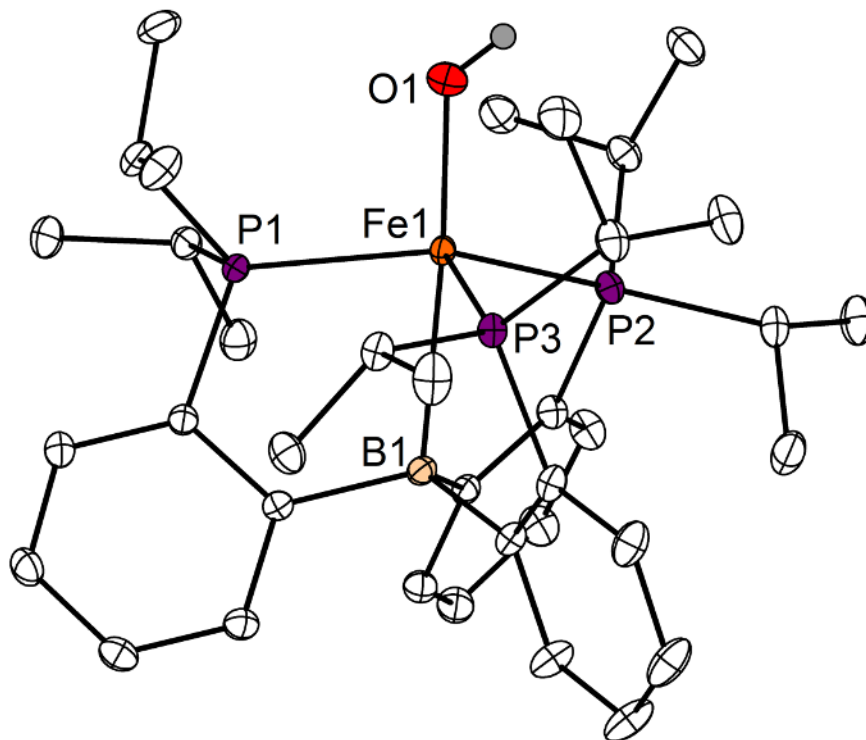
Figure A2.2. NMR traces of the monitored decomposition of **3.3** to **3.4**.
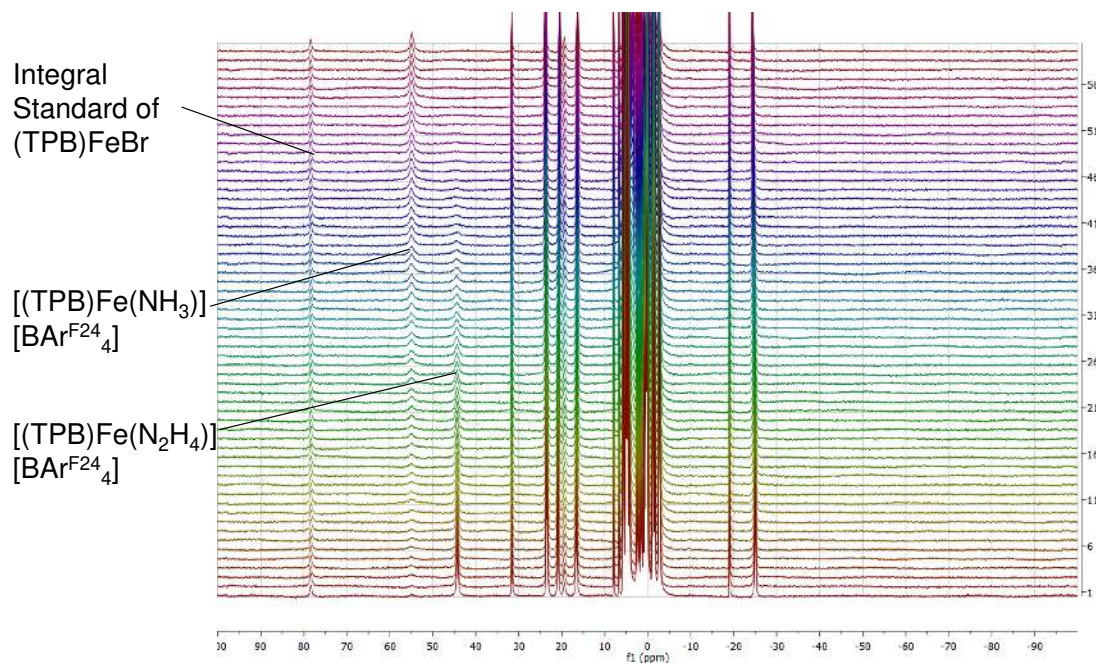
Conditions: 0.037 M, C_6D_6/THF-d^8, 60 °C, Total time = 4h. Only 2nd hour is shown.

Table A2.7. Product quantification for the decomposition of **3.3** to **3.4**.

Run	Equiv H_2	Equiv N_2H_4	Equiv NH_3
1	0.01	None det.	0.09
2	0.009	None det.	0.12
3	None det.	None det.	0.14

Figure A2.3. Titration of THF into a 4 mL ethereal solution of **3.2**.
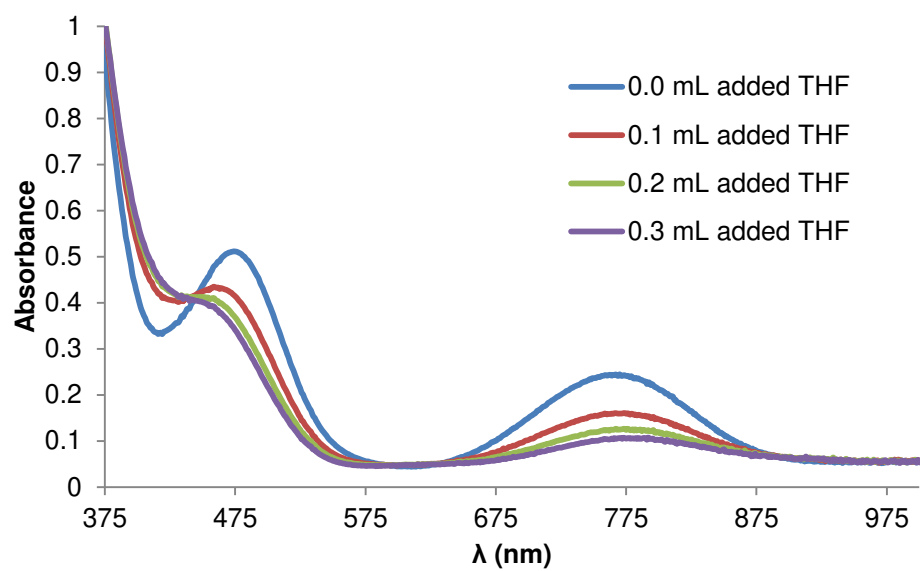
Figure A2.4. MO and spin density diagram of [(TPB)Fe]$^+$ (**3.2**) optimized at the B3LYP/6-31G(d) level.
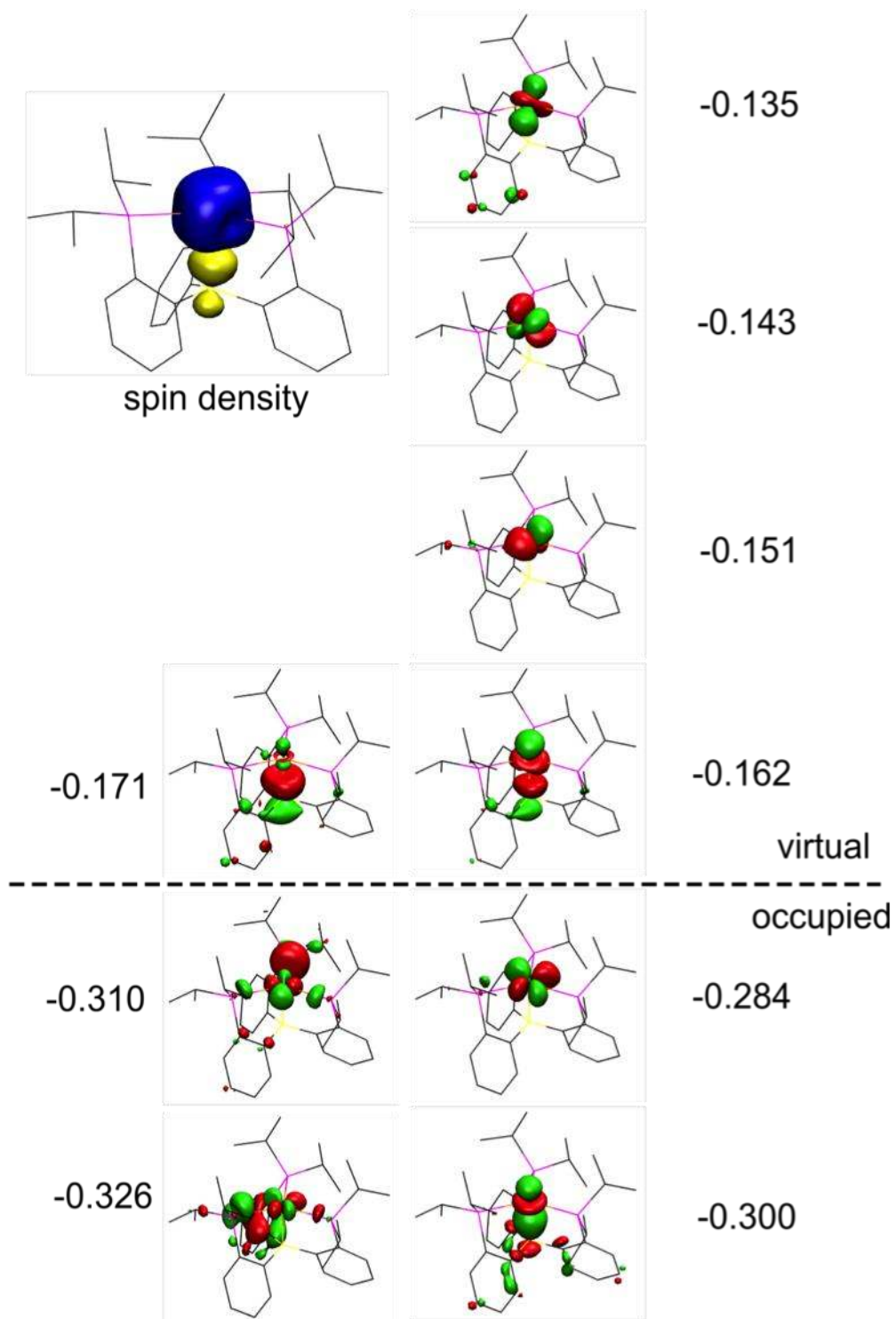
Figure A2.5. MO diagram addressing the T-shaped distortion in **3.2**.

trigonal planar

z

P—P
P

xy, x²-y²

xz, yz

z²

x²-y²

yz

xz
xy

z²

T-shaped

z

P

P—P

Highest doubly occupied *d* orbital:

P—P
P

d_{xz}

P

P—P

d_{xy}

strong p-backdonation with
all three phosphine ligands
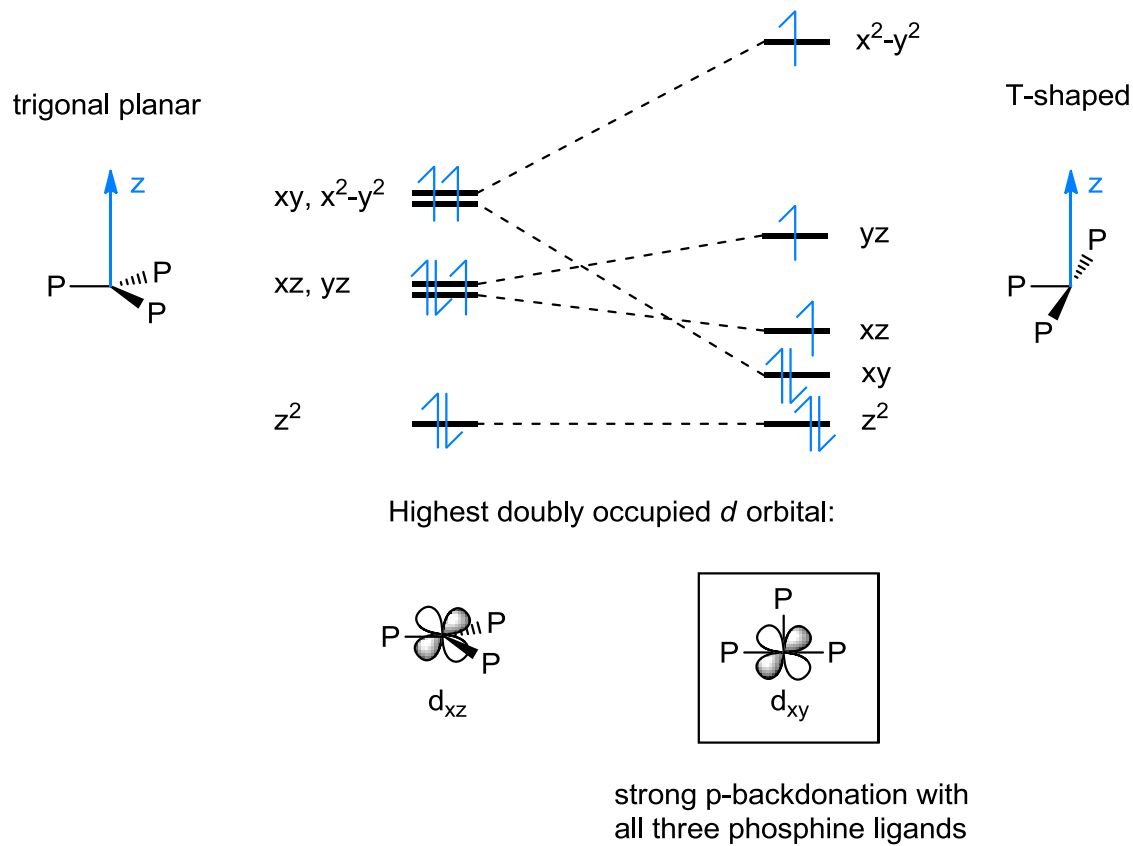
Figure A2.6. Variable Temperature Magnetic data for **3.2**-**3.5**.
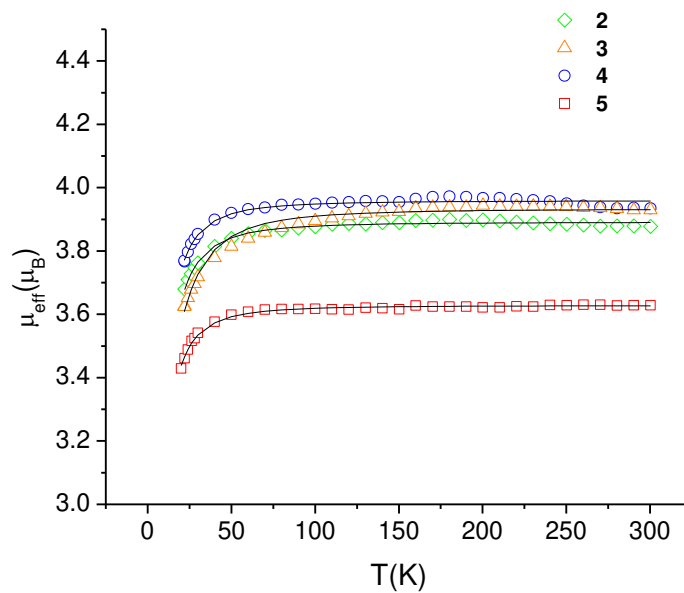
Data corrected for ~15% diamagnetic impurity of 12-crown-4, verified by ^{1}H NMR

integration, in **3.5.**
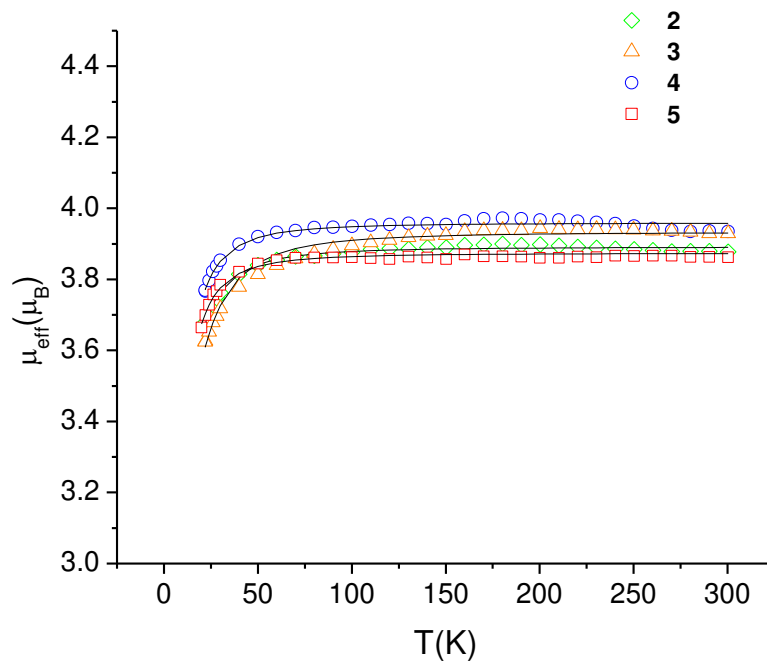
Table A2.8. Simulation parameters for the variable temperature data for complexes **3.2-**

3.5.

Compound	S	g	D (cm^{-1})
[TPB^{iPr}Fe][BAr$^F_4$]	3/2	2.009	13.933
[TPB^{iPr}Fe(N$_2$H$_4$)][BAr$^F_4$]	3/2	2.031	19.937
[TPB^{iPr}Fe(NH$_3$)][BAr$^F_4$]	3/2	2.044	12.162
(TPB^{iPr})Fe(NH$_2$)	3/2	2.000	11.348

Table A2.9. B3LYP/6-31G(d) DFT Optimized coordinates [Å] for [(TPB)Fe]⁺ (**3.2**).

Fe	0.00415000	-0.16241600	-0.77675900
P	-2.16349100	-1.24719000	-0.66738800
P	2.39121900	-0.83777200	-0.74771500
P	-0.31345400	2.27645200	-0.74537300
C	2.09021700	-1.73435800	0.82972400
C	4.02952400	1.02631900	0.64266200
H	3.98567100	0.45071500	1.57275400
H	3.19104000	1.72365500	0.64140500
H	4.95767100	1.60939200	0.65520800
C	-2.51735800	-0.85749000	1.09566800
C	-2.75787900	2.84164700	0.59302900
H	-2.24972100	3.20855200	1.49066600
H	-2.90111300	1.76680700	0.71127400
H	-3.74621500	3.31410800	0.55282800
C	0.96713000	-1.34366200	1.61726000
C	0.68267900	1.41376900	1.69824000
C	-3.77585900	-1.11913600	1.66212900
H	-4.53614800	-1.64204200	1.09100300
C	-1.50541500	-0.21277600	1.85301900
C	-1.85207300	0.20954700	3.15263700
H	-1.11562400	0.74145000	3.74897600
C	0.63534800	3.23145700	-2.06275600
H	0.57728600	4.28918000	-1.78194000
C	1.88147700	2.83955400	3.29296500
H	2.40769300	2.94283300	4.23815900
C	0.69310600	-2.13340400	2.75608400
H	-0.16599700	-1.88793000	3.37259400
C	4.03129200	0.10104900	-0.58072200
H	4.06604600	0.72216800	-1.48419000
C	1.38189800	1.59489600	2.90786900
H	1.54195100	0.73989400	3.56048800
B	0.03447200	-0.03107800	1.40854000
C	5.27977700	-0.79677000	-0.55921200
H	6.17024200	-0.16055800	-0.49330400
H	5.38965200	-1.41148800	-1.45674600
H	5.28761200	-1.45308000	0.31716600
C	1.72157800	3.94568000	2.45737900
H	2.12008100	4.91463800	2.74408600
C	1.05459100	3.79624400	1.24157800
H	0.95646000	4.65573100	0.58420600
C	2.77223500	-2.14130600	-2.05044100
H	3.66239200	-2.68641700	-1.71685100
C	-4.07155000	-0.72325700	2.96514500
H	-5.04800100	-0.93619400	3.39051300

C	-3.10700900	-0.04189100	3.70690700
H	-3.32936500	0.29181200	4.71691400
C	2.87573600	-2.83838200	1.19803000
H	3.71142600	-3.14386600	0.57548300
C	-1.96911100	3.20280400	-0.67407900
H	-2.51737400	2.81757600	-1.54509900
C	1.62859900	-3.14880400	-2.20719100
H	0.71343900	-2.65749200	-2.56047300
H	1.40294400	-3.66587600	-1.27050000
H	1.89809900	-3.90564800	-2.95299300
C	1.49436100	-3.21131000	3.13086000
H	1.25256900	-3.77768600	4.02619200
C	2.11687300	2.84858500	-2.14500700
H	2.24202800	1.80944900	-2.46700100
H	2.62947700	2.97816400	-1.18858400
H	2.61717700	3.48566700	-2.88385400
C	-2.49731300	-3.09116600	-0.81402900
H	-3.54555800	-3.21968300	-0.51323400
C	2.59216700	-3.56984800	2.34988300
H	3.21486600	-4.41610400	2.62556400
C	-1.61976400	-3.87498400	0.17378600
H	-1.85554000	-4.94310500	0.10319500
H	-1.78498100	-3.56065100	1.20749500
H	-0.55428900	-3.75363600	-0.04648600
C	0.53094900	2.55057600	0.86165400
C	-1.86943800	4.73224900	-0.80367000
H	-2.87736400	5.16043800	-0.75057800
H	-1.42999600	5.06125000	-1.74899100
H	-1.29175300	5.16729800	0.01900400
C	-2.95949200	-0.11225400	-3.13193300
H	-2.81329100	-1.04459900	-3.68700100
H	-2.00927500	0.43395300	-3.13573300
H	-3.68632300	0.48853300	-3.69112200
C	-3.47778300	-0.36144900	-1.70257400
H	-3.55367100	0.61070400	-1.20046300
C	-2.34128800	-3.61958100	-2.24860700
H	-1.32591600	-3.46834000	-2.62965700
H	-3.03896300	-3.15266000	-2.94927700
H	-2.53763200	-4.69785800	-2.26329900
C	-0.04759800	3.05060900	-3.43027100
H	-1.09647000	3.36299400	-3.42897900
H	-0.00706500	2.00371300	-3.75748600
C	3.08823800	-1.45897600	-3.39314100
H	3.31866300	-2.21769600	-4.14966000
H	3.94741000	-0.78399700	-3.33422400
H	2.22923900	-0.88166100	-3.75845100

C	-4.87834200	-0.99390800	-1.73157800
H	-5.54599600	-0.36236200	-2.32962300
H	-4.87513300	-1.98675200	-2.19255400
H	-5.32164500	-1.07767600	-0.73669900
H	0.47189800	3.64859800	-4.18772700

Table A2.10. B3LYP/6-31G(d) DFT Optimized coordinates [Å] for [(Me$_2$PhP)$_3$Fe]$^+$.

Fe	0.15864700	-0.18495700	-0.99760500
P	-0.96396300	1.83613500	-1.46879900
P	-0.45971000	-2.22271000	-0.05600500
P	2.48332300	-0.04211700	-1.31271800
C	-2.26951200	-2.22907300	0.27519800
C	-1.24228800	2.66879600	0.14383800
C	-2.79182200	-2.06800000	1.56749900
C	4.03948300	-1.45884400	0.61288100
C	-0.64552100	3.89539800	0.47185600
H	-0.02266300	4.41711100	-0.24807900
C	-2.04536400	2.02460300	1.10222300
C	-2.25786700	2.60533100	2.35188400
H	-2.89062600	2.10308200	3.07801800
C	3.22714900	-1.29680000	-2.44619800
H	4.32141000	-1.26188800	-2.43248400
C	4.38348500	-0.67980900	2.87994900
H	4.81234400	-0.82007700	3.86773800
C	-4.17301300	-2.01522100	1.77110700
H	-4.56274900	-1.90088900	2.77861400
C	0.31804700	-2.68760000	1.54990900
H	1.38960600	-2.83560300	1.38660000
C	4.58567000	-1.63819900	1.88602900
H	5.17639900	-2.52519600	2.09670500
C	3.63159400	0.46273300	2.59776700
H	3.47437400	1.21562800	3.36480600
C	3.08377800	0.64390800	1.32807100
H	2.50486800	1.54243900	1.12392600
C	-0.21389600	-3.73662900	-1.09026300
H	-0.63896300	-4.62100300	-0.60524200
C	-0.85737200	4.47065600	1.72657200
H	-0.39598100	5.42490200	1.96403800
C	-1.66358000	3.82933600	2.66729400
H	-1.83040700	4.28140300	3.64050500
C	-3.16079100	-2.32427200	-0.80796000
H	-2.78261000	-2.44971700	-1.82004800
C	3.28247400	1.51522500	-1.91488900
H	2.90698900	1.75077900	-2.91604500
C	-5.04871600	-2.11906600	0.69010800
H	-6.12191000	-2.08279500	0.85179800
C	-2.66656800	1.64342000	-2.16885400
H	-3.18590300	2.60610400	-2.21168900
C	-4.53907500	-2.27482500	-0.60131300
H	-5.21468500	-2.36443900	-1.44718900
C	3.28537900	-0.31297600	0.31747500

```
C     -0.23933400    3.11974200   -2.57722600
H      0.77356200    3.37847300   -2.25945300
H      2.88637400   -1.08677000   -3.46523900
H      2.89836600   -2.30593900   -2.18218500
H      3.02794700    2.34344400   -1.24739500
H      4.37260400    1.42000600   -1.95477900
H      0.85730500   -3.89883800   -1.24746400
H     -0.68525200   -3.61298900   -2.06920800
H     -0.11632500   -3.60480000    1.96078100
H      0.20638200   -1.87762100    2.27591300
H     -0.85392700    4.02578200   -2.60403500
H     -0.18044400    2.70383300   -3.58796700
H     -3.25191000    0.95080000   -1.55774000
H     -2.59769400    1.23085800   -3.18107000
H     -2.51936000    1.07248800    0.87329200
H      4.21949800   -2.21267100   -0.14752200
H     -2.13022700   -1.99363600    2.42490400
```

Appendix 3: Supplementary Data for Chapter 4

Table A3.1. Crystal data and structure refinement for (TPB)FeCl.

Identification code	mem105
Empirical formula	C36 H54 B Cl Fe P3
Formula weight	681.81
Temperature	296(2) K
Wavelength	0.71073 Å
Crystal system	Triclinic
Space group	P-1
Unit cell dimensions	a = 10.8929(7) Å α= 91.335(2)°.
	b = 11.5482(7) Å β= 97.048(2)°.
	c = 15.8266(9) Å γ = 117.325(2)°.
Volume	1748.20(18) Å^3
Z	2
Density (calculated)	1.295 Mg/m^3
Absorption coefficient	0.670 mm^{-1}
F(000)	726
Crystal size	
Theta range for data collection	1.99 to 40.25°.
Index ranges	-19<=h<=19, -20<=k<=20, -28<=l<=27
Reflections collected	104461
Independent reflections	21944 [R(int) = 0.0447]
Completeness to theta = 40.25°	99.9 %
Refinement method	Full-matrix least-squares on F^2
Data / restraints / parameters	21944 / 6 / 417
Goodness-of-fit on F^2	1.022
Final R indices [I>2sigma(I)]	R1 = 0.0363, wR2 = 0.0846
R indices (all data)	R1 = 0.0566, wR2 = 0.0940
Largest diff. peak and hole	0.668 and -0.982 e.Å^{-3}

Figure A3.1. Crystal Structure for (TPB)FeCl with ellipsoids at 50% and C-H hydrogens omitted for clarity.
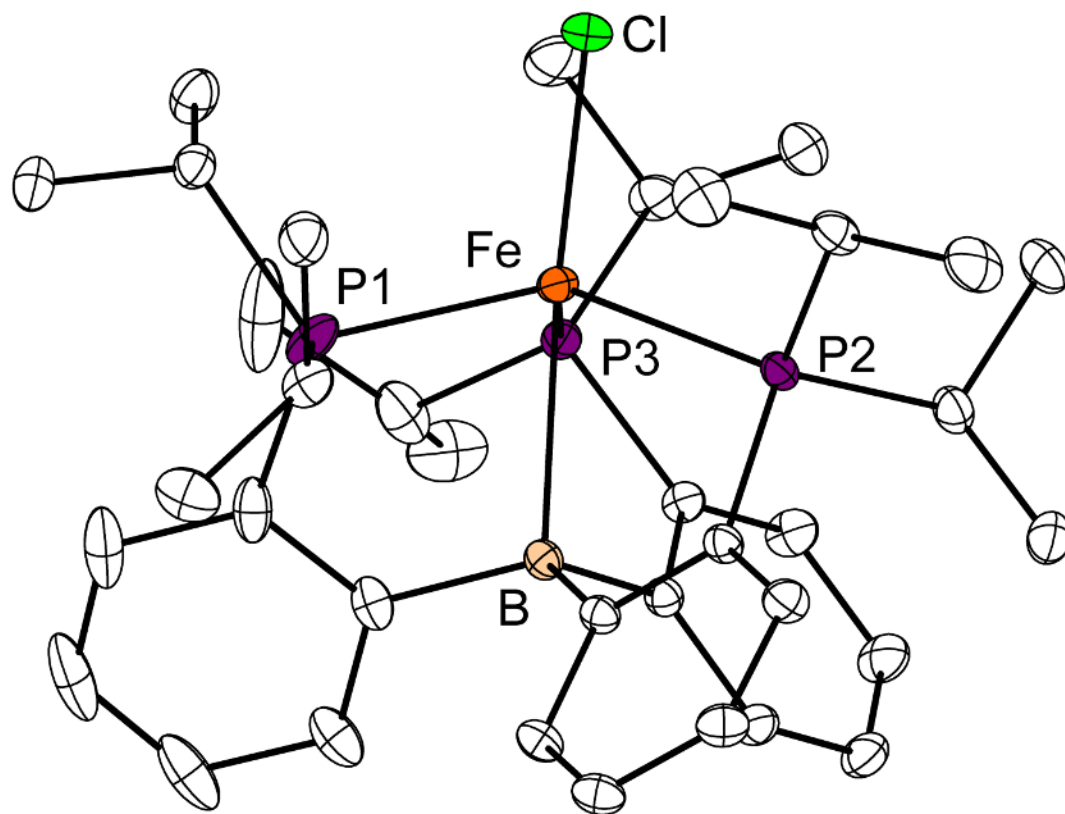
Figure A3.2. ^{1}H NMR spectrum of the reaction mixture following protonation of

[(TPB)Fe(N$_2$)][Na(12-crown-4)$_2$] compared with an authentic sample of

[(TPB)Fe(NH$_3$)][BAr$^F_4$].
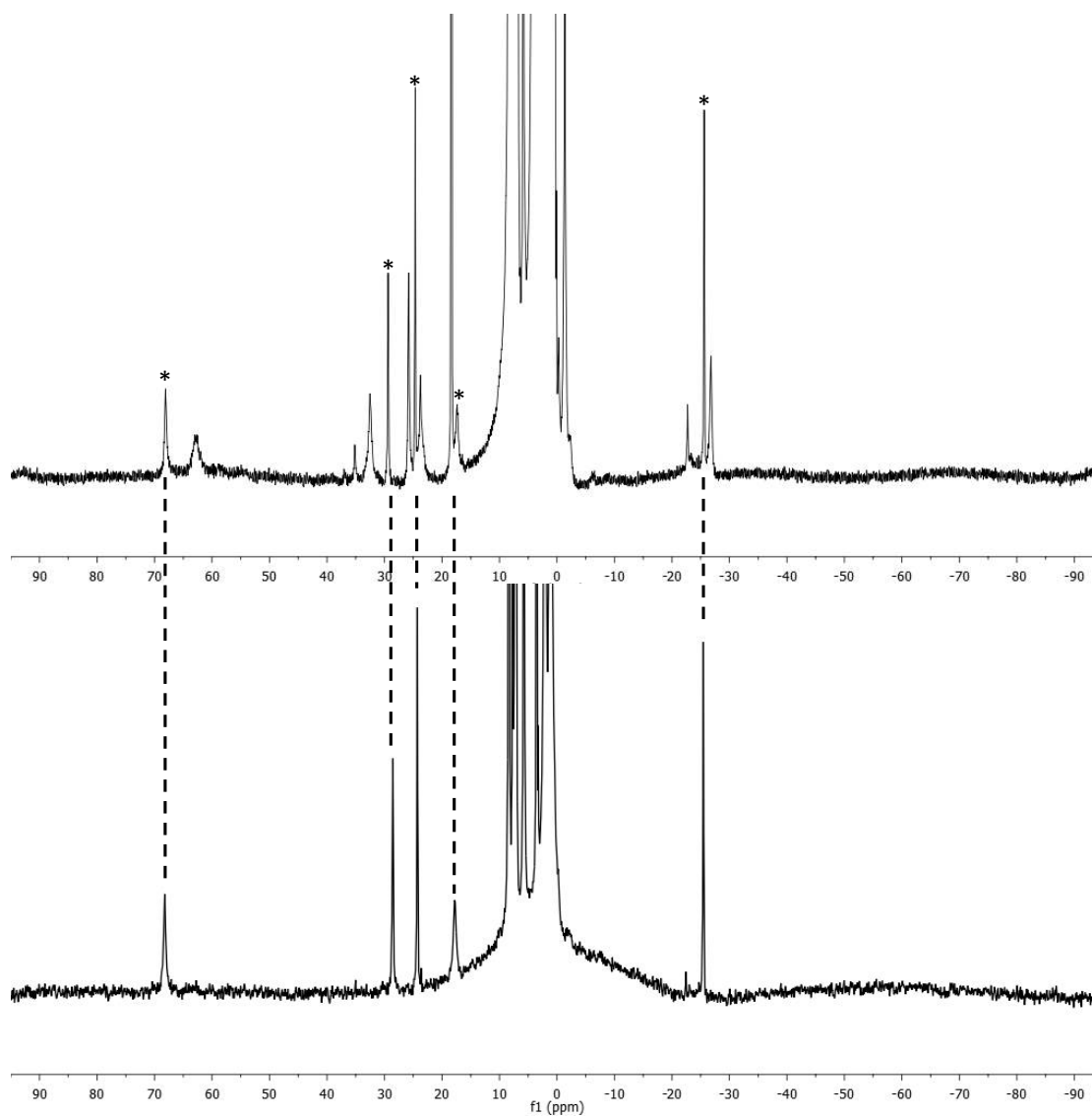
Top: reaction mixture
Bottom: authentic [(TPB)Fe(NH$_3$)][BAr$^F_4$]
Conditions: THF-d_8, 300 MHz

Figure A3.3. Calibration Curves for NH_3 and N_2H_4 UV-Vis quantification.

$y = 1.2487x + 0.0063$
$R^2 = 0.998$

$y = 0.0022x - 0.0064$
$R^2 = 0.9992$
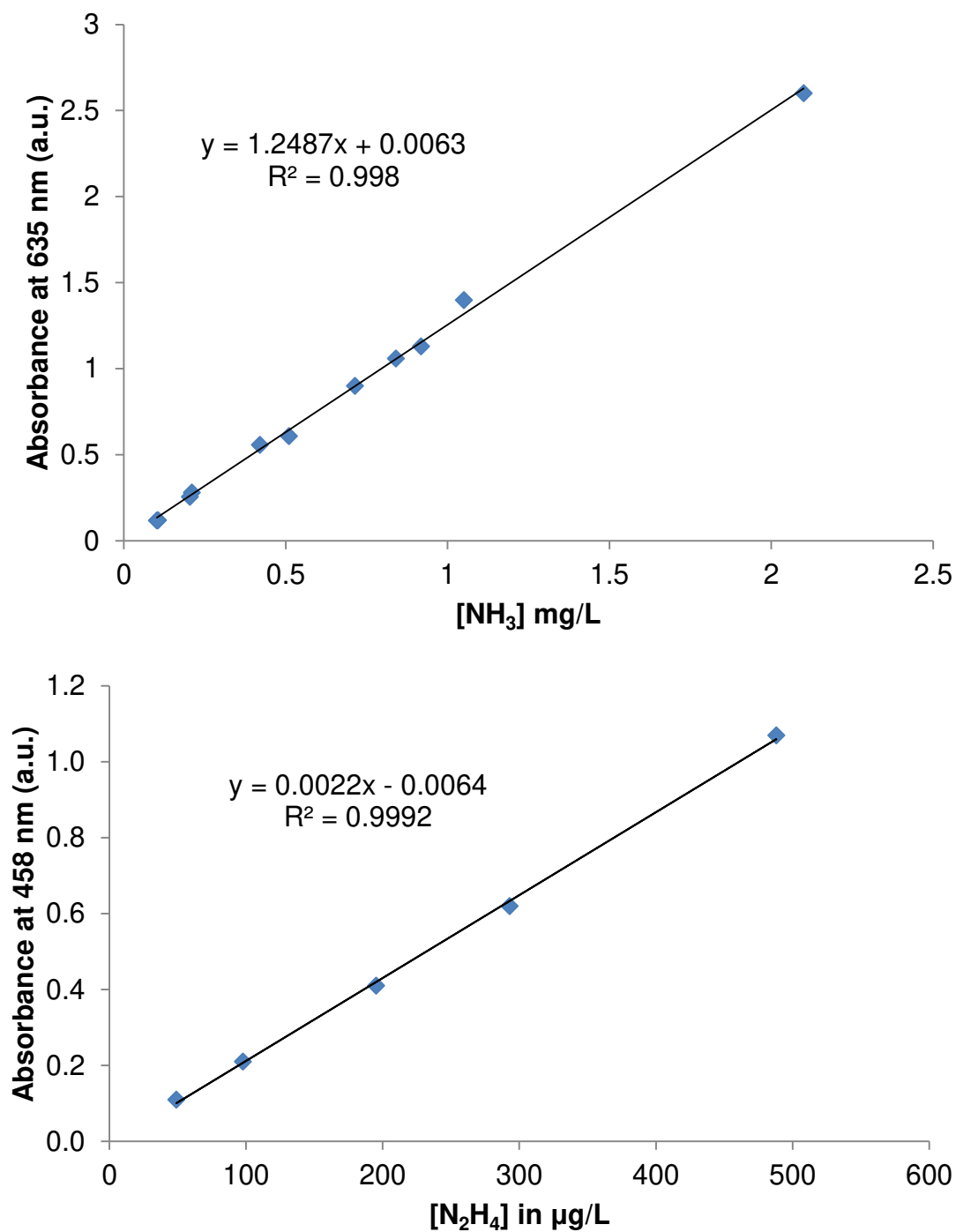
Figure A3.4. IR spectra of addition of 10 equiv HBAr$^F_4$ · 2 Et$_2$O to

[(TPB)Fe(N$_2$)][Na(12-crown-4)$_2$], followed by 12 equiv KC$_8$.
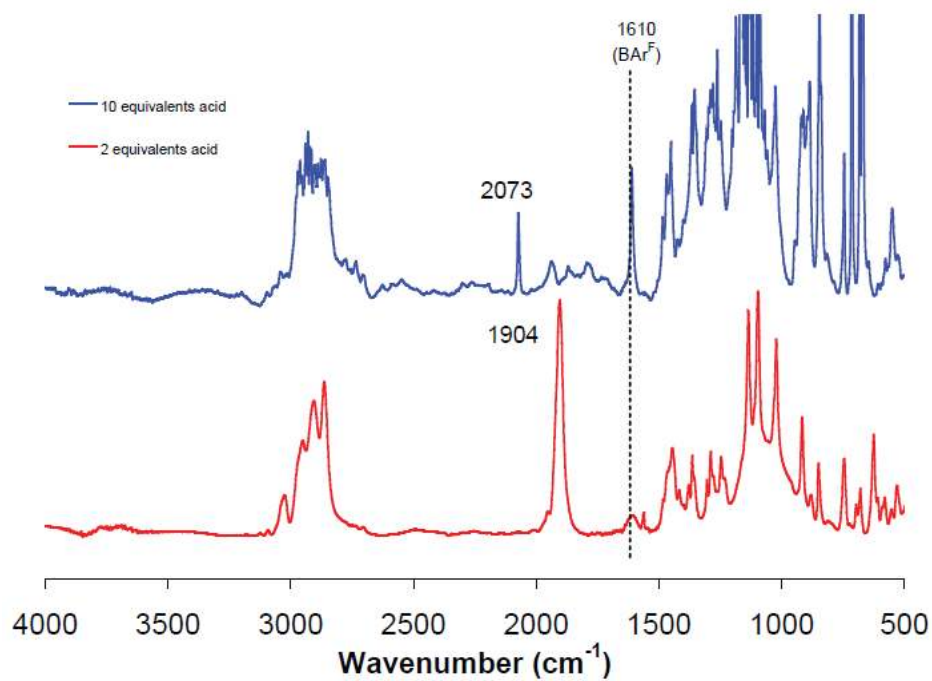
Figure A3.5. ^{31}P{^{1}H} NMR spectra of addition of 10 equiv HBAr$^F_4$ · 2 Et$_2$O to

[(TPB)Fe(N$_2$)][Na(12-crown-4)$_2$], followed by 12 equiv KC$_8$.
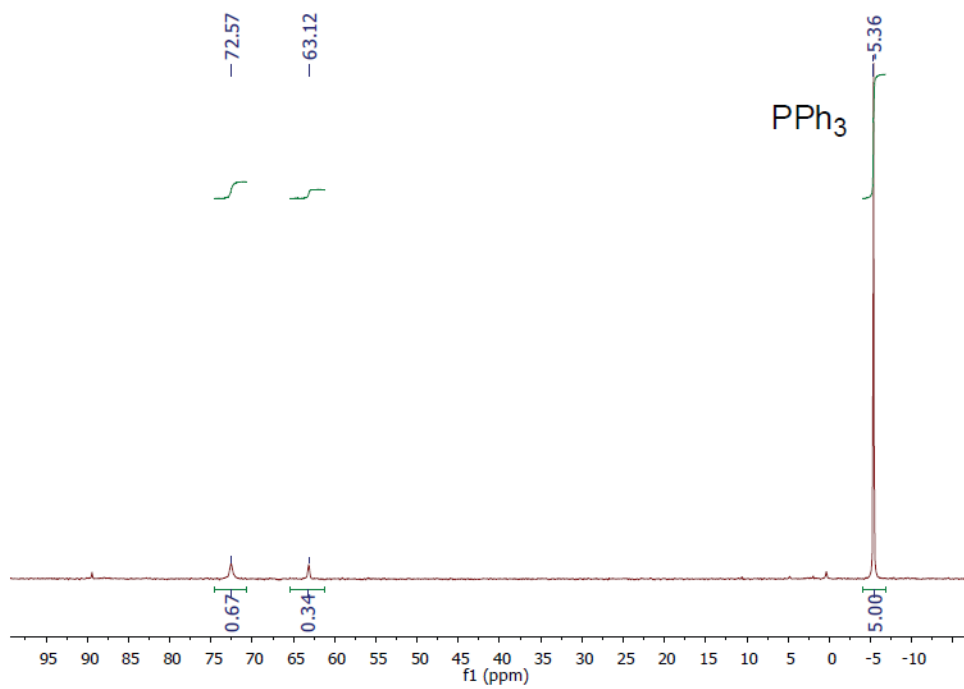
Catalytic Runs

All runs were analyzed via the methods indicated in chapter 4. Absorbances indicated

are from runs using a 20 µL aliquot from the aqueous 1 mL stock solution of the chloride

salts. Runs denoted with an asterisk indicate use of a 40 µL aliquot.

Table A3.2. N_2 reduction catalysis absorption data using $[(TPB)Fe(N_2)][Na(12\text{-crown-}4)_2]$.

Run	Absorbance	Equiv NH_3/Fe	% Yield based on H^+
A*	1.095	6.52	40.7
B*	1.150	6.84	42.7
C*	0.724	4.30	26.9
D*	1.105	6.58	41.1
E*	1.165	6.93	43.3
F*	1.339	7.97	49.8
G*	1.050	6.25	39.1
H*	1.428	8.49	53.1
I*	1.418	8.44	52.7
J*	1.008	6.00	37.5
L	0.608	7.24	45.2
M	0.579	6.89	43.1
N	0.640	7.62	47.6
O	0.592	7.05	44.1
P	0.616	7.33	45.8

Table A3.3. N_2 reduction catalysis absorption data using $[(TPB)Fe][BAr^F_4]$.

Run	Absorbance	Equiv NH_3/Fe	% Yield based on H^+
A*	1.169	6.96	43.5
B*	1.000	5.95	37.2
C*	0.911	5.42	33.9
D*	1.117	6.65	41.6

Table A3.4. Attempted N_2 reduction catalysis absorption data using (TPB)(μ-H)Fe(H)(N_2).

Run	Absorbance	Equiv NH_3/Fe	% Yield based on H^+
A*	0.084	0.50	3.1
B*	0.072	0.43	2.7
C	0.035	0.42	2.6
D	0.055	0.65	4.1

Table A3.5. Attempted N_2 reduction catalysis absorption data using $FeCl_2 \cdot 1.5$ THF.

Run	Absorbance	Equiv NH_3/Fe	% Yield based on H^+
A	0.002	0.02	0.1
B	0.011	0.13	0.8
C	0.005	0.06	0.4
D	0.007	0.08	0.5

Table A3.6. Attempted N_2 reduction catalysis absorption data using $FeCl_3$.

Run	Absorbance	Equiv NH_3/Fe	% Yield based on H^+
A	-0.0021	0	0
B	-0.0002	0	0
C	0.0002	0.002	0.01
D	0.0010	0.01	0.06

Table A3.7. Attempted N_2 reduction catalysis absorption data using $Fe(CO)_5$.

Run	Absorbance	Equiv NH_3/Fe	% Yield based on H^+
A	0.016	0.19	1.2
B	0.003	0.04	0.2
C	0.004	0.05	0.3
D	0.006	0.07	0.4

Table A3.8. Attempted N_2 reduction catalysis absorption data using $FeCp_2$.

Run	Absorbance	Equiv NH_3/Fe	% Yield based on H^+
A	0.007	0.08	0.5
B	0.018	0.21	1.3
C	0.027	0.32	2.0
D	0.015	0.18	1.1

Table A3.9. Attempted N_2 reduction catalysis absorption data in the absence of an Fe

precursor.

Run	Absorbance	Equiv NH_3/Fe	% Yield based on H^+
A	0.015	0.18	1.1
B	0.005	0.06	0.4
C	0.006	0.07	0.4
D	0.008	0.09	0.6

Table A3.10. N_2 reduction catalysis absorption data using (TPB)FeCl.

Run	Absorbance	Equiv NH_3/Fe	% Yield based on H^+
A	0.320	3.81	23.8
B	0.266	3.17	19.8
C	0.209	2.49	15.6

Table A3.11. N_2 reduction catalysis absorption data using $(TPB)FeN_2$.

Run	Absorbance	Equiv NH_3/Fe	% Yield based on H^+
A	0.177	2.11	13.2
B	0.158	1.88	11.7
C*	0.396	2.36	14.7
D*	0.580	3.45	21.6
E*	0.378	2.25	14.1
F*	0.423	2.52	15.7
G*	0.191	1.14	7.1
H*	0.460	2.74	17.1

Table A3.12. Attempted N_2 reduction catalysis absorption data using

$[(TPB)Fe(NH_3)][BAr^F_4]$.

Run	Absorbance	Equiv NH_3/Fe	% Yield based on H^+
A	0.475	5.65	35.3
B	0.487	5.80	36.2
C	0.493	5.87	36.7
D	0.472	5.62	35.1

Table A3.13. Attempted N_2 reduction catalysis absorption data using

$[(TPB)Fe(N_2H_4)][BAr^F_4]$.

Run	Absorbance	Equiv NH_3/Fe	% Yield based on H^+
A	0.531	6.32	39.5
B	0.417	4.96	31.0
C	0.580	6.90	43.1
D	0.441	5.25	32.8

Table A3.14. Absorption data for a standard catalytic run in which N_2H_4 was added prior

to $[(TPB)Fe(N_2)][Na(12\text{-}crown\text{-}4)_2]$ acid and reductant.

Run	Abs. for N_2H_4	Equiv N_2H_4/Fe	Abs. for NH_3	Equiv NH_3/Fe
A	0.085	0.16	0.771	9.18
B	0.116	0.22	0.424	5.05

Table A3.15. Absorption and gas chromatograph integration data for standard catalytic

runs.

Run	Absorbance	Equiv NH_3/Fe	% Yield based on H^+	% Yield of H_2
A	0.500	5.95	37.2	30
B	0.365	4.34	27.1	40

Table A3.16. Gas chromatograph H_2 yields for runs in the absence of an Fe precursor.

Run	% Yield of H_2
A	61
B	88

Appendix 4: Supplementary Data for Chapter 5

Table A4.1. Crystal data and structure refinement for [(TPB^{Cy})Fe(N$_2$)][Na(12-crown-4)$_2$]

(**5.1**).

Identification code	jsa32_0m
Empirical formula	C70 H114 B Fe N2 Na O9 P3
Formula weight	1310.19
Temperature	296(2) K
Wavelength	0.71073 Å
Crystal system	Orthorhombic
Space group	Pbca
Unit cell dimensions	a = 20.9220(11) Å α= 90°.
	b = 21.8896(13) Å β= 90°.
	c = 32.1770(19) Å γ = 90°.
Volume	14736.2(15) Å^3
Z	8
Density (calculated)	1.181 Mg/m^3
Absorption coefficient	0.328 mm^{-1}
F(000)	5656
Crystal size	0.45 x 0.27 x 0.03 mm^3
Theta range for data collection	1.60 to 26.38°.
Index ranges	-26<=h<=25, -27<=k<=27, -39<=l<=39
Reflections collected	228826
Independent reflections	14997 [R(int) = 0.1023]
Completeness to theta = 26.38°	99.4 %
Absorption correction	Semi-empirical from equivalents
Max. and min. transmission	0.9902 and 0.8663
Refinement method	Full-matrix least-squares on F^2
Data / restraints / parameters	14997 / 1861 / 1041
Goodness-of-fit on F^2	1.046
Final R indices [I>2sigma(I)]	R1 = 0.0567, wR2 = 0.1260
R indices (all data)	R1 = 0.0965, wR2 = 0.1458
Largest diff. peak and hole	0.964 and -0.495 e.Å^{-3}

Table A4.2. Crystal data and structure refinement for [(DPB)Fe(N$_2$)][K(Bz15-crown-5)$_2$]

(**5.3**).

Identification code	dlms120
Empirical formula	C66 H89 B Fe K N2 O12 P2
Formula weight	1270.09
Temperature	100(2) K
Wavelength	0.71073 Å
Crystal system	Triclinic
Space group	P-1
Unit cell dimensions	a = 15.072(4) Å α= 65.274(8)°.
	b = 16.020(2) Å β= 67.441(8)°.
	c = 16.354(3) Å γ= 76.842(10)°.
Volume	3301.5(11) Å^3
Z	2
Density (calculated)	1.278 Mg/m^3
Absorption coefficient	0.400 mm^{-1}
F(000)	1350
Crystal size	0.30 x 0.10 x 0.10 mm^3
Theta range for data collection	1.69 to 30.19°.
Index ranges	-21<=h<=21, -22<=k<=21, -22<=l<=22
Reflections collected	119765
Independent reflections	18004 [R(int) = 0.0608]
Completeness to theta = 25.00°	100.0 %
Absorption correction	Semi-empirical from equivalents
Max. and min. transmission	0.9611 and 0.8893
Refinement method	Full-matrix least-squares on F^2
Data / restraints / parameters	18004 / 848 / 797
Goodness-of-fit on F^2	1.024
Final R indices [I>2sigma(I)]	R1 = 0.0476, wR2 = 0.1120
R indices (all data)	R1 = 0.0840, wR2 = 0.1279
Largest diff. peak and hole	1.100 and -0.812 e.Å^{-3}

Table A4.3. Crystal data and structure refinement for (TPB^{Cy})FeCl (**5.9**).

Identification code	jsa31_0m
Empirical formula	C54 H78 B Cl Fe P3
Formula weight	922.18
Temperature	296(2) K
Wavelength	0.71073 Å
Crystal system	Triclinic
Space group	P-1
Unit cell dimensions	a = 20.7382(9) Å α= 88.578(3)°.
	b = 21.9442(10) Å β= 73.669(2)°.
	c = 23.5705(11) Å γ= 88.726(2)°.
Volume	10289.3(8) Å^3
Z	8
Density (calculated)	1.191 Mg/m^3
Absorption coefficient	0.472 mm^{-1}
F(000)	3960
Crystal size	0.21 x 0.21 x 0.11 mm^3
Theta range for data collection	1.37 to 33.14°.
Index ranges	-31<=h<=31, -33<=k<=33, -36<=l<=36
Reflections collected	456639
Independent reflections	77830 [R(int) = 0.0761]
Completeness to theta = 33.14°	99.2 %
Absorption correction	Semi-empirical from equivalents
Max. and min. transmission	0.9499 and 0.9073
Refinement method	Full-matrix least-squares on F^2
Data / restraints / parameters	77830 / 2511 / 2412
Goodness-of-fit on F^2	1.119
Final R indices [I>2sigma(I)]	R1 = 0.0704, wR2 = 0.1691
R indices (all data)	R1 = 0.1044, wR2 = 0.1862
Largest diff. peak and hole	2.352 and -0.854 e.Å^{-3}

Table A4.4. Crystal data and structure refinement for (TPB^{Ph})FeCl (**5.10**).

Identification code	snm03
Empirical formula	C54 H42 B Cl Fe P3
Formula weight	885.90
Temperature	296(2) K
Wavelength	0.71073 Å
Crystal system	Monoclinic
Space group	P2(1)/c
Unit cell dimensions	a = 12.9941(8) Å α= 90°.
	b = 17.1371(11) Å β= 98.255(3)°.
	c = 19.5570(11) Å γ = 90°.
Volume	4309.9(5) Å^3
Z	4
Density (calculated)	1.365 Mg/m^3
Absorption coefficient	0.562 mm^{-1}
F(000)	1836
Crystal size	
Theta range for data collection	1.58 to 33.16°.
Index ranges	-19<=h<=19, -26<=k<=26, -30<=l<=29
Reflections collected	92375
Independent reflections	16422 [R(int) = 0.0535]
Completeness to theta = 33.16°	99.8 %
Absorption correction	Semi-empirical by equivalents
Refinement method	Full-matrix least-squares on F^2
Data / restraints / parameters	16422 / 0 / 541
Goodness-of-fit on F^2	1.015
Final R indices [I>2sigma(I)]	R1 = 0.0408, wR2 = 0.0957
R indices (all data)	R1 = 0.0643, wR2 = 0.1063
Largest diff. peak and hole	1.247 and -0.403 e.Å^{-3}

Table A4.5. Crystal data and structure refinement for (TPB$^{Ph'}$) (**5.11**).

Identification code	snm01
Empirical formula	C56 H42 B Fe O P3
Formula weight	890.47
Temperature	296(2) K
Wavelength	0.71073 Å
Crystal system	Orthorhombic
Space group	P2(1)2(1)2(1)
Unit cell dimensions	a = 10.8211(6) Å α= 90°.
	b = 18.6466(12) Å β= 90°.
	c = 23.1518(13) Å γ = 90°.
Volume	4671.5(5) Å^3
Z	4
Density (calculated)	1.266 Mg/m^3
Absorption coefficient	0.465 mm^{-1}
F(000)	1848
Crystal size	0.259 x 0.192 x 0.085 mm^3
Theta range for data collection	1.76 to 30.51°.
Index ranges	-15<=h<=15, -26<=k<=26, -33<=l<=32
Reflections collected	60196
Independent reflections	14181 [R(int) = 0.0531]
Completeness to theta = 30.51°	99.9 %
Absorption correction	Semi-empirical by equivalents
Refinement method	Full-matrix least-squares on F^2
Data / restraints / parameters	14181 / 0 / 598
Goodness-of-fit on F^2	1.039
Final R indices [I>2sigma(I)]	R1 = 0.0582, wR2 = 0.1551
R indices (all data)	R1 = 0.0778, wR2 = 0.1673
Absolute structure parameter	0.182(16)
Largest diff. peak and hole	1.518 and -0.983 e.Å^{-3}

Catalytic Runs

All runs were analyzed via the methods indicated in Chapter 4. Absorbances indicated

are from runs using a 20 μL aliquot from the aqueous 1 mL stock solution of the chloride

salts. Runs denoted with an asterisk indicate use of a 40 μL aliquot.

Table A4.6. N_2 reduction catalysis absorption data using $[(TPB^{Cy})Fe(N_2)][Na(12-crown-4)_2]$ (**5.1**).

Run	Absorbance	Equiv NH_3/Fe	% Yield based on H^+
A	0.275	3.27	20.4
B	0.254	3.02	18.9
C	0.278	3.31	20.7

Table A4.7. N_2 reduction catalysis absorption data using $[(TPB^{Ph})Fe(N_2)][Na(12-crown-4)_2]$ (**5.2**).

Run	Absorbance	Equiv NH_3/Fe	% Yield based on H^+
A	0.155	1.84	11.5
B	0.155	1.84	11.5
C	0.209	2.49	15.6
D	0.222	2.64	16.5

Table A4.8. Attempted N_2 reduction catalysis absorption data using $[(DPB)Fe(N_2)][K(Bz15-crown-5)_2]$ (**5.3**).

Run	Absorbance	Equiv NH_3/Fe	% Yield based on H^+
A	0.133	1.73	10.8
B	0.131	1.70	10.6
C	0.170	2.10	13.1

Table A4.9. Attempted N_2 reduction catalysis absorption data using

$[(SiP^{iPr}_3)Fe(N_2)][Na(12\text{-}crown\text{-}4)_2]$.

Run	Absorbance	Equiv NH₃/Fe	% Yield based on H⁺
A*	0.203	1.21	7.5
B*	0.059	0.35	2.1
C*	0.064	0.38	2.3
D*	0.183	1.09	6.8

Table A4.10. Attempted N_2 reduction catalysis absorption data using

$[PhBP^{iPr}_3]FeN_2MgCl \cdot 2$ THF.

Run	Absorbance	Equiv NH₃/Fe	% Yield based on H⁺
A	0.115	1.37	8.6
B	0.112	1.33	8.3
C	0.085	1.01	6.3
D	0.088	1.05	6.6

Table A4.11. Attempted N_2 reduction catalysis absorption data using

$(C_2H_4PCy_2)_3PFe(N_2)$.

Run	Absorbance	Equiv NH₃/Fe	% Yield based on H⁺
A	0.102	0.74	4.6
B	0.068	0.50	3.1
C	0.122	0.75	4.7

Note that that the amount of catalyst varied in these runs, so the usual correlation between

absorbance and equiv. of NH₃ is off.

Table A4.12. Attempted N_2 reduction catalysis absorption data using Fe(depe)$_2$N$_2$.

Run	Absorbance	Equiv NH$_3$/Fe	% Yield based on H$^+$
A	0.028	0.33	2.1
B	0.057	0.67	4.2
C	0.033	0.39	2.4
D	0.021	0.25	1.6

Table A4.13. N_2 reduction catalysis absorption data using iPr$_2$O.

Run	Absorbance	Equiv NH$_3$/Fe	% Yield based on H$^+$
A	0.578	6.88	43.0
B	0.541	6.44	40.2
C	0.560	6.67	41.7
D	0.516	6.14	38.4

Table A4.14. N_2 reduction catalysis absorption data using DME.

Run	Absorbance	Equiv NH$_3$/Fe	% Yield based on H$^+$
A*	0.532	3.17	19.8
B*	0.586	3.49	21.8
C*	0.591	3.52	22.0
D*	0.555	3.30	20.6

Table A4.15. N_2 reduction catalysis absorption data using Bu$_2$O.

Run	Absorbance	Equiv NH$_3$/Fe	% Yield based on H$^+$
A*	0.534	3.17	19.8
B*	0.530	3.15	19.7

Table A4.16. Attempted N_2 reduction catalysis absorption data using toluene.

Run	Absorbance	Equiv NH_3/Fe	% Yield based on H^+
A*	0.178	1.06	6.6
B*	0.082	0.49	3.1

Table A4.17. N_2 reduction catalysis absorption data using 1:6 Et_2O:toluene.

Run	Absorbance	Equiv NH_3/Fe	% Yield based on H^+
A*	0.535	3.18	19.9
B*	0.516	3.07	19.2

Table A4.18. Attempted N_2 reduction catalysis absorption data using CoCp*$_2$.

Run	Absorbance	Equiv NH_3/Fe	% Yield based on H^+
A	0.103	1.23	7.7
B	0.062	0.74	4.6
C	0.045	0.27	1.7
D	0.069	0.41	2.6

Table A4.19. Attempted N_2 reduction catalysis absorption data using CrCp*$_2$.

Run	Absorbance	Equiv NH_3/Fe	% Yield based on H^+
A	0.012	0.14	0.9
B	0.016	0.19	1.2
C*	0.022	0.13	0.8
D*	0.007	0.04	0.2

Table A4.20. Attempted N_2 reduction catalysis absorption data using $NaC_{10}H_8$.

Run	Absorbance	Equiv NH_3/Fe	% Yield based on H^+
A	0.075	0.89	5.6
B	0.094	1.12	7.0

Table A4.21. Attempted N_2 reduction catalysis absorption data using K as the reductant.

Run	Absorbance	Equiv NH_3/Fe	% Yield based on H^+
A	0.060	0.71	4.4
B	0.049	0.58	3.6
C	0.025	0.30	1.9
D	0.019	0.23	1.4

Table A4.22. Attempted N_2 reduction catalysis absorption data using $MgC_{14}H_{10} \cdot$ 3 THF.

Run	Absorbance	Equiv NH_3/Fe	% Yield based on H^+
A	0.025	0.30	1.9
B	0.022	0.26	1.6

Table A4.23. N_2 reduction catalysis absorption data using Na/Hg.

Run	Absorbance	Equiv NH_3/Fe	% Yield based on H^+
A	0.170	2.02	12.6
B	0.179	2.13	13.3

Table A4.24. Attempted N_2 reduction catalysis absorption data using

trifluoromethanesulfonic acid.

Run	Absorbance	Equiv NH_3/Fe	% Yield based on H^+
A*	0.101	0.60	3.7
B*	0.069	0.41	2.6
C*	0.081	0.48	3.0
D*	0.067	0.40	2.5

Table A4.25. Attempted N_2 reduction catalysis absorption data using anhydrous HCl.

Run	Absorbance	Equiv NH_3/Fe	% Yield based on H^+
A	0.007	0.08	0.5
B	0.005	0.06	0.4
C	0.010	0.12	0.8
D	0.004	0.05	0.3

Table A4.26. Attempted N_2 reduction catalysis absorption data using

[Lutidinium][BAr$^F_4$] as the acid.

Run	Absorbance	Equiv NH_3/Fe	% Yield based on H^+
A	0.026	0.31	1.9
B	0.004	0.05	0.3
C*	0.013	0.08	0.5
D*	0.018	0.11	0.7

Table A4.27. N_2 reduction catalysis absorption data using [2,6-dimethylanilinium][OTf].

Run	Absorbance	Equiv NH_3/Fe	% Yield based on H^+
A*	0.415	2.47	15.4
B*	0.288	1.71	10.7

Table A4.28. N_2 reduction catalysis absorption data using [2,6-dimethylanilinium][BАr$^F_4$].

Run	Absorbance	Equiv NH$_3$/Fe	% Yield based on H$^+$
A	0.255	3.03	18.9
B	0.233	2.77	17.3

Table A4.29. Attempted N_2 reduction catalysis at RT.

Run	Absorbance	Equiv NH$_3$/Fe	% Yield based on H$^+$
A	0.158	1.88	11.7
B	0.130	1.55	9.7
C	0.114	1.36	8.5
D	0.045	0.54	3.4

Table A4.30. N_2 reduction catalysis absorption data at -110 °C.

Run	Absorbance	Equiv NH$_3$/Fe	% Yield based on H$^+$
A	0.452	5.38	33.6
B	0.450	5.36	33.5

Appendix 5: Supplementary Data for Chapter 6

Figure A5.1. 77 K EPR spectrum of the addition of 1 equivalent of HBAr$^F_4$ · 2 Et$_2$O to
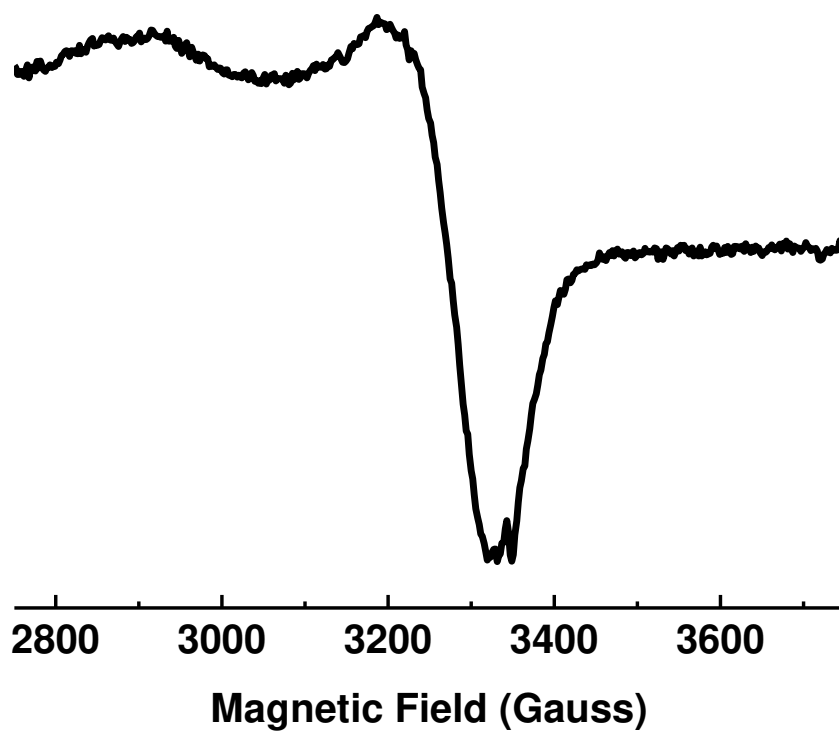
complex **4.1.**

Figure A5.2. 10 K EPR spectrum of the addition of 10 equivalents of HBAr$^F_4$ · 2 Et$_2$O to complex **4.1** followed by the addition of 20 equivalents of KC$_8$.
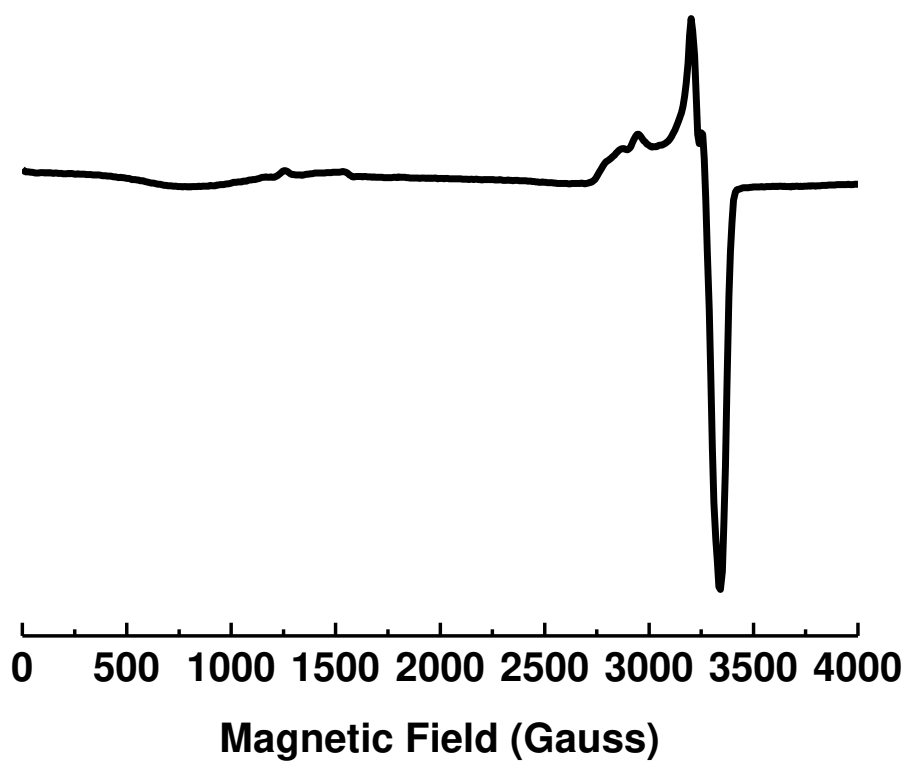
Figure A5.3. M06L/TZVP(Fe)/SVP(P,N,B)/6-31G(C, H) optimized structure of [(TPB)Fe(HNNH)]⁺.
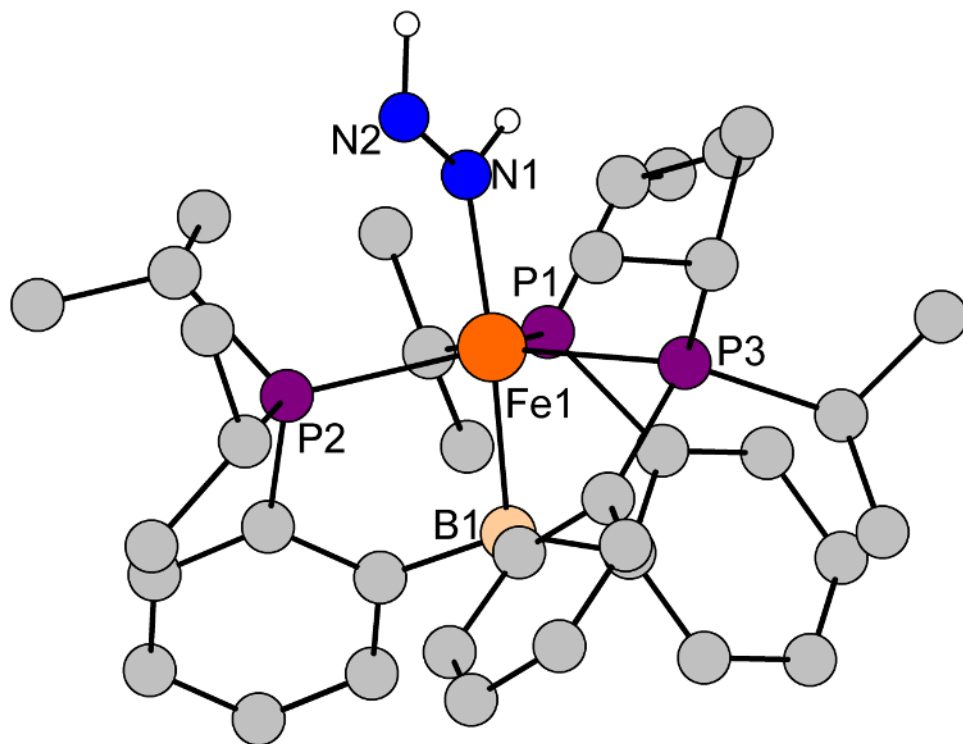
Selected bond lengths (Å) and angles (°): Fe1-N1 = 1.907, N1-N2 = 1.267, Fe1-P1 = 2.383, Fe1-P2 = 2.301, Fe1-P3 = 2.294, Fe1-B1 = 2.243, P1-Fe1-P2 = 107.42, P2-Fe1-P3 = 149.37, P3-Fe1-P1 = 98.61.

Figure A5.4. M06L/TZVP(Fe)/SVP(P,N,B)/6-31G(C, H) optimized structure of

[(TPB)Fe(HNNH)]$^+$ with spin density plotted with an isovalue of 0.006.
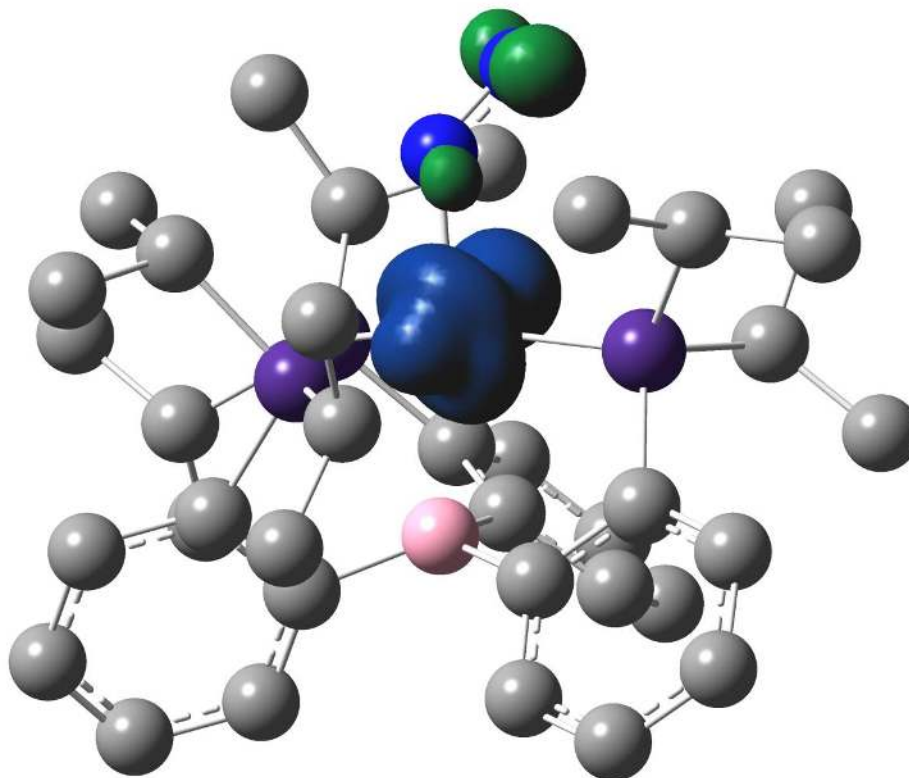
Table A5.1. M06L/TZVP(Fe)/SVP(P,N,B)/6-31G(C, H) DFT Optimized coordinates [Å]

for [(TPB)Fe≡N-NH$_2$], **6.1**.

```
Fe    0.042100   -0.321600   -1.074300
P    -0.433100    1.899600   -0.770400
P     2.243600   -0.595200   -0.421900
P    -1.966100   -1.314100   -0.315900
N     0.280800   -0.886100   -2.660100
C    -1.220100   -2.057900    1.178300
C     2.433700   -2.402800    0.086900
H     1.447200   -2.659500    0.495700
C    -0.222900   -1.280500    1.826500
C     2.651100    0.414000    1.032800
C    -1.378000    2.451200   -2.292800
H    -0.648500    2.305300   -3.102500
C    -1.159400    1.230700    1.689700
C     1.708100    1.631800    2.896800
H     0.844800    1.951500    3.478600
C    -2.409300   -2.791500   -1.393400
H    -3.262100   -3.295100   -0.909400
B     0.054700    0.233300    1.427800
C     0.426500   -1.852400    2.944600
H     1.198900   -1.277000    3.452400
C     0.088100   -3.120600    3.419400
H     0.598000   -3.531400    4.286900
C     3.935900    0.828200    1.417500
H     4.810700    0.512100    0.858700
C    -0.916900   -3.860200    2.784000
H    -1.193000   -4.842400    3.156300
C     4.102700    1.655800    2.532200
H     5.097700    1.983800    2.818900
C     2.986100    2.060900    3.268700
H     3.111300    2.710500    4.131000
C     3.482800   -0.364300   -1.798300
H     3.117800   -1.093100   -2.539000
C    -1.888300    1.263800    2.892500
H    -1.661800    0.539700    3.674200
C    -1.480300    2.176100    0.688800
C     1.005300    3.122800   -0.638000
H     1.835000    2.482600   -0.306200
C    -3.626700   -0.603600    0.271300
H    -3.412400    0.456500    0.461300
C    -2.488000    3.130300    0.889300
H    -2.724400    3.866000    0.127600
C    -2.909300    2.200800    3.088200
```

H	-3.473600	2.203500	4.017200
C	-2.815500	-2.356900	-2.811500
H	-3.021900	-3.243900	-3.422100
H	-1.998800	-1.802500	-3.288400
H	-3.706600	-1.727400	-2.837100
C	-3.208300	3.133700	2.089800
H	-3.999500	3.862200	2.242600
C	-1.232100	-3.774300	-1.505300
H	-1.474700	-4.560000	-2.230100
H	-0.974500	-4.255300	-0.559000
H	-0.336900	-3.247000	-1.857500
C	-1.826100	3.931000	-2.278900
H	-1.786000	4.344800	-3.292800
H	-1.216300	4.572900	-1.637200
H	-2.863600	4.010600	-1.939100
C	3.342100	1.030500	-2.413400
H	3.989900	1.130100	-3.292000
H	3.629400	1.812600	-1.698600
H	2.307600	1.213400	-2.723800
C	-1.566600	-3.329100	1.668000
H	-2.346500	-3.910000	1.180000
C	1.415400	3.778200	-1.969500
H	2.429500	4.183400	-1.871500
H	0.759500	4.613700	-2.231400
H	1.423100	3.083000	-2.814100
C	-2.587700	1.550000	-2.561400
H	-3.111200	1.878500	-3.466900
H	-3.296700	1.612700	-1.725000
H	-2.296900	0.501700	-2.692000
C	2.679600	-3.310900	-1.126200
H	2.586100	-4.360700	-0.826100
H	3.680600	-3.176400	-1.550600
H	1.945600	-3.126800	-1.920000
C	0.786500	4.193000	0.442100
H	1.689400	4.809600	0.530300
H	0.582000	3.751500	1.421600
H	-0.049300	4.858800	0.193100
C	3.466600	-2.634600	1.196800
H	3.447400	-3.689400	1.497200
H	3.248400	-2.030600	2.082600
H	4.487500	-2.400000	0.875000
C	-4.759200	-0.691800	-0.762100
H	-5.650300	-0.205800	-0.348100
H	-5.030300	-1.731800	-0.978600
H	-4.523400	-0.191900	-1.705100
C	4.957700	-0.686700	-1.510100

```
H     5.492800   -0.801400   -2.460800
H     5.097700   -1.610300   -0.941600
H     5.448300    0.127300   -0.968900
C    -4.089300   -1.245400    1.587700
H    -5.017700   -0.761200    1.913900
H    -3.352000   -1.134100    2.386800
H    -4.299900   -2.315700    1.463800
C     1.505500    0.800200    1.777800
N     0.678000   -1.514300   -3.702600
H     0.679500   -1.051700   -4.610700
H     0.860300   -2.519600   -3.697500
```

Table A5.2. M06L/TZVP(Fe)/SVP(P,N,B)/6-31G(C,H) DFT Optimized coordinates [Å]

for [(TPB)Fe(HNNH)]⁺.

```
Fe    0.044400   -0.524300   -0.675200
P    -0.661500    1.748300   -0.807700
P     2.333900   -0.522200   -0.450200
P    -1.983900   -1.486900   -0.206400
N     0.077800   -0.726900   -2.571300
C    -0.938100   -2.055400    1.163400
C     2.911100   -2.255000    0.020600
H     2.029400   -2.678800    0.520000
C     0.069500   -1.132800    1.595000
C     2.687200    0.633800    0.915300
C    -1.708400    2.120200   -2.328800
H    -1.014600    1.996000   -3.176300
C    -1.201700    1.279300    1.707600
C     1.733000    2.068800    2.619900
H     0.867300    2.440800    3.165600
C    -2.364900   -3.033300   -1.199600
H    -3.113100   -3.614800   -0.636200
B     0.106800    0.459500    1.339700
C     0.987900   -1.610000    2.578400
H     1.767800   -0.942300    2.932700
C     0.868700   -2.869700    3.153100
H     1.551500   -3.170200    3.943000
C     3.968000    1.097700    1.257000
H     4.847400    0.710300    0.751100
C    -0.137400   -3.747900    2.722100
H    -0.238200   -4.729700    3.175800
C     4.127300    2.055900    2.263500
H     5.121000    2.412900    2.518300
C     3.006600    2.549200    2.937900
H     3.127600    3.297400    3.716700
C     3.350200   -0.094400   -1.954500
H     3.053000   -0.893600   -2.651000
C    -1.857100    1.320300    2.949300
H    -1.464600    0.743700    3.785600
C    -1.731800    2.036800    0.636700
C     0.606200    3.166500   -0.791900
H     1.525600    2.652300   -0.477700
C    -3.615100   -0.931900    0.579500
H    -3.473500    0.138500    0.776100
C    -2.888400    2.811000    0.798800
H    -3.296500    3.396900   -0.018900
C    -3.023900    2.077400    3.110000
```

H	-3.536100	2.089600	4.068700
C	-2.946200	-2.668500	-2.578400
H	-3.195200	-3.585400	-3.124200
H	-2.199800	-2.127600	-3.173500
H	-3.849600	-2.056600	-2.529000
C	-3.538700	2.818000	2.039500
H	-4.444000	3.404200	2.170400
C	-1.104000	-3.888700	-1.427300
H	-1.354900	-4.729100	-2.084800
H	-0.683200	-4.301500	-0.508400
H	-0.317400	-3.307600	-1.924400
C	-2.266600	3.566100	-2.374000
H	-2.132800	4.003400	-3.369100
H	-1.795700	4.239000	-1.653100
H	-3.341200	3.560900	-2.163100
C	2.905700	1.242900	-2.546400
H	3.382800	1.413400	-3.518700
H	3.181400	2.078000	-1.889700
H	1.819000	1.269700	-2.685300
C	-1.014400	-3.350000	1.718700
H	-1.789700	-4.033300	1.381400
C	0.880400	3.830900	-2.155600
H	1.864100	4.314700	-2.124600
H	0.147900	4.611100	-2.380900
H	0.893100	3.130800	-2.996600
C	-2.864100	1.123300	-2.477700
H	-3.453700	1.351200	-3.373400
H	-3.531500	1.200000	-1.609200
H	-2.528300	0.082200	-2.543200
C	3.181200	-3.116300	-1.223800
H	3.294600	-4.163100	-0.919600
H	4.106600	-2.824300	-1.732700
H	2.361800	-3.059200	-1.949800
C	0.296300	4.242000	0.260200
H	1.120000	4.966200	0.292200
H	0.180700	3.819300	1.261700
H	-0.622700	4.792000	0.023000
C	4.074700	-2.296700	1.018300
H	4.253100	-3.334200	1.326900
H	3.864500	-1.709300	1.918200
H	5.008000	-1.920400	0.583800
C	-4.832400	-1.107100	-0.339400
H	-5.717800	-0.709100	0.169700
H	-5.029700	-2.164100	-0.553200
H	-4.736100	-0.575200	-1.290100
C	4.878800	-0.128100	-1.804100

```
H      5.340100   -0.113500   -2.799200
H      5.242300   -1.021400   -1.288700
H      5.243900    0.754200   -1.269100
C     -3.865600   -1.645000    1.915700
H     -4.799800   -1.271400    2.351900
H     -3.062600   -1.465800    2.635800
H     -3.974400   -2.729500    1.783700
C      1.535200    1.102400    1.614400
N      0.696100   -1.586000   -3.267700
H      0.524200   -1.437200   -4.272600
H     -0.471600   -0.036500   -3.111300
```

Table A5.3. DFT optimized energies [kcal/mol] for $[(TPB)Fe(N_2H_2)]^+$ congeners of different structures and spin states.

Complex	BP86	M06L
$S = 1/2$ [(TPB)Fe≡N-NH$_2$]$^+$	0	0
$S = 1/2$ [(TPB)Fe(HNNH)]$^+$	17.0	8.2
$S = 3/2$ [(TPB)Fe≡N-NH$_2$]$^+$	5.3	-6.9
$S = 3/2$ [(TPB)Fe(HNNH)]$^+$	11.0	-5.6